Structures Research Report 2026/ P0260410-P0260749

University of Florida Civil and Coastal Engineering

UF

University of Florida
Civil and Coastal Engineering

Deliverable 6: Final Report February 2026

Bond Performance of Post-tensioning Tendons with Corrosion Inhibitor

Principal investigator:
Gary R. Consolazio, Ph.D.

Technical advisor:
H.R. Trey Hamilton, Ph.D., P.E.

Graduate research assistant:
Mahesh Yumnam, Ph.D.

Department of Civil and Coastal Engineering
University of Florida
P.O. Box 116580
Gainesville, Florida 32611

Sponsor:
Florida Department of Transportation (FDOT)
Olga Iatsko, Ph.D., P.E. – Project manager

Contract:
UF Project No. P0260410-P0260749
FDOT Contract No. BED31-977-07

DISCLAIMER

The opinions, findings, and conclusions expressed in this publication are those of the authors and not necessarily those of the State of Florida Department of Transportation.

SI (MODERN METRIC) CONVERSION FACTORS

*APPROXIMATE CONVERSIONS **TO** SI UNITS*

SYMBOL	WHEN YOU KNOW	MULTIPLY BY	TO FIND	SYMBOL
LENGTH				
in	inches	25.4	millimeters	mm
ft	feet	0.305	meters	m
yd	yards	0.914	meters	m
mi	miles	1.61	kilometers	km
AREA				
in^2	square inches	645.2	square millimeters	mm^2
ft^2	square feet	0.093	square meters	m^2
yd^2	square yard	0.836	square meters	m^2
ac	acres	0.405	hectares	ha
mi^2	square miles	2.59	square kilometers	km^2
VOLUME				
fl oz	fluid ounces	29.57	milliliters	mL
gal	gallons	3.785	liters	L
ft^3	cubic feet	0.028	cubic meters	m^3
yd^3	cubic yards	0.765	cubic meters	m^3
NOTE: volumes greater than 1000 L shall be shown in m^3				
MASS				
oz	ounces	28.35	grams	g
lb	pounds	0.454	kilograms	kg
T	short tons (2,000 lb)	0.907	megagrams	Mg (or "t")
TEMPERATURE (exact degrees)				
°F	Fahrenheit	5(F-32)/9 or (F-32)/1.8	Celsius	°C
FORCE and PRESSURE or STRESS				
kip	1,000 pound force	4.45	kilonewtons	kN
lbf	pound force	4.45	newtons	N
lbf/in^2	pound force per square inch	6.89	kilopascals	kPa
ksi	kips force per square inch	6.89	megapascals	MPa

TECHNICAL REPORT DOCUMENTATION PAGE

1. Report No.	2. Government Accession No.	3. Recipient's Catalog No.

4. Title and Subtitle	5. Report Date
Bond Performance of Post-tensioning Tendons with Corrosion Inhibitor	February, 2026
	6. Performing Organization Code
	8. Performing Organization Report No.
7. Author(s)	
Gary R. Consolazio, H. R. Trey Hamilton, Mahesh Yumnam	2026/P0260410-P0260749
9. Performing Organization Name and Address	10. Work Unit No. (TRAIS)
University of Florida Department of Civil and Coastal Engineering 365 Weil Hall, P.O. Box 116580 Gainesville, FL 32611-6580	11. Contract or Grant No. BED31-977-07
12. Sponsoring Agency Name and Address	13. Type of Report and Period Covered
Florida Department of Transportation Research Management Center 605 Suwannee Street, MS 30 Tallahassee, FL 32399-0450	Final Report
	14. Sponsoring Agency Code

15. Supplementary Notes

16. Abstract

Corrosion of steel tendons in post-tensioned bridge girders can lead to section loss and, if left unaddressed, may result in strand rupture and a corresponding reduction in girder strength. In the state of Florida, a number of remedial measures have been explored and implemented to address such issues, including the use of corrosion inhibitors to mitigate strand corrosion. Impregnation of corrosion-inhibiting fluids into grouted post-tensioned tendons has been shown to be effective in reducing strand corrosion. However, the impregnation of these fluids may also have the potential to adversely affect the bond between steel tendons and the surrounding grout. Past studies involving pull-out tests of unstressed strands in grout have indicated that a reduction in bond strength may result from the use of corrosion-inhibiting fluids. However, relatively little research has been carried out to determine the effect that such fluids may have on the flexural performance of full-scale post-tensioned concrete bridge girders.

In this study, full-scale experimental flexural tests of post-tensioned concrete beams with grouted tendons were performed to directly evaluate the extent to which impregnation with a corrosion-inhibiting fluid might affect either the strength level performance (nominal flexural strength) or the service level performance (crack severity) of such beams. Variables that could potentially influence the bond condition between tendon and grout, due to the presence of corrosion inhibitor, were incorporated into the experimental test program. These variables included tendon size (6-, 12-, and 19-strands), tendon profile (straight, draped), grout type (pre-packaged, plain cement, legacy), duct type (metal, plastic), age of corrosion inhibitor impregnation at the time of testing (0.5 months to 2.5 months), and the beam condition when initially impregnated (uncracked, cracked). Five groups of beams were tested under four-point bending to evaluate both strength level nominal flexural resistance and service level crack behavior.

At the strength load level, test results and corresponding analyses indicated negligible differences (less than 2%) between the nominal flexural resistances of newly constructed beams treated with corrosion-inhibiting fluid and the nominal flexural resistances of corresponding untreated control beams. In regard to service load levels, a "cracking load" level was defined in this study as the applied load that produced a calculated tensile stress of $12\sqrt{f'_c}$ at the extreme tension fiber, consistent with the ACI 318 definition of a cracked section. This higher stress level was selected to ensure that cracking would be observed while remaining reasonably aligned with AASHTO LRFD serviceability limits, which typically allow $6\sqrt{f'_c}$ under Service III conditions. At the defined cracking load level, treatment with corrosion inhibiting fluid produced negligible changes in observed patterns of crack spacing and crack frequency. Conversely, alternate analyses of beam cracking produced mixed results wherein a limited number of tests indicated that impregnation of corrosion-inhibiting fluid was associated with moderately increased crack severity. It must be noted, however, that the presence of an adequately impregnated volume of corrosion-inhibiting fluid into a tendon could presumably protect such a tendon from any increased exposure risk that was associated with increased cracking.

17. Key Words	18. Distribution Statement
Post-tensioned concrete; Bonded tendon, Corrosion inhibitor; Concrete structures; Corrosion protection; Flexural strength; Girders; Grout; Material tendons; Posttensioning	No restrictions.

19. Security Classif. (of this report)	20. Security Classif. (of this page)	21. No. of Pages	22. Price
Unclassified	Unclassified	209	

Form DOT F 1700.7 (8-72). Reproduction of completed page authorized

ACKNOWLEDGEMENTS

The authors thank the Florida Department of Transportation (FDOT) for providing the funding that made this research possible. Additionally, the authors acknowledge the significant contributions made by the staff of the FDOT Marcus H. Ansley Structures Research Center in providing technical insights and suggestions, constructing the test setup, providing data acquisition, and conducting the experimental tests. Olga Iatsko, Christina Freeman, Stephen Eudy, Michael Waters, Paul Tighe, Chris Schild, Miguel Ramirez, Ben Allen, Wade Johnson, and Clark Conyers were all exceptional participants in this research. The authors also acknowledge the FDOT State Materials Office for their technical insights and assistance with the materials aspects of the project, especially Richard DeLorenzo and Andrew Pinkham.

The authors acknowledge Structural Technologies-VSL for permitting extended rental of post-tensioning equipment. The authors acknowledge Vector Corrosion Technologies for providing technical insights and on-site corrosion inhibitor impregnation services. The authors acknowledge Sumiden Wire Products for donation of prestressed concrete steel strand, Essvetech for donation of corrugated metal duct, and GTI for donation of corrugated plastic duct.

EXECUTIVE SUMMARY

Corrosion of steel tendons in post-tensioned bridge girders can lead to section loss and, if left unaddressed, may result in strand rupture and a corresponding reduction in girder strength. Post-tensioned bridge girder construction - bonded, unbonded, or mixed - has suffered notable corrosion failures (e.g., Niles Channel Bridge, Roosevelt Bridge), especially in Florida's post-tensioned bridges, where water-filled grout voids, improper grouting, and galvanic action accelerate deterioration. In the state of Florida, a number of remedial measures have been explored and implemented to address such issues, including the use of corrosion inhibitors to mitigate strand corrosion. Impregnation of corrosion-inhibiting fluids, most notably Vector's silicon-hydrocarbon PTI, into grouted post-tensioned tendons has been shown to be effective in reducing strand corrosion. However, the impregnation of these fluids may also have the potential to adversely affect bond between steel tendons and the surrounding grout. Past studies involving pull-out tests of unstressed strands in grout have indicated that a reduction in bond strength may result from the use of corrosion inhibiting fluids. However, relatively little research has been carried out to determine the effect that such fluids may have on the flexural performance of full-scale post-tensioned concrete bridge girders.

In this study, full-scale experimental flexural tests of post-tensioned concrete beams with grouted steel tendons were performed to evaluate the extent to which impregnation with a corrosion inhibiting fluid might affect either the strength level performance (nominal flexural strength) or the service level performance (crack severity) of such beams. Variables that could potentially influence the bond condition between tendon and grout, due to the presence of corrosion inhibitor, were incorporated into the experimental test program. These variables included tendon size (6-, 12-, and 19-strands), tendon profile (straight, draped), grout type (pre-packaged, plain cement, legacy), duct type (metal, plastic), age of corrosion inhibitor impregnation at the time of testing (0.5 months to 2.5 months), and the beam condition when initially impregnated (uncracked, cracked). Five groups of newly constructed post-tensioned concrete beams were tested under four-point bending to evaluate both nominal flexural resistance and service level cracking behavior. The findings of the study, as summarized below, are known to be valid for the beam construction conditions and corrosion inhibitor impregnation conditions that were tested. Application to other conditions may require additional investigation.

At the strength load level, the test results indicated negligible (less than 2%) differences between the nominal flexural resistances of newly constructed beams treated with corrosion inhibitor and the nominal flexural resistances of corresponding untreated control beams. In regard to service load levels, concrete cracking stress can vary due to inherent variability in tensile strength. For this study, a "cracking load" was defined as the applied load that produced a calculated tensile stress of $12\sqrt{f'_c}$ at the extreme tension fiber, consistent with the ACI 318 definition of a cracked section. This higher stress level was selected to ensure that cracking would be observed while remaining reasonably aligned with AASHTO LRFD serviceability limits, which typically allow $6\sqrt{f'_c}$ under Service III conditions. At the $12\sqrt{f'_c}$ cracking load level, multiple approaches were employed to compare the performance of treated beams to corresponding untreated beams. These included comparing crack patterns, crack widths, crack depth ratios, and estimated crack areas, all at a defined concrete tensile stress level of $12\sqrt{f'_c}$. Crack maps at this load level indicated negligible differences in crack patterns, with consistent crack spacing and frequency observed between corresponding treated and untreated specimens across all five beam groups. Crack width measurements taken during testing of three groups of beams (all with 19-

strand tendons) indicated that average crack widths were unaffected by treatment with corrosion inhibitor in two treated beams but increased by approximately 50% in one treated beam. Crack depth ratios were computed for all beam groups to evaluate the relative quantity of tensile cracks that crossed the tendon elevation - a condition that could lead to potential tendon exposure to the environment. In four of the five beam groups tested, the treated beams had equal or less severe crack depth ratio values than the corresponding control beams. In one group, the treated beam had a crack depth ratio 25% larger than the control beam. Finally, for two beam groups, an additional crack severity analysis was carried out by computing estimated crack areas from measured crack widths. The average increase in estimated crack area associated with treatment with corrosion inhibitor was approximately 17.5%.

For the beam configurations tested in this study, the results indicated a negligible influence of corrosion inhibitor on the strength level performance (nominal flexural resistance) of the beams. At the cracking load level, treatment with corrosion inhibitor likewise produced negligible changes in observed patterns of crack spacing and crack frequency. However, additional indices of beam cracking produced mixed results, wherein a limited number of tests indicated that impregnation of corrosion inhibitor may be associated with moderately increased crack severity. It must be noted, however, that the presence of an adequately impregnated volume of corrosion-inhibiting fluid into a tendon could presumably protect such a tendon from any increased exposure risk that was associated with increased cracking.

TABLE OF CONTENTS

LIST OF FIGURES

Figure Page

LIST OF TABLES

Table Page

CHAPTER 1 INTRODUCTION

Prestressed concrete bridge girders can be categorized based on whether the tendons are stressed before or after casting of the concrete. Pretensioned construction occurs when the strands are stressed prior to casting. Post-tensioned construction involves placing prestressing strands inside ducts embedded within the girder cross-section and stressing them against the hardened concrete. In pretensioned construction, the prestressing force is transferred continuously along the tendon length through direct bond at the concrete-tendon interface, while in post-tensioned construction, the prestressing force is transferred initially through end anchorages. Both methods offer application-specific advantages; however, multistrand post-tensioned tendons in long-span bridge girders are the predominant construction practice in Florida.

Post-tensioned girder construction can be further classified as bonded, unbonded**,** or mixed. In bonded construction, internal post-tensioned tendons are typically grouted with cementitious material, providing an additional load-transfer path and protecting the strands from corrosion. Historically, even external post-tensioned tendons were grouted, though they were often considered unbonded. Past failures have shown that poorly grouted tendons are highly susceptible to corrosion. Examples include severe tendon corrosion discovered in the Niles Channel Bridge (1999), Mid-Bay Bridge (2000), Sunshine Skyway Bridge (2002), and, more recently, the Roosevelt Bridge (2020). Corrosion issues are particularly challenging for Florida, which has more than 92 major bridges that utilize post-tensioned concrete members (Powers 2001). This underscores the need for effective methods to mitigate corrosion damage in grouted post-tensioned systems.

Investigations have shown that water-filled grout voids are the most common cause of tendon corrosion in post-tensioned systems. Such voids may form due to grout bleed, segregation from improper mix proportions, or water ingress through anchorage or duct leakage. Grout injection to fill voids may also introduce undesirable variations in porosity, pH, and chemical composition, which can accelerate corrosion. Furthermore, galvanic action between metallic anchorage components and steel strands in the presence of moisture can worsen corrosion (Powers 2001). These challenges make it difficult to ensure the 75-year design life expected of grouted post-tensioned bridges. A range of corrosion-control strategies have been investigated both within Florida and elsewhere, including the use of emulsifiable oils for temporary protection, prepackaged grouts, improved grouting techniques, and minimizing the time between tendon installation and grouting. While such measures address some contributing factors, corrosion prevention has remained elusive due to variable field conditions and inconsistent construction practices.

More recently, Florida has implemented, on a limited basis, the use of injected corrosion-inhibiting products intended to mitigate corrosion in existing grouted tendons. In particular, Vector Corrosion Technologies' proprietary post-tensioned impregnation (PTI) material has been applied in selected Florida bridges, including the I-95/I-295 Interchange in Jacksonville and the I-4 Connector in Tampa. Elsewhere in the United States, PTI has been deployed in Virginia (Varina Enon Bridge), New York, California, Ohio, South Carolina, Oklahoma, Rhode Island, and Washington. The Vector Post-Tech PTI system, a silicon hydrocarbon polymer, is intended to provide corrosion resistance by forming a protective barrier around the prestressing strands.

Preliminary testing on tendon samples from the Ringling Bridge in Sarasota (Whitmore 2018) showed a reduction in corrosion of approximately 90% compared to untreated samples.

However, subsequent investigations (Silnutzer et al. 2020) revealed that PTI treatment can significantly reduce the bond capacity of grouted tendons. A reduction in bond strength may in turn affect the structural behavior of post-tensioned girders, not only under service loading conditions but potentially at ultimate strength as well.

A post-tensioned bridge girder system typically is comprised of concrete, mild reinforcement, and one or more tendons installed according to the specified tendon profile (Figure 1.1). Ducts vary in diameter, material (Figure 1.2), and surface texture depending on project requirements. Prestressing strands are threaded through the ducts and stressed. Tendon sizes defined by the number of strands may range from 4 to 31 for 0.6-in. diameter strands. Tendon profiles are designed with different eccentricities and prestressing forces to counteract service loads and provide adequate flexural resistance. Regardless of tendon size, eccentricity, or force, all post-tensioned girders must comply with AASHTO LRFD Bridge Design Specifications and the Florida Structures Design Guidelines.

Figure 1.1. Assembly of reinforcement cages and ducts for the construction of a draped-tendon-profile post-tensioned girder.

Once the tendons are installed and jacked to the specified prestressing force at the live anchorage, cementitious grout is injected into the ducts. The grout hardens to form a solid barrier around the strands, enabling load transfer and providing long-term corrosion protection.

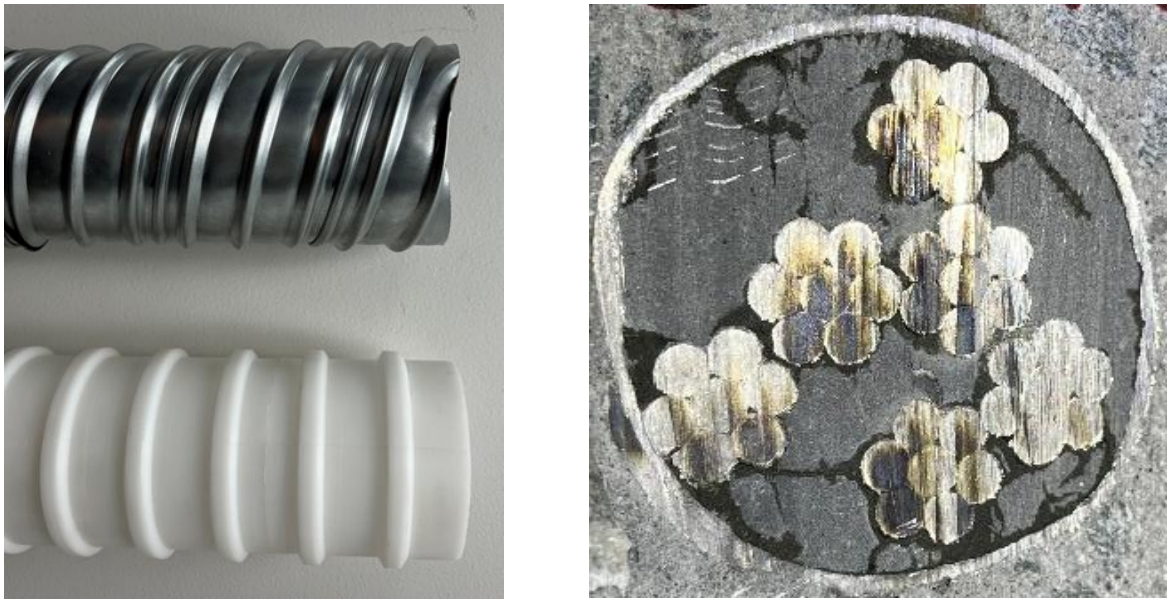

(a) (b)

Figure 1.2. Components of a bonded post-tensioning element: (a) Corrugated duct material types; (b) six-strand tendon surrounded by hardened cementitious grout inside a corrugated metal duct, shown in the cross-section of a cut post-tensioned girder.

CHAPTER 2 BACKGROUND

Pullout tests provide a small-scale experimental method for assessing the influence of corrosion inhibitors on the bond between tendon and grout. Although the bond mechanism and slip behavior between tendon and grout in a full-scale post-tensioned girder differ from those in pullout tests, the latter can still offer a general indication of whether a corrosion inhibitor affects bond performance. For instance, tendons in post-tensioned beams are typically stressed to approximately 70% of their ultimate strength, which reduces the surface profile of the strands and mechanical interlocking compared with unstressed strands used in pullout tests. Moreover, bond strength in ASTM A981 (ASTM 2023) pullout tests is measured at a tendon slip of 0.01 in. At such a small displacement, tendons in post-tensioned beams subjected to flexure may move relative to the grout while maintaining mechanical bond. In addition, the pullout specimen setup effectively creates a rigid body as the tendon is pulled, which contrasts with the expected shear deformation of the grout surrounding the tendon during flexure in full-scale beams.

A modified ASTM A981 pullout test on grouted, unstressed seven-wire monostrand tendon treated with a similar proprietary corrosion inhibitor reported an average reduction in bond strength of approximately 47% compared with untreated specimens, as well as specimens treated with other anti-corrosion materials such as PB Blaster and WD-40 (Silnutzer et al. 2020). Another study implemented a modified ASTM A981 pullout test designed to more closely simulate post-tensioned girder conditions by including grout and duct between the concrete and tendon and restraining strand screw-out during pulling. In that case, specimens coated with oil-based anti-corrosion materials exhibited a bond strength reduction exceeding 60% relative to the controls (Laco and Borzovič 2017).

However, when the same oil-based anti-corrosion material was used in post-tensioned beams with two mono strands in HDPE ducts and a draped tendon profile, flexural testing indicated little influence on either strength or serviceability (Laco and Borzovič 2017). While these results suggest that corrosion inhibitors may not significantly affect the flexural performance of post-tensioned beams, they cannot be generalized to existing post-tensioned girders that typically include multistrand stressed tendons, various grout types, duct materials, and tendon profiles.

Accordingly, the objective of the present experimental study is to investigate the flexural behavior of full-scale bonded post-tensioned girders representative of existing U.S. bridges, considering the combined influence of strand size, grout type, duct type, tendon profile, and tendon impregnation with a corrosion inhibitor.

2.1 Corrosion Inhibitor Material

The corrosion inhibitor material used in this study is a proprietary fluid designed specifically for tendon impregnation. When impregnated under pressure differential, the fluid travels along the tendon through the interstitial spaces between the wires in the strand, forming a protective coating around the steel and impregnating into the surrounding grout, as shown in Figure 2.1.

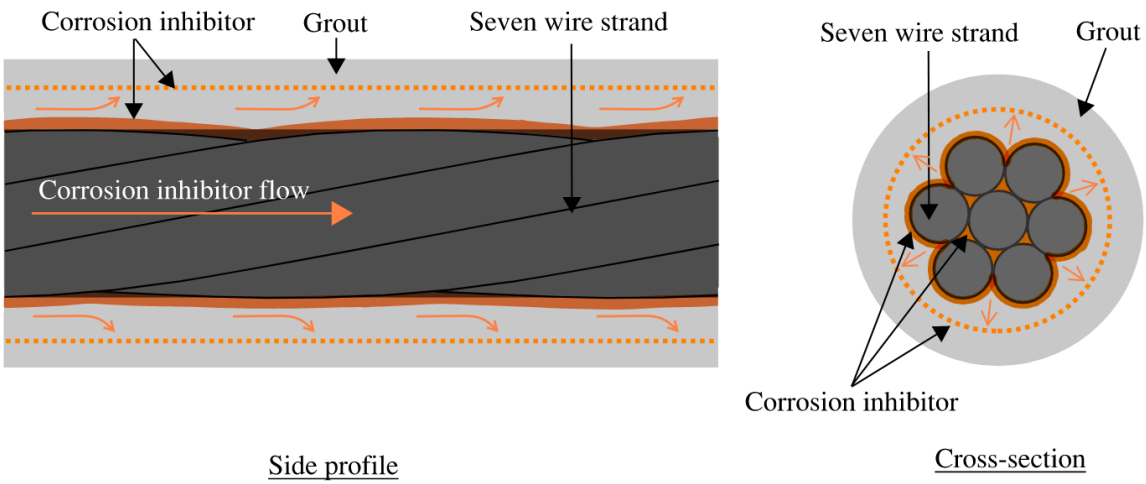

Figure 2.1. Impregnation of corrosion inhibitor, showing the flow of fluid through the interstitial spaces between the wires of a seven-wire strand and the subsequent impregnation of the grout surrounding the strand.

This dual-action protective coating and grout impregnation creates a barrier between moisture and the strands, thereby helping to mitigate corrosion in both existing and newly constructed tendons.

2.2 Tendon Bond Types

Post-tensioned concrete members typically consist of steel prestressing strands carried within the concrete and inside a duct. The duct containing the strands is filled with filler materials, which can be a cementitious pre-packaged grout or a microcrystalline petroleum-based wax, depending on the type of bond desired, . The construction procedure for post-tensioned concrete, whether bonded or unbonded, is exactly the same as discussed in the preceding section. The only difference lies in the material used as filler in the duct.

2.2.1 Unbonded Tendon

An unbonded tendon system has the duct filled with a flexible filler material, which is essentially a wax-like substance that protects the tendon from corrosion, resulting in increased durability and easier tendon replacement. However, since there is no bond between the tendon and the surrounding concrete, stress transfer by adhesion, friction, or mechanical restraint does not apply in this case.

2.2.2 Bonded Tendon

Once the cementitious grout is injected inside the duct, it cures and hardens around the strands, forming a bond between the grout and strands. This hardened grout helps transfer stress from the stressed tendon to the concrete, which is important for strain compatibility. The grout encasement protects the strand from corrosion by preventing the intrusion of moisture. Corrosion can be a problem in post-tensioned tendons when Portland cement is used as the grout, as it can result in segregation, bleeding, and voids filled with moisture, leading to tendon corrosion. With

the FDOT changes in tendon policy in 2002 (FDOT 2002), transitioning from Portland cement to pre-packaged grout, issues related to tendon corrosion have been addressed.

2.2.3 Partially Bonded or Treated Tendon

Partially bonded tendon refers to a tendon-grout bond condition where the presence of a foreign substance, typically a hydrophobic fluid, affects the bond. Depending on the type of fluid used, the treatment of the tendon may occur before the tendon is installed or after it has been grouted with a cementitious grout. These fluids may reduce friction and mechanical restraint, especially when the tendon is under stress from pullout or bending forces.

2.3 Tendon Bond Stress

In this context, bond refers to the stiffness and strength of the interface between the tendon and grout in a grouted post-tensioned system. Three bond types exist at different stages in the life of a bonded post-tensioning system. Adhesion is the chemical bond between the grout and tendon, while friction and mechanical restraint are the primary mechanisms for transferring the prestressing force through the interlocking of the strand surface profile and grout. In contrast, an unbonded tendon has no bond between the tendon and the surrounding system, so the transfer of force occurs only at the anchored ends or deviation points in the post-tensioned system.

2.3.1 Unbonded Tendon

An unbonded post-tensioned system is formed by injecting a flexible filler material, typically microcrystalline petroleum-based wax, into a post-tensioned duct. This wax provides a protective barrier against moisture, reducing corrosion issues in post-tensioned strands, but lacks a physical bond and the ability to transfer force from the tendon to the surrounding concrete, except when the post-tensioned tendon exerts an upward force to resist an applied bending force at intermediate points (kinks). In an unbonded post-tensioned tendon, similar to the bonded tendon, the transfer of compression force primarily occurs from anchor points at the ends of the post-tensioned concrete, resulting in precompression stress in the concrete. This improves serviceability. However, the absence of a bond along the tendon length and no transfer of bond stress between tendon-grout and grout-concrete, as shown in Figure 2.2, results in no strain compatibility and reduced flexural resistance of the unbonded post-tensioned girder relative to a fully bonded system.

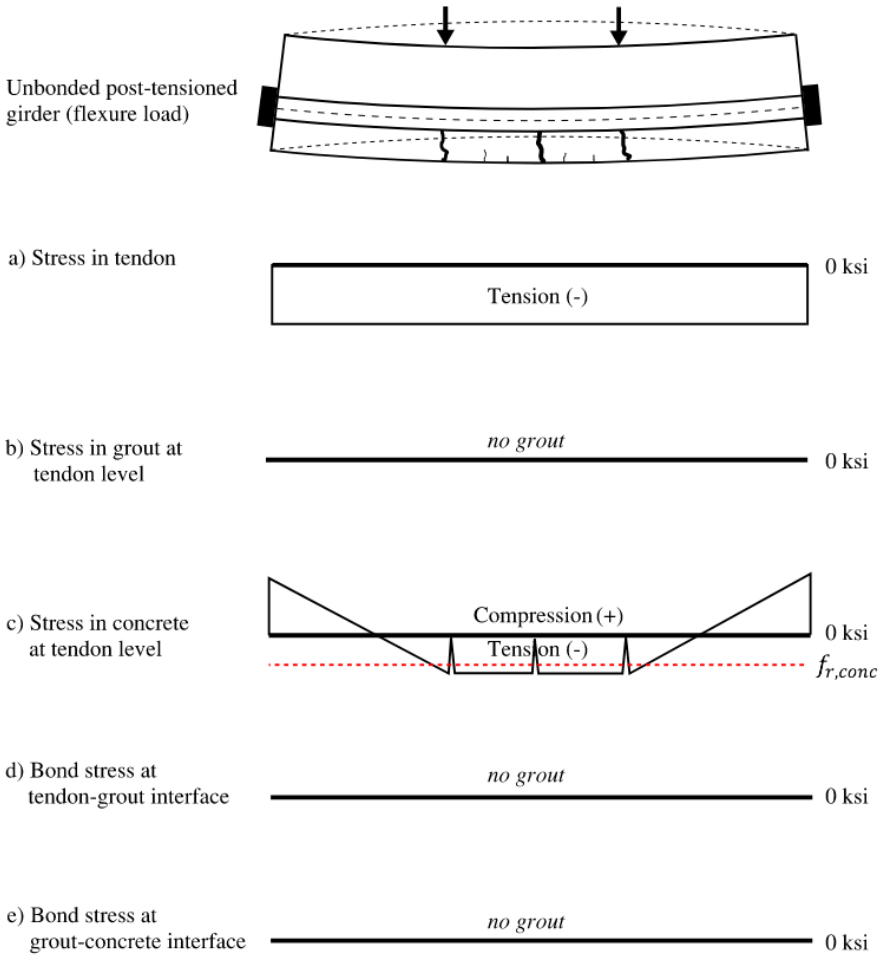

Figure 2.2. Bond stress distribution in an unbonded post-tensioned tendon subjected to flexural load.

2.3.2 Bonded Tendon

In a bonded tendon, adhesion refers to the chemical bond between the tendon and the grout that forms as the grout cures and hardens around the tendon strands. Adhesion is quickly lost as the tendon undergoes Poisson's contraction relative to the adjacent grout when a flexural load is applied in a bonded post-tensioned beam, or when the tendon is axially stressed under an applied pullout force. Hence, the contribution of adhesion is insignificant compared to that of the physical bond and can be lost early during flexural testing, when stress transfer from the tendon to the grout remains minimal. Friction and mechanical interlock develop due to the extensional movement of the tendon under tensile stress induced by the applied flexural load. This friction and mechanical interlocking of the strand with the grout form the mechanism by which tendon force is transferred to the concrete, enabling strain compatibility and mobilization of flexural resistance in bonded post-tensioned systems.

The development of the bond between the tendon, grout, and surrounding concrete in a bonded post-tensioned grouted tendon can be divided into four stages based on the characteristics

of bond stress that exist between the tendon and grout. These stages collectively describe how the bond evolves as loading progresses.

Stage 1: Grouted tendon before loading (uncracked grout)

As shown in Figure 2.3, in a post-tensioned grouted beam, the system remains unbonded until the duct is filled with cementitious grout and the grout sufficiently cures. Once the grout hardens around the post-tensioned tendon, a chemical bond, or adhesion, is formed between the grout and the tendon. At this stage, however, there is no transfer of stress from the tendon to the grout or from the grout to the concrete, since no flexural load has yet been applied to induce extensional strain in the tendon. The post-tensioning of the tendon produces a uniform compressive stress in the concrete due to the precompression force developed at the anchored ends prior to grouting. Therefore, at this state of stress in the post-tensioned element, there is no stress transfer from the tendon to the grout or to the surrounding concrete along the tendon length, as illustrated in Figure 2.3. The compressive stress in the concrete is contributed solely by the anchorage force applied at the tendon ends.

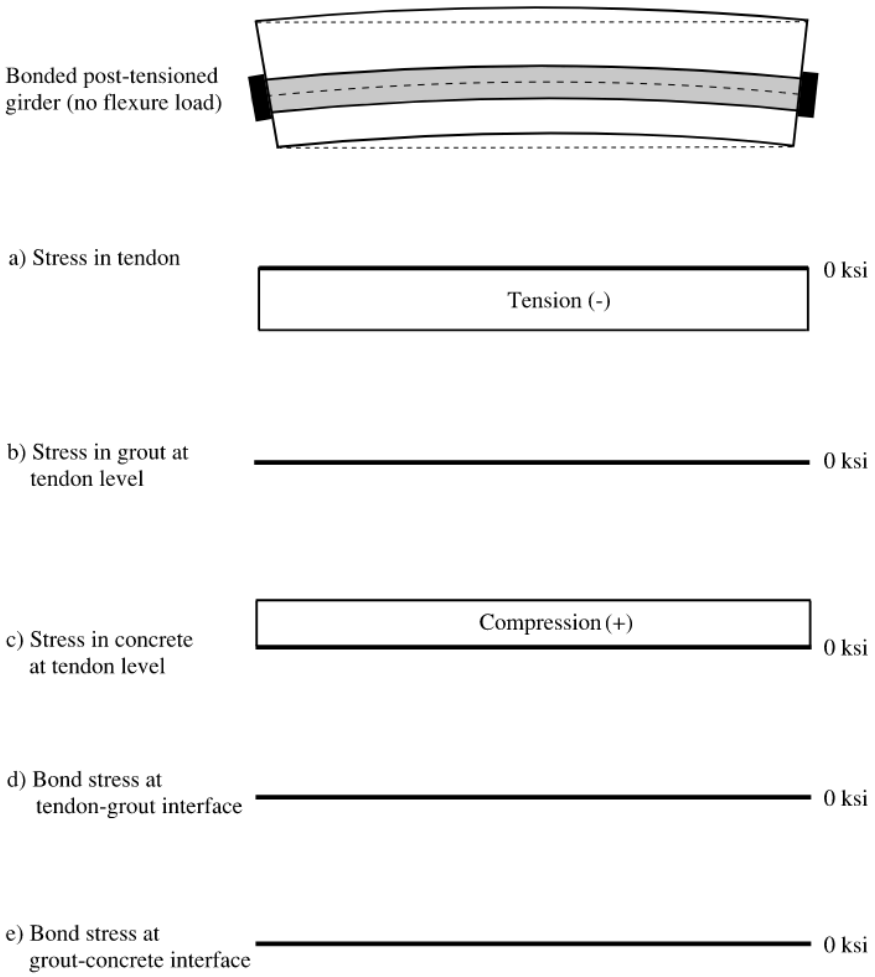

Figure 2.3. Bond stress distribution in a bonded post-tensioned tendon before applying flexural load.

Stage 2: Grouted tendon under flexural load (uncracked grout)

When the cementitious grout surrounding the post-tensioned tendon has sufficiently hardened, and a flexural load is applied, the axial tensile force in the tendon further increases while the precompression stress in the concrete reduces at the elevation of the tendon. Additionally, the applied bending moment causes the grout to develop tensile stress, as shown in Figure 2.4. At this stage, the extensional movement of the tendon, due to beam bending under the applied flexural load, transfers the tendon force to the surrounding grout and then to the concrete. This process results in the development of bond forces, first between the tendon and grout, and subsequently between the grout and concrete.

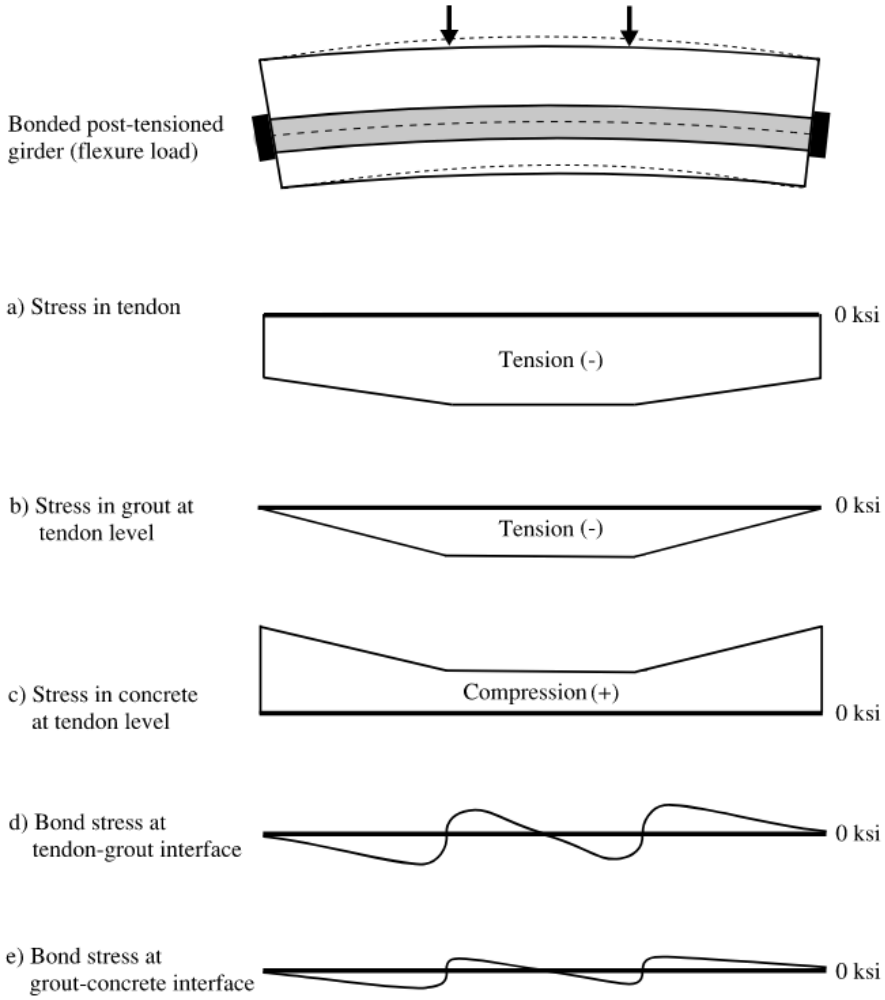

Figure 2.4. Bond stress distribution in grouted post-tensioned tendon subjected to flexural load (before tensile cracking of grout).

Stage 3: Grouted tendon under flexural load (cracked grout)

In a bonded post-tensioned tendon grouted with cementitious material, the concrete section is initially in precompression due to post-tensioning. However, the grout, injected after the tendons

are stressed, does not experience any initial stress until a flexural load is applied, causing tensile stress to develop in the grout. As a result, the grout reaches its tensile cracking limit first, cracking while the concrete at the same elevation is still decompressing or has not yet reached its tensile cracking limit. As shown in Figure 2.5, this intermediate cracking in the grout results in a redistribution of bond stress, referred to as in-and-out bond stress (MacGregor and Wight 2011). This concept explains how bond stress between the tendon and grout changes when cracks develop in the grout along the constant moment region. As illustrated in Figure 2.5, once cracks form, the tendon is effectively "pulled" from both ends of the cracked grout segment. The bond stress drops from a maximum at the midspan of the cracked segment to zero at the ends. Over the cracked region, no bond stress exists due to the lack of direct contact between the tendon and grout.

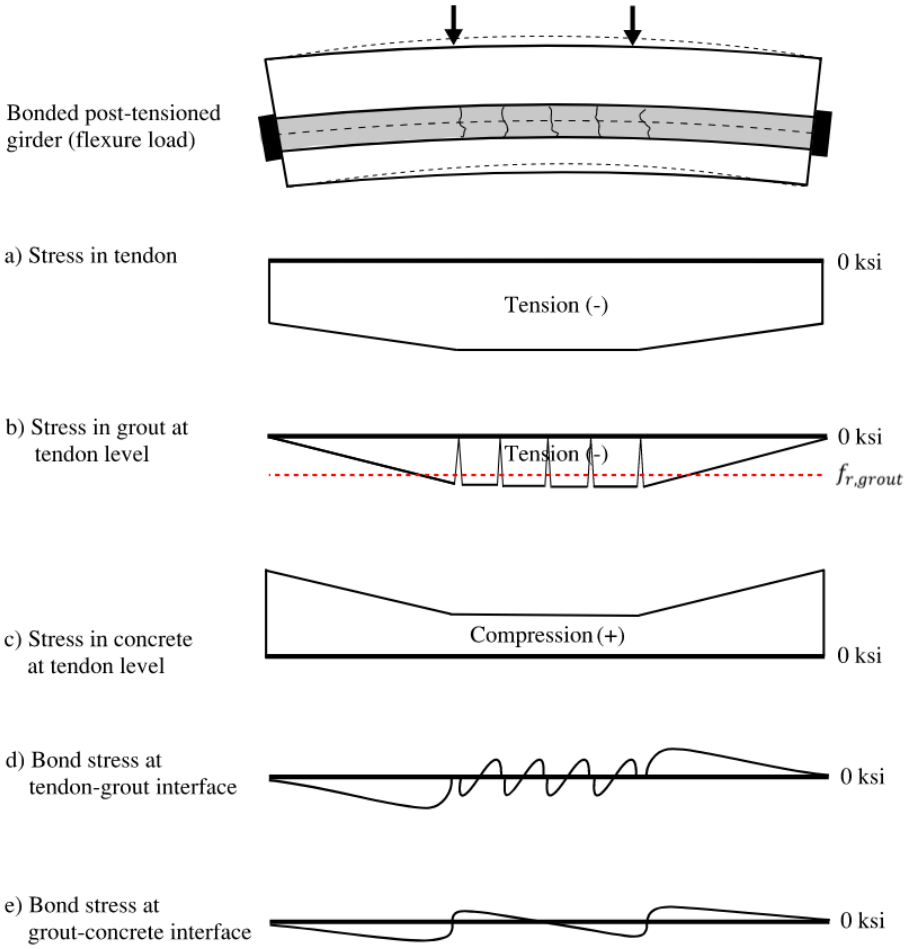

Figure 2.5. Bond stress distribution in grouted post-tensioned tendon subjected to flexural load (after tensile cracking of grout).

Stage 4: Grouted tendon under flexural load (cracked grout and cracked concrete)

At this stage (Figure 2.62.62.6), the applied bending force is further increased to the point that the precompression stress in the concrete is canceled out by the tensile stress from the flexural load. When the tensile stress exceeds the tensile cracking stress limit of the concrete, it causes

tensile cracking that extends from the bottom surface of the post-tensioned beam to the tendon elevation.

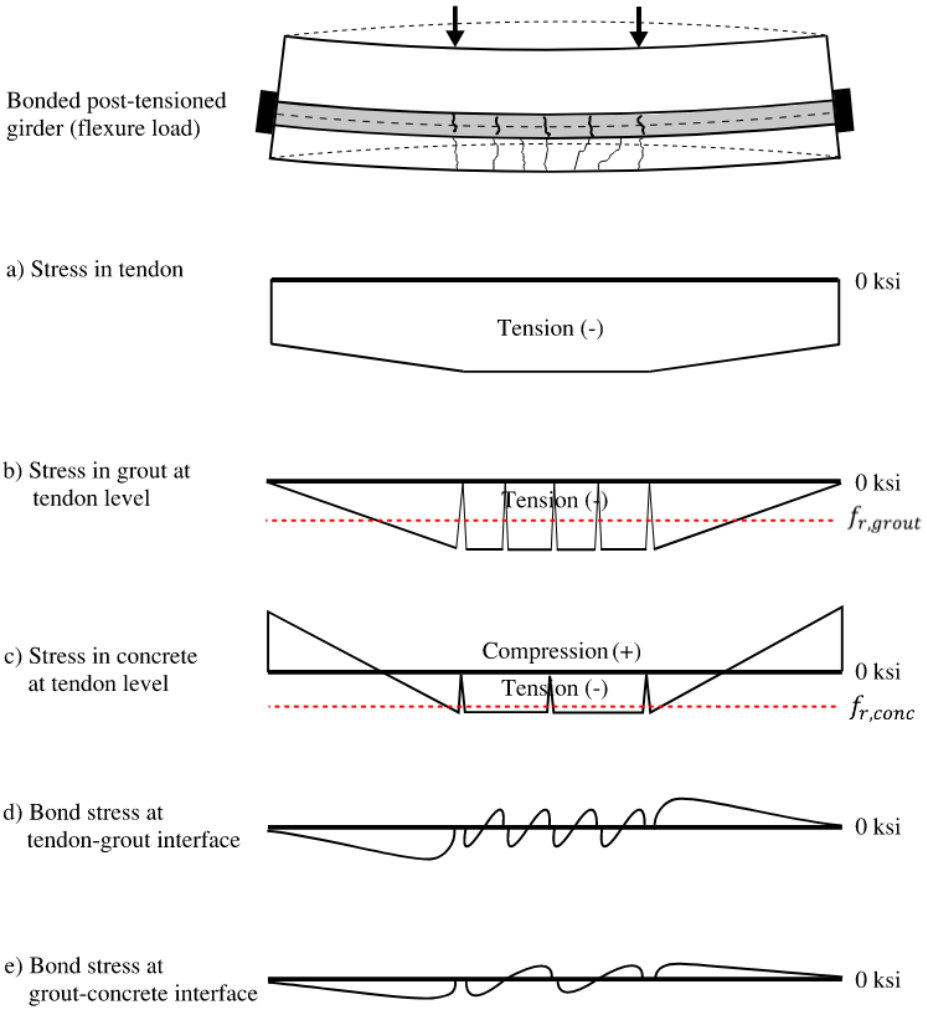

Figure 2.6. Bond stress distribution in grouted post-tensioned tendon subjected to flexural load (after tensile cracking of grout and tensile cracking of concrete).

At this point, the grout will have incurred significantly more cracking along the span relative to the tensile cracking in the concrete, resulting in a higher frequency of in-and-out bond stress distribution at the tendon-grout interface. Also, at this stage, the transfer of bond stress occurs from the grout to the surrounding concrete. This mechanism of bond transfer is the key to strain compatibility and significantly contributes to the flexural resistance of the beam.

2.3.3 Partially Bonded Tendon

A partially bonded tendon system may be formed when the bond strength between the tendon and cementitious grout in a fully bonded tendon is reduced by the presence of a foreign substance (e.g., a corrosion-inhibiting fluid). In this study, such tendons are called “treated” tendons since the corrosion-inhibiting treatment may cause bond strength degradation in this system.

Treatment of post-tensioning strands can occur in two ways. In the first technique, strands are applied with some emulsifiable oil to form a protective coat around the strands' surface, and then the tendons are inserted, post-tensioned, and grouted. Tendons treated in this manner will have little or no adhesion since the protective coat around the strand will inhibit the formation of a chemical bond between the tendon and adjacent grout.

In the second technique, the cementitious grout is allowed to cure and harden around the tendon. Later, the corrosion-inhibiting fluid is injected into the tendon from the ends or intermediate ports along the tendon profile using pressure differential. This form of tendon treatment does not affect the chemical adhesion that has already been formed when the grout has cured around the strands; rather, it impregnates and may degrade the mechanical strength of the grout around the strands, especially friction and mechanical restraint, which become critical when the tendon undergoes extensional movement caused by the applied flexural load on the post-tensioned beam. It is important to note that the corrosion inhibitor needs impregnation of only a small depth of grout around the deformed strand surface to overcome the mechanical interlock between the grout and strand.

2.4 Flexural Resistance

The nominal flexural resistance of a concrete element with bonded reinforcement may be computed using strain compatibility. This method applies to both non-prestressed and prestressed concrete members. The main differences lie in the material properties of the reinforcement steel and the additional strain component in prestressed concrete due to the initial precompression force in the tendon.

Nominal flexural resistance in an unbonded post-tensioned system, on the other hand, may be computed using an empirical equation that provides stress in the unbonded tendon (as an alternative to a rigorous kinematic analysis). Unlike fully bonded and fully unbonded systems, partially bonded systems do not have design specifications for determining nominal flexural resistance. Therefore, the flexural resistance of a partially bonded system can only be determined through experimental testing and finite-element modeling.

2.4.1 Bonded Tendon

For a post-tensioned concrete member with full bond between the tendon and adjacent cementitious grout, strain compatibility may be used to compute the nominal flexural resistance. The basic assumptions are: (i) plane sections remain plane after bending; (ii) strain in the tendon equals the strain in the concrete at the same elevation; and (iii) stresses in concrete and steel are determined from their respective stress-strain relationships. For specified material and geometric properties and a given tendon depth, the internal forces are found iteratively by enforcing equilibrium of compression and tension in the cross-section. The internal lever arm is the distance between the resultants of the concrete compressive stress block and the tendon force. The nominal flexural resistance is the sum of internal moments about either resultant.

Another assumption commonly used at nominal resistance is that the compressive concrete stress distribution may be represented by an equivalent rectangular stress block, a simplified approximation of the actual distribution.

The computation of stress in prestressing strands at flexure differs from that for deformed reinforcing bars. As illustrated in Figure 2.7, the strand strain at flexure is the cumulative strain

(ε_{ps}) of the sum of strain at effective prestress (ε_{pe}), strain at decompression (ε_{d}), and strain at flexure (ε_{f}) is given by:

$$\varepsilon_{ps} = \varepsilon_{pe} + \varepsilon_{d} + \varepsilon_{f} \tag{2-1}$$

$$\varepsilon_{pe} = \frac{f_{pe}}{E_{p}} \tag{2-2}$$

$$\varepsilon_{d} = \frac{P_{e}}{A_{g}E_{c}} + \frac{P_{e}e^{2}}{I_{g}E_{c}} \tag{2-3}$$

$$\varepsilon_{f} = \varepsilon_{cu}\left(\frac{d_{p} - c}{c}\right) \tag{2-4}$$

where:

f_{pe} = effective prestress in the tendon (after losses)

E_{p} = modulus of elasticity of prestressing steel

P_{e} = effective prestressing force

A_{g} = gross area of the section

E_{c} = modulus of elasticity of concrete

e = eccentricity of the tendon relative to the concrete centroid

I_{g} = gross moment of inertia of the section

ε_{cu} = code specified maximum usable strain of concrete (0.003 in./in.)

d_{p} = distance from the extreme compression fiber to the centroid of the tendon (effective depth)

c = depth of the neutral axis measured from the extreme compression fiber.

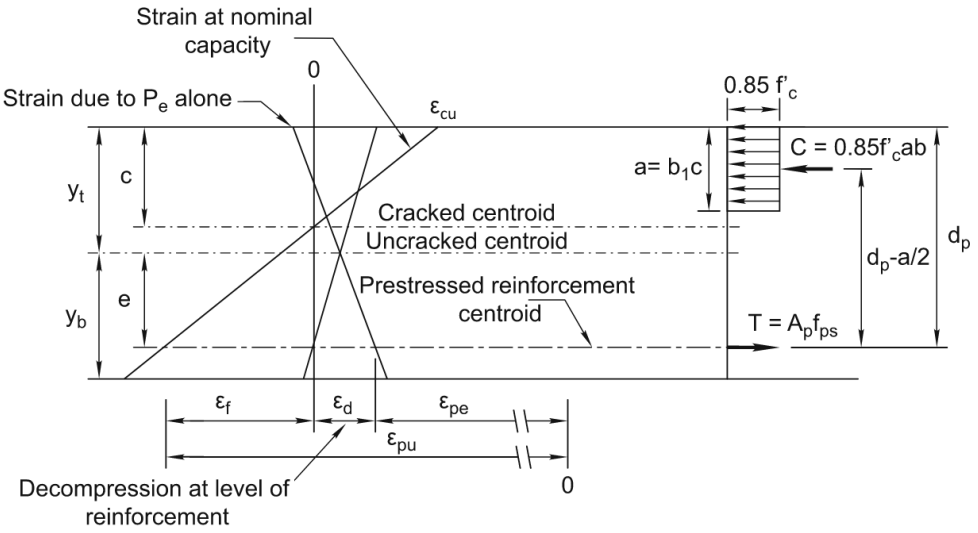

Figure 2.7. Strain profile of a prestressed concrete section and equivalent rectangular stress block at nominal flexure (Dolan and Hamilton 2019).

For a post-tensioned element, the stress in the prestressing strands up to rupture is obtained from the strand stress–strain curve (Figure 2.8).

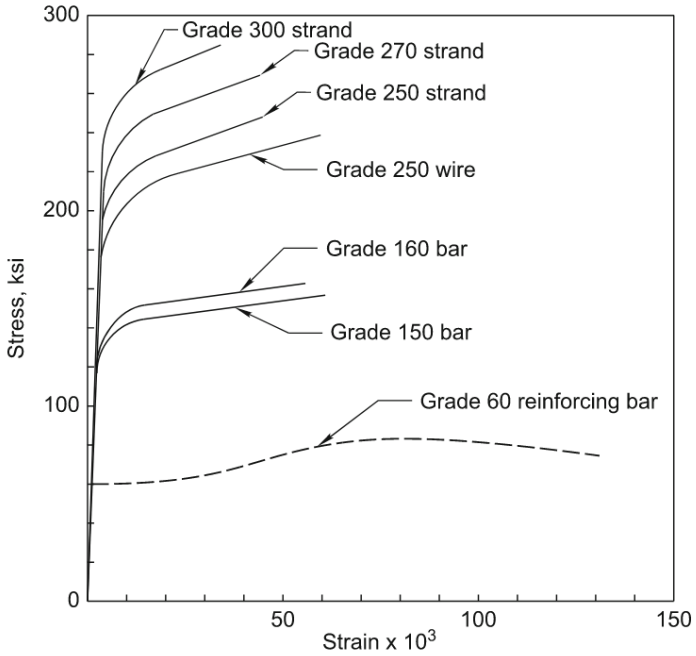

Figure 2.8. Stress-strain curves for different grades of prestressing steel (PCI 2010).

Prestressing steel does not exhibit a clear yield point like reinforcing bars; however, ASTM A416 defines the minimum yield strength as the stress corresponding to 1% elongation for 270-ksi and 250-ksi strand (ASTM 2017). Accordingly, the stress in prestressing steel may be estimated using the following piecewise approximation (PCI 2010):

$$f_{ps} = 28{,}800\varepsilon_{ps}(\text{ksi}) \quad \text{if} \quad \varepsilon_{ps} \leq 0.0085 \tag{2-5}$$

$$f_{ps} = 270 - \frac{0.04}{\varepsilon_{ps} - 0.07}(\text{ksi}) \quad \text{if} \quad \varepsilon_{ps} > 0.0085 \tag{2-6}$$

The tendon force at nominal flexure is then:

$$T = A_{ps}f_{ps} \tag{2-7}$$

The depth of the equivalent stress block and the neutral axis are:

$$a = \frac{A_{ps}f_{ps}}{0.85f'_c b} \tag{2-8}$$

$$c = \frac{a}{\beta_1} \tag{2-9}$$

where:

f'_c = specified compressive strength of concrete

b = width of the concrete compression zone

a = depth of the equivalent rectangular stress block

β_1 = factor for the depth of the equivalent rectangular stress block, given by

$$\beta_1 = 0.85 \quad \text{for} \quad 2500 \text{ psi} \leq f'_c \leq 4000 \text{ psi} \tag{2-10}$$

$$\beta_1 = 0.65 \quad \text{for} \quad f'_c \geq 8000 \text{ psi} \tag{2-11}$$

$$\beta_1 = 0.85 - \frac{0.05(f'_c - 4000)}{1000} \text{ for } 4000 \text{ psi} < f'_c < 8000 \text{ psi} \tag{2-12}$$

The resultant compressive force in the concrete is:

$$C = 0.85f'_c ba \tag{2-13}$$

The nominal flexural resistance is then:

$$M_n = A_p f_{ps}\left(d_p - \frac{a}{2}\right) \tag{2-14}$$

2.4.2 Unbonded Tendon

In post-tensioned concrete with unbonded tendons, a flexible filler (e.g., wax) is used, so no bond stress is transferred from tendon to surrounding concrete. Instead, force transfer occurs primarily at the anchorages and, in curved profiles, at deviation points due to friction and transverse contact forces as the beam rotates under flexure. Consequently, tendon strain develops independently of the concrete strain at the same elevation, and section-level strain compatibility is not applicable. A member-level evaluation is adopted to determine nominal flexural resistance,

requiring the tendon profile, loading pattern, span-to-depth ratio, effective stresses, and material properties.

The current AASHTO LRFD Bridge Design Specifications (AASHTO 2020), following (MacGregor et al 1989), estimate stress in unbonded tendons using:

$$f_{ps} = f_{pe} + 900\left(\frac{d_p - c}{l_e}\right) \leq f_{py} \tag{2-15}$$

$$l_e = \left(\frac{2l_i}{2 + N_s}\right) \tag{2-16}$$

The depth of the neutral axis for a T-section when the prestressing steel has yielded is:

$$c = \frac{A_{ps}f_{ps} + A_s f_s - A'_s f'_s - \alpha_1 f'_c(b - b_w)h_f}{\alpha_1 f'_c \beta_1 b_w} \tag{2-17}$$

where:

l_e = effective tendon length

l_i = tendon length between anchorages

N_s = number of plastic hinges at supports at a failure mechanism (0 for simple span)

f_{py} = yield stress of prestressing steel (per AASHTO/ASTM definition)

A_s, A'_s = areas of tension and compression reinforcing bars, respectively

f_s, f'_s = stresses in tension and compression, reinforcing bars, respectively

α_1 = concrete stress-block intensity factor

b_w = web width of the T-section

h_f = flange thickness

β_1 = stress-block depth factor as defined above.

2.4.3 Partially Bonded Tendon

A partially bonded tendon, in this context, is a fully bonded post-tensioned tendon whose bond to grout is degraded by a foreign substance (e.g., a corrosion-inhibiting fluid). The resulting bond condition lies between that of a fully bonded and a fully unbonded tendon. The exact bond condition depends on many factors, including tendon size, local tendon configuration, and grout quality. Because a full bond is not present, strain compatibility is not valid for computing flexural resistance; likewise, the AASHTO empirical equation for unbonded tendon stress cannot be used, since stress transfer from tendon to grout still occurs at locations where bond remains intact along the profile.

Accordingly, the approach in this study is to establish the nominal flexural resistance of partially bonded post-tensioned systems through flexural testing and then develop design recommendations from the results. Tests indicate that fully bonded tendons provide greater flexural

resistance than unbonded tendons due to differences in strain and stress distribution along the tendon length (Gerber and Burns 1971). For members under bending, post-cracking strain compatibility in bonded tendons and strain localization at cracks produce localized tendon stress increases over crack regions (Brenkus et al 2017). In unbonded tendons, the absence of strain compatibility spreads the crack-induced strain along the entire tendon length, so the stress increment is smaller and more uniform (Figure 2.9). Consequently, flexural resistance is smaller for unbonded than for bonded systems. Partially bonded tendons exhibit capacities between these two cases. The difference in behavior becomes most evident after cracking, near ultimate strength, where unbonded systems lose stiffness and contribute relatively little to the additional capacity from cracking to ultimate (Laco and Borzovič 2017).

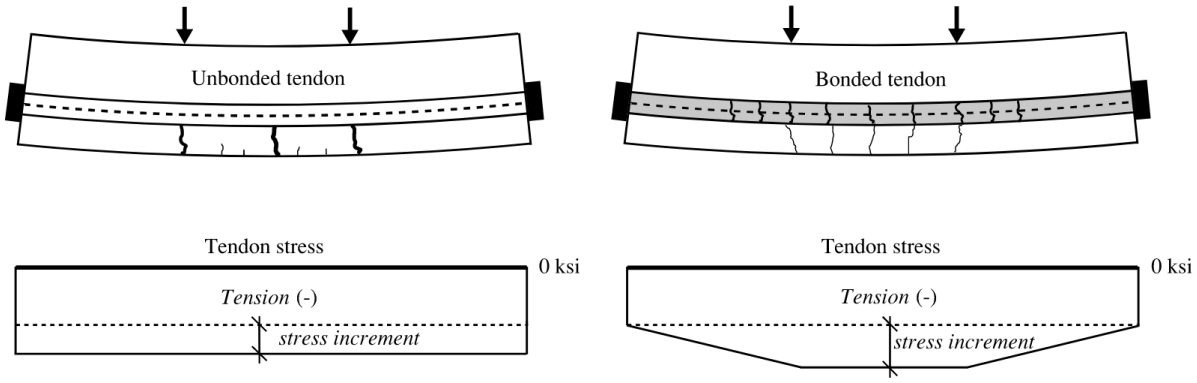

Figure 2.9. Stress increments due to applied flexural load in unbonded and bonded tendons.

CHAPTER 3 DEVELOPMENT OF TEST MATRIX

3.1 Variables Affecting Bond Performance of Impregnated Post-Tensioned Tendon

Bond performance of post-tensioned tendon is similar to that of mild steel reinforcement in that the prestressing strand is subject to both mechanical and adhesive bond. The mechanical bond is a result of the bearing of the surface irregularities caused by the spiral pattern of the six outer wires of the strand, called the strand surface profile, as shown in Figure 3.1. These wires bear directly against the surrounding grout, generating compressive and shear stresses in the grout that facilitate the transfer of bond stress. Adhesive bond contributes to the bond strength by transfer of shear through chemical bonding that occurs at the interface of the strand and cement paste as the fresh paste is hardening; this mechanism is independent of the strand surface profile.

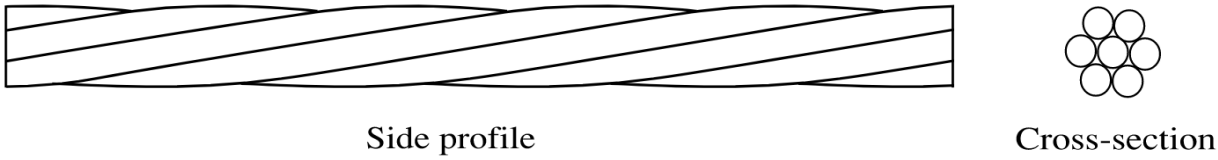

Figure 3.1. Seven-wire prestressing strand surface profile.

A third mechanism, known as the Hoyer effect only occurs in pretensioned strands. Very high friction forces develop between the concrete and prestressing strand when the strand is cut. These friction forces act as a bond transfer mechanism that develop the prestressing force in the strand and anchors it the surrounding concrete. These friction forces are due to the dilation of the strand, from Poisson's effect, as the strand tries to longitudinally shorten (and therefore transversely expand) following strand cutting. Ultimately the anchorage of the pretensioned strand is a combination of adhesive bond and friction forces. This Hoyer effect does not exist in post-tensioned tendons because they are prestressed and anchored before the grout is injected. Consequently, the grout remains non-prestressed and there are no significant frictional forces because the strands are not cut or released after the grout is injected and has hardened. Because the pretensioned strands are cut at the ends of the beam, they unwind slightly as the prestress is released, reducing the effect of mechanical interlock so that adhesion and friction dominate the bond near the transfer zone.

Much of the past work on prestressing strand bond strength has focused on the anchorage of pretensioned strands because of the overall loss of strength of a beam when a bond failure occurs. Testing has traditionally focused on pull-out type tests such as those defined in ASTM A981 (ASTM 2023). These tests isolate the adhesive bond strength of the prestressing strand by measuring the force required to pull a strand through grout. The result of the test is the tensile force measured on the loaded-end of the strand corresponding to a movement of 0.1 in. [2.5 mm] at the free-end of the strand as it begins to slip. The strand unwinds while slipping, thus minimizing the mechanical bond and isolating the adhesive bond strength of the strand.

In beams with post-tensioned tendons, however, the bond strength of the prestressing strand is not as critical to the ultimate strength of the beam. At the ends of the beam, the tendon is mechanically anchored rather than relying on bond strength. An exception is in existing post-tensioned girders with severely deteriorated anchorage due to corrosion, where the post-tensioning

force is primarily transferred along the tendon-grout interface by friction and mechanical restraint. Bond stresses develop only when external loads are applied. Flexural deformations caused by sufficiently large applied loads will cause cracking. Adequate mechanical and adhesive bond strength will ensure that the tendon behaves as a bonded tendon rather than as an unbonded tendon, exhibiting numerous well-distributed cracks rather than one or two large cracks. This type of bond strength is difficult to quantify and has received little research attention.

The hydrocarbon and silicon-based fluid known as Vector Post-Tech PTI impregnation material, a proprietary product of Vector Corrosion Technologies, has been shown to control the corrosion of tendons surrounded by grout. During impregnation, the fluid travels along the interstitial spaces between individual wires, displaces moisture, and forms a protective barrier around the strands. Pressure injection of the fluid occurs at locations such as end anchorages or intermediate points along the tendon profile. Despite the effectiveness of the Vector Post-Tech PTI product in terms of corrosion inhibition, questions related to possible changes in the structural behavior of post-tensioned concrete members treated with this material have arisen. For example, significant reductions in bond strength, as compared to untreated tendons, have been reported: more than 47% (Silnutzer et al. 2020). However, these tests were performed on unstressed single strand tendons and evaluated the adhesive bond strength between the tendon and grout rather than mechanical bond. Based on the procedures used in these pull-out tests, it is likely that the inhibitor, due to its highly fluid nature, penetrated the grout-strand interface and interrupted the adhesive bond strength. However, it is unclear what effect the inhibitor may have on the mechanical bond strength; the focus of this research is to evaluate the effect of the inhibitor on structural behavior as it is affected by both adhesive and mechanical bond strength.

3.1.1 Corrosion Inhibitor Type

Materials of varying compositions may be used to protect strands from corrosion. Such materials typically consist of lubricants that form a thin coat on the strand surface. However, in addition to protecting from corrosion, these agents may reduce, to some extent, the coefficient of friction between strands and the surrounding grout. This means that a grouted tendon, when treated with corrosion-inhibiting materials, may change from a fully bonded condition to a partially bonded condition. This type of change is undesirable since grouted post-tensioned tendons rely on the bond between tendon and grout to transfer stress between the tendon and surrounding concrete caused by the application of external loads to the post-tensioned member.

Silnutzer et al. (2020) carried out an experimental study focused on the influence of the Vector Post-Tech PTI impregnation material on the bond capacity of single-strand tendons as well as the long-term effectiveness of the corrosion protection provided to the strands. Pullout tests were conducted on concrete specimens 1-ft long with grouted seven-wire strands that had been treated with PTI material (Figure 3.2). Pullout test results revealed reductions of bond strength that ranged from 21% to 78%, with an average reduction of 47%. In contrast, tendons treated with other anti-corrosion materials such as PB Blaster and WD-40 showed no discernible reduction in bond strength relative to untreated control specimens. However, forecast models of future failure (Silnutzer et al. 2020), developed based on corrosion damage data, indicated that samples treated with the PTI material would extend the life of tendons up to three times longer than the untreated specimens or oil-treated specimens (PB Blaster and WD-40).

Figure 3.2. Pullout testing of grouted unstressed monostrand tendon (Silnutzer et al. 2020)

An additional factor investigated in the study was the effect of tendon size on the effectiveness of corrosion protection. It was found that protection against corrosion was superior in multistrand tendons as compared to single-strand tendons. This result was attributed to the increased interstitial space between strands in the multistrand tendons as compared to the single strand tendon. The increase in interstitial space allowed better penetration of corrosion inhibiting fluids in and around the tendon.

The use of emulsifiable oils has also been investigated as a corrosion protection technique. Correspondingly, the effect that such oils have on the bond capacity of tendons in concrete has been a topic of investigation for decades. Past investigations have typically focused on the final bond strength determined from standard pullout tests (e.g., ASTM A981 with modifications). However, flexural tests that are more relevant to concrete girder design have also been conducted. For example, (Laco 2018) and (Laco and Borzovič 2017) tested two-span post-tensioned concrete beams. The tendon-grout bond mechanism was investigated for different strand surface conditions (untreated and treated with Rustband 310) under flexural loading. Electromagnetic gages installed on the tendons were used to characterize: 1) tendon force during prestressing, and 2) incremental changes of tendon force caused by flexural deformation.

Coating bonded tendons with oil resulted in loss of bond (i.e., bond slip) at approximately 90% of ultimate strength. Laco and Borzovič 2017 observed and recorded differences in characteristic crack patterns that occurred during flexural tests of post-tensioned beams having different bond conditions. At low to moderate load levels, specimens utilizing fully bonded tendons, and specimens utilizing oil-treated tendons, both exhibited approximately uniform crack distributions on the tension faces. At higher applied loads, the crack patterns in beams with fully bonded tendons remained approximately uniform, but beams with oil-treated tendons developed fewer and wider cracks, similar in pattern to beams that utilized fully unbonded tendons.

Additional pullout tests, conducted using a modified ASTM A981 procedure, were carried out on tendons treated with emulsifiable oils. These tests indicated tendon-grout bond strengths

that decreased by as much as 17% and 67%, respectively, as compared to untreated tendons (Figure 3.3).

Figure 3.3. Setup for pullout test of monostrand unstressed tendon (Laco and Borzovič 2017).

3.1.2 Grout Type

Cementitious grout in bonded post-tensioned systems provides corrosion protection to the steel strands and contributes to the transfer of prestress force from the tendon to the concrete. Grouting of tendons increases the nominal flexural resistance of post-tensioned girders, as compared to post-tensioned girders with unbonded tendons. However, this improvement in flexural resistance is only achieved when the injected grout forms an adequate bond around the strands. In practice, improper grouting procedures or variations in grout material properties can result in porous, soft grout, or bleed water at high points along the duct curvature.

Corrosion-induced tendon damage, caused by poor grout, have been encountered in structures such as the Niles Channel Bridge, Midbay Bridge, and Sunshine Skyway Bridge. In these Florida bridges, grout void formation due to bleed water was observed. These findings led to changes in construction materials used in bridge construction in Florida. Specifically, around the year 2000, a shift was made from Portland cement grout to low-bleed prepacked grout for post-tensioned tendon grouting, as specified in the FDOT Standard Specifications for Road and Bridge Construction (FDOT 2023a). As an example, no-bleed and non-shrink MasterFlow 816 Cable Grout was used to repair grout voids in Mid-Bay Bridge as shown in Figure 3.4 (FDOT 2001). Around the same time, the use of prebagged grouts (from different manufacturers) was investigated to assess the potential for bleed water development under varying conditions of temperature, mixing time, and tendon size (Alvarez and Hamilton 2002). The study demonstrated a variation/increase in bleed water quantity at a higher temperature for all grout types except for Master Builder's MasterFlow GS 1205. Sika Cable Grout and Euclid Euco Cable Grout PTX were two grout types that performed better when longer mixing times were used.

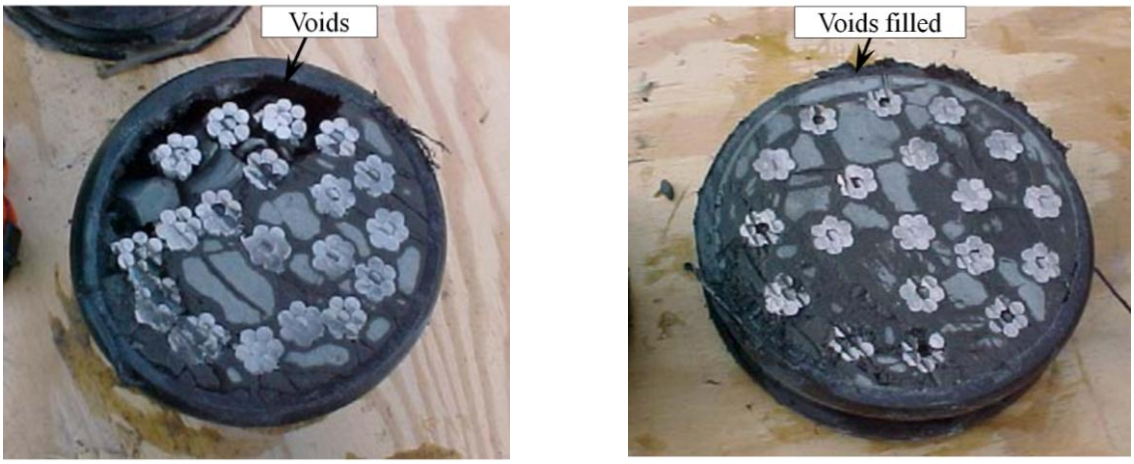

(a) (b)

Figure 3.4. Dissected mock-up bonded tendon. Grout injected using: (a) pressure injection; and (b) vacuum injection (Corven 2001)

The FDOT transition from Portland cement grout to prebagged grout around the year 2003 can be used as a reference point for classification of grouted post-tensioned bridges in Florida (Table 3.1).

Table 3.1. Types of grout materials used for grouting of post-tensioned bridges in Florida.

Bridges	Purpose	Grout types
Bridges constructed prior to 2003	Primary internal grouting	Portland cement with/without admixtures
Major bridges constructed in/after 2003	Primary internal grouting and reinjection for repair	Prebagged/preapproved grout meeting the requirements of FDOT standard specifications 938 "Post-tensioned grout"

3.1.3 Tendon Size

The tendon sizes used in post-tensioned concrete bridges control the amount of prestressing force that is transferred to the girders. Selection of tendon sizes is largely up to the discretion of the bridge designer and will vary based on the specific requirements of projects. However, the current FDOT Structures Design Guidelines (SDG) (FDOT 2023b) indicate that the sizes of tendons used in Florida bridge design may range from 4 to 31 strands (for 0.6-in. diameter seven-wire strands).

The FDOT Structures Design Guidelines have undergone many revisions over the years. Thus there are some differences in tendon sizes used in older bridges as compared to the newer bridges. However, the sizes of tendons used in construction generally fall within the same range as specified in the current FDOT SDG. For example, Ringling Causeway Bridge was constructed using tendons that contained 22 strands (Azizinamini 2018). Various segmental bridges in coastal Florida have been constructed using tendon sizes ranging from 19 to 24 strands (Sagüés 2008), where individual strand sizes were of either 0.5 in. or 0.6-in. nominal diameter.

Variations in tendon size can lead to variations in the serviceability of post-tensioned structures at later stages in the life of bridges. The interstitial spaces that are present between the wires and strands that makeup a complete tendon may allow moisture to enter and lead to corrosion (FDOT 2001). Variations in the amount of interstitial space present in a tendon may therefore affect the potential for corrosion issues. Experimental tests have shown, for example, that grout fills the spaces outside the tendon, but the interstitial spaces between the strands remain voided, as shown in Figure 3.5 (Alvarez and Hamilton 2002). Additionally, direct strand-to-strand contact is known to increase the potential for propagation of corrosion damage. Consequently, larger tendon sizes, which involve larger numbers of strand-to-strand contact interfaces, are more at risk for corrosion. Corrosion-inhibiting materials, such as Vector Corrosion Technologies PTI fluid, may be injected into the interstitial spaces of tendons to provide corrosion protection. This approach has been implemented internationally for a significant number of bridges to date.

(a) (b)

Figure 3.5. Examination of dissected specimen: (a) intact bond between grout and outside tendons; (b) grout penetration into the strand interstitial spaces. (Alvarez and Hamilton 2002).

Table 3.2 summarizes the number of bridges constructed using grouted tendons that have been treated with the Vector impregnation material to arrest or mitigate corrosion. The quantity and geometric configuration of strands contained within a grouted tendon determined the extent of interstitial space, as well as the number of wire-to-wire contacts, and thus will influence the effectiveness of treatment via injection of corrosion-inhibiting fluids such as the Vector Post-tech PTI Impregnation fluid.

Table 3.2. Number of bridges with grouted tendons treated with PTI impregnation material as of the year 2020. (Vector Corrosion Technologies 2021).

Number of strands (n)			Tendon length (ℓ in ft)		Tendon location	
$n \leq 12$	$12 < n \leq 19$	$19 < n \leq 31$	$\ell \leq 200$	$200 < \ell$	Exterior	Interior
6	5	5	10	9	10	10

3.1.4 Duct Type

In concrete bridge girders that utilize grouted post-tensioned internal tendons, the types of duct material that are commonly used in Florida include: corrugated metal (e.g., galvanized steel) duct; and corrugated (ribbed) plastic (e.g., polypropylene) duct (Figure 3.6). Rib patterns for a PT duct vary both by material type as well as manufacturer.

Figure 3.6. Corrugated ducts of different materials and ribs used for post-tensioning: corrugated metal duct on the left and corrugated plastic duct on the right.

During post-tensioning of a prestressed concrete system, the duct type plays a role in influencing friction losses that result in a decrease in effective prestress force. Friction losses may be contributed by the wobble effect due to geometric misalignment and duct curvature. During jacking, sliding of the tendon against the duct may occur when the duct is accidentally misaligned (causing wobble friction), intentionally curved (causing curvature friction), or both. Accidental duct misalignment occurs as a result of construction tolerances. In contrast, curved (or deviated) tendons profiles (e.g., parabolic or harped) occur intentionally as a result of the prestressing design process. In both cases (wobble and curvature), during jacking, frictional sliding forces develop between the strands in the PT tendon, and the walls of the duct. These frictional forces, which cause loss of effective prestress, are a function of tendon force, geometric duct/tendon alignment, and the coefficient of friction between the tendon and duct. Typical coefficients of friction for different duct types, when in contact with steel strands, are provided in Table 3.3.

Table 3.3. Coefficients of friction between steel strand and different duct types (adapted from ACI 423.10R-16, 2016).

Type of prestressing steel	Corrugated metal duct	Corrugated plastic duct
Strand	0.15-0.25	0.10-0.14

In a grouted post-tensioned girder, incremental strain compatibility is assumed between the tendon, grouted duct, and surrounding concrete. However, given that direct points of frictional contact will still exist between the tendon and the duct, even in fully-grouted system, the coefficient of friction between the tendon and duct could potentially play a role in affecting nominal flexural resistance. In particular, if the coefficient of friction is significantly reduced by the presence of injected corrosion-inhibiting fluids, this could potentially have an influence on post-tensioned system behavior. Moreover, the extent to which the presence of a corrosion-

inhibiting fluid may affect the coefficient of friction may be material dependent (i.e., different for metal vs. plastic duct), and thus multiple duct material types were investigated in this study.

One other possible effect that duct may have on bond strength relates to the confinement provided by the duct for the grout and strand. For mechanical bond to develop between the grout and strand, the grout within the duct must be sufficiently confined by the duct and surrounding concrete. It is possible that steel duct will provide better confinement than plastic duct and result in a higher mechanical bond strength. Thickness of concrete cover and quantity of confinement reinforcement around the duct may also affect the confinement of the grout in the duct.

3.1.5 Tendon Profile

Tendon profiles are chosen based on girder type (I-beam, box, etc.), girder configuration and boundary conditions (simple spans, continuous spans, etc.), and applicable serviceability requirements. In Figure 3.7, strand configurations at three distinct longitudinal positions are illustrated: near the wedge plate and within the trumpet length; partway between the anchor and midspan; and at midspan. In a straight profile (Figure 3.7), strands within the tendon may remain (ideally, at least) at a fixed (constant) position relative to each other over the length of the tendon. In contrast, draped profiles (Figure 3.7) cause the relative positions of strands within the tendon to change as a function of longitudinal position along the girder. Individual strands within the tendon are at their greatest relative separation distance as they emerge from the wedge plate at the anchorages.

As tension is applied during jacking, the tendon seeks the path of minimum length along the duct. In draped tendons, following the path of least length results in individual strands becoming tightly packed together against one another and against one surface of the duct (upper surface) at various locations along the tendon profile. At these locations, tendon strands are in direct and significant contact with the duct wall, thereby producing frictional forces. Additionally, given the dense packing of the strands against each other and against the duct wall, the possibility exists that grout may not be able to fully penetrate the strand bundle and completely envelope all strands at such locations. Under these conditions, the volume of injected corrosion-inhibiting liquid at the contact interface could be significantly greater than in a typical grouted straight tendon. It is not currently known how this condition might affect the behavior of a post-tensioned concrete cross-section or its flexural capacity.

Post-tensioned concrete bridges constructed in Florida prior to FDOT implementing the use of flexible fillers for internal unbonded girders were designed according to standards (including tendon profiles) applicable to grouted internal tendons. Such bridges are candidates for future injection of corrosion-inhibiting materials, and therefore, tendon profiles associated with these structures are of primary interest in this study.

For example, continuous-span Florida bridges with spliced precast girders historically used prestressed Florida Bulb-Tee girders. These structures utilized draped-profile multistrand post-tensioned tendons, along with straight pre-tensioned tendons. This type of bridge construction has been used in many bridges in Florida, including the Eau Gallie Bridge in Melbourne, the Howard Frankland Bridge in Tampa, the Edison Bridge in Fort Myers, the Flagler Beach Boulevard Bridge, and the St. George Island Bridge across Apalachicola Bay. The same general construction approach has more recently been used in bridges constructed using Florida I-beams (FIB) instead of Florida Bulb-Tees. Grouted internal post-tensioned tendons are also used in bridges constructed with box girder sections, either cast-in-place or precast. For example, the Acosta Bridge in Jacksonville uses

straight-profile grouted internal post-tensioned tendons in both the top slab and bottom slab of the box girder.

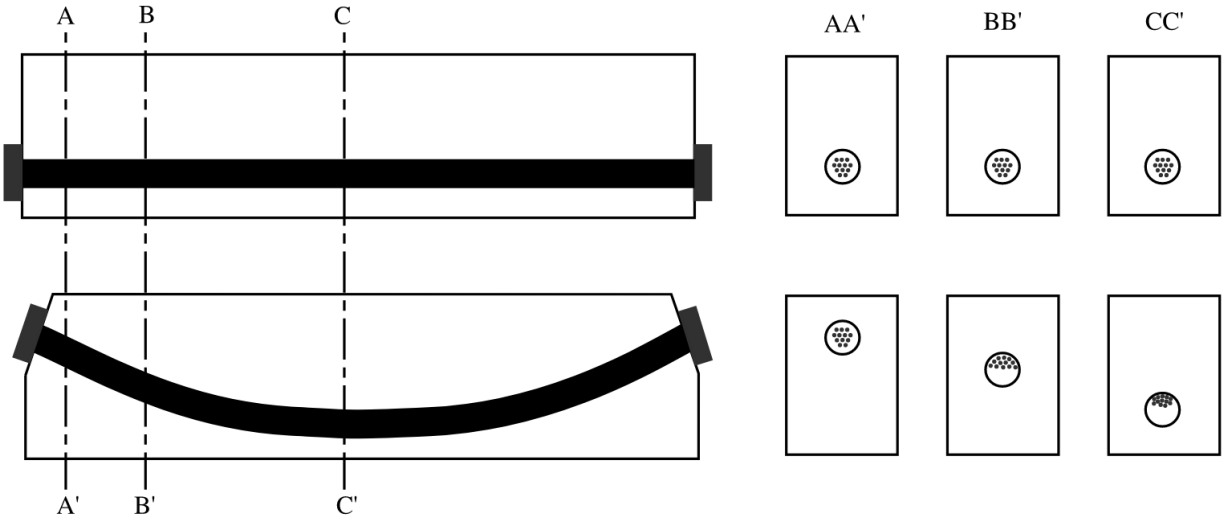

Figure 3.7. Example tendon profiles (straight and draped) used historically in Florida bridges that utilize grouted post-tensioned tendons.

3.1.6 Treatment Age

As noted earlier, the effect that the Vector PTI corrosion protection fluid (a hydrocarbon silicon polymer resin) has on bond strength has been investigated in the past using tests on individual unstressed strands. While these tests have indicated a significant reduction in bond strength, as compared to untreated strands, the effect that time has on the reduction in bond strength appears to be negligible (based on information available thus far). Tests conducted by the University of South Florida (Silnutzer et al. 2020) indicated a reduction in bond strength of approximately 47% compared to untreated tendons. However, the bond strength reduction at 1 week after injection, versus at 1 month after injection, were essentially the same. Based on the currently available data, the bond strength reduction caused by injection of the Vector Post-Tech PTI material occurs as early as one week after treatment and remains approximately constant in the long term.

A strong time dependency between elapsed time since corrosion inhibitor injection and resulting reduction of bond strength is not currently evidenced by available information. Nevertheless, the radius of inhibitor impregnation into surrounding grout will be a function of the length of time that injection pressure is maintained during tendon treatment. Additionally, the time since grouting was completed, and thus the age of the grout, may influence characteristics of the cured grout, and thus could influence the radius of impregnation of the corrosion protection fluid. Given these factors, maintaining consistency of various testing related time durations is considered warranted. For example, elapsed time between completion of grouting and the injection of corrosion inhibitor should be consistent across all treated beam specimens (i.e. those injected with corrosion inhibitor). Similarly, the time duration used to inject corrosion inhibitor, under pressure, into each beam specimen should be consistent. Additionally, the total elapsed time between completion of grouting and flexural testing should be as consistent as is feasible across both treated specimens, and untreated (control) specimens.

3.2 Matrix of Test Conditions

Based on the considerations discussed in the previous sections, the matrix of beam specimens for this project is provided in Table 3.4. Five unique groups of matched pair specimens are developed (S06, S12, S19, D19-M and D19-P). The groups exhibit variations in cross-sectional shape, tendon size (6, 12, 19 strands), tendon profile (straight, draped), duct type (metal, plastic), and grout type (plain, pre-packaged, and legacy). A total of 11 individual beam specimens are were constructed: four couplets (i.e., pairs consisting of a pristine control beam, and an injected [with Vector Post-Tech PTI material] beam), and one triplet (consisting of a pristine, an injected, and a cracked then injected specimen).

Table 3.4. Matrix of beam specimens

Beam Specimen ID	Tendon profile	Tendon size (num. strands)	Duct type	Grout type	Treatment with corrosion inhibitor
S06-M-U	Straight (S)	6	Metal (M)	Pre-Packaged	Un-treated (U)
S06-M-T	Straight (S)	6	Metal (M)	Pre-Packaged	Treated (T)
S06-M-TC*	Straight (S)	6	Metal (M)	Pre-Packaged	Treated (T)
S12-P-U	Straight (S)	12	Plastic (P)	Pre-Packaged	Un-treated (U)
S12-P-T	Straight (S)	12	Plastic (P)	Pre-Packaged	Treated (T)
S19-M-U	Straight (S)	19	Metal (M)	Plain	Un-treated (U)
S19-M-T	Straight (S)	19	Metal (M)	Plain	Treated (T)
D19-M-U	Draped (D)	19	Metal (M)	Legacy	Un-treated (U)
D19-M-T	Draped (D)	19	Metal (M)	Legacy	Treated (T)
D19-P-U	Draped (D)	19	Plastic (P)	Legacy	Un-treated (U)
D19-P-T	Draped (D)	19	Plastic (P)	Legacy	Treated (T)

* Specimen ‘TC’ treated ‘T’ with corrosion inhibitor after being cracked ‘C’

CHAPTER 4 DESIGN OF BEAM SPECIMENS

This section describes the methodologies employed in designing the beam specimens. A total of seven specimens varying in cross-sectional shape, tendon size, grout type, and duct type are designed for the flexural testing. All tendons in this study are straight. The following sections describe the design methodologies and rationale; the final fabrication drawings are enclosed in Appendix A.

4.1 Principle Governing the Design of Beam Specimens

It is anticipated that injecting corrosion-inhibitor fluid into a fully bonded post-tensioned tendon reduces the tendon-grout bond to a partially bonded condition. When inhibitor fluid is injected under a pressure differential, it travels along the tendon profile through interstitial spaces. The fluid mitigates corrosion in two ways: it forms a protective coating around the strands that limits moisture contact, and it displaces moisture around the strands.

In a fully bonded tendon, three bond mechanisms exist: adhesion, mechanical restraint (interlock), and friction. Adhesion arises from chemical bonding between grout and strand. Mechanical restraint and friction arise from the interlocking of the strand surface profile with the surrounding grout. As a bonded post-tensioned beam approaches nominal flexural resistance, adhesion is lost due to longitudinal (extensional) strain and Poisson's contraction of the strands; the strand surface pulls away from the adjacent grout, breaking chemical adhesion. Consequently, near nominal flexure, bond transfer from strands to grout is dominated by mechanical restraint and friction.

Prior pullout tests by (Laco 2017 and Borzovič 2017) indicate that bond measured in simple pullout setups develops strand stresses far below those reached in flexural beam tests. In the control condition, the pullout specimens mobilized only about 45% f_{pu}, while specimens affected by an emulsifiable oil mobilized roughly 15% f_{pu} (and a thixotropic-gel condition was around 37% f_{pu}). By contrast, post-tensioned girders approaching nominal flexural resistance commonly drive the tendons to ~70–80% f_{pu}. This mismatch in stress level and the associated deformation state means pullout tests capture a different bond regime than that governing a girder near nominal flexure, so their bond reductions should be interpreted with caution for beam behavior.

Although unlikely, the upper bound on bond degradation due to inhibitor injection is 100%, which would yield a fully unbonded system. Actual degradation is not expected to approach this limit. Importantly, for a given percentage reduction in bond strength, the corresponding reduction in nominal flexural resistance is much smaller. For perspective, the nominal strengths of otherwise identical girders that are fully bonded versus fully unbonded differ by a moderate amount. To maximize the chance of experimentally observing differences in cracking characteristics and nominal flexural strength between control and injected specimens, the beam specimens were therefore sized to maximize (within practical limits) the separability between the fully bonded and fully unbonded bounding cases. This objective informed choices of span-to-depth ratio and other parameters. In addition, four-point bending was selected to create an extended constant-moment region to facilitate observation and mapping of cracking differences.

4.2 Design Procedure

4.2.1 Nominal Flexural Resistance

Nominal flexural resistance was calculated using the strain-compatibility method. Concrete in compression was represented by an equivalent rectangular stress block, and the concrete strain at the extreme compression fiber was taken to reach the maximum usable strain of $\epsilon_{cu} = 0.003$. The design stress–strain curve for a 7-wire, low-relaxation, 270 ksi strand from Design Aid 15.3.3 of the PCI Design Handbook, 7th ed. (PCI 2010), was used to estimate strand stress at nominal flexural resistance.

Additionally, supplemental nominal flexural resistance calculations were performed using the moment-curvature analysis procedure described in Consolazio et al. (2004). In these analyses, the modified Hognestad parabola was used for concrete in compression, and the Ramberg-Osgood function suggested by Collins and Mitchell (1991) was used for the low-relaxation prestressing strands. Nominal flexural resistance calculated using strain-compatibility analysis and moment-curvature analysis differed by less than 1% for all beam cross-sections. Because strain-compatibility analysis is more computationally efficient, it was used to iterate cross-sectional shapes, span lengths, and tendon eccentricities at midspan. These analyses were used to investigate midspan behavior (e.g., tendon strain at the location of maximum tendon eccentricity), concrete stresses at post-tensioning, and to check designs against practical limits (e.g., FDOT actuator load capacity).

For estimated load-deflection diagrams, more detailed moment-curvature analysis was required. Nonlinear sectional moment-curvature relationships were computed at key stations (longitudinal locations) along the beam, then combined with the longitudinally varying moment diagram from the applied loading. Numeric integration with the moment-area method was used to compute midspan deflections at varying load levels.

4.2.2 Shear Strength

Shear capacities computed using ACI 318 (ACI 2022) and the AASHTO modified compression field theory (MCFT) method (Section 5.7.2, AASHTO LRFD 2020) were compared for one representative specimen. The AASHTO method was found to be conservative relative to ACI; therefore, the AASHTO approach was used to design shear reinforcement for all specimens. Because the study focuses on quantifying nominal flexural resistance (not shear capacity), sufficient transverse reinforcement was provided to ensure the beams can reach nominal flexural resistance without premature shear failure.

4.2.3 Anchorage Zone Design

Anchorage zone reinforcement for the end blocks of the beam specimens was designed using the strut-and-tie method. The strut-and-tie model noted in Figure C5.8.2.7.1-2(b) of AASHTO LRFD 2020, for a ‘large eccentricity’ tendon force, was chosen to design the anchorage zones for all beam specimens with straight (denoted ‘S’), i.e., constant eccentricity, tendon profiles. This includes beam specimens S19, S12, and S6, which utilize 19, 12, and 6 strand straight (constant eccentricity) tendons, respectively. The choice of the AASHTO C5.8.2.7.1-2(b) strut-and-tie model was based on similarities of stress flow and eccentricity at the point of action (tendon jacking force) on the cross-sections of beam specimen end blocks. For beam specimens that utilize

draped (denoted 'D') tendon profiles, the strut-and-tie model noted in Figure C5.8.2.7.1-2(e) of AASHTO LRFD 2020 was chosen to design the anchorage zone reinforcement. The Figure C5.8.2.7.1-2(e) strut-and-tie model is applicable to beams having the point of action (tendon jacking force) inclined at some angle relative to the horizontal axis and having no tensile stress present in the cross section. Specifically, the anchorage zone reinforcement for the end blocks of beam specimens D19 (19-strand, draped tendon) were designed using the Figure C5.8.2.7.1-2(e) strut-and-tie model.

4.2.4 Deflection

Deflection calculations were performed to ensure that final midspan deflections remain within the 18-in. stroke capacity of the FDOT Enerpac RR-40018 actuator. Initially, the PCI approximate bilinear method for Class-T (transitional) sections (PCI 2010) was used, in which the final deflection is the sum of deflections before cracking (gross-section properties) and after cracking (cracked-section properties). The transition from uncracked to cracked classification was determined using the modulus of rupture as defined in ACI 318-19, Section 19.2.3 (ACI 2022).

A more refined approach was then employed by combining moment-curvature sectional analysis (Consolazio et al. 2004), the moment-area method, and numeric integration to compute midspan deflections over load levels up to nominal flexural resistance. This approach used a concrete constitutive model that accounts for nonlinear compressive behavior (Consolazio et al. 2004) and tensile behavior (Consolazio and Woolf, 2007), together with a nonlinear tensile constitutive relationship for prestressing strands. The moment-curvature component can predict sectional responses beyond ϵ_{cu} = 0.003. However, in this study, the nominal flexural resistance M_n defined by the condition $\epsilon_{c,max} = \epsilon_{cu}$ = 0.003 is of primary interest. Accordingly, anticipated midspan deflections were computed for load points including the nominal strength condition.

4.3 Experimental Variables

4.3.1 Beam Geometry

<u>Beam cross-section</u>

Cross-sectional dimensions of the beam specimens were controlled by the tendon sizes and by the strain levels that are targeted to be generated (during testing) in the tendons at the nominal strength flexural condition. Since concrete below the neutral axis of a cross-section has only a negligible contribution to section flexural strength, T-shaped cross-sections were designed with wide compression flanges and narrower web widths. The web widths that were selected were adequate to accommodate post-tensioning ducts, surrounding transverse reinforcing bars, and clear cover. The section depth and flange width of each beam were iterated to keep the target strain (~2%) in the strands consistent across all of the specimens. While increasing the depth of a cross-section is beneficial in terms of generating higher tendon strains, there were practical concerns regarding girder stability during laboratory testing. Consequently, the beam cross-sectional depths (heights) were limited to a maximum of 36 in. to reduce the potential for instabilities during testing.

Beam span length

The primary objective during flexural testing of the beams will be to distinguish if there are differences in nominal flexural capacity between the pristine (control) specimens and those injected with corrosion inhibitor. Some degree of bond degradation will occur when corrosion inhibitor is injected, as discussed in Chapter 2, therefore it is expected that the injected beam specimens will exhibit a partially bonded flexural behavior somewhere between that of the pristine, fully bonded condition, and a fully unbonded condition. Accordingly, the beam specimens have been designed in such a way that the separation between the nominal flexural capacity of the fully bonded condition ($M_{n_{bonded}}$) and that of the theoretically fully unbonded condition ($M_{n_{unbonded}}$) is sufficiently large as to be outside the range of experimental measurement error. If the separation between the boundary values $M_{n_{bonded}}$ and $M_{n_{unbonded}}$ is too small, it will not be feasible to meaningfully distinguish between $M_{n_{bonded}}$ and $M_{n_{injected}}$, where the injected (i.e., partially bonded) condition lies between the bounding values (i.e., $M_{n_{bonded}} \geq M_{n_{injected}} \geq M_{n_{unbonded}}$).

The span-to-depth ratio (L/d) of each beam significantly influences the difference between the nominal flexural capacity of the fully bonded condition and the fully unbonded conditions. Namely, increasing the L/d increases the separation between these bounding conditions. Clearly, increasing L/d can be achieved by increasing L, or by decreasing d. However, as section depth d decreases, it becomes more challenging to experimentally achieve the target strain level in the strands (~2%) at nominal flexural capacity (M_n) in a manner that is consistent across all beam specimens. Consequently, instead, the span length L of the test beams was iteratively increased until a reasonable separation between $M_{n_{bonded}}$ and $M_{n_{unbonded}}$ was obtained. It was determined that at a span length of L =40 ft, $M_{n_{bonded}}$ and $M_{n_{unbonded}}$ differed by ~19% for the beam specimen cross-sections described here.

For comparison, decreasing the span length to L =30 ft caused the differences in nominal flexural capacities at the bounding conditions (bonded and fully unbonded) to be reduced to ~11% which would make experimentally distinguishing between the bonded and partially bonded (injected) conditions more challenging. Additionally, increasing the span length to L =50 ft resulted in $M_{n_{bonded}}$ and $M_{n_{unbonded}}$ differing by ~21%, just ~2% larger than at L =40 ft. Thus, for the cross-sectional shapes and tendons sizes being studied here, a span length of L=40 ft was found to be reasonably optimal.

Note that nominal flexural capacity calculations used in setting the span length of the specimens were computed 1) using the moment-curvature analysis procedure described in Consolazio et al. (2004) for bonded conditions, and 2) using the empirical equations given in Art 5.6.3.1.2 AASHTO LRFD 2020 for unbonded conditions.

4.3.2 Tendon Properties

Tendon profile

Two different tendon profiles - straight ‘S’ and draped ‘D’- have been included in the test matrix to study the effects that the injected corrosion inhibitor has on the bond between the tendon and grout. A significant fraction of the beam specimens will utilize straight tendon profiles to investigate the influence that the corrosion inhibitor has when the tendon is fully encased within grout. In this context, ‘fully encased’ refers to the condition where the entire outer perimeter surface area of the tendon is in direct contact with grout, and no portion of the tendon perimeter

surface is instead in direct contact with the inner surface of the duct. That is, a straight tendon in a grouted post-tensioned beam will result in maximum grout encasement of the strands. This condition eliminates direct frictional contact between the tendon and the duct and maximizes the amount of grout volume that can be impregnated, and possibly degraded, by the injection of corrosion inhibitor.

In contrast, when draped tendon profiles are utilized, individual strands in the tendon will bundle up against the inner surface of the duct wall during post-tensioning and before grouting (see Chapter 3, Figure 3.7). This direct contact between the tendon surface and the duct surface 1) will reduce the volume of surrounding grout that directly encases, and is bonded to, the tendon, and 2) will reduce the volume of surrounding grout that may be degraded by injection of liquid corrosion inhibitor. Conversely, because there will be direct contact between the tendon and the duct in the draped and harped profile cases, tendon-to-duct frictional forces will develop in these specimens that will not be present in the straight tendon specimens. To investigate the effects that corrosion inhibitor may have under these conditions, a limited number of the beam specimens will therefore utilize draped and harped tendon profiles. Additionally, because frictional forces between the tendon and duct will be affected by duct type (i.e., duct material), different types of duct material will also be investigated, as described in a later section.

Tendon size

The three largest post-tensioned tendon sizes typically used in FDOT bridge construction are 19, 27, and 31 strand tendons (0.6-in. dia. strands, each). To maintain a level of consistency between the sizes of tendons to be tested in this study, and those used in typical bridge construction, yet to also remain within practical constraints (such as laboratory actuator capacity, maximum laboratory span length, stability/safety considerations, and budget considerations), 19-strand tendons were selected as the largest tendon size that will be tested. Approximately one-half of the beam specimens to be tested will utilize 19-strand grouted post-tensioned tendons.

However, it is also of interest to investigate whether different-sized tendons may be affected differently by the injection of corrosion inhibitor. For example, it is desirable to determine whether the use of the same injection equipment for 6, 12, and 19 strand tendons produces a consistent % of relative grout volume that is impregnated and affected by injection of corrosion inhibitor. If so, then a consistent level of bond degradation would be expected, with a consistent influence on measured nominal flexural capacity. Injection and flexural testing of beams with smaller tendon sizes (6, 12), in addition to the larger 19 strand tendons, will facilitate this type of evaluation.

Note that all tendons utilized in this study will consist of 0.6-in. diameter, 270 ksi, low-relaxation A416 steel strands. Furthermore, for the sake of efficiency in preparation (post-tensioning) of the beam specimens, all tendon sizes will utilize the same 19-strand anchorage (VSL ECI 6-19). Use of a single anchorage size will enable a single multistrand jack to be used to post-tension all of the beam specimens (6, 12, 19 strands). However, it must be noted that a single duct size (corresponding to a 19-strand tendon) will not be used for all specimens. Instead, the smaller tendon sizes (6, 12) will utilize appropriately sized ducts (per FDOT design guidelines). In this way, the relative ratio of cross-sectional area of tendon to cross-sectional area of duct will be maintained within limits that are representative of design.

Tendon eccentricity

As noted in Section 4.3.1, all beam specimens were designed with the goal of reaching a target tendon strain level of approximately 2% at the beam mid-span and at the stage when nominal flexural capacity is reached during testing. Achieving this level of tendon strain at nominal flexural capacity requires significant section depth and tendon eccentricity. As noted earlier, section depths were limited to a 36-in. maximum due to safety considerations regarding girder stability during testing. Thus, the maximum feasible tendon eccentricity was constrained first by overall cross-sectional depth.

Additionally, however, for all straight tendon specimens, the maximum tendon eccentricity was also constrained by the physical dimensions of the post-tensioning anchorage, plus the required concrete clear cover beneath the anchorage. Specifically, the lowest possible elevation of the tendon within the cross-section, measured from the bottom of the beam upward to the centroid of the tendon, is one half of the anchorage bearing plate height plus the required concrete clear cover. This lowest possible elevation within the beam produces the maximum possible tendon eccentricity for the straight tendon beam specimens. Note also that this constraint (minimum tendon elevation) was the same for all straight tendon specimens - 6, 12, and 19 strand - since a single size anchorage (VSL ECI 6-19, for a tendon with 19 0.6-in. dia. strands) will be used to post-tension of all beams, for the construction efficiency reasons noted above. Thus, the tendon eccentricities for all straight tendon specimens (6, 12, 19 strands) were set at their respective practical maximums, subject to the constraints of overall section depth and minimum tendon centroidal distance from the bottom face of the beams.

For draped beam specimens, all of which will utilize 19-strand tendons, maximum overall beam section depth enforces one constraint on the maximum possible tendon eccentricity, as was the case for the straight tendon specimens. However, for the draped specimens, the proximity of the tendon centroid to the bottom surface of the beam (near mid span) is not constrained by the physical dimensions of the anchorage because the anchorages for these beams are located near the top of the cross-section. Thus, in concept at least, a greater eccentricity between the concrete girder centroid and tendon centroid could have been achieved in the draped beam specimens.

However, the intent in testing draped tendon configurations is to investigate whether differences are observed(relative to corresponding straight tendon beams) in the extent of bond degradation and flexural capacity reduction that are produced by corrosion inhibitor injection. Isolating the effect of tendon profile then requires that the same tendon size (19 strand) be used for the straight and draped specimens, and that the same tendon eccentricity (near mid-span) also be used for all such specimens. Consequently, the mid-span elevation (and eccentricity) of the tendon centroid near midspan of the draped specimens was set at (and essentially constrained by) that of the straight 19-strand tendon beams.

4.3.3 Duct Properties

Duct size (diameter)

A unique duct size was selected for each of the three tendon sizes discussed above (6, 12, 19 strands). The size of each duct was selected primarily based on the recommended minimum internal duct diameter as given in Article 960-2.2.1.4 FDOT Standard Specifications for Road and Bridges Construction 2023. These specifications require that the minimum cross-sectional area of the duct for a multistrand tendon be at least 2.5 times the cross-sectional area of the tendon. This

requirement establishes a lower bound on the duct diameter, and on the duct area. Complementing this condition is FDOT SDG (2023) Article 1.11.4 which stipulates the upper bound (maximum) duct size that is permitted. For the beam specimens to be tested in this study, minimizing the duct area (within the permissible FDOT limits) will minimize the grout volume inside the duct. This condition would then be expected to maximize the relative volume of grout that is impregnated by injection of corrosion inhibitor and maximize the potential for observing changes of bond strength and changes of nominal flexural capacity (if any such changes are to occur). Consequently, the duct size for each beam specimen in this study was selected to be the smallest commercially available duct diameter that would provide an internal duct area equal to or larger than 2.5 times the respective tendon area.

Duct material

For straight tendon profiles at the span lengths that will be investigated in this study, the tendon is not expected to make significant direct contact with the inner walls of the post-tensioning duct. However, for draped and harped tendon profiles, the tendon will be in direct contact with the inner wall of the duct, and frictional interactions (e.g., development of frictional forces) between the tendon and duct are expected to occur. The magnitude of the frictional forces that develop during these interactions will depend, in part, on the material that the duct is constructed from since different duct materials possess different coefficients of friction.

In Florida bridge construction, post-tensioning ducts typically take the form of either corrugated metal duct (used prominently in the past) or corrugated plastic (polypropylene) duct (used commonly at present). Since the results of this research project are intended to apply primarily to existing (historical) bridges that were likely constructed using metal duct, greater emphasis has been given to this type of duct in establishing the test program. Injection of corrosion inhibitor into grouted post-tensioned tendons is primarily viewed as a means of protecting existing (historical) bridge structures from tendon corrosion. Consequently, more than half (approximately 60%) of the beam specimens will utilize metal duct that is representative of past bridge construction practices. However, there are also possible applications of corrosion inhibitor injection to newer bridge construction. Consequently, the remaining (approximately 40%) beam specimens will utilize plastic duct that is representative of current bridge construction practices.

4.3.4 Grout Type

In conjunction with the historical changes in duct type that have occurred in Florida bridge construction, similar changes in the type of grout used in Florida have also occurred, although along a slightly different timeline. Plain cement grout (Portland cement and water without admixtures) and legacy grout (Portland cement and water with admixtures) were used prominently in bridge construction prior to approximately 2000, whereas bridges constructed after approximately 2000 have generally used pre-packaged non-bleed grout.

In recent history, three general practices for grouted post-tensioned bridges in Florida can be identified: past practice (before 2000, metal duct with plain cement grout), transitional practice (2000-2003, metal duct with pre-packaged grout), and current practice (2003 to present, plastic duct with pre-packaged grout).

The grout types selected for the beam specimens are intended to primarily simulate bridge girders constructed in accordance with past practice (metal duct with plain cement grout, and metal or plastic duct with legacy grout) and transitional practice (metal duct with pre-packaged grout).

Approximately 36% of the beam specimens correspond to either pre-packaged or legacy grout, while the remaining approximately 18% of the beam specimens represent plain cement grout without admixtures.

4.3.5 Final Specimen Geometry

The design procedures and experimental variables described above result in straight- and draped tendon specimen matrix consisting of three unique T-beam geometries S06, S12, S19 and D19 tested over a 40-ft span under four-point bending. For each geometry, the tendon profile is either straight or draped with constant eccentricity at midspan set at the practical maximum permitted by anchorage dimensions and concrete cover. Cross-sectional dimensions were iterated to achieve a target strand strain of approximately 2% at nominal flexural resistance while limiting overall depth to 36 in. Duct sizes satisfy the FDOT 2.5× tendon-area requirement, and duct materials (metal and plastic) together with grout types (plain cement, pre-packaged, and legacy) are varied across the matrix to represent past, transitional, and current Florida practice. Figure 4.1 presents the overall elevation and the three T-beam cross-sections used in the matrix.

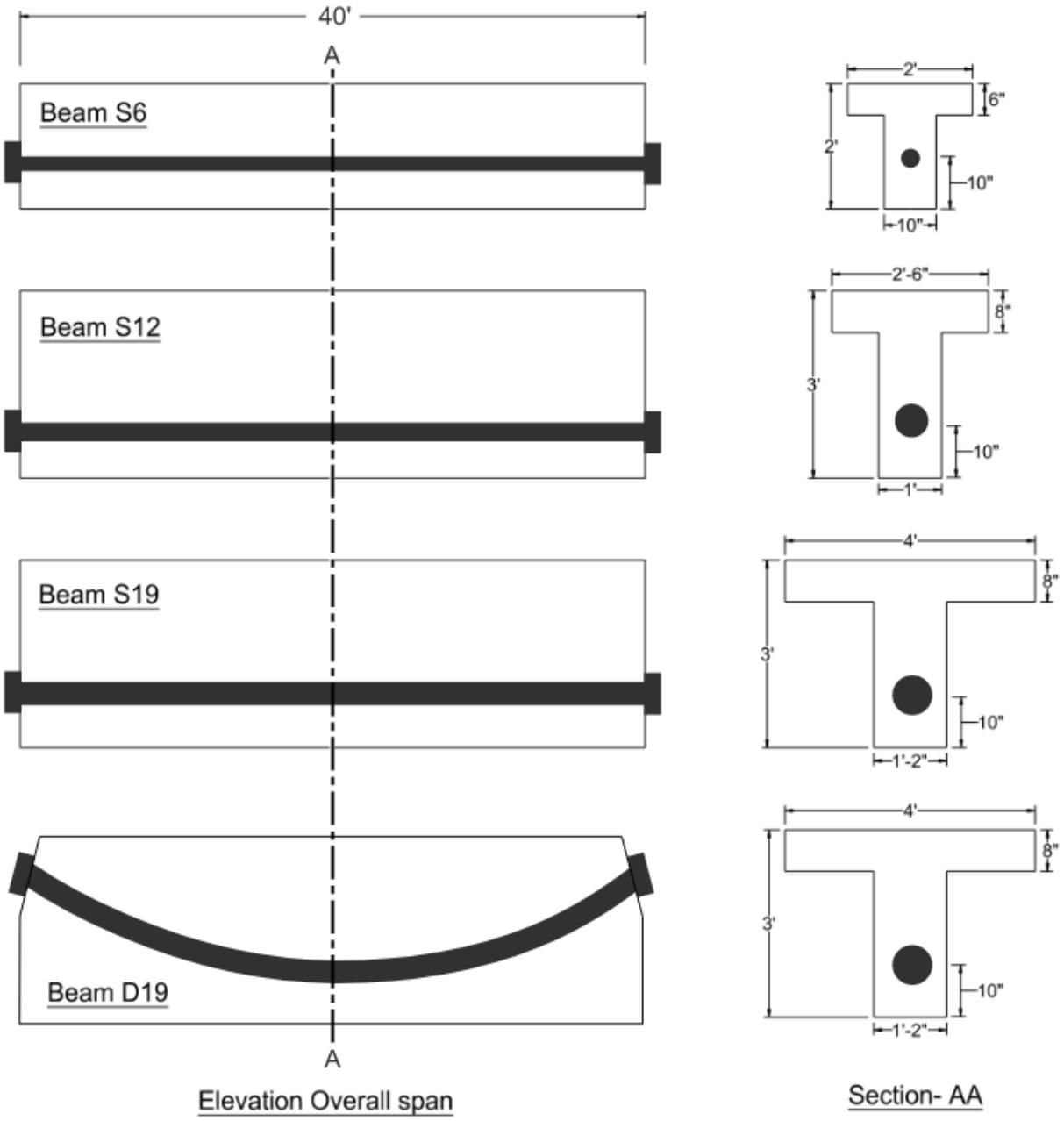

Figure 4.1. Elevation (L = 40 ft) and cross-sections of the straight- and draped-tendon specimens: S06 (small T-beam, 6 strands), S12 (medium T-beam, 12 strands), S19 (large T-beam, 19 strands), and D19 (large T-beam with draped tendon profile, 19 strands).

CHAPTER 5 DEVELOPMENT OF TEST PLAN

The experimental test plan described in this chapter includes an instrumentation plan, procedures for beam specimen preparation, testing protocols, and expected beam specimen loads. Development of the instrumentation plan included identifying sensor types, quantities, positions, and sampling rates. Procedures for preparing the beam specimens include post-tensioning, grouting, and injection of corrosion inhibitor. Test procedures - load rates, loading pauses, expected loads, and expected girder responses (such as deflections) are also addressed in this chapter.

5.1 Instrumentation Plan

Beam specimen instrumentation (Table 5.1) includes laser displacement transducers, fiber-optic strain sensors, surface-mounted concrete strain gages, and internally installed vibrating-wire strain gages. Additionally, strain and displacement are measured using a digital image correlation (DIC) system during load testing. Data from most sensors are gathered during load testing. Data from the vibrating-wire strain gages are also recorded during the concrete pouring, formwork removal, post-tensioning, and grouting stages. Detailed instrumentation plans for each unique test beam are provided in Appendix B.

Table 5.1. Instrumentation plan.

Response measured	Sensor type	Stage
Vertical displacement	Laser displacement transducer Digital image correlation	Flexural testing
Concrete strain (surface)	Foil strain gage Fiber optic sensors Digital image correlation	Flexural testing
Concrete strain (internal)	Vibrating wire strain gage	Flexural testing/Post-tensioning

5.2 Beam Specimen Preparation

5.2.1 Post-tensioning

Once the concrete beam specimens reach adequate compressive strength, they are post-tensioned using a multistrand hydraulic jack. Details of the procedures followed during post-tensioning are included in Appendix C. The procedures list the post-tensioning hardware (wedge plate, wedges, etc.), strand configuration within each wedge plate, target post-tensioning (PT) forces, and planned pauses in PT jacking force.

5.2.2 Grouting

All specimens are internally grouted using a grout pump provided by the FDOT State Materials Office (SMO). A colloidal mixer (ChemGrout CG-630) is used to mix grout before filling the PT ducts. The mixing and pumping procedure (Appendix D) is the same for both plain cement grout and pre-packaged grout. The grout is cured for at least 28 days before treatment with injected corrosion inhibitor. All beam specimens are grouted on the same day.

5.2.3 Specimen Cracking Before Impregnation

After the grout has reached an age of at least 28 days and the required strength, specimen S06-M-CT (Table 5.2) is subjected to four-point bending to produce initial cracking prior to injection of the corrosion inhibitor. Load is applied to produce a maximum moment of approximately $M_{cracked}$, that is, the moment corresponding to first cracking in the tensile zone (Appendix E). Actual confirmation of the cracked condition is based on direct observation of crack development rather than solely on computed cracking load and moment. Once initial cracks are observed, load is removed, and the pre-cracked specimen is readied for inhibitor injection.

5.2.4 Corrosion Inhibitor Impregnation

A total of six specimens, one specimen from each couplet (S12, S19, D19-M, and D19-P) and two specimens from the S06 triplet are treated with corrosion inhibitor by personnel from Vector Corrosion Technologies using their equipment and materials. Injection was completed within a 24-hour period (Table 5.2). Treated specimens were left for one week prior to four-point bending tests. The procedure for impregnation of the corrosion inhibitor of one of the beam specimen is described in Appendix F.

Table 5.2. Preparation and injection of beam specimens

Beam specimen identifier	Grouting type	Cracked before injection	Impregnated with corrosion inhibitor
S06-M-U	Pre-packaged	No	No
S06-M-T	Pre-packaged	No	Yes
S06-M-CT	Pre-packaged	Yes	Yes
S12-P-U	Pre-packaged	No	No
S12-P-T	Pre-packaged	No	Yes
S19-M-U	Plain	No	No
S19-M-T	Plain	No	Yes
D19-M-U	Legacy	No	No
D19-M-T	Legacy	No	Yes
D19-P-U	Legacy	No	No
D19-P-T	Legacy	No	Yes

5.2.5 Testing Protocol

Flexural testing utilizes a four-point bending setup. Load is applied to a spreader beam at midspan (Appendix G) to produce a central region of constant moment in each specimen. Load is applied at a rate of 0.25 kip/sec (15 kip/min), with load pauses (holds) at several key stages (Appendix G). At each pause, the beam is visually inspected for cracks. All identified cracks, or extensions relative to the previous pause are marked so the evolving crack pattern can be mapped.

Load and midspan-deflection data were continually monitored using selected instrumentation channels as detailed in Appendix G. Testing is terminated upon compressive failure in the top flange or after peak load has been reached and a subsequent drop-off in load with increasing deflection is observed.

For each couplet, the untreated control specimen is tested first, followed by the specimen treated with the corrosion inhibitor. For the S06 triplet, testing is proceed in the sequence: pre-cracked then treated (S06-M-CT), untreated (S06-M-U), and treated (S06-M-T).

CHAPTER 6 CONSTRUCTION OF BEAMS

6.1 Introduction

The construction details of the beams in this task report include fabrication, casting, post-tensioning, grouting, and corrosion inhibitor impregnation for the treated beams. The beams were divided into two groups, and corrosion inhibitor was impregnated into treated beams. The first group comprised a total of seven beams: S06 (S06-3-U, S06-M-T and S06-M-TC), S12 (S12-P-U and S12-P-T), and S19 (S19-M-U and S19-M-T). Once the construction of these seven beams was completed, they were instrumented and subjected to flexural strength testing. A similar procedure was followed for the four beams in the second group, which consisted of: D19-M (D19-M-U and D19-M-T) and D19-P (D19-P-U and D19-P-T). The test results in this report include flexural capacity and deflection of the beams, and crack characteristics.

6.2 Fabrication and Casting

Beams were fabricated at the FDOT Structures Research Center (SRC) in Tallahassee. The beams were constructed in batches of three (triplets for the six-strand beams) or batches of two (couplets for the 12- and 19-strand beams). Plywood formwork was constructed for each test beam, and assembled rebar cages were placed inside the formwork (Figure 6.2, Figure 6.3, Figure 6.4 and Figure 6.5).As S12 and S19 beams are the same depth, the formwork was fabricated with wider flange panels to be retrofitted and reused for S19 couplet (Figure 25b).Post-tensioning ducts were then placed and secured within the rebar cages and connected to the anchorage hardware attached to the formwork at both ends. For a deviated tendon profile, the duct was tied to the rebar cage at the specified elevations every 2 ft along the beam (Figure 23a). Lifting loops, made of prestressing strands, were bent and tied to the bottom longitudinal reinforcement bars at predetermined locations. Couplets of lifting loops were installed to lift the beams without causing tensile cracking. The lifting loops were used to lift the beams for stripping the formboards before post-tensioning and to place the beams in the test frame after post-tensioning. The S06 beams have two couplets of lifting loops, with the interior couplet used before post-tensioning and the exterior couplet used after post-tensioning. The S12, S19, and D19 beams have three couplets of lifting loops, with two interior couplets used before post-tensioning and the exterior couplet used after post-tensioning (Figure 6.1). Additionally, vibrating wire strain gages were placed at midspan of the beams to monitor concrete strain during post-tensioning and testing.

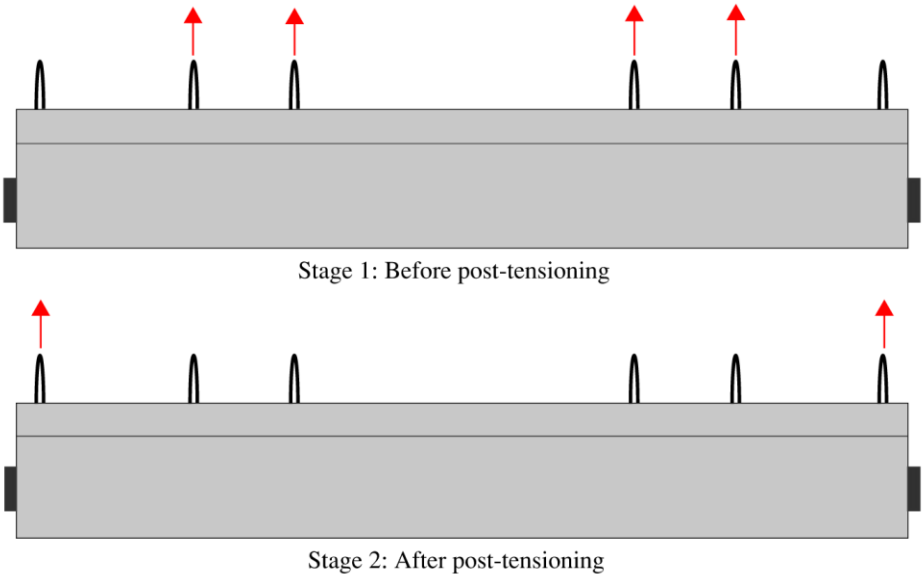

Figure 6.1. Lifting of S19 beam specimens using different sets of pick points at various stages of construction.

(a)

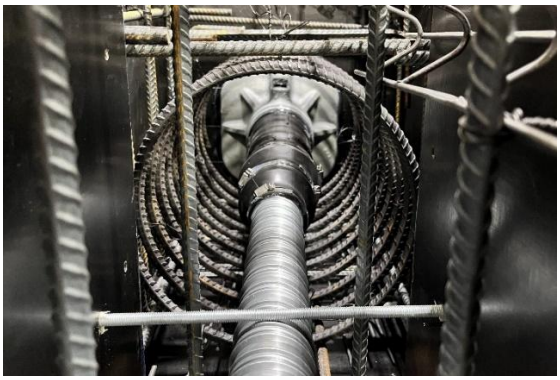

(b)

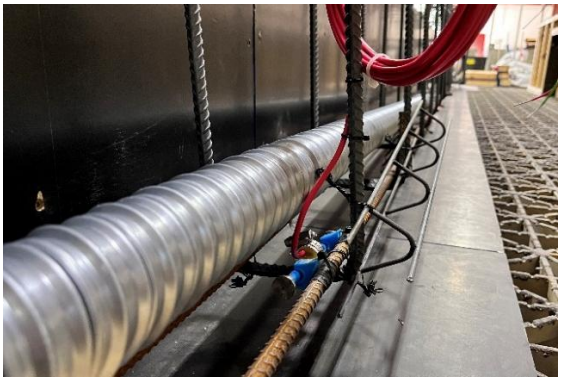

(c)

Figure 6.2. Fabrication of S06 beams: (a) End block rebar cage; (b) Trumpet and duct connection at end block; (c) vibrating wire strain gage installed at bottom longitudinal rebar.

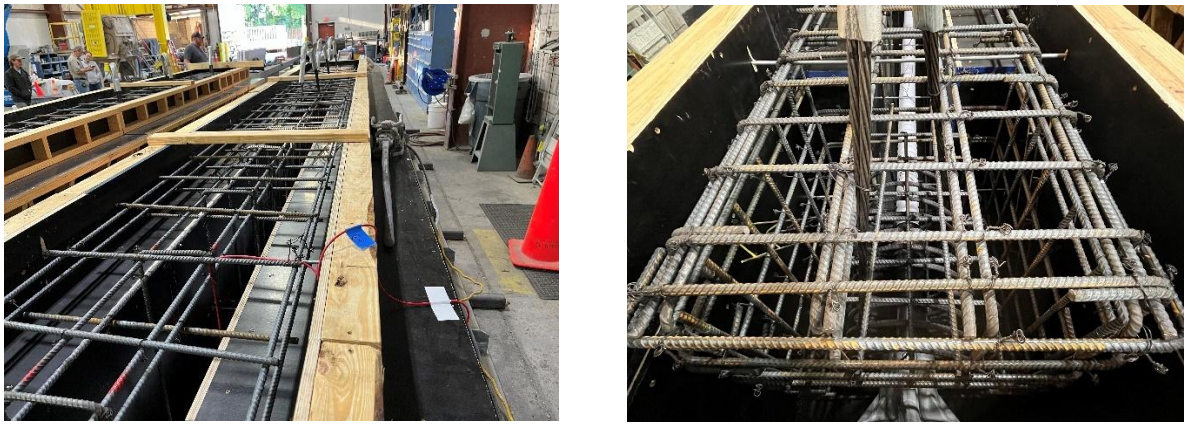

(a) (b)

Figure 6.3. Fabrication of S12 beams: (a) Flange rebar cages in formwork; (b) End block reinforcement bars in formwork.

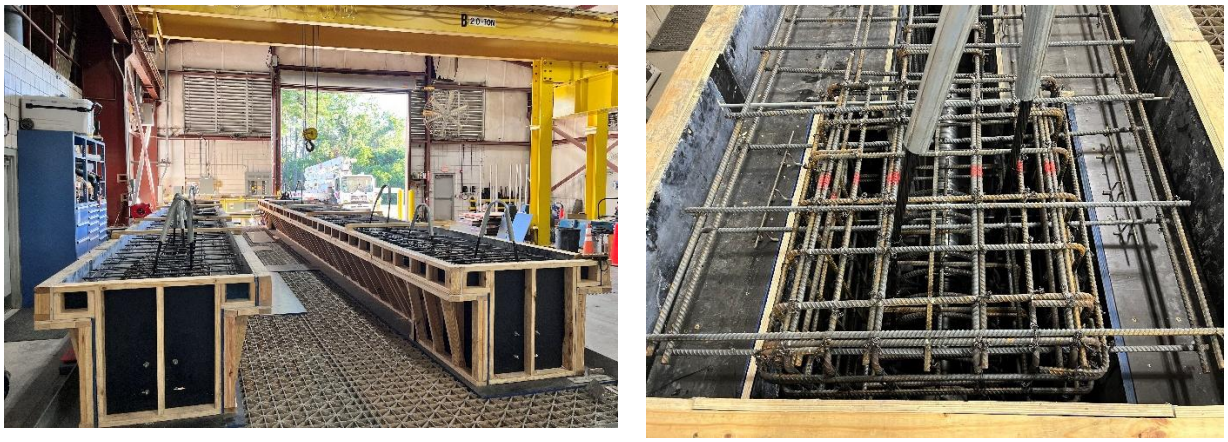

(a) (b)

Figure 6.4. Fabrication of S19 beams: (a) Fully assembled reinforcement bars in formwork; (b) End block reinforcement bars in formwork.

(a) (b)

Figure 6.5. Fabrication of D19 beams: (a) Live end of the D19-M-T beam with fully assembled rebar cage and open-ended plastic duct; (b) Fully assembled rebar cage and deviated metal duct in the D19-M-T beam.

Ready-mix pumpable (high-slump) concrete was used to cast the beams in a single pour. Beams were cast in triplets (S06) and couples (S12, S19, D19P and D19M) on different dates (Table 6.1). The S06 beams (Figure 6.6), which had the smallest web height, were cast in a single lift of concrete pumping, while the S12 (Figure 6.7), S19 beams (Figure 6.8) and D19 beams (Figure 6.9), with taller webs, were cast in two lifts to ensure proper concrete consolidation. Concrete cylinders were cast from concrete used in each of the beams.

Table 6.1.Concrete placement dates and volumes.

Beam	Concrete placement date	Concrete volume (cu-yd)
S06-M-U	2024-03-04	3.8
S06-M-T	2024-03-04	3.8
S06-M-TC	2024-03-04	6.7
S12-P-U	2024-04-15	6.7
S12-P-T	2024-04-15	8.5
S19-M-U	2024-07-23	8.7
S19-M-T	2024-07-23	8.7
D19-P-U	2025-06-05	8.7
D19-P-T	2025-06-05	8.7
D19-M-U	2025-07-28	8.7
D19-M-T	2025-07-28	8.7

(a) (b)

Figure 6.6. Casting of S06 beams: (a) Concrete pumping inside the formwork; (b) Surface finishing at the end of casting.

(a) (b)

Figure 6.7. Casting of S12 beams: (a) Pumping second lift of concrete inside the formwork; (b) Finished surface after casting.

All beams were cast using a Class V 8500 Granite concrete type. This concrete mix (Table 6.2), with a target slump of 6.0 ± 1 in. and a water–cement ratio of 0.30, was designed for a minimum 28-day compressive strength of 8,500 psi.

Table 6.2. Mix proportion of concrete mix per 1000 lb. of concrete.

Group	Material Description	Specific Gravity	Mass (lb.)
Cement	Cement	3.03	207.6
Additive	Fly Ash	2.42	30.5
Aggregate	Coarse Aggregate	2.80	445.8
	Fine Aggregate	2.64	244.2
Water	Water	1.00	71.3
Admixture	Air Entrainer	1.00	0.04
	Water Reducer	1.00	0.54

(a) (b)

Figure 6.8. Casting of S19 beams: (a) Placement and vibration of second lift; (b) Finished surface after casting.

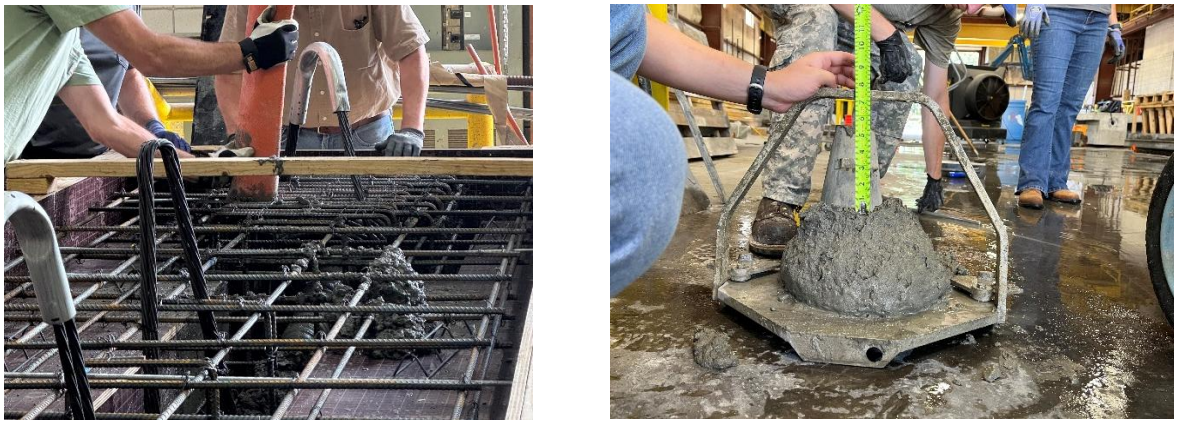

(a) (b)

Figure 6.9. Casting of D19 beams: (a) Pumping of concrete in the end-block region of the D19-P-U beam; (b) Slump testing of concrete obtained from the truck before pumping into the S19-M-U beam.

6.3 Post-tensioning

Tendons were assembled and post-tensioned per FDOT Standard Specifications Section 462 (FDOT 2024) and the PTI Post-Tensioning Manual (PTI 2023) at the FDOT SRC after confirming, through concrete cylinder compressive strength tests, that the concrete in the beams had reached the design strength required for post-tensioning. The strands were pushed individually into the ducts and secured in the wedge plate (with wedges seated inside) at both beam ends against the anchor face (Figure 6.10). To ensure that the tendon strands were parallel, the strands were marked based on the position of the holes through which they were inserted in the wedge plate at the live end and inserted into the corresponding holes in the wedge plate at the dead end. Although the tendon sizes varied for each category of beam (6, 12, and 19 strands), the same size anchorage hardware (19-strand) was used for all beams to simplify construction and allow a single multistrand stressing jack to be used for post-tensioning of all beams. A gas-powered 6-19 multistrand jack (0.6 in. strand diameter, maximum of 19 strands), with a capacity of 1,048 kips and a 4-in. stroke length, was used to post-tension all tendons (Table 6.3).

Table 6.3. Specifications of the multistrand jack used for post-tensioning the beams.

Specification	Value
Jack capacity	1048 kip
Stroke	3.94 in
Anchorage unit	6-19
Type	Gas powered
Jack model	VSL Jack ZPE-460

(a) (b)

Figure 6.10. Prestressing strands projecting out of the wedge plate at live ends: (a) S06; (b) S12 beams.

The tendons were post-tensioned to the target tendon force (Figure 6.11) using pressure gages (primary and secondary gages) attached to the hydraulic stressing jack. The stressing jack and gages were calibrated before post-tensioning to ensure that the tendons were stressed to the target design force. Additionally, the elongation of the strands at the live end was measured and checked against the calculated elongation to verify the accuracy of the applied post-tensioning

force. Tendon force was also estimated by using the measured concrete strain and concrete modulus to compute concrete stress.

(a) (b)

(c) (d)

Figure 6.11. Post-tensioning of beams: (a) S06; (b) S12; (c) S19; (d) D19.

The post-tensioning force was applied in increments, with pauses at multiple predetermined force levels, to ensure a gradual increase in tendon stress. During the pauses, tendon elongation was measured at the live end and compared to the expected value to verify the accuracy of the applied post-tensioning force. In addition, jack displacement measurements taken at 100% of maximum prestress and at 20% of maximum prestress were extrapolated to zero force so that live-end anchor set (i.e. seating movement) at tendon release could be estimated. The live-end anchor set displacement for each beam was then used to estimate the loss of prestress force associated with wedge seating.

The post-tensioning forces applied to the beams ranged from 246 kips to 779 kips. The measured tendon elongation and the maximum post-tensioning force applied to the beams are listed in Table 6.4.

Table 6.4. Post-tensioning force and tendon elongation in beams.

Beam	Number of 0.6 in. diameter strands	Target stress[1]	Post-tensioning force (kip.)	Tendon length during jacking[2] (in.)	Expected tendon elongation (in.)	Measured tendon elongation (in.)
S06-M-U	6	$0.7f_{pu}$	246	508	3.37	3.00
S06-M-T	6	$0.7f_{pu}$	246	508	3.37	3.45
S06-M-TC	6	$0.7f_{pu}$	246	508	3.37	2.90
S12-P-U	12	$0.7f_{pu}$	492	508	3.37	3.20
S12-P-T	12	$0.7f_{pu}$	492	508	3.37	3.30
S19-M-U	19	$0.7f_{pu}$	779	508	3.37	3.20
S19-M-T	19	$0.7f_{pu}$	779	508	3.37	3.00
D19-P-U	19	$0.7f_{pu}$	779	512	3.39	3.60
D19-P-T	19	$0.7f_{pu}$	779	512	3.39	3.30
D19-M-U	19	$0.7f_{pu}$	779	512	3.39	2.95
D19-M-T	19	$0.7f_{pu}$	779	512	3.39	3.20

Note:

[1] Target stress is expressed as a fraction of the ultimate tensile strength (f_{pu}) of the strand (270 ksi).

[2] Tendon length is the length of tendon from the wedge plate at the post-tensioning dead end to the end face of the stressing jack at the post-tensioning live end.

6.4 Grout Injection

Three different grout types were used to grout the tendons, as shown in Table 6.5. Euco Cable Grout PTX is an FDOT-approved pre-packaged cementitious grout for post-tensioned cables and ducts. The grout mix was prepared following the manufacturer's recommendations, using a water-cement ratio of 0.25.

A plain cement grout mix was prepared using water and Type I/II Portland cement at a water-cement ratio of 0.44. No admixtures were added to the plain cement grout mix to avoid potential reactions with the corrosion inhibitor. The water-cement ratio of 0.44 was based on past recommendations when plain cement grout was still commonly used for grouting post-tensioned ducts (Lankard et al., 1993; FHWA, 1993; FHWA, 2003). This neat plain cement grout was found to produce a minimum 28-day compressive strength of 7400 psi (FHWA, 1993).

To represent an example of past construction practices in the state of Florida (prior to approximately the year 2000), a legacy grout mix was prepared using materials and proportions that simulated the grout type used in the Roosevelt Bridge in Stuart, Florida.

Table 6.5. Details of the grout types used for the grouting of beams

Grout type	Water-cement ratio	Additives	Quantity per batch	Injected beams
Pre-packaged (Euclid Euco Cable PTX)	0.25	Proprietary		S06-M-U S06-M-T S06-M-TC S12-P-U S12-P-T
Plain cement (Portland cement type I/II)	0.44	None		S19-M-U S19-M-T
Legacy grout (Portland cement type I/II)	0.45	Sika Intraplast N WRDA 60	0.13% weight of cement 2.4% volume of cement	D19-P-U D19-P-T D19-M-U D19-M-U

Prior to grouting, plumbing was installed to facilitate grout injection (Figure 6.12). This process included the installation of grout caps and grout ports – one at the grout cap and another at the bearing plate above the anchor head at both ends of the beams. A pressure test, as per PTI M55 Specifications for grouting of Post-Tensioned Structures (up to approximately 30 psi), was then conducted on each beam to ensure there were no leaks in the plumbing (PTI 2019).

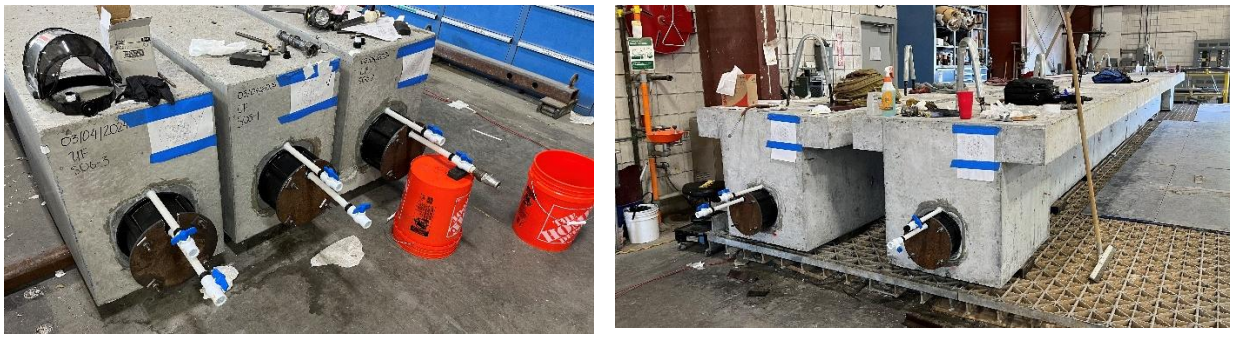

(a) (b)

Figure 6.12. Plumbing of beams for injection of grout: (a) S06 beams PT dead end (b) S19 beams PT live end.

A colloidal grout plant, equipped with a 13-cubic-foot capacity agitating holding tank and capable of delivering slurries at pressures up to approximately 260 psi was used for grouting the beams (Figure 6.13). However, for purposes of grouting the test beams, the grout injection pressure was consistently maintained between 15-30 psi for all beams.

Figure 6.13. Pre-packaged grout being mixed in the colloidal grout plant.

To ensure that the grout mixes achieved the desired consistency and properties, flow cone and mud balance tests recommended by the Post-Tensioning Tendon Installation and Grouting Manual (FHWA, 2013) were conducted (Figure 6.14a and Figure 6.14b). The details of the tests performed during grout injection of the beams are presented in Table 6.6. Additionally, grout cubes were cast (Figure 6.14c) for each batch of grout so that the hardened compressive strength of the grout injected into the beams could be determined.

(a)

(b)

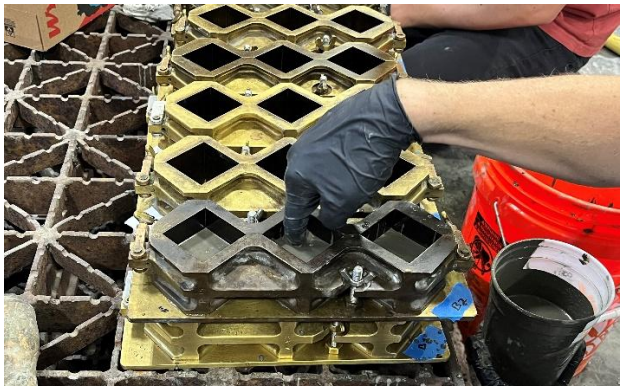

(c)

Figure 6.14. Laboratory tests and activities performed during grouting of beams: (a) Flow cone test; (b) Mud balance test; (c) Casting of grout cubes.

Table 6.6. Laboratory tests performed during grouting of the beams

Tests name	Specifications	Purpose	Test frequency
Flow Cone	ASTM C939	Measure fluidity of grout mix	Two tests per beam (on grout mix collected at upstream and downstream ends of the grout flow direction)
Mud Balance	API Recommended Practice 13B-1	Measure wet density of grout mix	One test per grout mix batch

6.4.1 Pre-packaged Grout

The S06 and S12 beams were grouted using a single batch of pre-packaged grout mix. The grout mix was injected from the post-tensioning dead end to the post-tensioning live end for all beams grouted with pre-packaged grout. Of the two grout ports at the injection live end, the lower-elevation port connected to the grout cap was used as the injection inlet (Figure 6.15). This approach was feasible because, of the 19 available strand openings in the wedge plates, only 6 or 12, respectively, were filled with strands for the S06 and S12 beams. The remaining unfilled strand

openings in the wedge plate provided an ample flow path for the injected grout. The grout was injected at a constant pressure of approximately 15 psi, while the remaining three grout ports, one at the live end and two at the dead end, were monitored visually with the valves opened to await discharge flow.

(a) (b)

Figure 6.15. Grout injection of S06-M-TC beam in process: (a) Injection of grout at PT dead end; (b) Excess grout discharged at PT dead end grout ports.

The grout injection was stopped once approximately 1 gallon of grout was discharged from each grout port (except the injection port). All valves were then closed. Real-time laboratory tests of the grout mix, as indicated in Table 6.6, were performed in parallel with grout injection to ensure that the water-cement ratio of the grout mix produced by the grout plant was as intended and that the grout mix had the desired fluidity for injection into the ducts in the beams. Details of the beams injected with pre-packaged grout are provided in Table 6.7.

Table 6.7. Details of pre-packaged grout injections in the beams

Beam	Grout product name	Grout injection end	Injection site	Grout date
S06-M-U	Euco Cable Grout PTX	PT dead end	Grout cap	2024-09-23
S06-M-T	Euco Cable Grout PTX	PT dead end	Grout cap	2024-09-23
S06-M-TC	Euco Cable Grout PTX	PT dead end	Grout cap	2024-09-23
S12-P-U	Euco Cable Grout PTX	PT dead end	Grout cap	2024-09-23
S12-P-U	Euco Cable Grout PTX	PT dead end	Grout cap	2024-09-23

6.4.2 Plain Cement Grout

Mixing of the plain cement grout was conducted using the same colloidal mixing plant used for the pre-packaged grout and was injected into the beams of the S19 couplet. Of the total water quantity used in the mix, 35% by volume was replaced by ice chips. Ice was used to prevent an excess exothermic reaction from potentially occurring due to the heat generated by the combined effects of cement hydration, high laboratory temperature, and high-shear mixing in the colloidal plant. In contrast to the 6- and 12- strand beams, for the 19-strand beams all 19 openings in the wedge plates were filled (and essentially blocked) with strand. Therefore, grout could not be injected through the lower elevation port on the grout cap. Instead, grout was injected through the higher elevation port located at the top of the bearing plate (Figure 6.16). Use of this port allowed grout to flow through the bearing plate, into the trumpet, and along the length of the duct with minimal resistance.

Similar to the grout injection process in the previous beams, the grout was injected at a constant pressure of approximately 15 psi, and the remaining three grout ports - one at the live end and two at the dead end were monitored visually with their valves open until grout discharge occurred. Grout injection was stopped once approximately 1 gallon of grout had been discharged from each grout port (except the injection port), after which all valves were closed.

Figure 6.16. Grout injection at PT live end of beam S19-M-U

Real-time laboratory tests of the fluid grout mix, as indicated in Table 6.6, were performed in parallel with grout injection. Details of the beams injected with plain cement grout are presented in Table 6.8.

Table 6.8. Details of plain cement grout injections in the beams

	Grout product name	Grout injection end	Injection site	Grout date
S19-M-U	Portland cement Type I/II	PT live end	Bearing plate	2024-09-23
S19-M-T	Portland cement Type I/II	PT live end	Bearing plate	2024-09-23

6.4.3 Legacy Grout

The mixing and injection of legacy grout into the D19 beams were carried out using the same grout plant and setup as the S06 and S19 straight-tendon beams. A single batch of grout, with sufficient volume to inject the two D19 couplets (4 beams in total), was prepared in the grout plant. Similar to the plain cement grout mix, a predetermined amount of water (50% of the total water volume) was replaced with ice chips to prevent an excessive exothermic reaction from potentially occurring due to heat generated by the combined effects of cement hydration, high laboratory temperature, and high-shear mixing in the colloidal plant (Figure 6.17). Laboratory tests (Table

6.6) were performed during the grout injection. These tests included flow cone tests on the grout mix collected at the inlet port (injection live end) before injection and on the grout flowing out from the outlet port (injection dead end) on each D19 beam, as well as mud balance tests conducted at three points during the testing: before injection of grout into the first beam (D19-P-T), at the end of the second beam (D19-P-U), and before the injection of the last beam (D19-M-T). In addition, grout cubes were cast to monitor the compressive strength of the control and soaked specimens.

Grout injection ports in the D19 beams were similar to those of the straight-tendon 19-strand beams (S19-M-U and S19-M-T). Since all 19 openings in the wedge plates were filled with strands, grout could not be injected through the lower-elevation port on the grout cap. Instead, grout was injected through the higher-elevation port located at the top of the bearing plate, and which bypasses the wedge plate.

The grout injection process for the D19 beams was similar to that of the S19 beams in that the grout was injected at a constant pressure of approximately 15 psi, and the remaining three grout ports, one at the live end and two at the dead end, were monitored visually with their valves open until grout discharge occurred. Grout injection was stopped once approximately 1 gallon of grout was discharged from each grout port (except the injection port), after which all valves were closed.

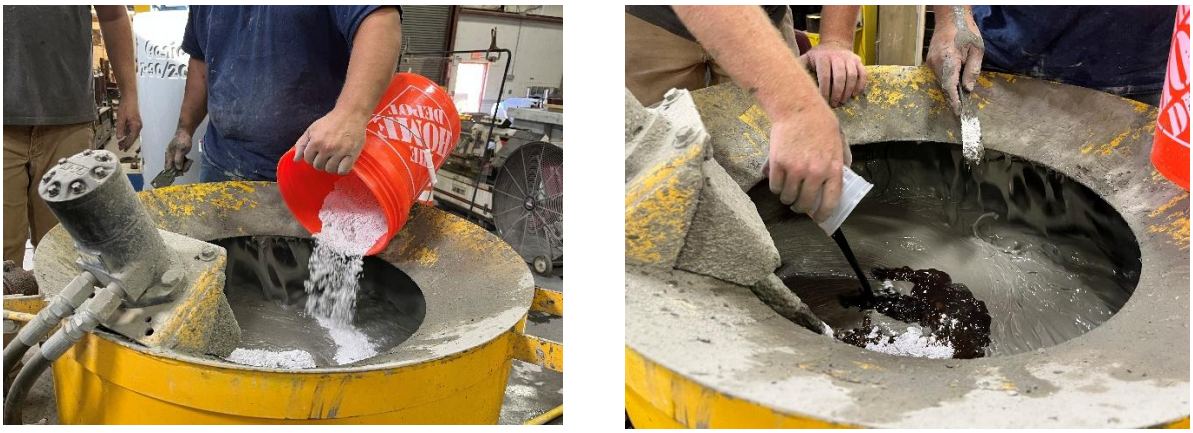

(a) (b)

Figure 6.17. Legacy grout mixing in the grout plant: (a) Adding Intraplast N admixture into the grout mix; (b) Adding WRDA 60 water-reducing admixture into the mix.

CHAPTER 7 GROUT CUBE PREPARATION AND TESTING

7.1 FDOT Structures Research Center (SRC) In-situ Grout Mixes

All grout cubes were fabricated from the same batches of grout mixes used to grout the beams. Four batches of grout mixes were prepared in the colloidal grout plant, with the intent to inject one batch into each group of beams (S06, S12, S19, D19). Although there were two separate batches of pre-packaged grout mixed for the S06 and S12 beams, their mix design and target properties were the same.

7.1.1 Casting of Grout Cubes

For each batch of grout mix, twenty-four (24) grout cubes were prepared. The grout used for fabricating the cubes was obtained directly from the grout plant after the mud balance and flow cone tests were conducted. The grout cubes were cast in accordance with ASTM C109, as shown in Figure 7.1.

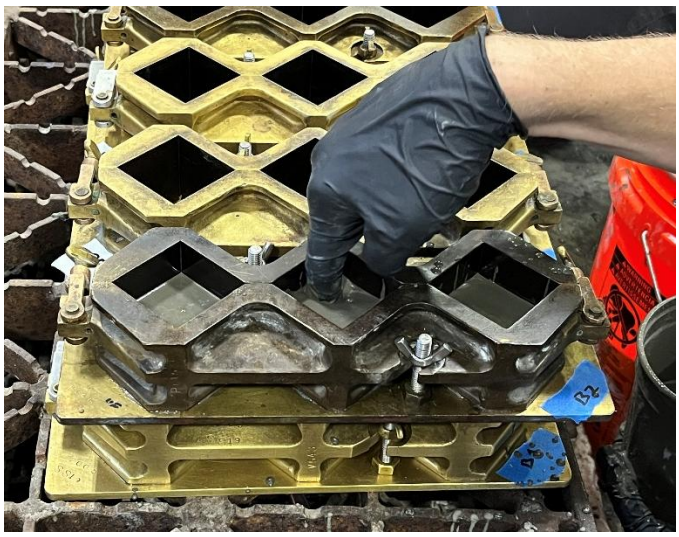

Figure 7.1. Tamping of the first layer of grout in the mold.

7.1.2 Curing

The grout cubes from all batches used to inject the beams were cured under the same conditions, procedures, and durations (slight variation in duration of legacy grout cube) until the time of testing. The adopted curing procedure followed ASTM C942/C942M for standard storage and curing of grout cubes. Table 7.1 presents the curing time and conditions the grout cubes were exposed to until the time of testing.

Table 7.1. Curing time and conditions of grout cubes.

Day	Curing condition	Grout cubes surface condition	Grout type
1 – 5	Room temperature (75°F)	In molds	All
5 - testing	Moist room (Temp 73°F, 95% RH)	Demolded	Untreated
5 – 40	Moist room (Temp 73°F, 95% RH)	Demolded	Treated
40 – 45	Room temperature (75°F)	Demolded	Treated
45 – testing	Soaked in corrosion inhibitor	Demolded	Treated

7.1.3 Corrosion Inhibitor Treatment

After several days of storage in the moist curing room, the grout cubes designated for corrosion inhibitor treatment were prepared. The cubes were sanded to remove any minor top and bottom edge irregularities and thereby produce completely even surfaces for compressive testing. Next, the cubes were left to dry for few days to remove excess moisture near the cube surface. The surface-dried cubes were then soaked in the corrosion inhibitor fluid in an airtight container at room temperature (75°F), as shown in Figure 7.2. Cubes were placed to allow fluid access to each surface of the cubes.

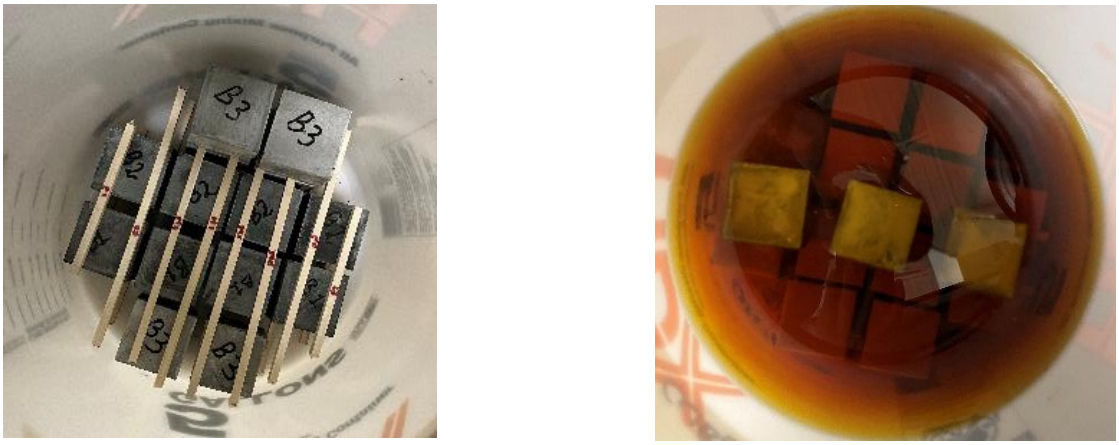

(a) (b)

Figure 7.2. Grout cubes soaked in corrosion inhibitor fluid: (a) Stacked for soaking; (b) Immediately after immersion.

7.1.4 Testing and Results

The untreated (control) grout cubes were tested for compressive strength at 7, 14 and 28 days from the day of casting to assess strength gain over time. On the day of testing, the grout

cubes were removed from the moist room and air-dried for about one hour before testing. The 14-day and 28-day strengths of the untreated grout cubes are presented in Table 7.2.

Table 7.2. Compressive strength of untreated grout cubes.

Grout type	14-day strength (psi)	28-day strength (psi)
Pre-packaged (S06)	12,000	11,190
Pre-packaged (S12)	10,550	11,900
Plain cement (S19)	7260	6980
Legacy (D19)	3600	3500

Further strength testing was conducted to compare treated and untreated grout cubes. Treated cubes were tested after soaking in corrosion inhibitor fluid for 7 days, 2 months, and 3 months, and the results were compared to untreated (control) cubes stored in the moist room until testing. Before testing, the treated cubes were removed from the fluid, their surfaces were blotted with a cloth and allowed to sit for about one hour. The difference in compressive strength between the treated and untreated cubes is presented in Table 7.3. In almost all cases, the strengths of the cubes increased when they were treated with (or immersed in) the corrosion-inhibiting fluid.

Table 7.3. Compressive strength comparison between treated and untreated grout cubes.

Treatment age (days)	Grout batch	Untreated strength (psi)	Treated strength (psi)	Strength change[1] (%)
7	Pre-packaged (S06)	12,561	14,446	+15
	Pre-packaged (S12)	10,287	15,232	+48
	Plain cement (S19)	5849	9360	+60
	Legacy (D19)	3370	4060	+20
28	Pre-packaged (S06)	N/A	N/A	N/A
	Pre-packaged (S12)	N/A	N/A	N/A
	Plain cement (S19)	N/A	N/A	N/A
	Legacy (D19)	4000	3800	-5
56	Pre-packaged (S06)	12,117	14,927	+23
	Pre-packaged (S12)	N/A	N/A	N/A
	Plain cement (S19)	6370	9360	+47
	Legay (D19)	N/A	N/A	N/A
84	Pre-packaged (S06)	13,837	14,858	+7
	Pre-packaged (S12)	14,327	15,227	+10
	Plain cement (S19)	7142	10,175	+43
	Legacy (D19)	N/A	N/A	N/A

Note:
[1] Positive indicates an increase in strength from the untreated to the treated condition.

7.2 FDOT State Materials Office (SMO) In-house Grout Mixes

The strength results presented in the previous section corresponded to grout that was produced in substantial volume, using a grout plant (at the FDOT SRC in Tallahassee, FL), and then moist-room cured in accordance with ASTM C942. To investigate the effect that corrosion-inhibiting fluid might have on older in-service bridge structures that contain mature grout, additional smaller batches of grout were mixed, cast, subjected to accelerated curing, and tested at the FDOT State Materials Office (SMO) in Gainesville, FL. In this additional phase of the

investigation, the range of grout types investigated included pre-packaged grout, plain cement grout, and a legacy grout (recall Table 6.5).

7.2.1 Fabrication

Grout mixes with a yield volume of 0.2 cubic feet per batch were prepared at room temperature for all three grout types. Initial mixing was performed using a planetary mixer to maintain consistent mixing speed across all batches, as shown in Figure 7.3(a). A second stage of mixing was then conducted using a handheld mixer to achieve the desired fluidity and to break down any remaining lumps in the mix, as shown in Figure 7.3(b). Grout cubes were then cast in accordance with ASTM C942, as shown in Figure 7.4.

(a) (b)

Figure 7.3. In-house grout mixing at FDOT SMO: (a) First stage (planetary mixer); (b) Second stage (handheld mixer).

Figure 7.4. Pouring grout mix into cube molds.

7.2.2 Curing

Curing conditions and curing durations were modified from ASTM C942/C942M to include accelerated curing for 21 days at 140°F and 95% RH. Untreated cubes were stored at room temperature (75°F) until the time of testing. Limewater soaking, as recommended in ASTM C942,

was avoided to better replicate in-situ (field condition) grout curing conditions. Table 7.4 summarizes the curing protocols adopted.

Table 7.4. Curing time and conditions of SMO grout cubes.

Day	Curing condition	Grout cubes surface condition	Grout type
1 – 3	Room temperature (75°F)	In molds	All
3 – 7	Moist room (Temp 73°F, RH 95%)	In molds	All
7 – 28	Accelerated curing chamber (Temp 140°F, 95% RH)	Demolded	All
28 – 30	Room temperature (75°F) and air drying	Demolded	All
30 – testing	Room temperature (75°F)	Demolded	Untreated
30 – testing	Soaked in corrosion inhibitor	Demolded	Treated

7.2.3 Corrosion Inhibitor Treatment

After being removed from the accelerated curing chamber, the grout cubes were sanded to remove any minor top and bottom edge irregularities and thereby produce completely even surfaces for compressive testing. They were then air-dried for two days at room temperature (75°F). Before soaking in the corrosion inhibitor, the initial weight of each cube was recorded. Cubes from each grout type were then soaked in the corrosion-inhibiting fluid separately in airtight containers to prevent cross-contamination.

7.2.4 Testing and Results

The grout cubes were tested at 7, 28, 56 and 128 days to compare compressive strengths between treated and untreated beams. On the day of testing, the treated cubes were blotted to remove surface moisture and then weighed again to assess any weight change. Strength and weight comparisons of the control and treated grout cubes are presented in Table 7.5.

The grout cube strength results indicate that the effect of corrosion inhibitor treatment varies with grout type and curing age. For the pre-packaged grout, the treated specimens exhibited comparable or slightly higher compressive strengths than the untreated specimens at early ages (7–56 days), with strength changes (increase) ranging from 1% to 2%. At 168 days, the treated specimens exhibited a reduction in compressive strength of approximately 16%.

For the plain cement grout, the treated specimens showed lower compressive strength than the untreated specimens at all curing ages, with strength reductions ranging from approximately 7% to 20%. Similarly, the legacy grout exhibited strength reductions in the treated specimens at all curing ages, with reductions ranging from about 12% to 20%. In all cases, the percent change in the weight of the cubes between the control and treated is less than 2%.

Table 7.5. Compressive strength and weight change in treated grout cubes.

Treatment age (days)	Grout batch	Untreated strength (psi)	Treated strength (psi)	Strength change[1] (%)	Untreated weight (gram)	Treated weight (gram)	Weight change (%)
7	Pre-packaged	11,052	11,160	+1	220.9	220.7	-0.1
	Plain cement	10,062	9336	-7	244.5	246.1	+0.7
	Legacy	6877	5493	-20	230.9	234.3	+1.4
28	Pre-packaged	10,588	10,761	+2	215.1	214.3	-0.3
	Plain cement	10823	8807	-19	245.4	246.1	+0.3
	Legacy	6884	5926	-14	232.0	234.9	+1.3
56	Pre-packaged	10,666	10,933	+2	215.7	214.3	-0.7
	Plain cement	10,933	8902	-19	246.1	245.2	-0.4
	Legacy	6662	5860	-12	231.6	233.8	+1.0
168	Pre-packaged	11,348	9486	-16	213.9	212.3	-0.8
	Plain cement	10,754	9070	-20	243.4	239.1	-0.3
	Legacy	7049	5606	-16	235.4	229.4	-1.7

Note:
[1] Positive indicates an increase in strength or weight from the untreated to the treated condition. Negative indicates a decrease in strength or weight from the untreated to the treated condition.

CHAPTER 8 BEAM PREPARATION

8.1 Pre-impregnation Cracking of Beam S06-M-TC

After grout injection, the grout in each beam was allowed to cure for at least 28 days at the FDOT SRC. As described in the previous section, grout cube strength tests were conducted at the FDOT SMO to determine the 28-day compressive grout strengths. Following this, the S06-M-TC beam (where TC = "treated/cracked") was subjected to a limited range loading to induce tensile cracking before impregnation of the beam with the corrosion inhibitor material.

Beam S06-M-TC was loaded until tensile cracking was visually observed and cracking had propagated up to the tendon elevation. Once this condition was reached, the beam was unloaded before impregnation of the corrosion inhibitor material into the tendon. The intent of this limited loading was to subject the beam to a stress level that was comparable to the operating stress level of $7.5\sqrt{f_c'}$, specified for concrete with bonded prestressed tendons and non-segmental girders, as per the FDOT Bridge Load Rating Manual (2023).

The fully instrumented beam was placed under the test frame for four-point bending, and load was applied at a constant rate. The applied load was paused at multiple predetermined levels prior to reaching the theoretical (calculated) cracking load to visually inspect for cracks. At the load level corresponding to theoretical decompression of the bottom surface of the beam, the slope of the load-deflection plot remained linear. At this same load level, there was no indication of cracking from the strain data provided by the fiber optic sensor installed on the beam bottom, nor were there any visually identifiable cracks.

Beyond theoretical decompression of the bottom surface of the beam, load pauses were made more frequently to visually inspect for first crack formation. The first crack was visually observed at an applied load of 25.0 kips, corresponding to a tensile stress at the bottom surface of the beam of $6.8\sqrt{f_c'}$. This also corresponds to the point on the load-deflection plot where a change in slope was noted, as shown in Figure 8.1.

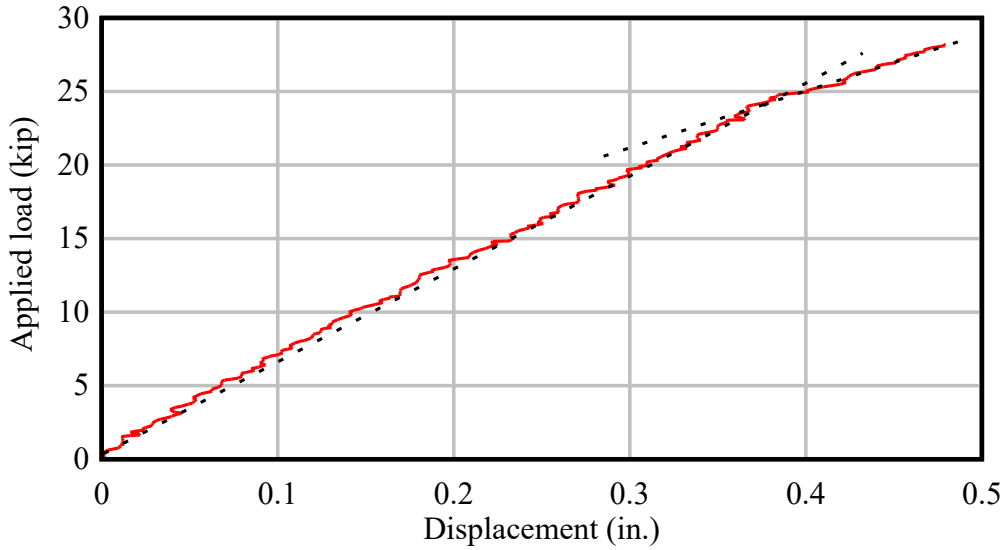

Figure 8.1. Load-deflection plot: S06-M-TC pre-impregnation cracking.

The first tensile crack appeared near the midspan of the beam, and extended across the full width of the bottom of beam, and up to a height 4 in. above the bottom surface. The crack width at the beam bottom surface was measured using a crack microscope during this load pause. The load was then slowly increased again until the crack propagated approximately 1 in. further at an applied load of 28 kips, reaching 5 in. from the bottom surface, after which the load was paused. At this level, the crack width and dimensions were measured, as shown in Table 8.1, then the beam was unloaded.

Table 8.1. Details of pre-impregnation cracking process.

Instance	Applied load (kip)	Crack location from midspan (in)	Crack height from bottom (in)	Deflection (in)	Crack width[1] (in)
First crack	25.0	2	3	0.38	0.001
Final load	28.0	2	8	0.47	0.005

Note:
[1]Crack width was measured at the bottom surface of the beams using a crack width microscope

The cracking stress calculated from the measured cracking load (25.0 kip) indicated that S06-M-TC cracked at a lower load than the other two S06 beams (Table 8.2). One possible contributing factor to the low cracking stress in S06-M-TC (i.e., $6.8\sqrt{f_c'}$ rather than $7.5\sqrt{f_c'}$.) is the extended length of time that the applied load was held during the load holds. This longer hold period may have allowed sufficient time for tensile creep to occur in the flexural tension zone, leading to a reduced cracking load. Additionally, the variability in the tensile strength of concrete and the subjectivity associated with visually identifying cracks particularly, due to the additional attention and longer pauses during the limited load testing, may have also contributed to the apparent lower cracking load.

Table 8.2. Duration between decompression and the first tensile crack in the beams.

Beam ID	Decompression load (kip)	Cracking load (kip)	Time elapsed (hh:mm:ss)
S06-M-U	13.4	30.0	00:17:16
S06-M-T	13.4	27.7	00:07:17
S06-M-TC	13.4	24.7	00:29:31
S12-M-U	58.7	95.0	00:21:51
S12-M-T	58.7	85.0	00:17:18
S19-M-U	103.2	142.6	00:19:40
S19-M-T	103.2	142.6	00:21:18

8.2 Corrosion Inhibitor Impregnation

Vector Corrosion Technologies (referred to as "Vector" herein) was subcontracted to conduct impregnation of corrosion inhibitor into the tendons of selected beams using standard Vector materials, procedures, equipment, and protocols. To impregnate the tendons, the grout caps were removed, and grout surrounding the strand tails was removed by mechanical means. Next, the strand tails projecting from the wedge plate were tapped (agitated) with a hammer to loosen and remove grout trapped inside the interstitial spaces between individual wires (Figure 8.2). The ends of the individual wires in each strand were then sanded flush to provide a clear flow path for the corrosion inhibitor into the interstitial spaces between the wires.

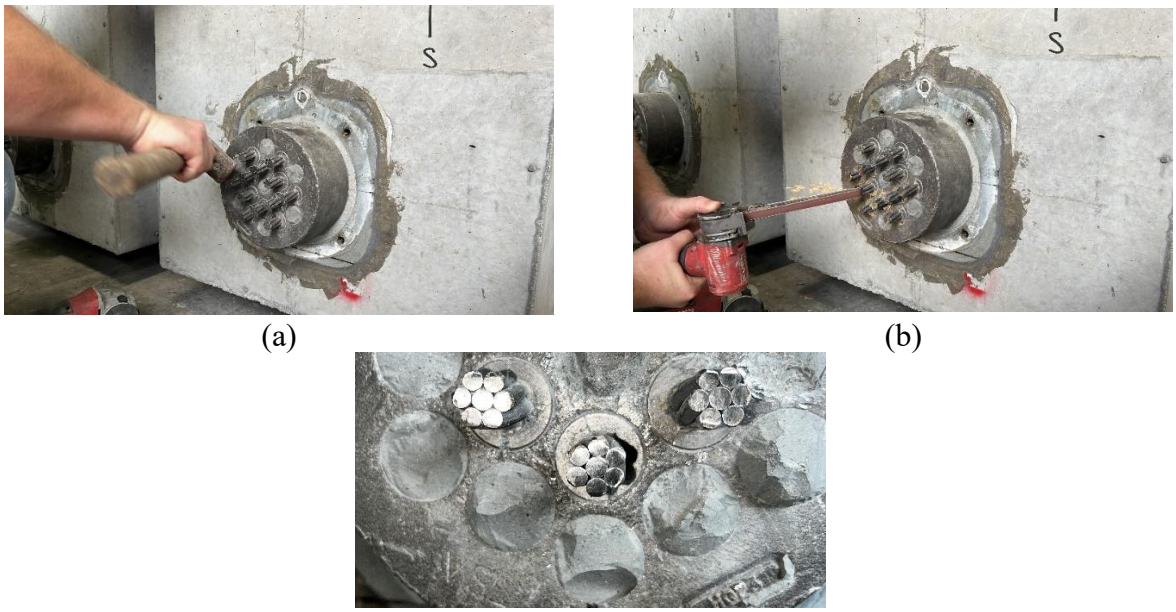

(a) (b)

(c)

Figure 8.2. Preparing strand tails for corrosion inhibitor impregnation in S12-P-T beam: (a) Tapping strand ends to dislodge grout between wires; (b) Sanding of strand ends; (c) Cleaned strand ends.

Once the strands at both ends of the beams were prepared, they were cleaned using compressed air (Figure 8.3a). Customized end caps (with sealed original grout ports and a new port added at the bottom for corrosion inhibitor) were then reinstalled at the live end of the beam (Figure 8.3b), where the corrosion inhibitor was to be introduced, while the dead-end anchor head remained exposed. Finally, all visible gaps between the bearing plates and surrounding concrete on both end faces of the beam were filled with epoxy to prevent corrosion inhibitor leakage.

(a) (b)

Figure 8.3. Preparing the PT live end of beam S12-P-T for impregnation of corrosion inhibitor: (a) Cleaning strands and anchorage end with compressed air; (b) Installation of customized end cap.

Air pressure tests were performed on each beam after anchorage end preparations were completed. Compressed air was injected through the customized port in the end cap at the live end, and the exposed strands at the dead end were visually inspected to confirm a free-flow path through every strand. This was accomplished by spraying a soapy film of water on the strands and observing the formation of bubbles from the interstitial spaces in each strand, as shown in Figure 8.4.

(a) (b)

Figure 8.4. Air flow tests on S12-P-T beam: (a) Checking for leaks at the bearing plate-concrete joint at PT live end; (b) Bubbles confirming air flow at the PT dead end.

8.2.1 Uncracked Beams

All uncracked treated beams were impregnated with corrosion inhibitor at the post-tensioning (PT) live end. A pressure pot was attached to the port in the end cap at the live end of each beam. The pressure pot had a capacity of 2.8 gallons and weighed approximately 29 lbs. The amount of fluid impregnated into the beam was determined by recording and calculating the change in the weight of the pressure pot before and after impregnation of the corrosion inhibitor.

The uncracked beams were impregnated with corrosion inhibitor at the PT live end three times over a 72-hour (3-day) period. The purpose of the first impregnation was to saturate the strands and the surrounding grout along the full length of the tendon. This was performed by impregnating the corrosion inhibitor fluid under pressure from the live end while leaving the caps open at the dead end, and visually checking fluid discharge from the individual strands (Figure 8.5).

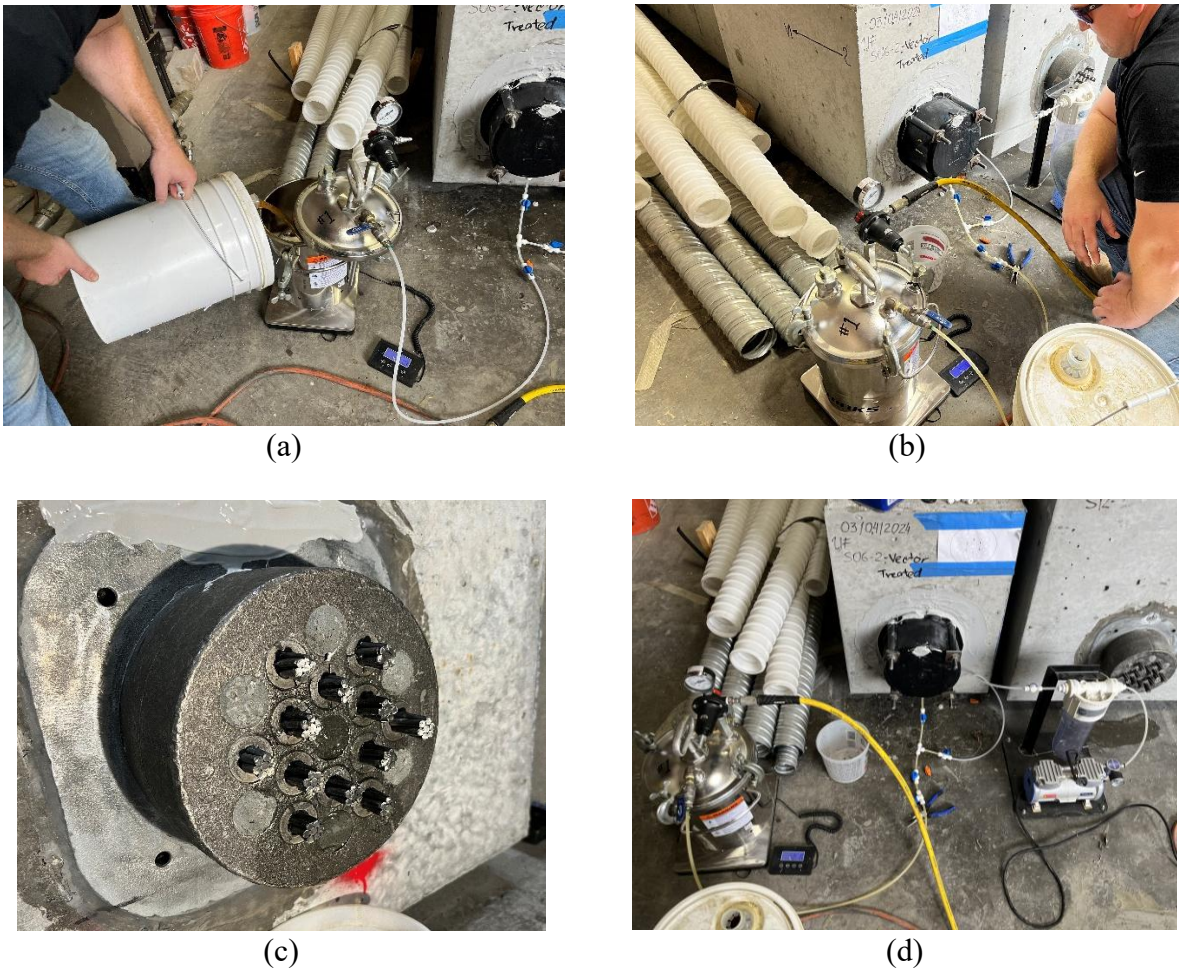

Figure 8.5. Impregnation of first volume of corrosion inhibitor in S06-M-T beam: (a) Filling the pressure pot with corrosion inhibitor fluid; (b) Pressure impregnation of corrosion inhibitor fluid into the PT live end of the beam; (c) Free-flowing corrosion inhibitor fluid exiting from the strands at the downstream end of the beam; (d) Impregnation set-up at the live end during the 24 hours pressure hold.

The second impregnation was performed to saturate any strands that did not show signs of inhibitor discharge at the dead end during the first impregnation. The first two impregnations were conducted using a free-flow impregnation method, in which the corrosion inhibitor fluid was impregnated under pressure at the live end, while the dead end remained open (at atmospheric pressure) to allow free flow of fluid.

However, a third impregnation was also performed. During this step, the PT dead-end wedge plate was covered with a sealed end cap, and a vacuum was applied to the tendon. Thus, the corrosion inhibitor was impregnated under a higher differential pressure than in the free-flow method. Among all the impregnated beams, the maximum impregnation pressure was recorded in the D19-M-T and D19-P-T beams, reaching 60 psi at the final step, which was also vacuum-assisted.

Each time the impregnation process was restarted at the live end, the pressure pot was refilled and weighed. The total weight of fluid impregnated into the tendon and grout was

determined by calculating the weight difference of the pressure pot before and after each impregnation, then subtracting the weight of fluid collected at the dead end and from end caps.

The volume of fluid impregnated into the strands and grout was then calculated from the measured weight and the Vector Post-Tech PTI fluid volume-to-weight conversion, provided by the manufacturer (Vector) as: 1 gallon = 121 oz, by weight. The details of corrosion inhibitor impregnation into the uncracked treated beams are presented in Table 8.3.

Table 8.3. Details of corrosion inhibitor impregnation in the beams.

Beam	Impregnation step	Impregnation point	Impregnation type	Duration (hh:mm)	Total volume impregnated (gal.)
S06-M-T	1	PT live end	Free flow	02:00	0.264
	2	PT live end	Free flow	04:30	
	3	PT live end	Vacuum-assisted	24:00	
S12-M-T	1	PT live end	Free flow	01:40	0.504
	2	PT live end	Free flow	02:45	
	3	PT live end	Vacuum-assisted	24:00	
S19-M-T	1	PT live end	Free flow	01:19	0.736
	2	PT live end	Free flow	06:08	
	3	PT live end	Free flow	00:53	
	4	PT live end	Vacuum-assisted	24:00	
D19-M-T	1	PT live end	Free flow	01:30	0.670
	2	PT live end	Vacuum-assisted	02:00	
	3	PT live end	Free flow	07:00	
	4	PT live end	Vacuum assisted	21:00	
D19-P-T	1	PT live end	Free flow	01:30	0.670
	2	PT live end	Vacuum-assisted	02:00	
	3	PT live end	Free flow	07:00	
	4	PT live end	Vacuum-assisted	21:00	

8.2.2 Cracked Beam

As described in Section 8.1, beam S06-M-TC was subjected to limited flexural loading until a single tensile crack at the bottom of the beam was visually identified. To prepare this beam for impregnation, the strand tails were cleaned, the anchorage ends were prepared, and customized end caps were installed, similar to the treated uncracked beams described above. An air leak test was also performed on this beam following the same procedure as was used for the uncracked beams. Compressed air was injected at the sealed PT live-end end cap, and the exposed strand ends at the PT dead end were visually inspected for the formation of air bubbles by applying soapy water to the strand ends (Figure 8.6).

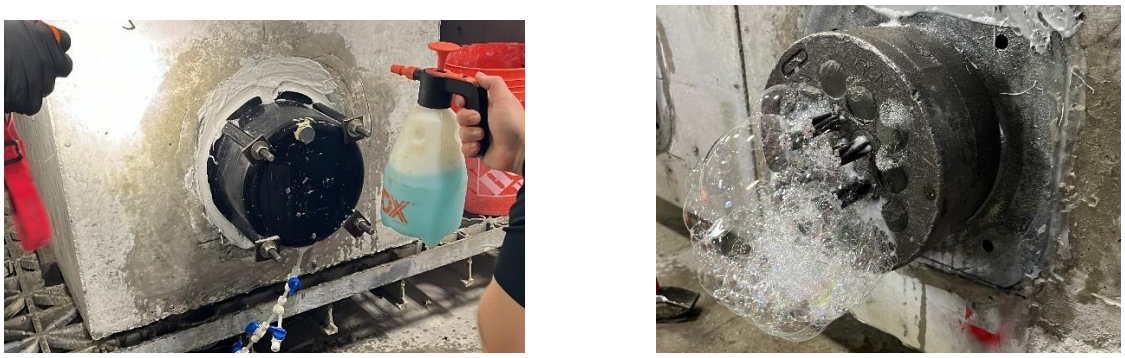

(a) (b)

Figure 8.6. Air leak tests on S06-M-T beam: (a) Checking for leaks at the bearing plate-concrete joint at PT live end; (b) Bubbles forming due to air flow at the PT dead end.

After confirming a flow path existed through the interstitial spaces in the strands, the pressure pot containing the corrosion inhibitor material was attached to the end cap and impregnated at a pressure of approximately 15 psi. Three steps of corrosion inhibitor impregnation were required to visually confirm the flow of material from impregnation end to the discharge end (Table 8.4). A comparison of the uncracked beam S06-M-T (Table 8.3) and the cracked beam S06-M-TC (Table 8.4) shows that a larger volume of corrosion inhibitor fluid was impregnated into the cracked beam. This observation was expected. Pre-impregnation cracking of the concrete in beam S06-M-TC also cracked the grout inside the PT duct. However, since the grout inside the PT duct was not subjected to pre-compression stresses from post-tensioning, when formation of the initial *concrete* tensile crack in beam S06-M-TC occurred (recall Figure 8.1) an even greater extent of cracking had already occurred in the *grout*. Given this fact, it was expected that corrosion inhibitor would fill transverse tension cracks in the grout (thus increasing the impregnated fluid volume) as it flowed longitudinally along the tendon and eventually discharged from the PT dead end.

Table 8.4. Details of corrosion inhibitor impregnation in the beams.

Beam	Injection step	Impregnation point	Impregnation type	Fluid discharge[1]	Total volume impregnated (gal.)
S06-M-TC	1	PT live end	Free flow	No	0.339
	2	PT dead end	Free flow	No	
	3	PT live end	Vacuum-assisted at dead end	Yes	

Note
[1]Fluid discharge is the visual indication of fluid leaking out of strands at the opposite end of the corrosion inhibitor impregnation.

CHAPTER 9 EXPERIMENTAL TEST RESULTS

9.1 Introduction

This section presents results obtained from the flexural testing of the beams. The beams have been categorized into multiple groups, with the beams in each group being similar in design and construction, differing only in whether the grout was impregnated with corrosion inhibitor material (Table 9.1) or not. The only exception is the S06 (6-strand) beams, which included a beam that was cracked before impregnating with the corrosion inhibitor material.

Table 9.1. Matrix of beams.

Test beam group ID	Test Beam ID	Tendon profile	Number of strands	Duct type	Grout type	Treatment with corrosion inhibitor
S06	S06-M-U	Straight (S)	6	Metal (M)	Pre-Packaged	Un-treated (U)
	S06-M-T	Straight (S)	6	Metal (M)	Pre-Packaged	Treated (T)
	S06-M-TC	Straight (S)	6	Metal (M)	Pre-Packaged	Cracked & Treated (T)
S12	S12-P-U	Straight (S)	12	Plastic (P)	Pre-Packaged	Un-treated (U)
	S12-P-T	Straight (S)	12	Plastic (P)	Pre-Packaged	Treated (T)
S19	S19-M-U	Straight (S)	19	Metal (M)	Plain	Un-treated (U)
	S19-M-T	Straight (S)	19	Metal (M)	Plain	Treated (T)
D19M	D19-M-U	Draped (D)	19	Metal (M)	Legacy	Un-treated (U)
	D19-M-T	Draped (D)	19	Metal (M)	Legacy	Treated (T)
D19P	D19-P-U	Draped (D)	19	Plastic (P)	Legacy	Un-treated (U)
	D19-P-T	Draped (D)	19	Plastic (P)	Legacy	Treated (T)

9.2 Parameters Used to Compare Test Results

For each unique group of beams, the experimental test results between the untreated and treated beams are compared at two stages during flexural testing: nominal flexural resistance and cracking load.

9.2.1 Observed Flexural Resistance

The term “observed flexural resistance” is defined as the point during testing at which the strain value measured by the foil strain gages located at the extreme concrete compression fiber of the beams reached 0.003 in./in., which is the code-specified maximum usable compressive strain. The term “nominal flexural resistance” is defined as the theoretical (calculated) value at which a compressive strain of 0.003 in./in. would occur based on the material properties, section properties, and span of the beam.

Based on the manner in which the beams were designed (span-to-depth ratio, amount and eccentricity of prestressing, etc., as described in earlier task reports), a maximum possible reduction of nominal flexural resistance between a fully bonded condition and a fully unbonded condition was calculated to be approximately 24%. By comparing the actual experimental applied loads of control beams to corresponding treated beams, when both beams were at a compressive strain level of 0.003 in./in., the possible influences that the corrosion inhibitor had on the treated beam strengths were assessed.

9.2.2 Cracking Load

It is recognized that the actual cracking stress of concrete members can vary considerably, as it depends on the concrete tensile strength, which exhibits inherent material variability. For the purposes of this study, the "cracking load" is defined as the applied load that results in a calculated tensile stress of $12\sqrt{f_c'}$ at the extreme tension fiber of the concrete beam specimen. This stress level is consistent with the criterion used in ACI 318 to classify a section as cracked.

ACI 318 also indicates that a calculated tensile stress of approximately $7.5\sqrt{f_c'}$ is generally associated with the initiation of cracking. By comparison, AASHTO LRFD limits the calculated concrete tensile stress under the Service III load combination to $6\sqrt{f_c'}$, a level that typically results in uncracked behavior under normal service conditions. The higher stress limit of $12\sqrt{f_c'}$ was selected for this study to provide increased confidence that cracking would be observed, while remaining reasonably consistent with the intent of AASHTO LRFD serviceability design provisions. The consistency of using $12\sqrt{f_c'}$ allowed a direct comparison of crack characteristics (crack maps) and crack significance (crack depth ratios and estimated crack areas) between the control beams and treated beams. If treatment of a beam with corrosion inhibitor were to cause an increase in the computed crack significance indices (defined below), such conditions could increase the chance of the tendon being exposed to the environment and could potentially lead to durability issues.

Crack depth ratio

The crack significance index called "crack depth ratio" is defined as the number of cracks that intersected the tendon in a beam divided by the number of cracks that intersected the tendon in the control (untreated) beam. At the hypothetical service load (where the maximum tensile stress was $12\sqrt{f_c'}$) the crack depth ratio of a control beam is simply unity (1.0). In contrast, for treated beams, a crack depth ratio greater than 1.0 indicates that the treated beam had more cracks intersecting the tendon than the corresponding control beam. Conversely, a ratio less than 1.0 indicates fewer cracks intersected the tendon in the treated beam than in the corresponding control beam.

Estimated crack area

Following the observation of the first tensile crack during the flexural testing, crack widths were measured at each load pause using a crack width microscope (Model 3894, manufactured by Cole-Parmer) with a magnification of 100× and a resolution of 0.001 in (Figure 9.1). Measurements were taken at three longitudinal locations along the beam span, specifically within and adjacent to the constant-moment region. For each crack, two elevations were considered: one at the depth of the clear cover (2 in. from the bottom surface of the beam) and the other at the elevation of the tendon centroid (10 in. from the bottom surface of the beam). Crack widths were recorded at four successive load pauses, beginning at first cracking and continuing up to a load corresponding to the last load hold during the beam testing at a moment of 70% of M_n (the calculated nominal flexural resistance).

(a) (b)

Figure 9.1. Crack width measurement during flexural testing of beam specimens: (a) Crack microscope used for crack width measurement; (b) crack width measurement at 2 in. from the bottom of the beam in the S19-1 beam specimen.

From the measured crack width, the crack significance index called “estimated crack area” (ECA) is computed. This method utilizes a computed crack area to compare cracking intensity between control and treated beams. For each crack observed during the test, the crack area was approximated as a triangular region that followed the profile of the crack and had a linear variation of crack width from a maximum at the bottom surface of the beam to zero width at the tip of the crack (Figure 27). A best-fit line was determined using the least-squares error method based on crack-width measurements (w_1, w_2) made at two elevations (h_1, h_2). Elevation h_1 was 2 in. above the surface and represented an approximate concrete clear cover dimension. Elevation h_2 was at the tendon elevation. Elevation h_3 was determined from the least square error fitting process and corresponded to the hypothetical crack tip with zero width ($w_3 = 0$). This best-fit line then modeled a linear variation of crack width from the zero width crack tip to the maximum width at the bottom surface of the beam. The crack area was calculated as the area of a triangle defined by the best-fit line (Figure 27).

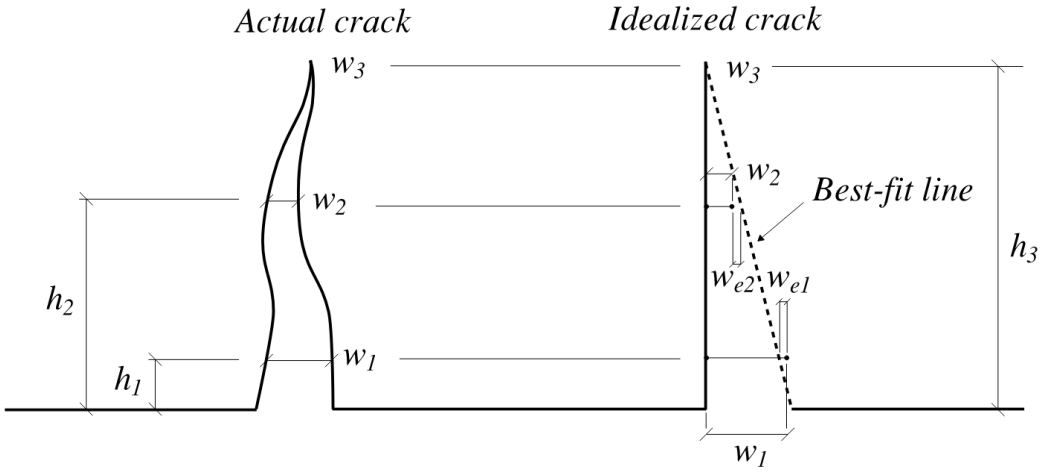

Figure 9.2. Idealization of crack and computation of crack area based on a best-fit line.

For each beam (control or treated), an estimated crack area (ECA) was computed from crack-width measurements taken from three cracks, each one located at a distinct longitudinal position (or station) along the length of each beam. The three selected cracks from each control beam and the three selected cracks from the corresponding treated beam were chosen to be reasonably similar in relative longitudinal position along the beam length. The estimated crack area (ECA) provides a quantitative measure of crack significance by incorporating both the total crack area and the number of cracks that cross the tendon. The ECA is defined as:

$$\text{ECA} = \frac{\sum A_{crack}}{N_{crack\_measured}} \times \frac{N_{crack\_Xtendon}}{N_{crack\_measured}} \quad (1)$$

Where,

A_{crack} = calculated area of an individual crack determined from the measured widths
$N_{crack\_measured}$ = number of cracks for which the area was computed (=3)
$N_{crack\_Xtendon}$ = number of cracks crossing the tendon (based on crack map).

9.3 Flexural Resistance at Ultimate Load

9.3.1 S06 Beams

All three S06 beams were tested under the same four-point bending test setup (Figure 9.3). Details of the four-point bending test setup were provided previously, along with the testing protocol. The beams were subjected to loading at an incremental rate of 0.25 kip/sec, with periodic pauses at specified load levels to inspect and mark cracks. Beyond 70% of the calculated nominal flexural resistance (M_n), where M_n is defined as the applied load at which the concrete in compression reached the code-specified maximum usable strain of 0.003 in./in., the load was increased continuously until failure. All beams exhibited concrete crushing in the compression flange, with compressive strains exceeding 0.003 in./in. (Figure 9.4), surpassing the calculated nominal flexural resistance.

Figure 9.3 Flexural testing of S06-M-T beam

(a)

(b)

(c)

Figure 9.4. Crushing of concrete at the compression flange: (a) S06-M-U; (b) S06-M-T; (c) S06-M-TC.

A summary of the results from flexural testing of the S06 beams is presented in Table 9.2. The average age of corrosion inhibitor treatment at the time of testing S06-M-T and S06-M-TC was approximately 2 weeks. When the concrete in compression reached the code-specified maximum usable strain of 0.003 in./in. (Figure 9.5), the comparison between the control beam (S06-M-U) and the treated beams (S06-M-T and S06-M-TC) showed very similar observed flexural resistance, with less than a 2% difference between the control and treated beams. Additionally, all the S06 beams exhibited similar ductility, with less than a 10% difference in deflection values at ε_c= 0.003.

Table 9.2. Observed flexural resistance and deflection of S06 beams.

Test Beam ID	Concrete compressive strength (psi)	Concrete age (days)	Treatment age (days)	Applied load (kip) at $\varepsilon_c = 0.003$	Deflection at $\varepsilon_c =$ 0.003	Maximum observed load (P_{max}, kip)
S06 – M – U	9,270	273	-	60.4	8.9	60.5
S06 – M – T	9,270	274	18	60.3	9.3	60.7
S06 – M – TC	11,900	267	11	61.0	9.8	61.9

Note:
Based on the average concrete compressive strength of the three S06 beams on the day of flexural testing, the calculated nominal flexural resistance is 52 kip, and the corresponding displacement is 12.8 in.

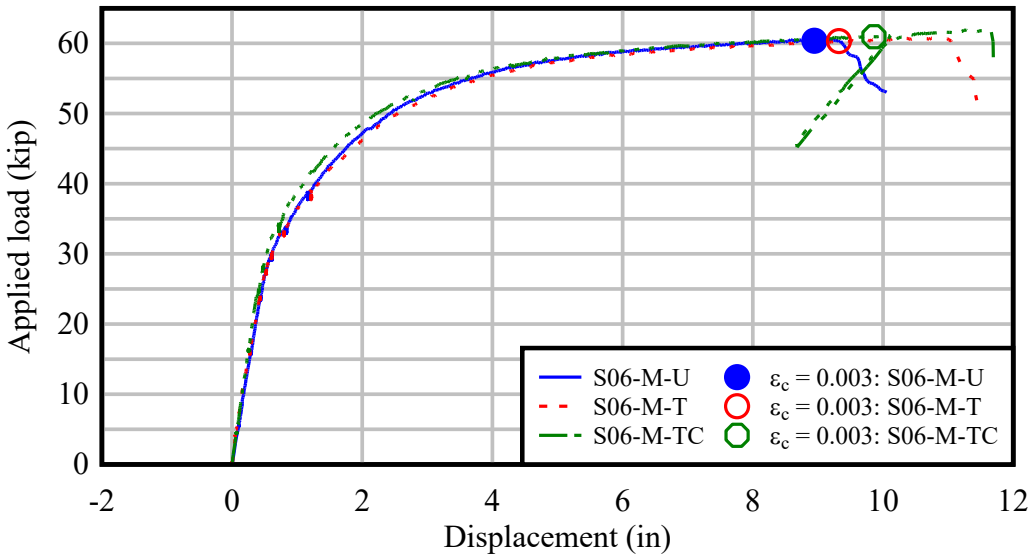

Figure 9.5. Load-deflection plot: S06 beams.

Cracks were marked during each load pause, starting from the first observed tensile crack to the final pause at 70% of the calculated nominal flexural resistance ($0.7M_n$). Final crack patterns produced by maximum load application are shown in Figure 9.6. All S06 beams exhibited similar crack patterns in terms of the number and spacing of cracks. The flexural cracks were distributed relatively evenly under the load points for a length of approximately 12 feet; the average crack spacing was approximately 1.5 feet.

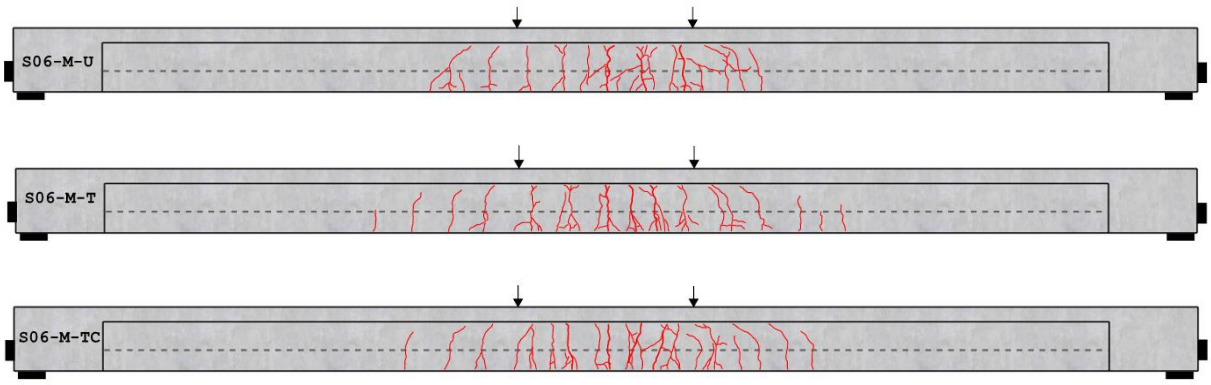

Figure 9.6. Final crack map after flexural testing of S06 beams.

9.3.2 S12 Beams

The S12 beams were subjected to flexural loading using a four-point bending setup, and the load was applied at a constant rate of 0.25 kip/sec (Figure 9.7). The load was applied in eight steps, with pauses at each step to inspect and mark cracks. After the last pause at $0.7M_n$, the load was increased continuously until the load began to drop, which indicated maximum observed flexural resistance had been reached.

Figure 9.7. Flexural testing of S12-P-T beam

Both the S12-P-U and S12-P-T beams exhibited crushing of concrete in the top compression flange (Figure 9.8). Crushing occurred at a measured concrete strain exceeding 0.003 in./in., and the load in the actuator dropped beyond this point, indicating a loss of beam strength.

(a) (b)

Figure 9.8. Crushing of concrete at the compression flange: (a) S12-P-U; (b) S12-P-T

A summary of the results from the flexural testing of the S12 beams is presented in Table 9.3. In contrast to the S06 beams (described above), where the average corrosion inhibitor treatment age at the time of testing was approximately 2 weeks, the average corrosion inhibitor treatment age at the time of testing the S12-P-T beam was approximately 2 months. Thus, taken together, the tests conducted in this study addressed both short-term corrosion inhibitor treatment age (2 week) as well as considerably longer corrosion inhibitor (2 month) treatment age.

Both S12 beams had the same concrete strength on the day of testing. A comparison of the load–displacement plots from the flexural testing is shown in Figure 9.9. The observed flexural resistance of the control and treated beams was the same when $\varepsilon_c = 0.003$ in./in. although the deflections differed by about 18% between the two beams.

Table 9.3. Observed flexural strength and deflection of S12 beams.

Test Beam ID	Concrete compressive strength (psi)	Concrete age (days)	Treatment age (days)	Applied load (kip) at $\varepsilon_c = 0.003$	Deflection at $\varepsilon_c = 0.003$	Maximum observed load (P_{max}, kip)
S12-P-U	10,215	274	-	167.8	6.5	171.1
S12-P-T	10,215	276	64	167.8	5.3	175.3

Note:
Based on the average concrete compressive strength of the two S12 beams on the day of flexural testing, the calculated nominal flexural resistance is 159.6 kip, and the corresponding displacement is 9.1 in.

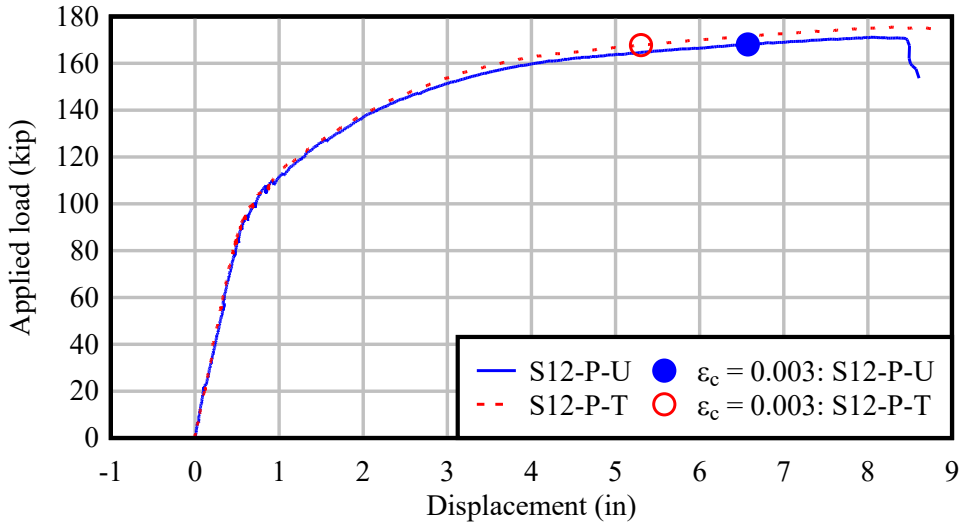

Figure 9.9. Load-deflection plot: S12 beams.

During the testing, the progression of flexural cracks was marked at every load pause, starting from the step when the first tensile crack was observed, and continuing up to $0.7M_n$. Final crack patterns produced by maximum load application are shown in Figure 9.10.

The crack patterns were very similar in both the control and treated beams in terms of the extent of cracking along the beam length relative to midspan, as well as the spacing between flexural cracks.

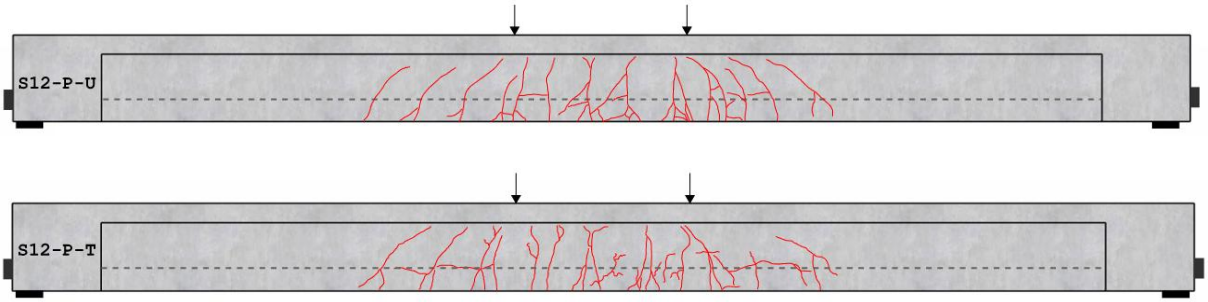

Figure 9.10. Final crack map after flexural testing of S12 beams.

9.3.3 S19 Beams

The S19 beams were tested using a similar setup and loading rate as the S06 and S12 beams (Figure 9.11). The number of pauses for crack inspection and marking up to $0.7M_n$ was seven, followed by continued loading until the maximum load was reached.

Figure 9.11. Flexural testing of S19-M-T test beam.

Similar to the S06 and S12 beams, the S19 beams reached maximum load when crushing of the concrete in the compression flange occurred. The crushing occurred near midspan between the ends of the spreader beam that transferred the applied load to two points on the test beams (Figure 9.12).

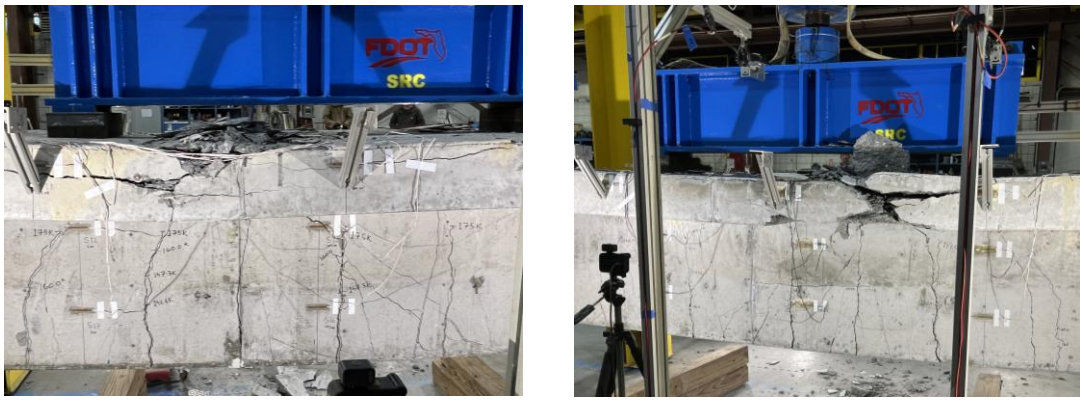

(a) (b)

Figure 9.12. Crushing of concrete at the compression flange: (a) S19-M-U; (b) S19-M-T.

A summary of results from the flexural testing of the S19 beams is presented in Table 9.4. The concrete strengths on the day of beam testing for the two beams differed by only 4%. The treated beam was tested at approximately 2.5 months after corrosion inhibitor impregnation. As shown in Figure 9.13 the observed flexural resistance of the control and treated beams were very close at $\varepsilon_c = 0.003$ in./in. with less than a 2% difference.

Table 9.4. Observed flexural resistance and deflection of S19 beams.

Test Beam ID	Concrete compressive strength (psi)	Concrete age (days)	Treatment age (days)	Applied load (kip) at $\varepsilon_c = 0.003$	Deflection at $\varepsilon_c = 0.003$	Maximum observed load (P_{max}, kip)
S19-M-U	11,483	178	-	288.4	10.2	290.5
S19-M-T	10,987	188	77	281.4	9.7	287.1

Note:
Based on the average concrete compressive strength of the two S19 beams on the day of flexural testing, the calculated nominal flexural resistance is 260 kip, and the corresponding displacement is 10.2 in.

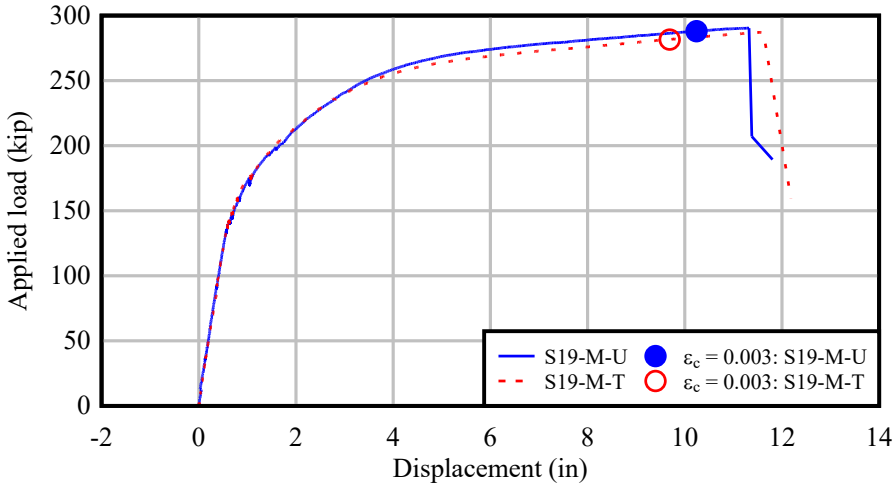

Figure 9.13. Load-deflection plot: S19 beams.

The final crack maps of the S19 beams (Figure 9.14) were created from the cracks marked on the beams during and after flexural testing. Compared to the S06 and S12 beams, the cracks in the S19 beams were denser (more closely spaced) within the constant moment region. A few large-width cracks (more prominent than other cracks observed after flexural testing) occurred inside this region at a spacing of approximately 1.5 ft. Overall, the crack patterns and extent of cracking in the two S19 beams were very similar, with no clear differences being exhibited as a result of treatment with corrosion inhibitor.

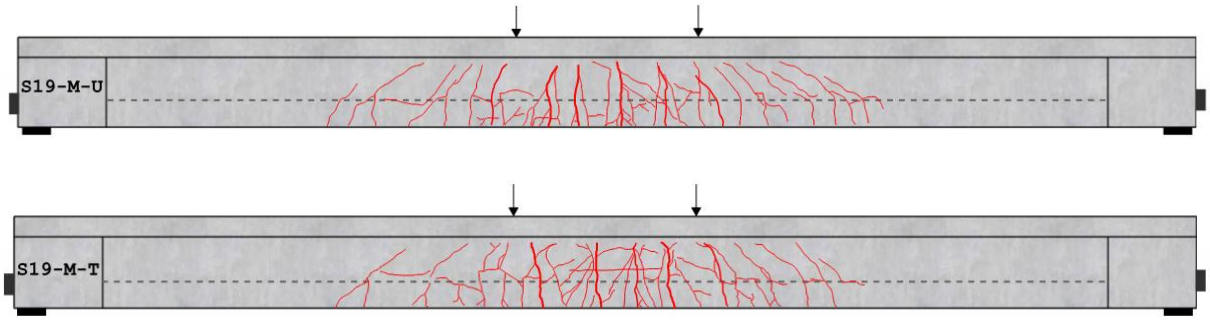

Figure 9.14. Final crack map after flexural testing of S19 beams.

9.3.4 D19-M Beams

The draped tendon beams, D19-M and D19-P couplets, by design had the same theoretical nominal flexural resistance as the straight tendon beams (S19-M-U and S19-M-T). The physical dimensions of the beams were also identical by design in terms of span and cross-sectional properties. Accordingly, the D19 beams had a similar test setup as the S19 beams. However, for the D19 beams, the test protocol was slightly different such that there were five load pauses for crack inspection and marking up to $0.7M_n$ instead of seven pauses used in the testing of the S19 beams. For loads causing moment greater than $0.7M_n$ load was applied continuously until the maximum load was reached (Figure 9.15).

Figure 9.15. Failure of D19-M-U beam by crushing of top flange.

Both beams in the D19-M couplet (D19-M-U and D19-M-T) failed by crushing of concrete on the top flange of the beam. Crushing of the top flange occurred at the same location under the southern load point (under the bearing pad of the south end of the spreader beam) in both D19-M beams (Figure 9.16).

(a) (b)

Figure 9.16. Crushing of concrete at the compression flange: (a) D19-M-U; (b) D19-M-T.

Both beams in the D19-M beam couplet were tested within the same week, with D19-M-U being the first to be tested at approximately 3 months from the day of casting. The treated beam (D19-M-T) was tested approximately one month after the impregnation of the corrosion inhibitor. Details are provided in Table 9.5. At the time of flexural testing, the difference in the compressive strength of the concrete between the two beams was only about 1.5%. Figure 9.17 shows the comparison of the flexural behavior of the D19-M couplet, where the observed flexural resistance of the control and treated beams was very close at $\varepsilon_c = 0.003$ in./in. with less than a 1% difference.

Table 9.5. Observed flexural resistance and deflection of D19-M beams.

Test Beam ID	Concrete compressive strength (psi)	Concrete age (days)	Treatment age (days)	Applied load (kip) at $\varepsilon_c = 0.003$	Deflection at $\varepsilon_c = 0.003$	Maximum observed load (P_{max}, kip)
D19-M-U	11,157	93	-	273.1	8.1	279.2
D19-M-T	11,008	98	26	273.2	7.4	280.7

Note:
Based on the average concrete compressive strength of the two D19-M beams on the day of flexural testing, the calculated nominal flexural resistance is 266.6 kip, and the corresponding displacement is 11.9 in.

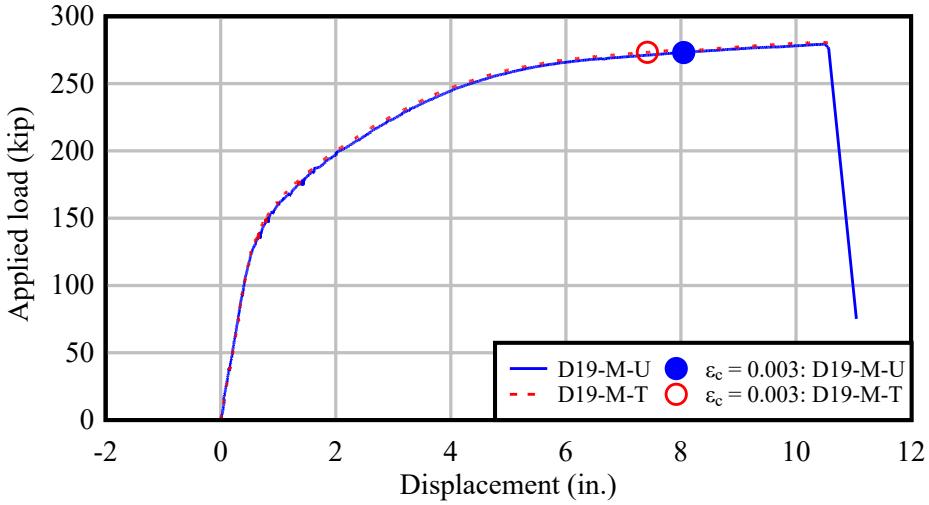

Figure 9.17. Load-deflection plot: D19-M beams.

Similar to the straight-tendon beams (S19), visually observed cracks during and after the flexural testing of the draped-tendon D19-M beams were marked on the east web face and recreated as shown in Figure 9.18. The extent of flexural cracking in both the control (D19-M-U) and treated (D19-M-T) beams was very similar, extending from midspan up to about 12 ft toward both the north and south ends of the beam. The crack pattern was also similar, especially within the constant moment region, where approximately four cracks of large width formed at a spacing of about 1.5 ft in both beams.

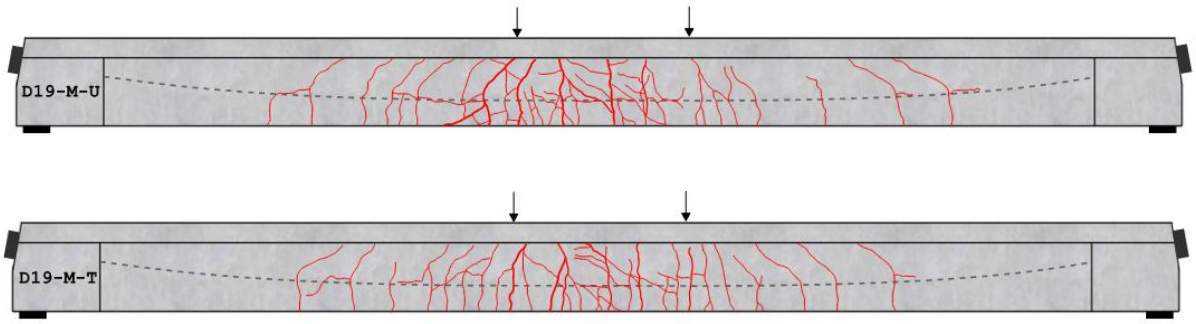

Figure 9.18. Final crack map after flexural testing of D19-M beams.

9.3.5 D19-P Beams

As shown in Table 9.1, the variables in the D19-P couplet were identical to those in the D19-M couplet except for the duct type (plastic vs. metal). The design variables, target design strength, and geometrical properties were also the same for both draped tendon couplets (D19-M, D19-P). Accordingly, the D19-P beams had the same test setup (Figure 9.19) as the D19-M beams, including the test protocol, which included five load pauses for crack inspection and marking up to $0.7M_n$, followed by the final continued load application until the maximum capacity load was reached.

Figure 9.19. Flexural testing of the D19-P-T test beam.

Both beams in the D19-P couplet (D19-P-U and D19-P-T) failed by crushing of concrete on the top flange of the beam. Crushing of the top flanges of both beams occurred at the same location under the northern load point (under the bearing pad of the north end of the spreader beam) in the D19-P beams (Figure 9.20).

(a) (b)

Figure 9.20. Crushing of concrete at the compression flange: (a) D19-P-U; (b) D19-P-T.

The beams in the D19-P beam couplet were tested two weeks apart, with D19-P-U being the first to be tested at approximately 3 months from the day of casting. The treated beam (D19-P-T) was tested approximately one month after the impregnation of corrosion inhibitor. Details are provided in Table 9.6. At the time of flexural testing, the difference in the compressive strength of the concrete between the D19-P beams was only about 0.5%. Figure 9.21 shows the comparison of the flexural behavior of beams in the D19-P couplet. The untreated control beam D19-P-U exhibited a marginally reduced stiffness relative to the treated D19-P-T beam. The control beam D19-P-U was unique among all beams tested in this study in that it had a presumed shrinkage crack (Figure 9.22) that extended through the full depth of the beam section (from bottom surface to top surface) and across the full width of the bottom surface of the beam at about 1 ft south of midspan (also discussed later in Section 9.4.5). The reduced stiffness apparent in Figure 9.21 is attributed to the presence of this crack. Ultimately, however, the observed flexural resistance of the control and treated beams was very close at $\varepsilon_c = 0.003$ in./in., with less than a 2% difference.

Table 9.6. Observed flexural resistance and deflection of D19-P beams.

Test Beam ID	Concrete compressive strength (psi)	Test age (days)	Treatment age (days)	Applied load (kip) at $\varepsilon_c = 0.003$	Deflection at $\varepsilon_c = 0.003$	Maximum observed load (P_{max}, kip)
D19-P-U	12,636	86	-	271.1	8.2	278.2
D19-P-T	12,558	101	29	275.9	8.9	280.1

Note:
Based on the average concrete compressive strength of the two D19-P beams on the day of flexural testing, the calculated nominal flexural resistance is 268.3 kip, and the corresponding displacement is in.

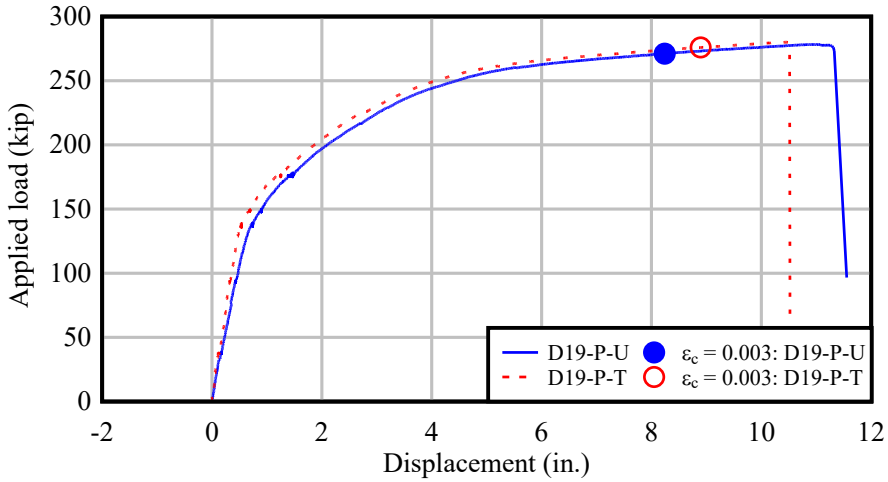

Figure 9.21. Load-deflection plot: D19-P beams.

The post-testing crack maps on the east faces of the beams in the D19-P couplet are shown in Figure 9.22. Note that the D19-P-U beam had an existing crack within the constant moment region that occurred before application of load. This crack, which was presumed to have been caused by shrinkage, extended through the full depth of the beam section (from bottom surface to top surface) and across the full width of the bottom surface of the beam. This crack can be identified in the D19-P-U crack map as the only crack that extended through the top (compression) flange of the beam. Aside from the shrinkage crack, between the control (D19-P-U) and the treated (D19-P-T) beams, the patterns of flexural cracks within and outside the constant moment region were similar in terms of crack spacing, crack shape, and the distance to which the cracks extended from the midspan toward both beam ends. Flexural cracks with larger widths that occurred within the constant moment region were also spaced at similar distances in both beams, at approximately 1.5 ft.

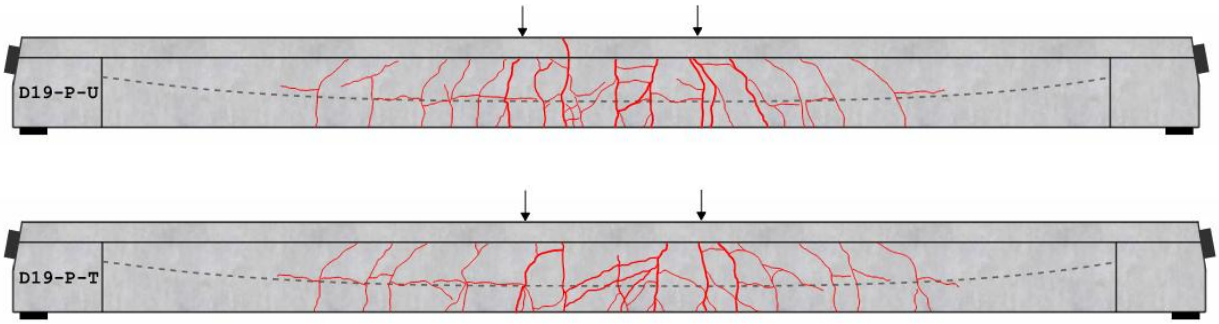

Figure 9.22. Final crack map after flexural testing of D19 beams.

9.4 Cracking at Service Load

9.4.1 S06 Beams

Applied load was held constant at predefined load steps, each corresponding to a percentage of the calculated nominal flexural resistance. Load was also held constant to inspect for cracks when the calculated net tensile stress in the beam reached $7.5\sqrt{f_c'}$. At each load pause, starting at $0.2M_n$ (20% of the calculated nominal flexural resistance), the beams were visually inspected for cracks. If cracks were observed, they were marked, and loading was continued to the next predefined step, up to 70% of the calculated nominal flexural resistance. In addition, the real-time load-displacement behavior of the beam was monitored. If any change in slope was observed between load steps, the applied load was paused and held constant, and the beam was inspected for cracks, which were then marked.

Although all the S06 beams were intended to be identical in design and construction, various factors affected their behavior and resulted in some variations in observed cracking. The applied loads at which the first tensile cracks were identified in the S06 beams are shown in Table 9.7 along with the calculated tensile stress at cracking. As Table 9.7 notes, there were differences in concrete compressive strengths and concrete tensile strengths between the cracked and treated beam (S06-M-TC) and the other two S06 beams (S06-M-U and S06-M-T). Additionally, when load was applied to the S06-M-TC beam to bring about initial cracking - prior to impregnating the beam with corrosion inhibitor - the load was increased slowly (with more intermediate load holds for crack inspection than were used in the other two S06 beams), and the beam was methodically inspected for the presence of cracks (recall Section 8.1). The durations of the load pauses during the S06-M-TC inspection process were somewhat longer than those used during standard flexural testing of the other two S06 beams. The longer load pauses used to detect cracking in S06-M-TC could have caused tensile creep, thus resulting in the lower calculated stress at cracking (Table 9.7).

Table 9.7. Cracking load in S06 beams.

Test beam ID	Concrete compressive strength (psi)	Cracking load (Kip)	Tensile stress at cracking ($n\sqrt{f_c'}$)
S06 – M – U	9,270	30.0	10.9
S06 – M – T	9,270	27.7	9.5
S06 – M – TC	11,900	24.7	6.6

A service load level comparison of the behavior of the S06 beams was conducted at a consistent concrete tensile stress of $12\sqrt{f_c'}$ across all three beams. This stress level was selected to allow comparison of crack characteristics after multiple cracks had formed, rather than at appearance of a first visible crack. For S06-M-U and S06-M-T beams, the $12\sqrt{f_c'}$ stress level was reached at an applied load of 33.7 kips, while for S06-M-TC, the associated load was 34.2 kips (Figure 9.23). At the same stress level, no discernible difference in cracking behavior was observed among the untreated (S06-M-U), treated (S06-M-T), and cracked-and-treated (S06-M-TC) beams; specifically, comparisons of S06-M-U vs. S06-M-T vs. S06-M-TC showed similar responses. Because the cracked-and-treated (TC) beam exhibited behavior essentially identical to the treated (T) beam, the TC category was not included in subsequent beam couplets.

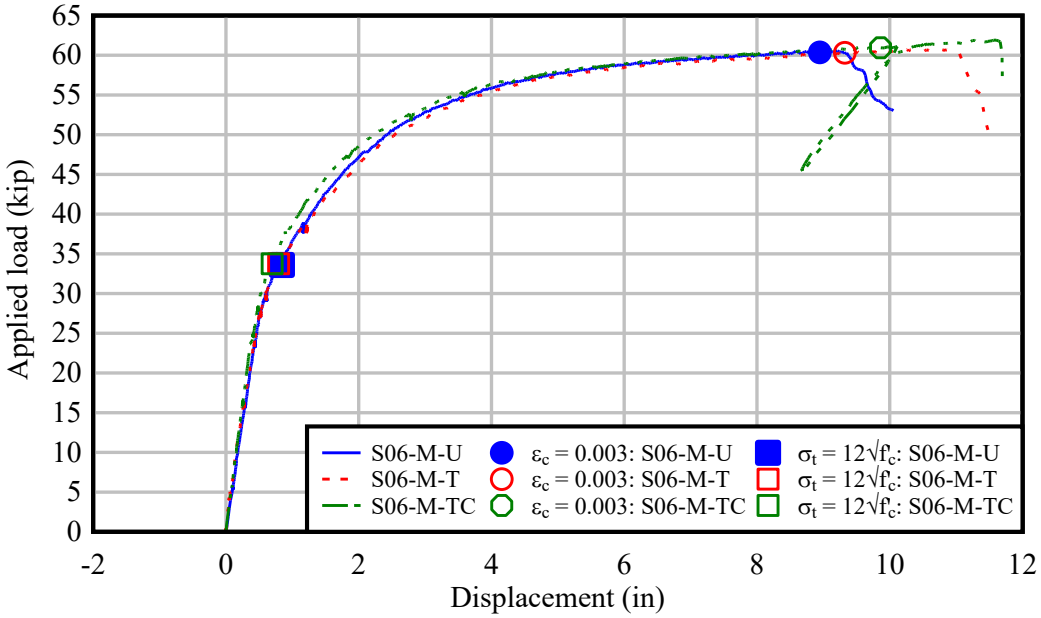

Figure 9.23. Load-deflection plot: S06 beams.

Crack map

In contrast to crack maps shown in earlier sections, which corresponded to observed flexural resistance (at ultimate load) of the beams, the crack maps shown in Figure 9.24 correspond to loads that were representative of service conditions, causing tensile stress of up to $12\sqrt{f_c'}$. Except for minor variations in the number of cracks, the crack spacing, crack height, and crack locations were all reasonably consistent among the S06 beams.

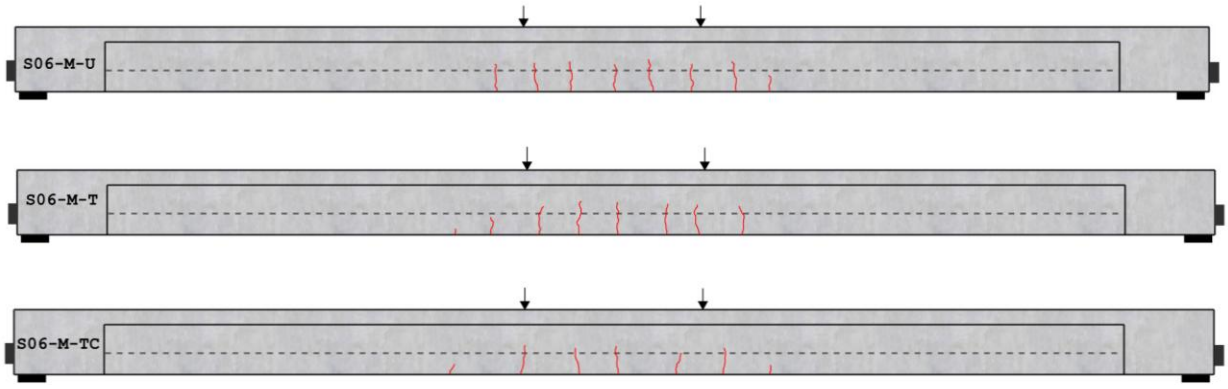

Figure 9.24. S06 beams crack patterns at tensile stress in concrete of $12\sqrt{f_c'}$

Crack depth ratio

In the S06 beam triplet, the crack depth ratio of both the treated (S06-M-T) and cracked-treated (S06-M-TC) beams was less than unity, as presented in Table 9.8. This indicates that the crack significance was lower in both treated beams as compared to the control beam (S06-M-U), resulting in a lower possibility of tendon exposure to the environment at the hypothetical service load level.

Table 9.8. Comparison of crack depth ratio for S06 beams at service load level ($12\sqrt{f_c'}$)

Beam ID	Number of cracks crossing tendon elevation [1]	Number of cracks crossing tendon elevation in the control [2]	Crack depth ratio = [1]/[2]
S06-M-U	7	7	1.0
S06-M-T	6		0.9
S06-M-TC	5		0.7

9.4.2 S12 Beams

As with the S06 beams, the S12 beams were tested under a stepped loading protocol with pauses at predefined percentages of calculated nominal flexural resistance. A total of eight load steps (pauses) up to 70% of the calculated nominal flexural resistance were applied before loading was continued to failure in flexure. At each load pause, the beams were visually inspected for the presence of tensile cracks.

The cracking loads of the beams are presented in Table 9.9. The first tensile cracks in beam S12-P-U was identified at an applied load of 95 kips, with two cracks forming at the longitudinal locations of the two loading points. In contrast, the first tensile crack in beam S12-P-T occurred at 85 kips and was located at the beam midspan. For both beams, the calculated tensile stress at first cracking exceeded the value of $7.5\sqrt{f_c'}$. Although the concrete strengths were the same in both beams, the difference in cracking load was be attributed to variations in stress distribution caused by aggregate distribution, test setup, and minor construction inconsistencies.

Table 9.9. Cracking load in S12 beams.

Test beam ID	Concrete compressive strength (psi)	Cracking load (Kip)	Tensile stress at cracking (n$\sqrt{f_c'}$)
S12 – P – U	10,215	95.0	11.1
S12 – P – T	10,215	85.0	8.0

With the same reasoning discussed in the previous section for the S06 beams, the cracking behaviors of the untreated (S12-P-U) and treated (S12-P-T) beams were compared at a concrete stress level of $12\sqrt{f_c'}$, corresponding to an applied load of 100 kips (Figure 9.25). Similar to the observations from the 6-strand metal-duct S06 beam triplet, no appreciable difference in cracking behavior was observed between the untreated and treated beams in the 12-strand plastic-duct S12 couplet. This result indicated that, despite the larger tendon size and the different duct type, impregnation of corrosion inhibitor in the S12-P-T beam did appear to influence cracking behavior.

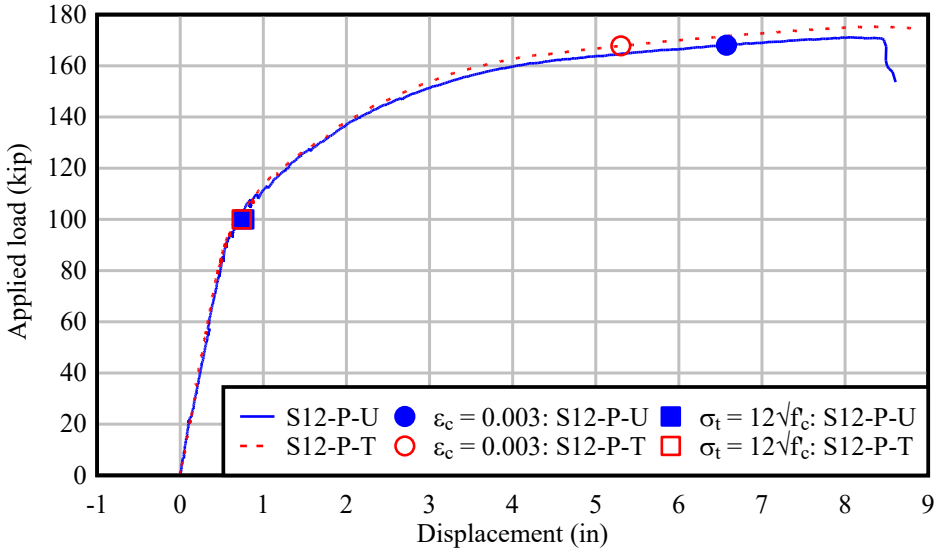

Figure 9.25. Load-deflection plot: S12 beams.

Crack map

The crack maps in Figure 9.26 correspond to an applied load of 100 kips, representing a stress state where the tensile stress reached $12\sqrt{f_c'}$. The crack patterns were consistent between the two S12 beams in both the number of cracks and crack spacing. Although the first tensile cracks initiated at different locations and at slightly different stress levels, the overall crack patterns at this service-level stress were very similar between the untreated (S12-P-U) and treated (S12-P-T) beams.

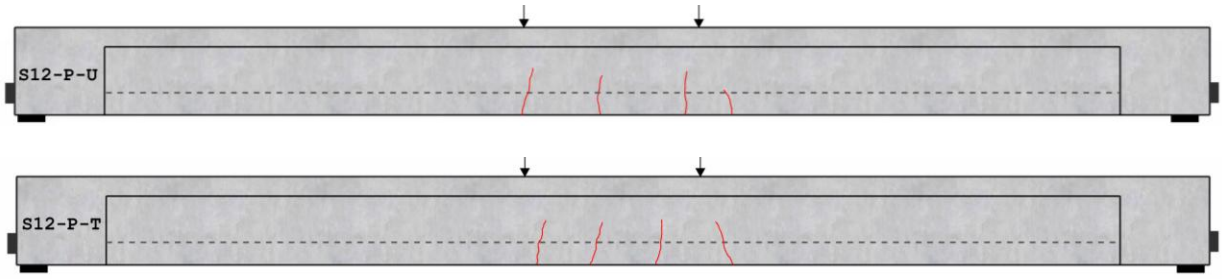

Figure 9.26. S12 beams with marked cracks at tensile stress in concrete at $12\sqrt{f_c'}$

Crack depth ratio

For the S12 beam couplet, the crack depth ratio was the same for the control (S12-P-U) and the treated (S12-P-T) beams at unity, as presented in Table 9.10. This indicates that impregnation of the corrosion inhibitor did not have an apparent effect on crack significance.

Table 9.10. Comparison of crack depth ratio for S12 beams at service load level ($12\sqrt{f_c'}$)

Beam ID	Number of cracks crossing tendon [1]	Number of cracks crossing tendon in the control [2]	Crack depth ratio = [1]/[2]
S12-P-U	4	4	1.0
S12-P-T	4		1.0

9.4.3 S19 Beams

As with the previously tested beams, the S19 beams were subjected to a stepped loading protocol with pauses at predefined percentages of calculated nominal flexural resistance. For both beams, the first visible tensile cracks were identified at the fourth load pause, corresponding to an applied load of 142.6 kips, as shown in Table 9.11. In beam S19-M-U, the first crack occurred at the longitudinal location of the southern loading point, while in beam S19-M-T the initial tensile crack formed at midspan. For both beams, the calculated tensile stress at first cracking exceeded the value of $7.5\sqrt{f_c'}$, reaching values of approximately $9.2\sqrt{f_c'}$ and $9.4\sqrt{f_c'}$, respectively. The final crack maps after flexural failure appeared similar for both beams, with differences in the location of initial cracking being attributed to variability in aggregate distribution, slight asymmetries in the test setup, and minor construction inconsistencies.

Table 9.11. Cracking load in S19 beams.

Test beam ID	Concrete compressive strength (psi)	Cracking load (Kip)	Tensile stress at cracking ($n\sqrt{f_c'}$)
S19-M-U	11,483	142.6	9.2
S19-M-T	10,987	142.6	9.4

The service-load performance of the control and treated S19 beams (S19-M-U and S19-M-T) was compared based on crack characteristics when the tensile stress at the bottom fiber reached $12\sqrt{f_c'}$ which corresponded to an applied load of 160 kip, as shown in Figure 9.27. Similar to the observations from the S06 and S12 beams, no appreciable difference in cracking behavior was observed between the untreated and treated beams in the S19 couplet. This indicates that impregnation of the corrosion inhibitor in the S19-M-T beam also did not appear to influence the service level cracking behavior of beams constructed with 19-strand tendons, metal ducts, and plain cement grout.

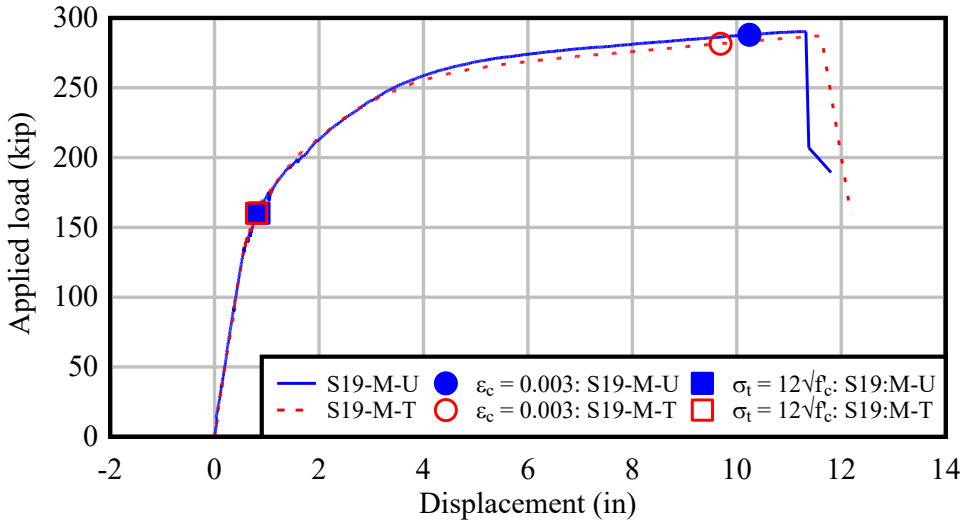

Figure 9.27. Load-deflection plot: S19 beams.

Crack map

At the service load level corresponding to an applied load of 160 kips, the cracks that formed on the east face of the S19 beams were visually identified, marked, and their widths were measured. The cracks were marked on the beam surface to create the crack maps shown in Figure 9.28. Consistent with the observations from the S06 and S12 beams, the crack patterns in the untreated and treated S19 beams showed no significant differences. The number of cracks and the crack spacings were comparable, and the flexural cracks exhibited similar shapes in both beams (S19-M-U and S19-M-T).

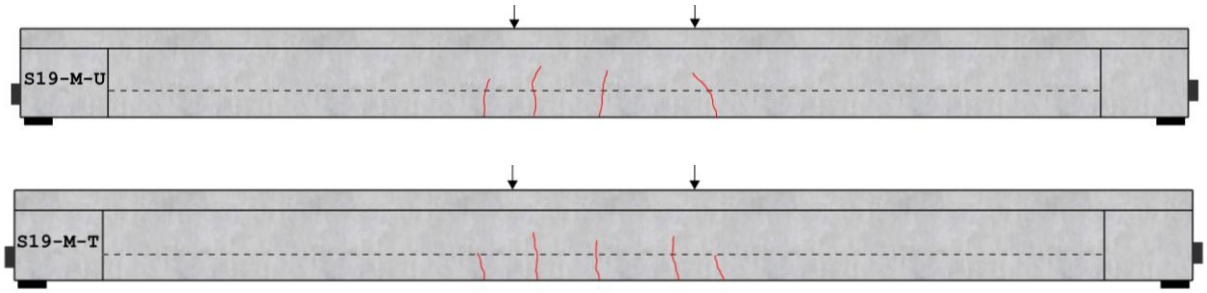

Figure 9.28. S19 beams showing observed and marked cracks at the service load level.

Crack depth ratio

Contrary to the previous two beam groups, in the S19 beam couplet, the crack depth ratio was 25% higher than unity for the treated (S19-M-T) beam, as shown in Table 9.12. This indicated that the corrosion inhibitor impregnation moderately increased the crack significance and the possibility of the tendon becoming exposed to the environment at this service load level. A summary of the maximum, minimum, and average measured crack widths from three crack

locations along the beam length, and at 2 in. from the bottom surface, is provided for reference in Table 9.12. The maximum and average crack widths were the same in both the control and treated beams; however, the minimum crack width was slightly larger in the treated beam.

Table 9.12. Comparison of crack depth ratio for S19-M-U and S19-M-T beams at service load level ($12\sqrt{f_c'}$)

Beam ID	Number of cracks crossing tendon [1]	Number of cracks crossing tendon in the control [2]	Crack depth ratio = [1]/[2]	Measured crack widths at 2 in. from the bottom surface (in)		
				Minimum	Average	Maximum
S19-M-U	4	4	1.0	0.011	0.012	0.013
S19-M-T	5		1.25	0.012	0.012	0.013

Crack area

Estimated crack areas were calculated from the measured crack widths in the S19 beam couplet and are presented in Table 9.13. The untreated beam (S19-M-U) exhibited a slightly larger crack area (summed for the three measured cracks), by approximately 10%. However, because the treated beam (S19-M-T) had more cracks crossing the tendon, the overall ECA value for the treated beam was higher. This result indicated that, although the untreated beam showed somewhat larger individual crack areas, the treated beam exhibited a greater overall significance of cracking in terms of potential tendon exposure.

Table 9.13. Comparison of estimated crack area for S19-M-U and S19-M-T

Beam	Crack ID	Computed crack area (in^2)	Summed 3-crack area $\Sigma(A,B,C)$ (in^2)	Number of cracks crossing tendon	Number of cracks width measured	Estimated crack area (in^2)	Difference (%)
S19-M-U	A	0.1472	0.4039	4	3	0.18	10
	B	0.1187					
	C	0.1380					
S19-M-T	A	0.1350	0.3537	5	3	0.20	
	B	0.0011					
	C	0.1176					

9.4.4 D19-M Beams

The testing protocol for the D19-M beams followed procedures similar to those used for the previous beams, with stepped loading and pauses to observe and mark flexural cracks. The D19-M beam couplet included a total of five load pauses before applying the final load step up to failure by crushing of the compression flange. The initial cracks occurred between the second and third load pauses during flexural testing in both D19-M beams (Table 9.14). Although the cracks were not visually observed at the moment they formed, a change in the slope of the load–displacement plot was used to identify the applied load at which the first tensile crack occurred. The tensile stresses on the bottom surfaces of the beams, computed from the applied cracking loads, were found to be $8.4\sqrt{f_c'}$ in D19-M-U and $7.6\sqrt{f_c'}$ in D19-M-T.

Table 9.14. Cracking load in D19-M beams.

Test beam ID	Concrete compressive strength (psi)	Cracking load (Kip)	Tensile stress at cracking ($n\sqrt{f_c'}$)
D19-M-U	11,157	123.5	8.4
D19-M-T	10,008	118.6	7.6

For the D19-M couplet, an applied load of 139.4 kip at the third load step was determined as the load closest to the service load level, defined as the applied load at which the tensile stress at the bottom concrete surface reached $12\sqrt{f_c'}$ (Figure 9.29). At this load level, four flexural cracks were visually observed in the D19-M-U beam, out of which three cracks were selected for crack width measurement at 2 in. from the bottom surface and at the tendon centroid elevation at each load pause. In the D19-M-T beam, a larger number of flexural cracks were visually observed at the same load level as compared to the D19-M-U beam. However, three out of the seven cracks in the D19-M-T beam were relatively small, leaving four cracks that were more prominent and which were comparable to the four cracks observed in the D19-M-U beam.

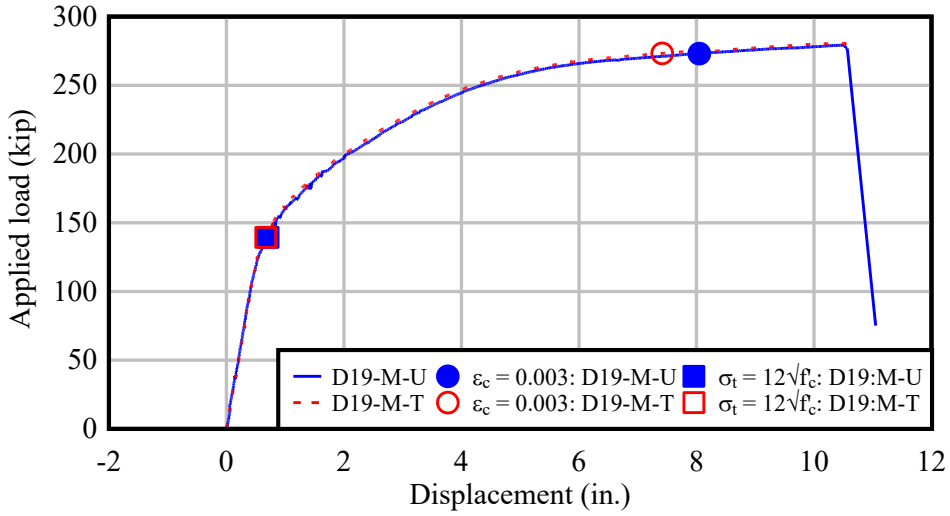

Figure 9.29. Load-deflection plot: D19M beams.

Crack map

At the service load level corresponding to the third load pause, with an applied load of 139.4 kip, the cracks that formed on the east face of the D19-M beams were visually identified and marked. Crack widths were measured on three selected cracks. The marked cracks were used to create the crack map shown in Figure 9.30. Except for small cracks that occurred about 3 ft outside the constant moment region in the D19-M-T beam, the crack maps on the east faces of the D19-M beams were very similar in terms of the number of cracks, crack spacing, and height of cracks occurring near and within the constant moment region.

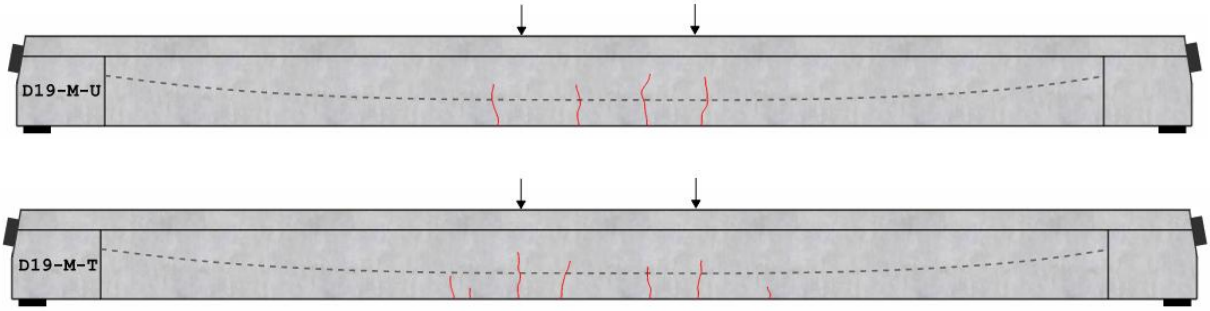

Figure 9.30. D19M beams showing observed and marked cracks at the service load level.

Crack depth ratio

The crack depth ratio for the treated beam (D19-M-T) was equal to unity, as shown in Table 9.15 . Therefore, impregnation of corrosion inhibitor in the D19 metal-duct beam did not cause an apparent increase in the significance of cracking or tendon exposure relative to the control (D19-M-U) beam. However, crack widths measured near the bottom surface of the treated D19-M-T beam were larger than in the control beam D19-M-U, as shown in Table 9.15.

Table 9.15. Comparison of crack depth ratio for D19-M-U and D19-M-T beams at service load level ($12\sqrt{f_c'}$).

Beam ID	Number of cracks crossing tendon [1]	Number of cracks crossing tendon in the control [2]	Crack depth ratio = [1]/[2]	Measured crack widths at 2 in. from the bottom surface (in)		
				Minimum	Average	Maximum
D19-M-U	4	4	1.0	0.006	0.007	0.009
D19-M-T	4		1.0	0.007	0.011	0.015

Crack area

The estimated crack area for the treated beam (D19-M-T) was about 25% larger than for the untreated beam (D19-M-U), as shown in Table 9.16. Although the number of cracks intersecting the tendon was the same in both the control and treated beams, the treated beam had a larger overall estimated crack area. As a result, the treated beam exhibited a moderately increased potential for tendon exposure.

Table 9.16. Comparison of estimated crack area for D19-M-U and D19-M-T

Beam	Crack ID	Computed crack area (in^2)	Summed 3-crack area $\Sigma(A,B,C)$ (in^2)	Number of cracks crossing tendon	Number of cracks width measured	Estimated crack area (in^2)	Difference (%)
D19-M-U	A	0.0595	0.2136	4	3	0.09	25
	B	0.0702					
	C	0.0839					
D19-M-T	A	0.0814	0.2644	4	3	0.12	
	B	0.1292					
	C	0.0539					

9.4.5 D19-P Beams

The testing protocol for the D19-P beams followed the same procedures as the D19-M couplet, with stepped loading and pauses to observe and mark flexural cracks. The D19-P beam couplet included a total of five load pauses before applying the final load step up to failure by crushing of the compression flange. Initial flexural cracks occurred between the second and third load pauses in both D19-P beams (Table 9.17). Although these cracks were not visually observed at the moment of formation, a change in the slope of the load–displacement plot was used to identify the applied loads at which the first tensile cracks occurred. The tensile stresses on the bottom surfaces of the beams, computed from the applied cracking loads, were found to be $7.8\sqrt{f_c'}$ in D19-P-U and $9.7\sqrt{f_c'}$ in D19-P-T.

Table 9.17. Cracking load in D19-P beams.

Test beam ID	Concrete compressive strength (psi)	Cracking load (Kip)	Tensile stress at cracking ($n\sqrt{f_c'}$)
D19-P-U	12,636	123.4	7.8
D19-P-T	12,558	131.8	9.7

Similar to the D19-M couplet, for the D19-P couplet an applied load of 139.4 kip at the third load step was determined as the load closest to the service load level, defined as the applied load at which the tensile stress at the bottom concrete surface reached $12\sqrt{f_c'}$ (Figure 9.31).

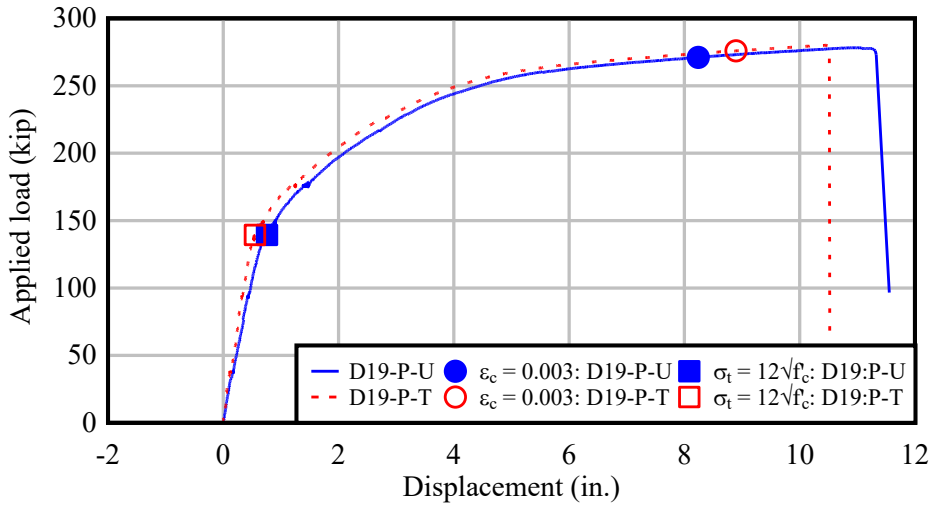

Figure 9.31. Load-deflection plot: D19P beams.

Crack map

At the service load level corresponding to the third load pause, with an applied load of 139.4 kip, the cracks that formed on the east face of the D19-P beams were visually identified, marked, and widths were measured on three selected cracks. The marked cracks were used to create the crack map. As noted earlier, the D19-P-U beam had a presumed shrinkage crack that

extended through the full depth of the beam section and across the full width of the bottom surface of the beam at about 1 ft south of midspan (Figure 9.32).

Crack widths on both faces of the untreated control beam (D19-P-U) were measured before the application of load. On the east face of the beam, the crack width across the depth at five elevations was measured and found to be consistently about 0.005 in., while on the west face at the same elevations, the average crack width was consistently about 0.002 in.

At the service load level during testing, only one prominent flexural crack was visually observed in the D19-P-U beam. This crack was marked on the east face of the beam to create the crack map shown in Figure 9.32. The D19-P-T beam, on the other hand, without any shrinkage crack, exhibited four flexural cracks within the constant moment region, similar to the D19-M couplet. The presence of the shrinkage crack likely altered the distribution of tensile stress in the D19-P-U beam during flexural testing, resulting in a flexural crack pattern that was less comparable to the treated beam.

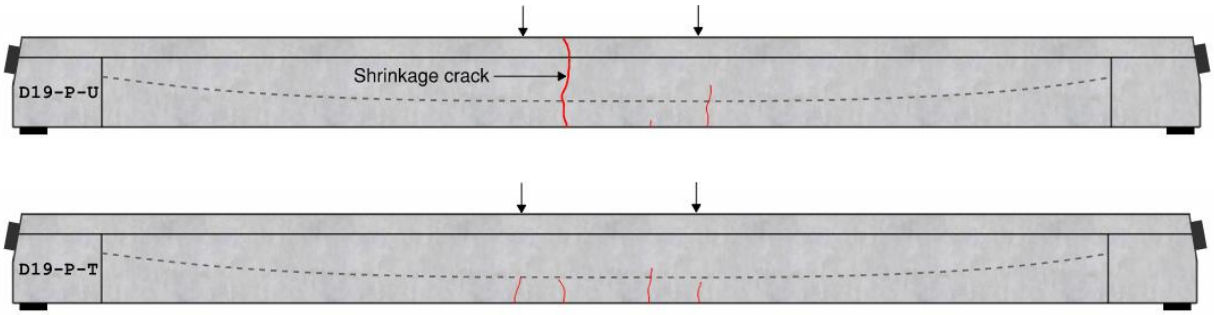

Figure 9.32. D19P beams showing observed and marked cracks at the service load level.

Crack depth ratio

In calculating the crack depth ratio for the D19-P (plastic duct) couplet, the shrinkage crack was omitted, and only the newly formed flexural crack in the control (D19-P-U) beam was considered. For the treated beam (D19-P-T), which exhibited four flexural cracks, with only one crack intersecting the tendon, therefore the crack depth ratio was equal to unity. Results are presented in Table 9.18 for consistency, however, crack significance and potential tendon exposure have not been directly compared, since the presence of the shrinkage crack in the control beam likely altered crack formation at the service load level. The summary of measured crack widths from the flexural crack intersecting the tendon in the control beam and from three flexural cracks in the treated beam at the service load level is also presented in Table 9.18.

Table 9.18. Crack depth ratio for D19-P-T beam at service load level ($12\sqrt{f_c'}$)

Beam ID	Number of cracks crossing tendon [1]	Number of cracks crossing tendon in the control [2]	Crack depth ratio = [1]/[2]	Measured crack widths at 2 in. from the bottom surface (in)		
				Minimum	Average	Maximum
D19-P-U	1	1	1.0	0.004	0.004	0.004
D19-P-T	1		1.0	0.003	0.004	0.005

Crack area

In the D19-P (plastic duct) couplet, the estimated crack area was calculated only for the D19-P-T beam (Table 9.19). Due to the presence of the shrinkage crack, the estimated crack area for the D19-P-U beam was omitted and is not presented. This omission is primarily due to the significantly larger change in crack width that was recorded in the existing shrinkage crack under applied flexural load as compared to the newly formed flexural crack.

Table 9.19. Estimated crack area for D19-P-T beam

Beam	Crack ID	Computed crack area (in^2)	Summed 3-crack area $\Sigma(A, B, C)$ (in^2)	Number of cracks crossing tendon	Number of cracks width measured	Estimated crack area (in^2)
D19-P-T	A	0.0274	0.0845	2	3	0.018
	B	0.0385				
	C	0.0185				

However, by comparing the crack data from the treated metal duct beam D19-M-T to the treated plastic duct beam D19-P-T, it was possible to further evaluate potential differences in serviceability behavior associated with corrosion inhibitor impregnation. The D19-M-T and D19-P-T beams had identical tendon sizes, tendon profiles, and grout types, with the only difference being the duct type (metal vs. plastic). The maximum D19-M-T (metal duct) crack width (0.015 in.) from Table 9.15 was larger than the maximum D19-P-T (plastic duct) crack width (0.005 in.) from Table 9.18. Similarly, D19-M-T (metal duct) estimated crack area (0.12 in^2) from Table 9.16 was larger than the D19-P-T (plastic duct) estimated crack area (0.018 in^2) from Table 9.18. From these crack significance measures, it appears that the impregnation of corrosion inhibitor had more influence, at the service load level, on the behavior of the metal duct beam than on the plastic duct beam.

CHAPTER 10 DIGITAL IMAGE CORRELATION (DIC)

10.1 Introduction

As introduced briefly in Chapter 5, this study employed digital image correlation (DIC) to investigate the service-level performance of beams during flexural testing. DIC was used to obtain full-field surface displacements from a sequence of frames captured with a high-speed camera during testing. These images captured the displaced state of the speckled surface on the web of each beam specimen. Spatial derivatives of the measured displacement field were computed in post-processing to obtain the normal (extensional) strain fields, from which crack maps were produced for each specific frame at the service-load level.

The objective of using DIC instrumentation was to obtain crack maps at any instant during flexural testing, particularly at the service-load level, and to more accurately capture crack initiation and growth than was possible through live observation. Three DIC post-processing tools were explored and compared to verify crack occurrence at the same instant across multiple platforms (both open-source and commercial software packages). The commercial tool used in this study was Imetrum Video Gauge (Imetrum 2022), and the open-source tools were DICe (Turner 2015) and Ncorr (Blaber 2015). The goal of this comparison across tools was to evaluate whether open-source tools could serve as an inexpensive and reliable alternative to commercial tools for mapping service-level flexural cracks in large concrete specimens under laboratory conditions.

10.2 Introduction to 2D-DIC

10.2.1 Basic Concepts

Two-dimensional digital image correlation (2D-DIC) is a non-contact, full-field, in-plane tracking method that uses a random, high-contrast speckle pattern on the surface of a specimen undergoing deformation. The technique uses a reference image (undeformed state) and a sequence of deformed images, with capture the frequency selected by the user based on the test. To measure deformation, the reference frame is partitioned into small segments called subsets. Each subset, centered at (x_c, y_c) within the defined region of interest (ROI), typically contains a matte white background with dark speckles forming a unique gray-level texture.

Subset deformation is represented with a first-order (affine) subset shape function that captures translation, small rotation, and in-plane normal/shear within the subset (Sutton et al., 2009):

$$\mathrm{ZNSSD} = \sum_{i}^{\mathrm{subset}} \left[\frac{R_i - \overline{R}}{\sigma_R} - \frac{D_i - \overline{D}}{\sigma_D} \right]^2 \tag{10-1}$$

where,

ZNSSD = zero-normalized sum of squared differences

R_i = intensity of pixel i in the reference subset

$\overline{R}$ = mean intensity over the reference subset

D_i = deformed-image intensity at the deformed mapped (sub-pixel) location

$\overline{D}$ = mean intensity over the mapped subset

σ_R = standard deviation of reference subset

σ_D = standard deviation over the deformed mapped subset.

Subset deformations are represented with first-order shape functions that capture translation, small rotation, and in-plane normal/shear within the subset:

$$u(x,y) = u_t + u_x(x - x_c) + u_y(y - y_c) \quad (10\text{-}2)$$

$$v(x,y) = v_t + v_x(x - x_c) + v_y(y - y_c) \quad (10\text{-}3)$$

where,

u_t, v_t = in-plane translations of the subset center

x, y = coordinates in the reference frame

x_c, y_c = coordinates of the subset center in the reference frame.

u_x, u_y, v_x, v_y = local displacement-gradient components at subset center.

From the computed displacement field, strain fields are obtained over the ROI by differentiating the displacement values between subset centers; the spacing between centers is the "step size" used in the post-processing tools. It is important to note that 2D-DIC assumes the ROI is effectively planar and that the ROI is imaged at near-normal incidence, with negligible out-of-plane motion relative to the measurement resolution.

10.2.2 Setup

The instrumentation setup for 2D-DIC includes a high-resolution camera with a fixed focal-length (prime) lens. A longer focal length is desirable, within practical limits, to reduce perspective distortion for a given field of view. The camera is mounted on a rigid tripod, with the optical axis of the camera set approximately perpendicular to the specimen surface. The camera distance is selected to cover the ROI while maintaining sufficient pixels per physical distance measure (e.g., inches, millimeters) to identify crack locations. Uniform, diffuse, flicker-free lighting should be used to minimize glare and radiometric drift on the speckled surface.

The ROI should be smooth and clean, with a thin matte white base coat applied. Matte black speckles should be randomly distributed and similar in size, with each speckle spanning several pixels for reliable correlation. The speckle layer must adhere well and not flake or tear as the surface deforms, to maintain measurement accuracy throughout the test.

10.2.3 Parameters

Parameter selection in DIC is the next most important step after the setup. Although the robustness of the post-processing tool is critical, appropriate parameter choices are equally important. The key user-selected parameters are:

- Region of Interest (ROI) – The ROI is the boundary within which strain fields are computed. Define the ROI in areas of good speckle quality and lighting. Keep the ROI

boundary at least one subset width inside the physical speckled edge to reduce edge artifacts (i.e., non-physical strain patterns introduced by boundary effects, poor correlation, or image noise) (Fig 79).

- Subset size – The subset side length controls the trade-off between noise robustness and spatial resolution. Larger subsets reduce noise but smooth gradients; smaller subsets improve localization near cracks but can be less stable if texture is weak. As a general rule, select a subset that contains multiple speckles across each side, then tune the subset size based on correlation quality and rigid-body noise checks.
- Step size – The step size (grid spacing between subset centers) sets the field density. Choose a step that is a fraction of the subset size so that neighboring subsets overlap sufficiently to yield smooth fields. For crack-zone refinement, use a smaller step size locally while keeping the same subset size, or reduce the subset size slightly, but only if the speckle statistics still ensure unique texture within each subset.

For consistency across software platforms, the same ROI bounds, subset/step values, correlation criterion (ZNSSD), and affine shape function should be used for a given processing pass.

10.3 Literature Review

DIC is typically employed as a more robust alternative to strain gauges, which are consumable and only provide discrete measurements rather than full-field data. The DIC non-contact technique for measuring displacement and strain fields is common in testing small-scale specimens, which can be prepared and set up with good precision. However, DIC is not yet well established for measuring strain fields in highly heterogeneous and large-scale specimens such as structural concrete elements. A few recent studies using robust cameras, careful set-up, and advanced post-processing tools have shown promise on larger concrete specimens, indicating potential for both laboratory applications or field deployment.

Several studies highlight these developments. Suryanto and Staniforth (2019) applied 2D-DIC with an open-source tool called Ncorr to investigate reinforced concrete beams tested under monotonic, pulsating, and moving loads. The beams were of dimensions 155 mm × 300 mm × 2200 mm, and the region on interest for the DIC covered the shear span. The study used displacement and strain fields to automate crack mapping and track fatigue damage progression, showing the influence of the moving loads on fatigue life. Similarly, Tambusay et al. (2020) demonstrated a low-cost 2D-DIC workflow on a RC beam (100 mm × 150 mm × 2000 mm) and on ECC (engineered cementitious composite) coupons, again using the post-processing tool, Ncorr. The study primarily focused on parameter sensitivity (subset size, step size) and strain-field quality, showing that the DIC-derived crack maps aligned well with physical observations.

In contrast, Huang et al. (2019) employed 3D-DIC to investigate shear deformation in large RC beams with thin webs using four stereo-camera systems and large-area speckle patterns. The region of interest for the DIC measured 600 × 1200 mm, and the 3D-DIC setup enabled full-field displacement and strain measurements in the shear spans. Crack patterns were reconstructed from principal strain fields, and comparisons showed significant deviations from some existing shear-deformation models. Palipana and Proestos (2024) also used 3D-DIC on deep beams (4877 mm × 305 mm × 1105 mm) using three stereo pairs of cameras for full face coverage. With speckles scaled to the large ROI, they produced full-field strain fields, tracked crack patterns, quantified

crack widths and slips along critical shear cracks, and presented a different perspective to investigating shear-transfer mechanisms at the large structural scale.

Together, these studies demonstrate that 2D-DIC is reliable for small- and medium-scale specimens, while 3D-DIC has been employed for larger and more complex members to overcome out-of-plane effects. However, the application of 2D-DIC to full-scale structural concrete members remains uncommon. Moreover, these studies do not address the reproducibility of DIC strain fields when the same setup is processed using different commercial and open-source software tools, which is an important step toward validating DIC as a reliable, inexpensive and lab- or field-deployable instrumentation technique.

10.4 Application in Flexural Testing

10.4.1 Experimental Setup

In the present study, the experimental setup for applying DIC during flexural testing used two Imetrum Flexi cameras (IM-CAM-034) mounted on rigid tripods in front of the constant-moment region. To cover the full region of interest, the speckled surface was imaged as two fields of view that were stitched together after post-processing. Each camera utilized a 1456 × 1088 pixel sensor. Cameras were fitted with C-mount GP-series lenses, allowing flexibility to frame the beam web while maintaining sufficient pixel density for strain-field measurements.

The standard camera and lighting configuration used during the flexural testing of all beams is shown in Figure 10.1.

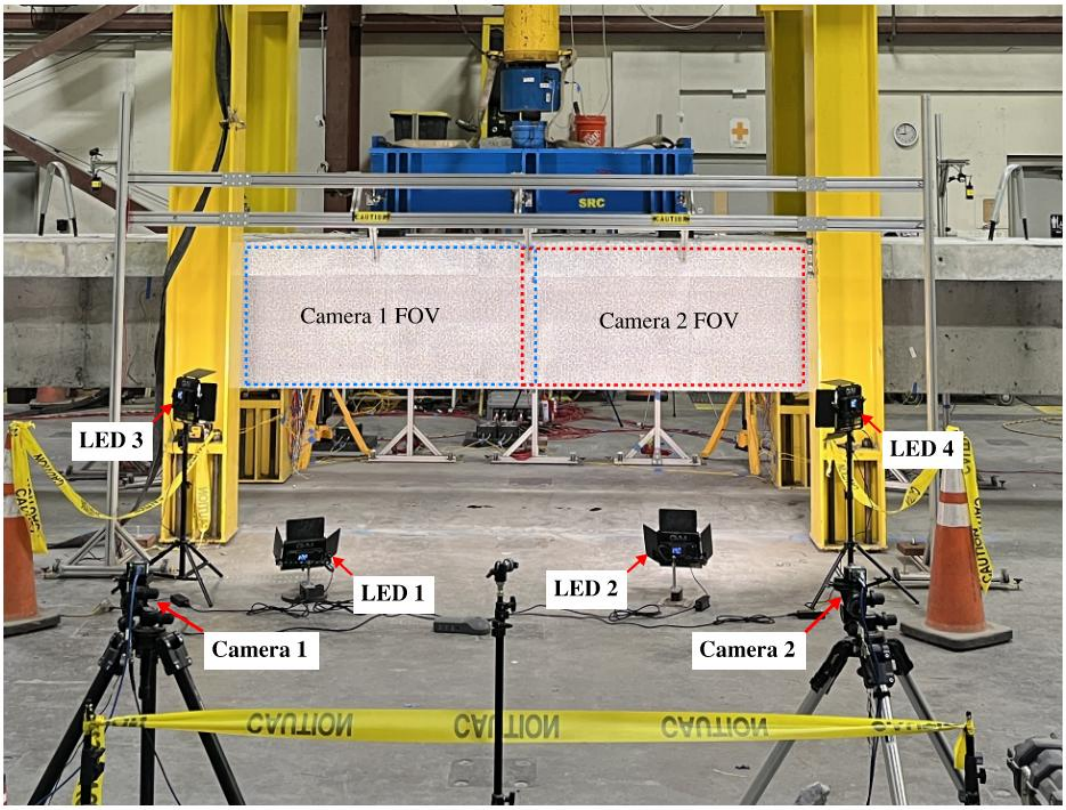

Figure 10.1. DIC instrumentation set-up for flexural testing of S19-M-U beam.

For illumination, continuous, flicker-free LED panel lights were used to provide uniform radiance across the FOV. Two panels were positioned on floor stands 4 ft in front of the speckled surface to act as the primary lights, and two additional panels placed laterally near the reaction frame to act as cross-fill secondary lights. The panels were oriented to minimize shadows and glare on the matte speckle coat, producing a uniform, shadow-free image suitable for DIC.

Speckles were applied over the entire region of interest in the constant-moment zone spanning about 12 ft along the beam length, centered at midspan and over a height equal to the web height of the specimen (see the instrumentation plan in Chapter 5). The web surface was cleaned, smoothed, and painted with a thin matte white base coat. A speckle stencil sheet with holes of random shape, size, and distribution (kept within a narrow range) was placed on the surface and sprayed with matte black paint. This produced a uniform, high-contrast speckle field with a typical speckle diameter of approximately 4 pixels and a center-to-center spacing of about 8 pixels. The paint adhered well and did not flake during testing. A cropped view of the speckled surface from one specimen is shown in Figure 10.2.

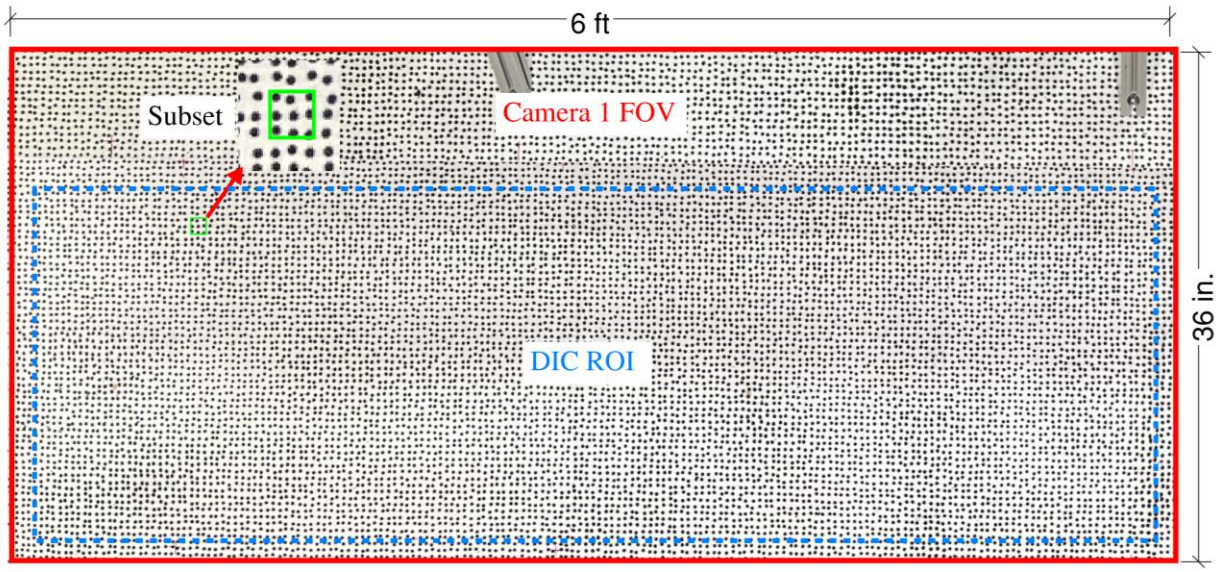

Figure 10.2. Speckled surface region of interest (ROI) from Camera 1 frame in beam specimen S19-M-U.

10.4.2 DIC Parameters

Across all the DIC post-processing tools explored in this study, all other parameters were kept at their default settings except for three basic user-defined inputs. These were the subset size, region of interest, and step size.

- Subset size – 23 pixels (enclosing approximately three features in each direction)
- Region of interest – web surface, leaving a subset-size width at the edges
- Step size – 7 pixels (about one-third of the subset size).

The other post-processing settings were kept at their standard defaults across the DIC platforms. Correlation used the zero-normalized sum of squared differences (ZNSSD) function. Sub-pixel

displacement was determined using bicubic (spline) interpolation. The shape functions were first-order affine, which included translation, rotation, and both normal and shear stretch.

10.5 DIC Crack Map

The DIC crack maps presented here correspond to the normal (extensional) strain field along the beam span direction, computed from the deformation of the speckled surface. For all beam specimens, the web face shown in the DIC crack maps (west face) were opposite to (i.e., spatially-mirrored representations of) the observed crack map (east face) presented in Chapter 9. For convenience in comparing the DIC maps and observed crack maps, the two DIC ROIs for each beam (the north and south ROIs) were horizontally mirrored and then stitched together at midspan.(Fig. 78) This means that if the cracks forming on the DIC crack map (west face of the beam) were identical to those on the observed crack map (east face of the beam), the stitched and mirrored DIC crack map would coincide with the observed crack map when overlaid. DIC crack maps were also plotted at the same stress level of $12\sqrt{f_c'}$ on the bottom surface of the beam as that of the observed crack map.

10.5.1 S06 Beam Specimens

During the flexural testing of the beam specimens, cracks that formed on the east face at each load pause were visually observed and marked. A crack map at the cracking load (corresponding to a concrete tensile stress level of $12\sqrt{f_c'}$) was recreated from the marked cracks and is shown in Figure 10.3. The region of interest (ROI), enclosed with a dashed line in Figure 10.3 and labeled as DIC ROI for each beam specimen, corresponds to the area of the crack map obtained from the DIC on the west face of the beam specimen at the same load level, as shown in Figure 10.4.

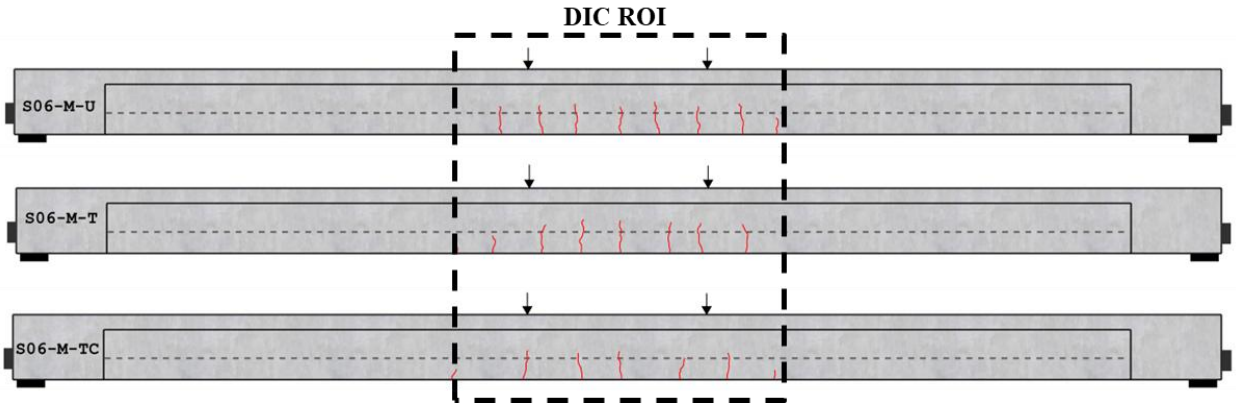

Figure 10.3. Crack map showing the observed cracks on the east face of the S06 beam specimens at the cracking load (concrete tensile stress at $12\sqrt{f_c'}$).

Between the observed crack map (Figure 10.3) and the DIC crack map (Figure 10.4), a comparison was made based on the number of cracks to evaluate whether DIC could produce an accurate crack map at the service load level. In the first two S06 beam specimens (S06-M-U and

S06-M-T), the DIC crack maps obtained from Video Gauge and DICe showed only three cracks compared to seven cracks observed visually. However, the Ncorr crack map was able to detect smaller cracks that the other two DIC tools failed to capture, resulting in a total of five cracks in the DIC crack map. The DIC crack map for the third S06 beam specimen (S06-M-TC) performed relatively better, successfully capturing all five cracks observed in the visual crack map.

Furthermore, when comparing the performance of the three DIC tools, it is apparent that the strain field generated from Ncorr provided clearer crack features and less noise than the maps obtained from Video Gauge or DICe. In addition, Ncorr was able to detect smaller cracks that were not clearly identifiable using the other two DIC tools.

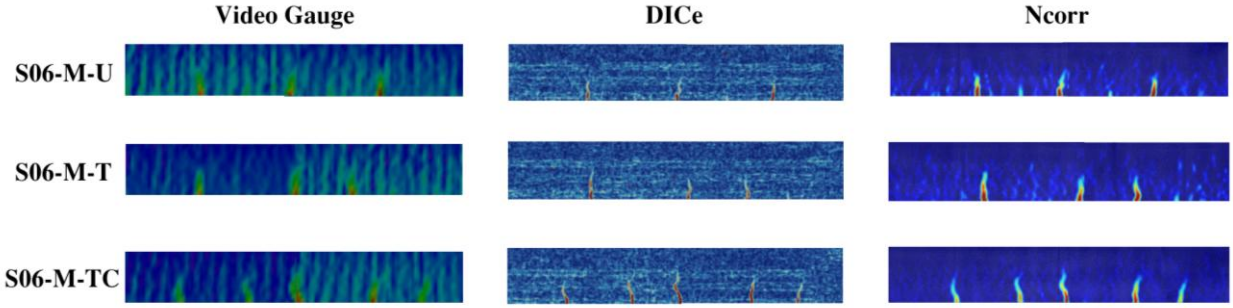

Figure 10.4. DIC normal strain map showing the cracks on the west face of the S06 beam specimens at the cracking load (concrete tensile stress at $12\sqrt{f_c'}$).

10.5.2 S12 Beam Specimens

Similar to the previous beam specimens, cracks that formed on the east face at each load pause were visually observed and marked. A crack map at the cracking load (corresponding to a concrete tensile stress level of $12\sqrt{f_c'}$) was recreated from the marked cracks and is shown in Figure 10.5. The region of interest (ROI), enclosed with a dashed line in Figure 10.5 and labeled as DIC ROI for each beam specimen, corresponds to the area of the crack map obtained from the DIC on the west face of the beam specimen at the same load level, as shown in Figure 10.6.

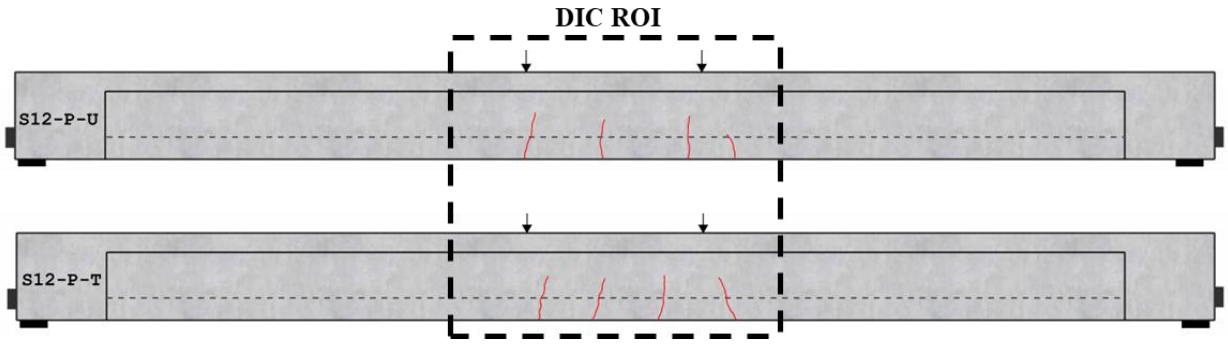

Figure 10.5. Crack map showing the observed cracks on the east face of the S12 beam specimens at the cracking load (concrete tensile stress at $12\sqrt{f_c'}$).

Between the observed crack map (Figure 10.5) and the DIC crack map (Figure 10.6), the DIC crack map of the first beam specimen (S12-M-U) captured all four cracks observed visually on the east face of the beam specimen. However, the DIC crack map for the second beam specimen (S12-M-T) was able to map only two out of the four visually observed cracks. The smaller cracks near the midspan, which developed later during flexural testing, could not be detected by Video Gauge nor DICe. Ncorr, on the other hand, was able to map one of the smaller cracks near the midspan, which appears close to the bottom edge in Figure 10.6.

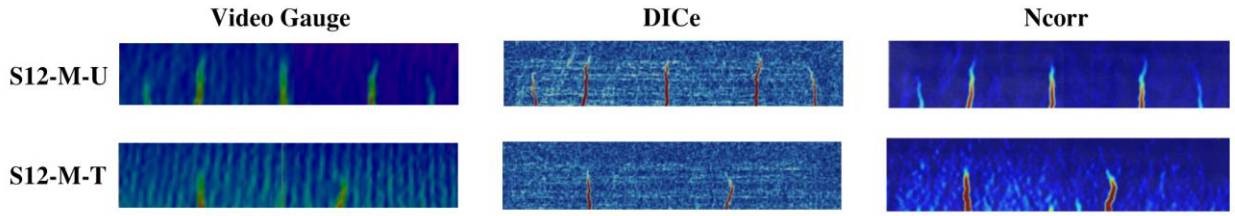

Figure 10.6. DIC normal strain map showing the cracks on the west face of the S12 beam specimens at the cracking load (concrete tensile stress at $12\sqrt{f_c'}$).

10.5.3 S19 Beam Specimens

Following a similar procedure as that used for the previous beam specimen groups, cracks that formed on the east face at each load pause were visually observed and marked. A crack map at the cracking load (corresponding to a tensile concrete stress level of $12\sqrt{f_c'}$) was recreated from the marked cracks and is shown in Figure 10.7. The region of interest (ROI), enclosed with a dashed line in Figure 10.7 and labeled as DIC ROI for each beam specimen, corresponds to the area of the crack map obtained from the DIC on the west face of the beam specimen at the same load level, as shown in Figure 10.8.

Between the observed crack map (Figure 10.7) and the DIC crack map (Figure 10.8), the DIC crack map of the first beam specimen (S19-M-U) captured three out of the four cracks observed visually on the east face of the beam specimen.

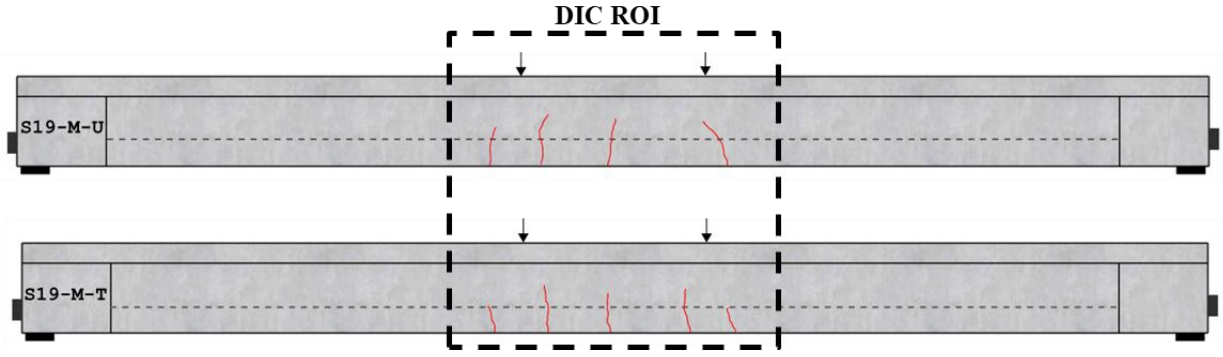

Figure 10.7. Crack map showing the observed cracks on the east face of the S19 beam specimens at the cracking load (concrete tensile stress at $12\sqrt{f_c'}$).

The DIC crack map for the second beam specimen (S19-M-T) was able to map three out of the five cracks observed. In terms of DIC tool performance, Ncorr and DICe produced clearer crack features, particularly for the crack located near the right end of the ROI in the beam specimen S19-M-U, as shown in Figure 10.8.

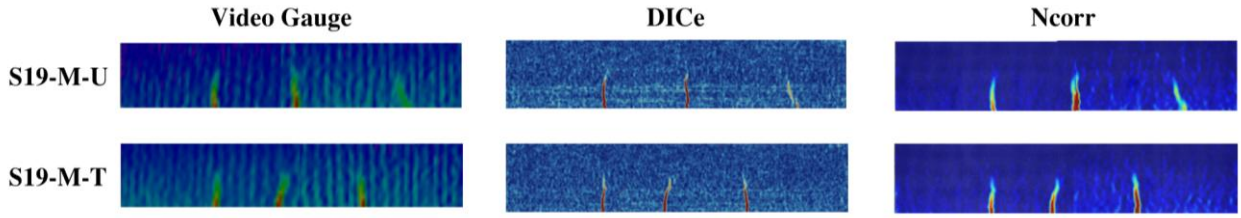

Figure 10.8. DIC normal strain map showing the cracks on the west face of the S19 beam specimens at the cracking load (concrete tensile stress at $12\sqrt{f_c'}$).

10.5.4 D19-M Beam Specimens

The crack maps of the D19-M beam couplet shown in Figure 10.9 represent the cracks that were visually observed, marked, and recreated on the east face of the beam specimens. The area of the beam specimen enclosed within the dashed line labeled DIC ROI represents the region on the beam surface covered by the DIC camera for crack mapping. The cracks marked and recorded during flexural testing, when the concrete tensile stress at the bottom of the beam corresponded to$12\sqrt{f_c'}$ were used for comparison with the crack maps obtained at the same stress level using DIC post-processing tools.

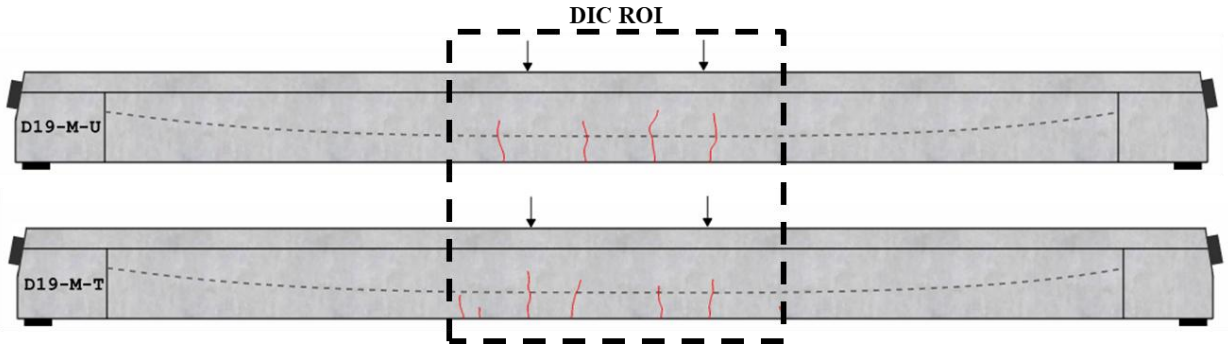

Figure 10.9. Crack map showing the observed cracks on the east face of the D19-M beam specimens at the cracking load (concrete tensile stress at $12\sqrt{f_c'}$).

The DIC crack maps generated using all three tools (Figure 10.10) successfully identified all four cracks that were visually observed and marked on the D19-M-U beam specimen. For the D19-M-T beam specimen, the DIC tools identified the four major cracks that crossed the tendon elevation. However, the smaller cracks located near the edges of the DIC crack map were not consistently detected.

Comparing the performance of the three DIC tools, the crack maps indicate that Ncorr performed better than Video Gauge and DICe in terms of crack definition and background noise for both beam specimens. Although DICe was able to clearly capture crack features, it also

introduced a significant amount of background noise, which reduced the clarity of crack identification. In contrast, Video Gauge performed poorly in both the amount of background noise present and the sharpness with which crack features were defined.

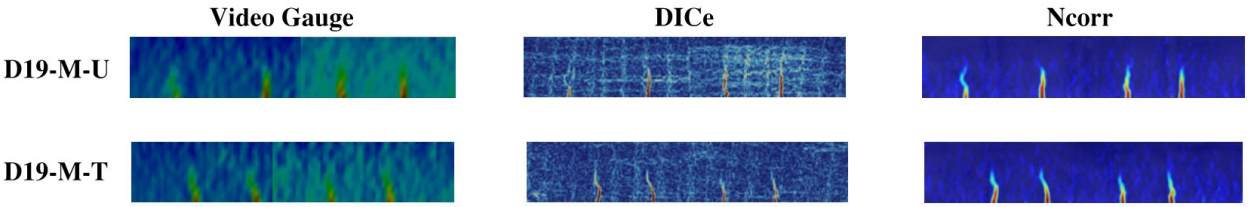

Figure 10.10. DIC normal strain map showing the cracks on the west face of the D19-M beam specimens at the cracking load (concrete tensile stress at $12\sqrt{f_c'}$).

10.5.5 D19-P Beam Specimens

The cracks at the service load level (concrete tensile stress at $12\sqrt{f_c'}$) that were visually observed and marked during flexural testing on the east face of the D19-P beam specimens are shown in Figure 10.11. As discussed in Chapter 9, the D19-P-U beam specimen already had a shrinkage crack on both the east and west faces before the application of flexural load, as shown in Figure 10.11. Upon application of flexural load, this shrinkage crack widened, and two additional flexural cracks formed. All of these cracks fell within the area recorded by the DIC for crack mapping, which is enclosed by the dashed line labeled DIC ROI in Figure 10.11. The D19-P-T beam specimen, on the other hand, had no pre-existing shrinkage crack and exhibited four flexural cracks at the same service load level. These cracks were extended to near or above the tendon elevation.

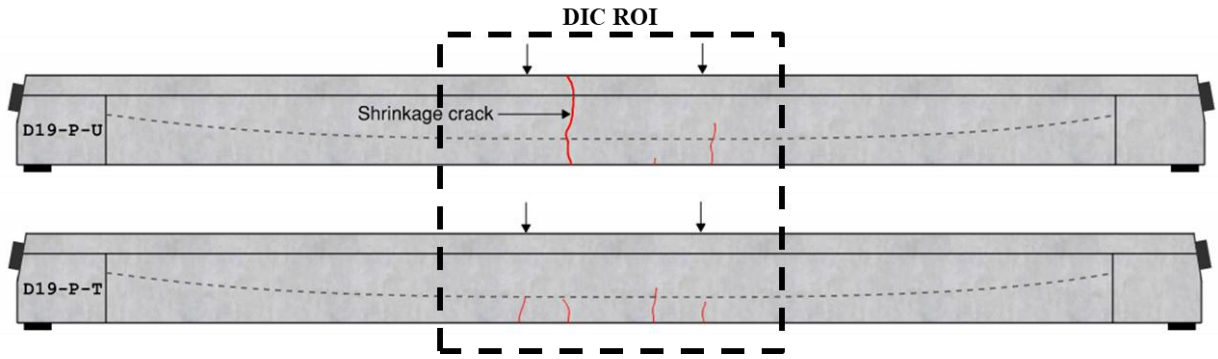

Figure 10.11. Crack map showing the observed cracks on the east face of the D19-P beam specimens at the cracking load (concrete tensile stress at $12\sqrt{f_c'}$).

In the DIC crack maps at the service load level for the D19-P-U beam specimen, the widening of the shrinkage crack due to the applied flexural load can be observed in Figure 10.12. In addition, the two flexural cracks in the same beam specimen were also captured by DIC. Although all three DIC tools detected the opening of the shrinkage crack and the additional flexural crack crossing the tendon elevation, only Ncorr clearly identified the third, smaller flexural crack near midspan. For the D19-P-T beam specimen, Video Gauge and Ncorr clearly identified three of

the four flexural cracks, whereas DICe identified only one flexural crack. Among the three DIC tools, Ncorr again provided the clearest representation of crack features with the least background noise.

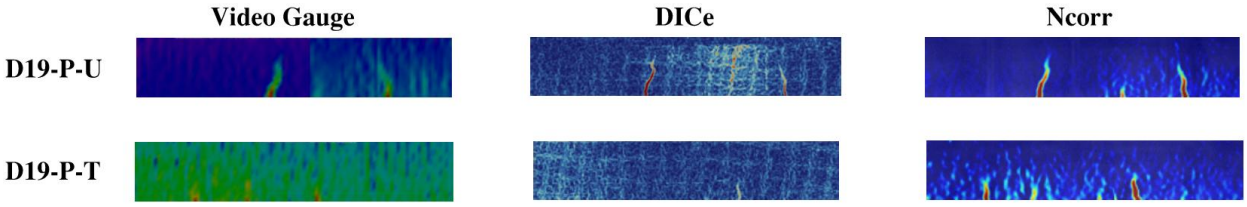

Figure 10.12. DIC normal strain map showing the cracks on the west face of the D19-P beam specimens at the cracking load (concrete tensile stress at $12\sqrt{f_c'}$).

CHAPTER 11 SUMMARY, CONCLUSIONS, AND RECOMMENDATIONS

11.1 Summary and Conclusions

In this experimental study, full-scale bonded post-tensioned beams were constructed, treated (impregnated) with a corrosion inhibitor material, tested in flexure, and compared to untreated counterparts. Flexural testing was carried out to evaluate the performance of the beams in terms of the observed nominal flexural resistance and the extent of cracking at service load level. The objective of this study was to determine, through experimental testing, the influence that impregnation of corrosion inhibitor might have on the performance of bonded post-tensioned concrete bridge girders.

The experimental program consisted of 11 beams (Table 11.1): one triplet (S06, untreated, treated, and cracked-treated) and four couplets (S12, S19, D19M, D19P, untreated and treated). Variables that could influence the bond condition between tendon and grout due to the presence of corrosion inhibitor were incorporated into the design and construction of the specimens. These variables were: tendon size (6-, 12-, and 19-strands), tendon profile (straight, draped), grout type (pre-packaged, plain cement, legacy), duct type (metal, plastic), age of corrosion inhibitor impregnation at the time of testing (0.5 months to 2.5 months), and the beam condition when initially impregnated (uncracked, cracked). All of the newly constructed post-tensioned concrete beams were tested under four-point bending to evaluate both strength level nominal flexural resistance and service level crack behavior. The findings of the study, as summarized below, are known to be valid for the beam construction conditions and corrosion inhibitor impregnation conditions that were tested. Application to other conditions may require additional investigation.

Nominal flexural resistance was defined as the applied actuator load at which the strain at the top surface of the compression flange reached 0.003 in./in, which is the code specified maximum usable compressive strain of concrete. Test results (Table 11.1) indicated that the differences of nominal flexural resistance between untreated (control) beams, and corrosion inhibitor treated (impregnated) beams ranged from 0% (no-detectable change) to a maximum of approximately 2%. It is noted that this narrow range of variation is within the typical limits of experimental test variability.

Table 11.1. Summary of test results

Beam Specimen	Tendon profile	Tendon size (num. of strands)	Duct type	Grout type	Corrosion inhibitor impregnation age (months)	Difference of nominal flexural resistance	Average service-level crack width (in.)
S06-M-U	Straight	6	Metal	Pre-Pkg'd	~0.5	<2%	N/A
S06-M-T	Straight	6	Metal	Pre-Pkg'd			N/A
S06-M-TC	Straight	6	Metal	Pre-Pkg'd			N/A
S12-P-U	Straight	12	Plastic	Pre-Pkg'd	~2	0%	N/A
S12-P-T	Straight	12	Plastic	Pre-Pkg'd			N/A
S19-M-U	Straight	19	Metal	Plain cement	~2.5	<2%	0.012
S19-M-T	Straight	19	Metal	Plain cement			0.012
D19-M-U	Draped	19	Metal	Legacy	~1	<1%	0.007
D19-M-T	Draped	19	Metal	Legacy			0.011
D19-P-U	Draped	19	Plastic	Legacy	~1	<2%	0.004
D19-P-T	Draped	19	Plastic	Legacy			0.004

In regard to service load levels, concrete cracking stress can vary due to inherent variability in tensile strength. For this study, a "cracking load" was defined as the applied load that produced a calculated tensile stress of $12\sqrt{f'_c}$ at the extreme tension fiber, consistent with the ACI 318 definition of a cracked section. This higher stress level was selected (see Section 9.2.2 for additional discussion) to ensure that cracking would be observed while remaining reasonably aligned with AASHTO LRFD serviceability limits, which typically allow $6\sqrt{f'_c}$ under Service III conditions. Crack maps at the cracking load level of $12\sqrt{f'_c}$ indicated negligible differences in crack patterns, with consistent spacing and frequency observed between corresponding untreated and treated specimens within each beam group (S06, S12, S19, D19M, D19P). During testing of the 19-strand beam groups (S19, D19M, D19P), crack width measurements were performed. For the S19 and D19P beam groups, the average measured crack widths were unaffected by treatment with corrosion inhibitor, (Table 11.1), whereas for the D19M beams, an increase of average crack width of approximately 50% was observed. Crack depth ratios were computed for all beam groups to evaluate the relative quantity of tensile cracks that crossed the tendon elevation - a condition that could lead to potential tendon exposure to the environment. In four of the five beam groups tested (S06, S12, D19M, D19P) the treated beams had equal or less severe crack depth ratio values than the corresponding control beams. In the S19 group, the treated beam had a crack depth ratio 25% larger than the control beam. Finally, for the S19 and D19M beam groups, an additional crack severity analysis was carried out by computing estimated crack areas from measured crack widths. Across these two beam groups, the average increase in estimated crack area associated with treatment with corrosion inhibitor was approximately 17.5%.

Digital image correlation (DIC) was employed during experimental testing to produce crack maps at the service load level and to compare these crack maps to visually observed and marked crack maps. Three different DIC software tools were evaluated: two open-source codes (DICe and Ncorr), and one commercial code (Imetrum Video Gauge). Overall, all three DIC packages performed reasonably well in mapping cracks at the service load level, although some smaller cracks were not detected by DIC. More than 50% of the visually observed and marked cracks were indicated in the corresponding DIC-generated crack maps. The two open-source DIC tools that were evaluated (DICe and Ncorr), performed consistently similar to, and in some cases better than, the commercial tool (Imetrum Video Gauge) in identifying smaller cracks. Ncorr, in particular, was able to detect smaller cracks and produce crack maps of higher quality (with fewer artifacts) than the other packages.

11.2 Recommendations for Future Research

The following recommendations are offered for future research efforts that could extend the range of applicability of the findings presented in this study.

- Extended duration of grout exposure to corrosion inhibitor

  As noted earlier in this report, prior research conducted by the FDOT SMO on grout cubes that were subjected to accelerated curing indicated that the effects of corrosion inhibitor on grout properties were generally observed to occur within 1 week (or less) of exposure. Based on those findings, and to provide a conservative amount of exposure time, the beams tested in the present study were exposed to corrosion inhibitor for periods of time ranging from approximately 0.5 to 2.5 months. Nevertheless, future investigation should be

considered wherein grouted beams are exposed to corrosion inhibitor for even longer periods of time. After impregnation, the beams could be exposed to outdoor temperature variations and moisture conditions (representative of in-service girders) for a year or more. Optionally, methods for imposing accelerated curing of grout inside the beams could be explored so as to simulate grout maturity conditions in older bridge structures. The design, materials, and construction methodology used for such beams should remain as consistent as possible with the beams tested in this study to allow for direct comparison.

- Influence of anchorage deterioration

  Future research should include testing of grouted, bonded, and impregnated beams wherein deterioration of the post-tensioning anchorages is simulated.

- Methods of evaluating potential interactions between grout and corrosion inhibitor

  Additional research on potential material level interactions between corrosion-inhibiting fluids and cured grout is recommended. This could include further investigation of grout cube preparation protocols, including curing and impregnation protocols that produce saturated conditions within the tested cubes, as well as further material characterization.

- Impregnation and testing of beams recovered from a bridge replacement project

  If a future bridge replacement project within the state offers an opportunity to extract and recover intact post-tensioned and grouted concrete beams, it is recommended that such beams be brought to the FDOT SRC, impregnated with corrosion inhibitor, and tested. Such beams would have been exposed to service conditions—cycles of loading, temperature, and moisture—for multiple decades. Testing such beams would provide valuable insights into the effects of corrosion inhibitor on in-situ bridge beams.

- Crack measurement with digital image correlation (DIC)

  The scope of this study included an assessment of digital image correlation (DIC) as a non-contact method for identifying cracks in concrete beams at service level loading, as well as an assessment of the relative performance of commonly available DIC software tools. Future investigation should extend this work toward the goal of quantifying crack lengths and crack widths using DIC techniques.

REFERENCES

AASHTO. 2020. AASHTO LRFD Bridge Design Specifications (8th ed.). American Association of State Highway and Transportation Officials, Washington, DC.

ACI (American Concrete Institute). 2022. Building Code Requirements for Structural Concrete (ACI 318-19) and Commentary (ACI 318R-19). American Concrete Institute, Farmington Hills, MI.

ACI Committee 423. 2016. Guide to Estimating Prestressing Losses (ACI 423.10-16). American Concrete Institute, Farmington Hills, MI.

Alvarez, G. A., and Hamilton, H. R. 2002. "Post-tensioning grout bleed, duct, and anchorage protection test." FDOT Research Rep. No. BC-34 RPWO #73, Univ. of Florida, Gainesville, FL.

American Petroleum Institute (API). 2019. Recommended Practice for Field Testing Water-Based Drilling Fluids (API RP 13B-1, 5th ed.). American Petroleum Institute, Washington, DC.

ASTM International. 2017. Standard Specification for Low-Relaxation, Seven-Wire Steel Strand for Prestressed Concrete (ASTM A416/A416M-17). ASTM International, West Conshohocken, PA.

ASTM International. 2021. Standard Test Method for Compressive Strength of Grouts for Preplaced-Aggregate Concrete in the Laboratory (ASTM C942/C942M-21). ASTM International, West Conshohocken, PA.

ASTM International. 2022. Standard Test Method for Flow of Grout for Preplaced-Aggregate Concrete (Flow Cone Method) (ASTM C939-22). ASTM International, West Conshohocken, PA.

ASTM International. 2023. Standard Test Method for Evaluating Bond Strength for 0.600-in. [15.24 mm] Diameter Seven-Wire Steel Strand, Grade 270 [1860], Used in Prestressed Ground Anchors (ASTM A981/A981M-23). ASTM International, West Conshohocken, PA.

ASTM International. 2024. Standard Test Method for Compressive Strength of Hydraulic Cement Mortars (Using 2-in. or [50 mm] Cube Specimens) (ASTM C109/C109M-24). ASTM International, West Conshohocken, PA.

Ayub, M. 2019. "Investigation of March 15, 2018, pedestrian bridge collapse at Florida International University, Miami, FL." Rep., U.S. Dept. of Labor, Directorate of Construction, Washington, DC.

Azizinamini, A. 2018. "Development of quality assurance and quality control system for post-tensioned segmental bridges in Florida: Case of Ringling Bridge—Phase II." FDOT Research Rep. No. BDV29-977-34, Florida International Univ., Miami, FL.

Blaber, J., Adair, B., and Antoniou, A. 2015. “Ncorr: Open-source 2D digital image correlation MATLAB software.” Experimental Mechanics, 55(6), 1105–1122.

Brenkus, N. R., Hamilton, H. R., and Potter, W. A. 2017. “Flexural strength and hinge behavior of internally post-tensioned members with mixed bonded and unbonded tendons.” PTI Journal, 13(2).

Collins, M. P., and Mitchell, D. 1991. Prestressed Concrete Structures. Prentice Hall, Englewood Cliffs, NJ.

Consolazio, G. R., Fung, J., and Ansley, M. 2004. “M–φ–P diagrams for concrete sections under biaxial flexure and axial compression.” ACI Structural Journal, 101(1), 114–123.

Consolazio, G. R., and Woolf, E. 2007. Advanced Algorithms for Computing Moment–Curvature Relationships for Concrete Sections. Structures Research Rep. No. 2007/65163, Univ. of Florida, Gainesville, FL.

Corven, J. A. 2001. “Mid-Bay Bridge post-tensioning evaluation.” FDOT Rep., Corven Engineering, Inc., Tallahassee, FL.

Dolan, C. W., and Hamilton, H. R. 2019. Prestressed Concrete. Springer Nature, Cham, Switzerland.

FDOT (Florida Department of Transportation). 2013. Post-Tensioning Vertical Profiles, Index 21801, Tallahassee, FL.

FDOT (Florida Department of Transportation). 2023a. Standard Specifications for Road and Bridge Construction. Tallahassee, FL.

FDOT (Florida Department of Transportation). 2023b. Structures Design Guidelines (SDG), Structures Manual, Vol. 1. Tallahassee, FL.

FDOT (Florida Department of Transportation). 2023c. Bridge Load Rating Manual, Topic No. 850-010-035. Tallahassee, FL.

FDOT (Florida Department of Transportation). 2024. Standard Specifications for Road and Bridge Construction, Section 462: Post-Tensioning. Tallahassee, FL.

FHWA (Federal Highway Administration). 1993. Performance of Grouts for Post-Tensioned Bridge Structures. FHWA-RD-92-095, U.S. Dept. of Transportation, Washington, DC.

FHWA (Federal Highway Administration). 2003. Post-Tensioning Tendon Installation and Grouting Manual. U.S. Dept. of Transportation, Washington, DC.

FHWA (Federal Highway Administration). 2013. Post-Tensioning Tendon Installation and Grouting Manual. U.S. Dept. of Transportation, Washington, DC.

Gerber, L. L., and Burns, N. H. 1971. “Ultimate strength tests of post-tensioned flat plates.” PCI Journal, 16(6), 40–58.

Huang, T., Li, J., Sun, Q., and Xu, S. 2019. “Experimental shear deformation of reinforced concrete beams with thin webs using three-dimensional digital image correlation.” Engineering Structures, 197, 109393.

Imetrum. 2022. Video Gauge User Manual, Version 6.0.5. Imetrum Limited, Bristol, U.K.

Laco, J., and Borzovič, V. 2017. “Experimental investigation of prestressing strand bond on behavior of concrete members.” ACI Structural Journal, 114(1), 15–24.

Laco, J. 2018. “Primary mechanism behavior of post-tensioned 7-wire strand during load exposition.” Journal of Bridge Engineering (ASCE), 23(5).

Lankard, D. R., Thompson, N., Sprinkel, M. M., and Virmani, Y. P. 1993. “Grouts for bonded post-tensioned concrete construction: Protecting prestressing steel from corrosion.” ACI Materials Journal, 90(5), 449–457.

Lüthi, T., Diephuis, J., Icaza, J. J., Breen, E., and Kerger, M. E. 2004. “Factors affecting friction losses in multi-strand post-tensioning tendons including the effect of emulsifiable oils.” TxDOT–FHWA Technical Rep., Univ. of Texas at Austin, Austin, TX.

MacGregor, J. G., and Wight, J. K. 2011. Reinforced Concrete: Mechanics and Design (6th ed.). Pearson, Upper Saddle River, NJ.

Palipana, M. P. C., and Proestos, G. T. 2024. “Behavior of large-scale reinforced concrete deep beams using full field-of-view digital image correlation.” ACI Structural Journal, 121(2), 41–52.

PCI (Precast/Prestressed Concrete Institute). 2010. PCI Design Handbook: Precast and Prestressed Concrete (MNL-120-10) (7th ed.). PCI, Chicago, IL.

Powers, R. G., Sagüés, A. A., and Virmani, Y. P. 2002. “Corrosion of post-tensioned tendons in Florida bridges.” In Proc., 17th U.S.–Japan Bridge Engineering Workshop, U.S. Dept. of Transportation, Washington, DC, 879–892.

Sagüés, A. A., Eason, T., Cotrim, C., and Lopez-Sabando, J. 2008. “Validation of practical procedure for vibrational evaluation of tendons.” FDOT Research Rep. No. BC 353-44, Univ. of South Florida, Tampa, FL.

Silnutzer, J., Mraied, H., Mullins, G., Sagüés, A. A., and Alexander, C. L. 2020. “Evaluation of corrosion-inhibiting materials applied by impregnation (pressure injection) methods to prevent corrosion of post-tensioned tendons.” FDOT Research Rep. No. BDV25-977-35, Univ. of South Florida, Tampa, FL.

Sutton, M. A., Orteu, J.-J., and Schreier, H. W. 2009. Image Correlation for Shape, Motion and Deformation Measurements: Basic Concepts, Theory and Applications. Springer, New York.

Tambusay, F., Suryanto, B., and Suprobo, P. 2020. “Application of 2D digital image correlation for automated crack mapping of reinforced concrete and ECC specimens.” Civil Engineering Dimension, 22(2), 125–133.

Turner, D. Z. 2015. Digital Image Correlation Engine (DICe) Reference Manual. Sandia Report No. SAND2015-10606 O, Sandia National Laboratories, Albuquerque, NM.

Vector Corrosion Technologies. 2021. “Post-Tech PTI impregnation system project reference list.” Vector Corrosion Technologies, Winnipeg, MB, Canada.

Whitmore, D., and Arnesen, T. 2018. “Evaluation and mitigation of post-tensioned corrosion.” In Forensic Engineering 2018: Proc., Eighth Congress on Forensic Engineering, ASCE, Reston, VA, 879–892.

APPENDIX A
BEAM SPECIMEN FABRICATION DRAWINGS

Fabrication drawings for the beam specimens are provided on the following pages.

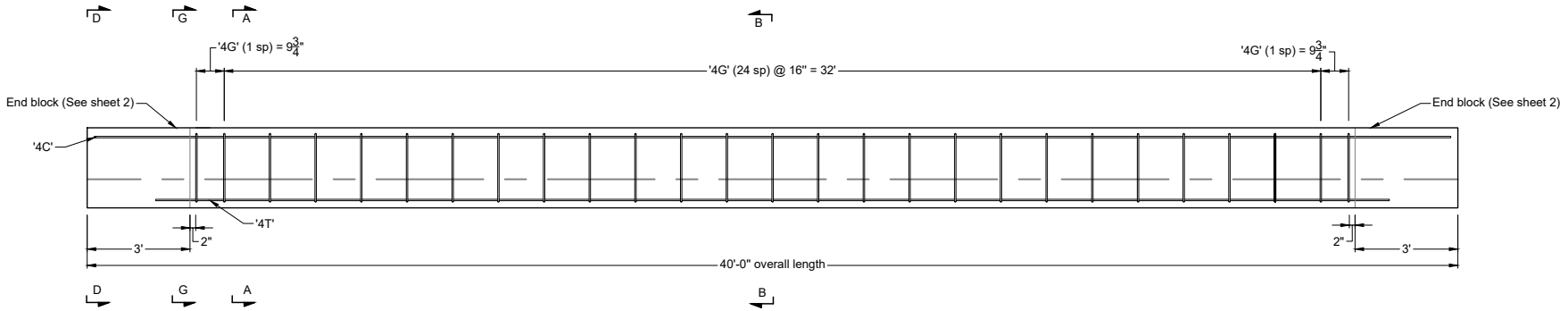

Elevation: S06

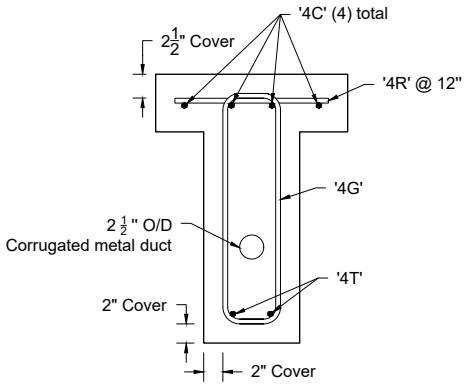

Cross Section A - A

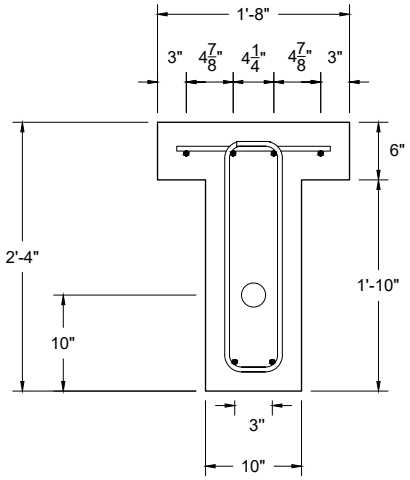

Cross Section B - B

FDOT Research
Bond performance of post-tensioning tendons with corrosion Inhibitor
BED31-977-07

University of Florida
Dept. of Civil and Coastal Engineering

Task 2:Design Drawings
Specimen S06
Sheet 1 of 15

1

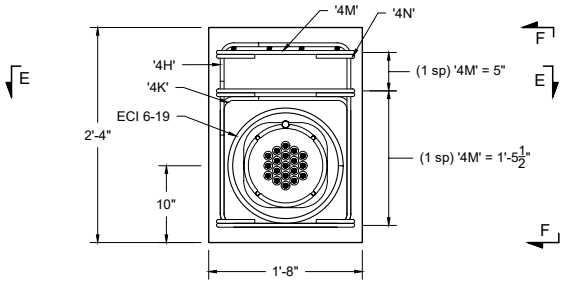

Section D - D
Refer to sheet 1

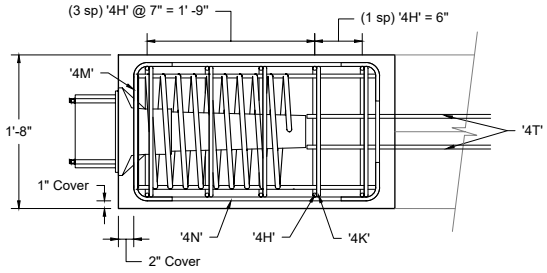

Section E - E

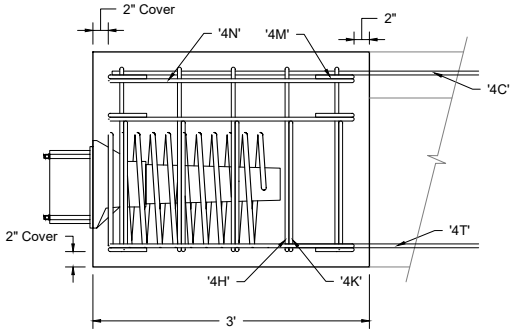

Section F - F

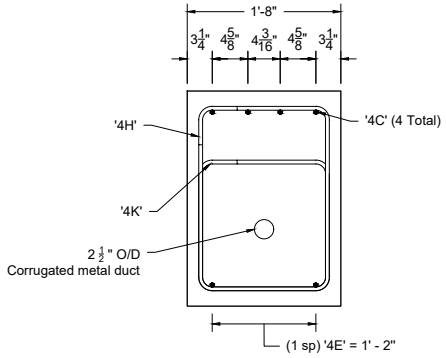

Section G - G
Refer to sheet 1

FDOT Research
Bond performance of post-tensioning tendons with corrosion inhibitor
BED31-977-07

University of Florida
Dept. of Civil and Coastal Engineering

Task 2: Design Drawings
Specimen S06: End Block Details
Sheet 2 of 15

2

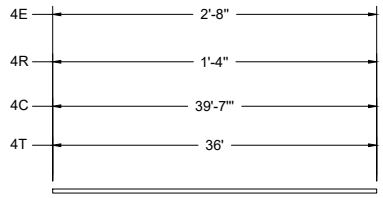

4R, 4C, 4T

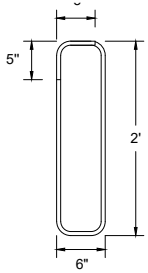

4G

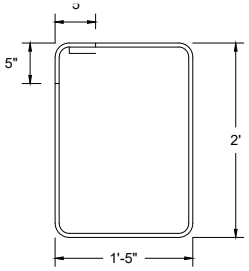

4H

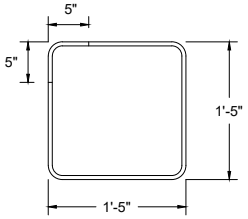

4K

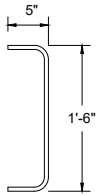

4M

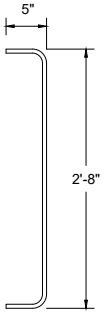

4N

Bill of material: S06 beam				
Piece	**Size**	**Qty.**	**Length**	**Notes**
4C	#4	4	39' -7''	
4T	#4	2	36'	
4R	#4	35	1' -4''	
4G	#4	27	5'-3''	
4H	#4	10	7' -1''	
4K	#4	10	5' -10''	
4M	#4	12	2' -1''	
4N	#4	12	3' -3''	
4E	#4	4	2'-8''	

FDOT Research
Bond performance of post-tensioning tendons with corrosion Inhibitor
BED31-977-07

University of Florida
Dept. of Civil and Coastal Engineering

Task 2: Design Drawings
Specimen S06: Rebar Schedule & Handling Details
Sheet 3 of 15

3

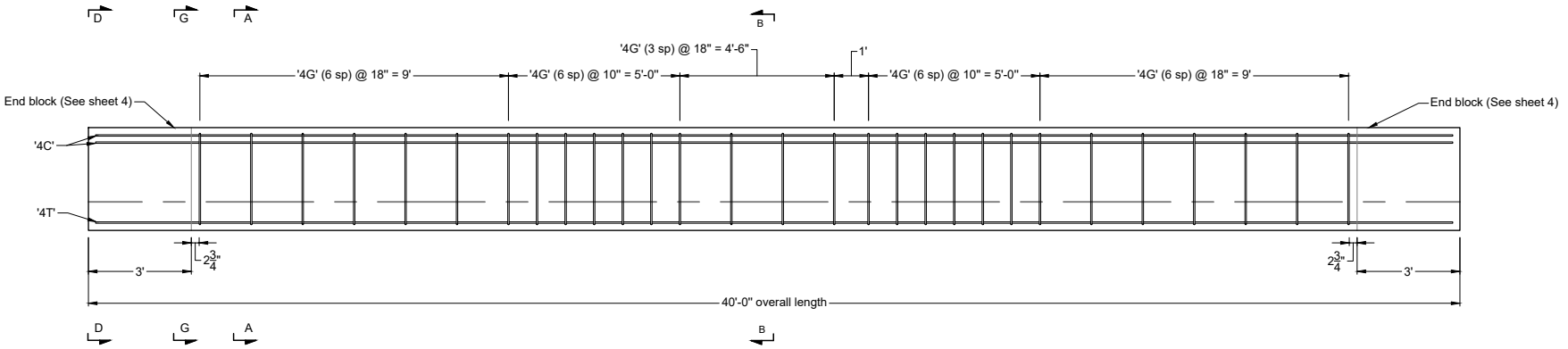

Elevation: S12

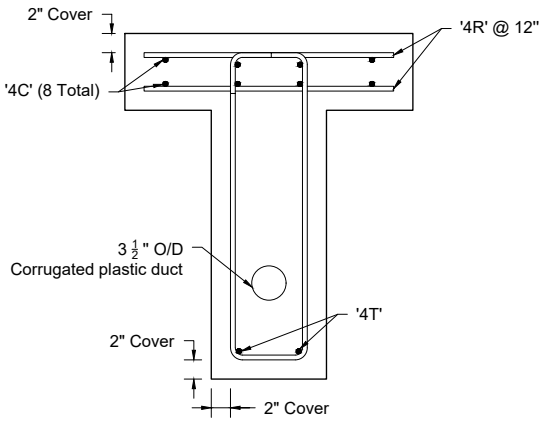

Cross Section A - A

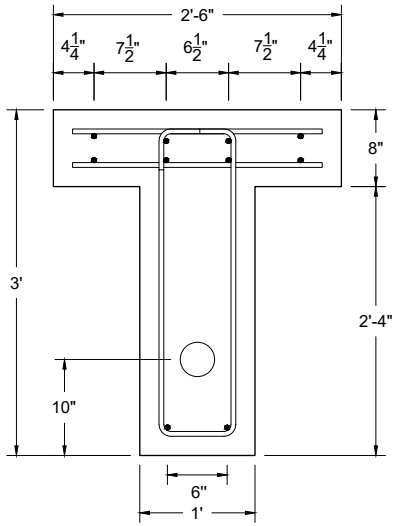

Cross Section B - B

FDOT Research
Bond performance of post-tensioning tendons with corrosion inhibitor
BED31-977-07

University of Florida
Dept. of Civil and Coastal Engineering

Task 2: Design Drawings
Specimen S12
Sheet 4 of 15

4

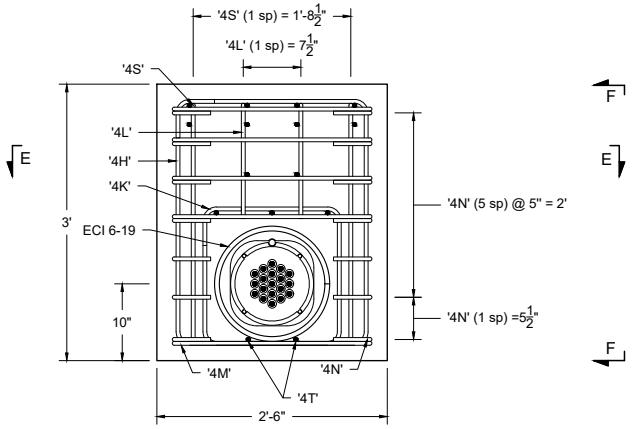

Section D - D
Refer to sheet 4

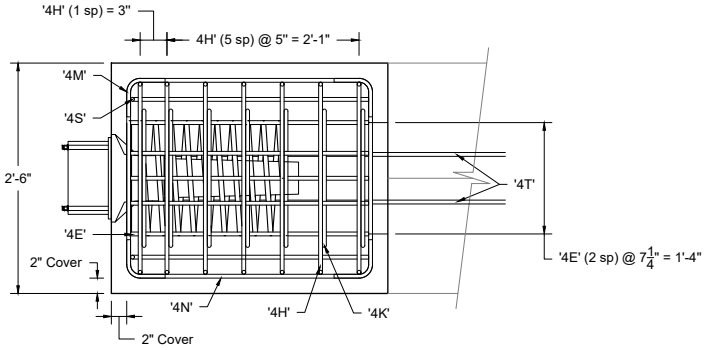

Section E - E

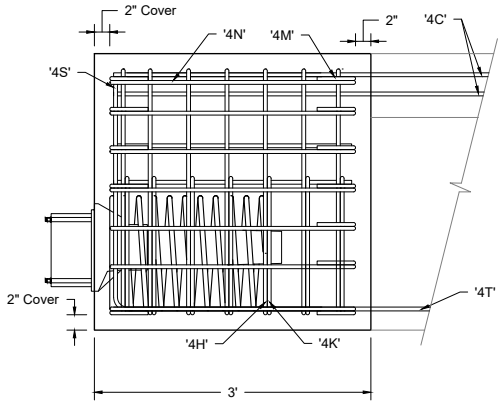

Section F - F

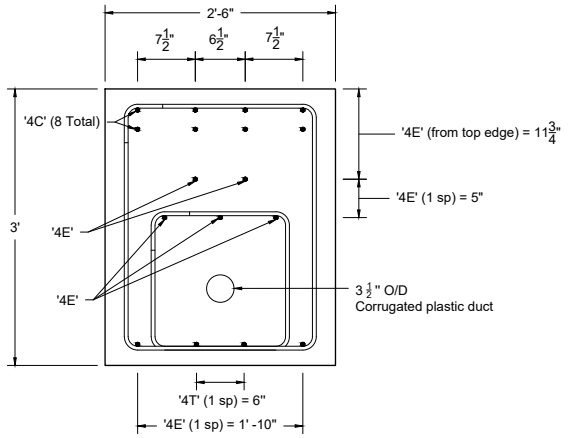

Section G - G
Refer to sheet 4

FDOT Research
Bond performance of post-tensioning tendons with corrosion Inhibitor
BED31-977-07

University of Florida
Dept. of Civil and Coastal Engineering

Task 2: Design Drawings
Specimen S12: End Block Details
Sheet 5 of 15

5

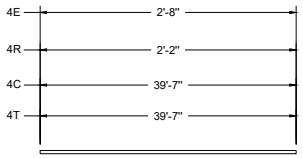

4E, 4R, 4C, 4T

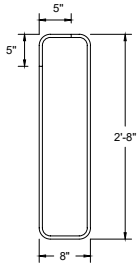

4G

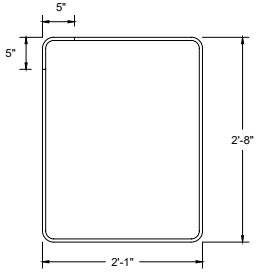

4H

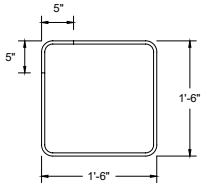

4K

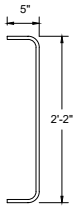

4M

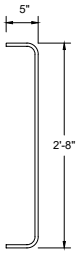

4N

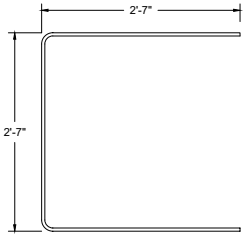

4S

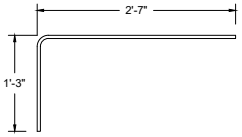

4L

Bill of material: S12 beam				
Piece	Size	Qty.	Length	Notes
4C	#4	8	39' -7"	
4T	#4	2	39' -7"	
4R	#4	35	2' -2"	
4E	#4	14	2' -8"	
4G	#4	29	6'-10"	
4H	#4	14	9'-8"	
4K	#4	14	6'-2"	
4M	#4	24	2'-9"	
4N	#4	28	3'-3"	
4S	#4	4	7'-6"	
4L	#4	4	3'-9"	

FDOT Research
Bond performance of post-tensioning tendons with corrosion Inhibitor
BED31-977-07

University of Florida
Dept. of Civil and Coastal Engineering

Task 2: Design Drawings
Specimen S12: Rebar Schedule
Sheet 6 of 15

6

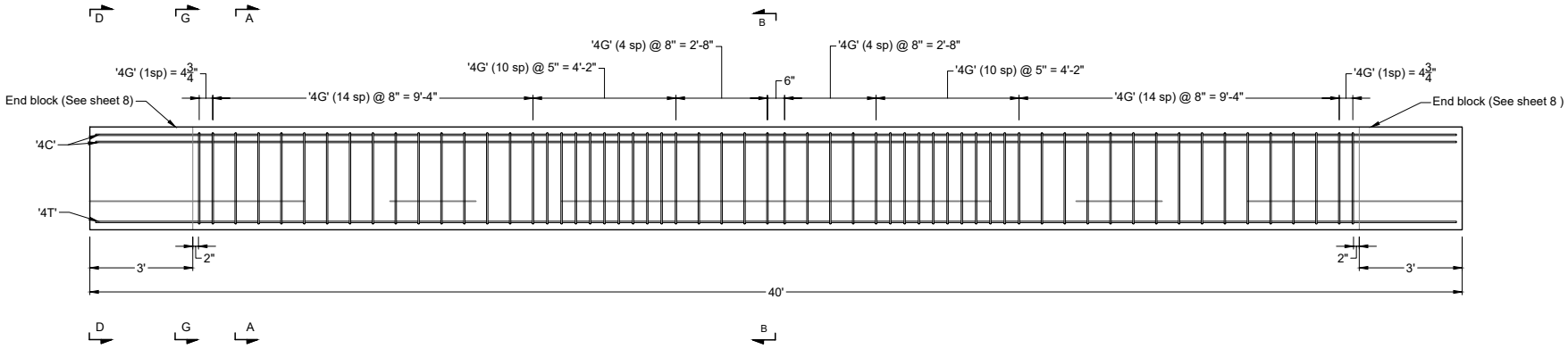

Elevation: S19

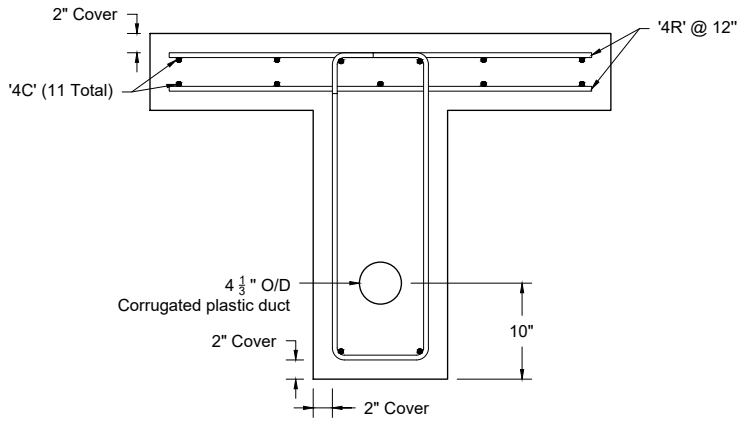

Cross Section A - A

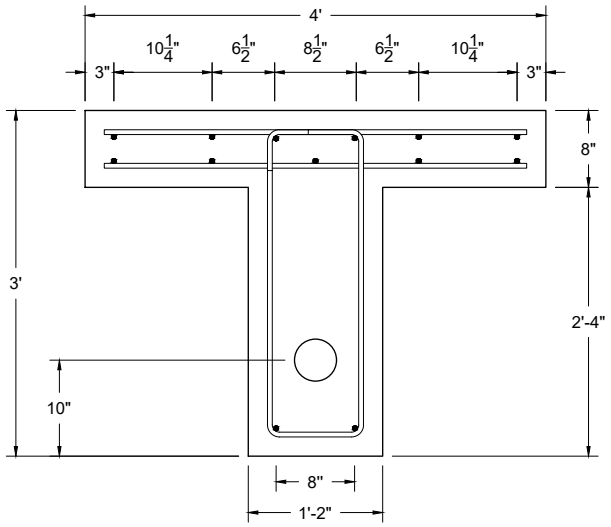

Cross Section B - B

FDOT Research
Bond performance of post-tensioning tendons with corrosion inhibitor
BED31-977-07

University of Florida
Dept. of Civil and Coastal Engineering

Task 2: Design Drawings
Specimen S19
Sheet 7 of 15

7

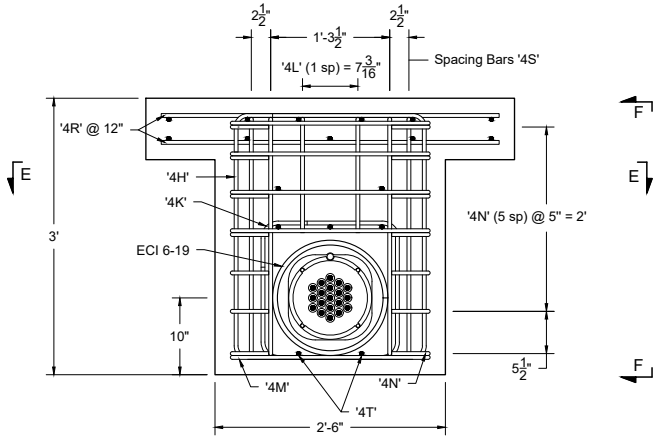

Section D - D
Refer to sheet 4

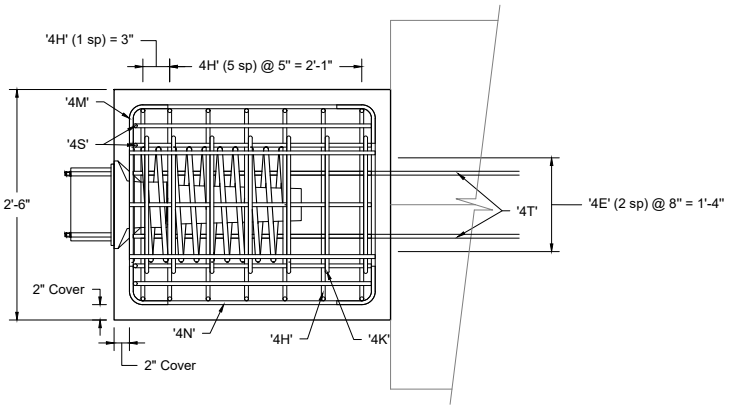

Section E - E

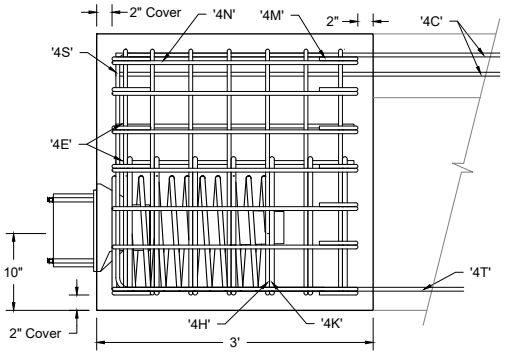

Section F - F

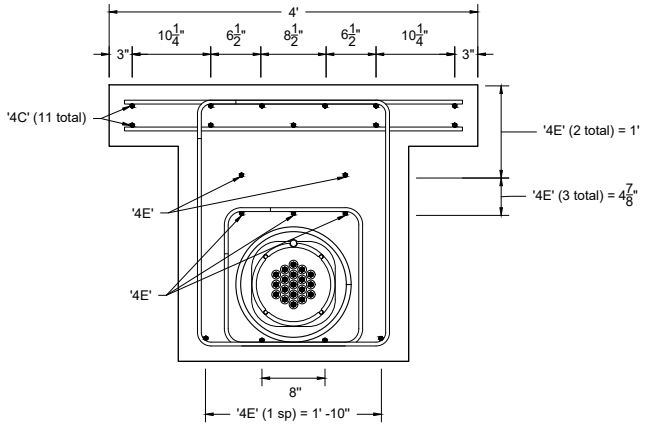

Section G - G
Refer to sheet 7

FDOT Research
Bond performance of post-tensioning tendons with corrosion Inhibitor
BED31-977-07

University of Florida
Dept. of Civil and Coastal Engineering

Task 2: Design Drawings
Specimen S19: End Block Details
Sheet 8 of 15

8

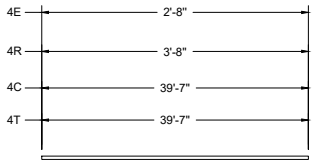

4E, 4R, 4C, 4T

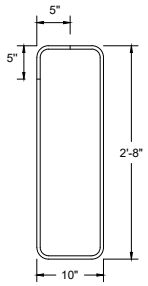

4G

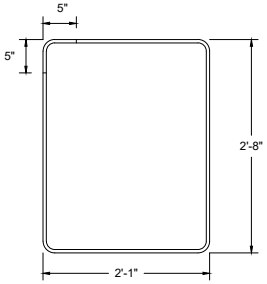

4H

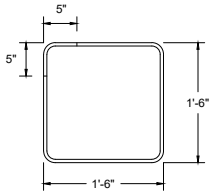

4K

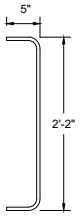

4M

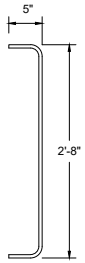

4N

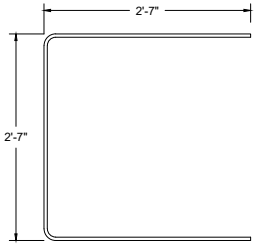

4S

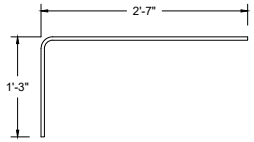

4L

Bill of material: S19 beam				
Piece	Size	Qty.	Length	Notes
4C	#4	11	39' -7"	
4T	#4	2	39' -7"	
4R	#4	40	3'-8"	
4E	#4	14	2' -8"	
4G	#4	60	7'-2"	
4H	#4	14	9'-8"	
4K	#4	14	6'-2"	
4M	#4	24	2'-9"	
4N	#4	28	3'-3"	
4S	#4	8	7'-6"	
4L	#4	4	3'-9"	

FDOT Research
Bond performance of post-tensioning tendons with corrosion Inhibitor
BED31-977-07

University of Florida
Dept. of Civil and Coastal Engineering

Task 2: Design Drawings
Specimen S19: Rebar Schedule
Sheet 9 of 15

9

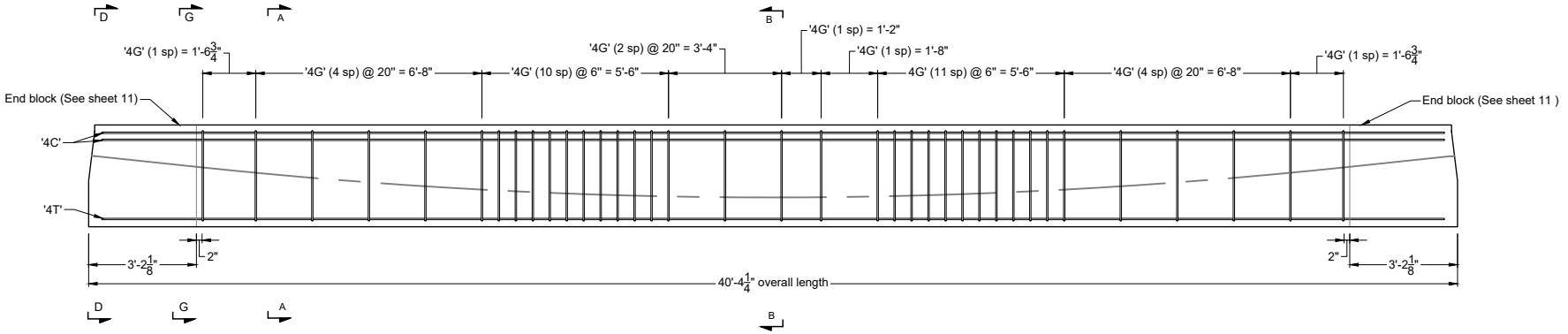

Elevation: D19

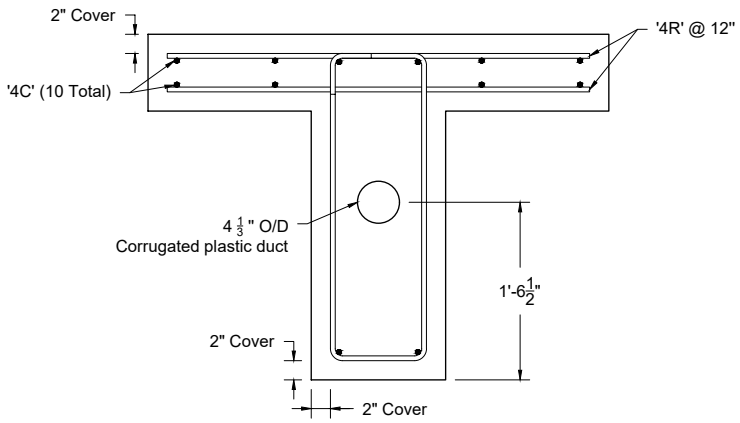

Cross Section A - A

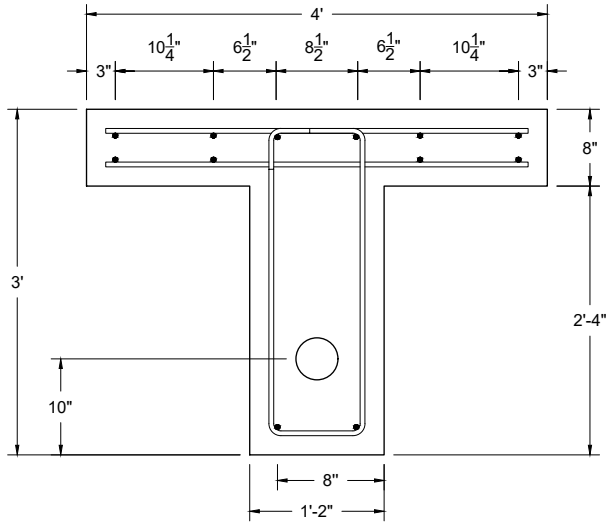

Cross Section B - B

FDOT Research
Bond performance of post-tensioning tendons with corrosion inhibitor
BED31-977-07

University of Florida
Dept. of Civil and Coastal Engineering

Task 2: Design Drawings
Specimen D19M
Sheet 10 of 15

10

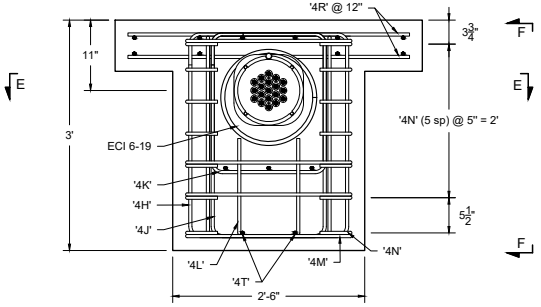

Section D - D
Refer to sheet 4

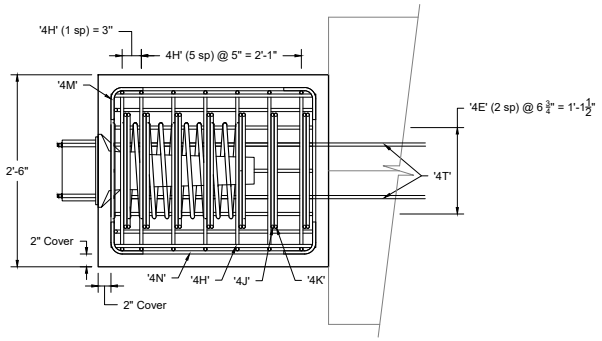

Section E - E

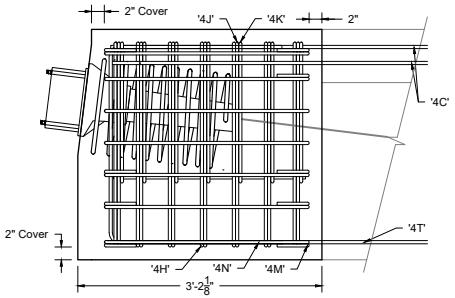

Section F - F

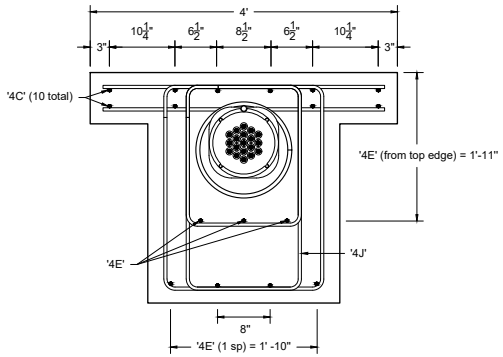

Section G - G
Refer to sheet 10

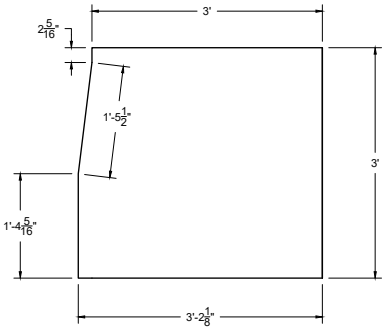

End Block Dimensions

FDOT Research
Bond performance of post-tensioning tendons with corrosion Inhibitor
BED31-977-07

University of Florida
Dept. of Civil and Coastal Engineering

Task 2: Design Drawings
Specimen D19MI: End Block Details
Sheet 11 of 15

11

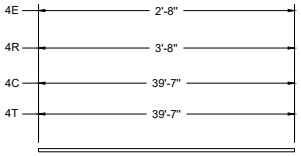

4E, 4R, 4C, 4T

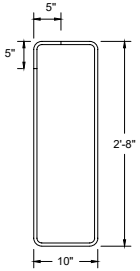

4G

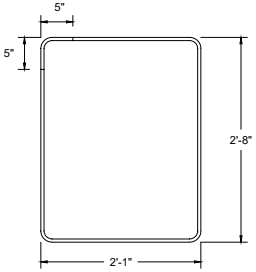

4H

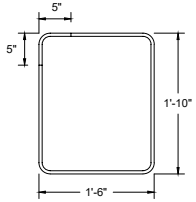

4K

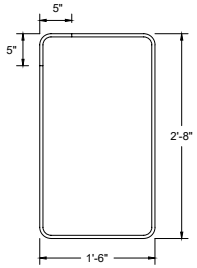

4J

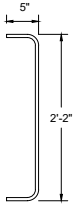

4M

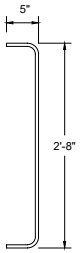

4N

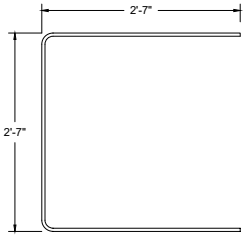

4S

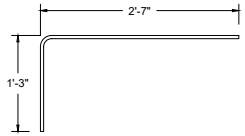

4L

Bill of material: D19 beam				
Piece	Size	Qty.	Length	Notes
4C	#4	10	39' -7"	
4T	#4	2	39' -7"	
4R	#4	40	3'-8"	
4E	#4	10	2' -8"	
4G	#4	37	7'-2"	
4H	#4	14	9'-8"	
4J	#4	14	8'-6"	
4K	#4	14	6'-10"	
4M	#4	18	2'-9"	
4N	#4	28	3'-3"	
4S	#4	4	7'-6"	
4L	#4	4	3'-9"	

FDOT Research
Bond performance of post-tensioning tendons with corrosion inhibitor
BED31-977-07

University of Florida
Dept. of Civil and Coastal Engineering

Task 2: Design Drawings
Specimen D19M: Rebar Schedule
Sheet 12 of 15

12

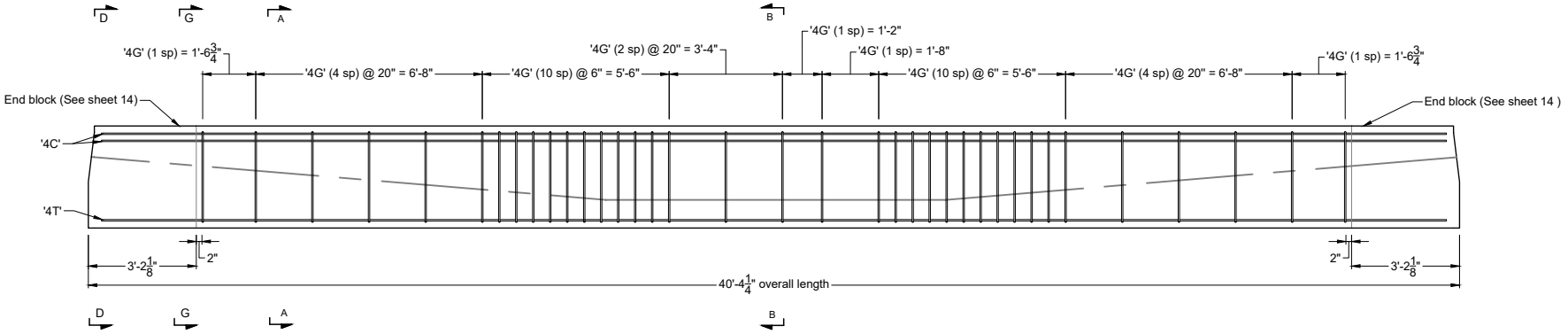

Elevation: H19

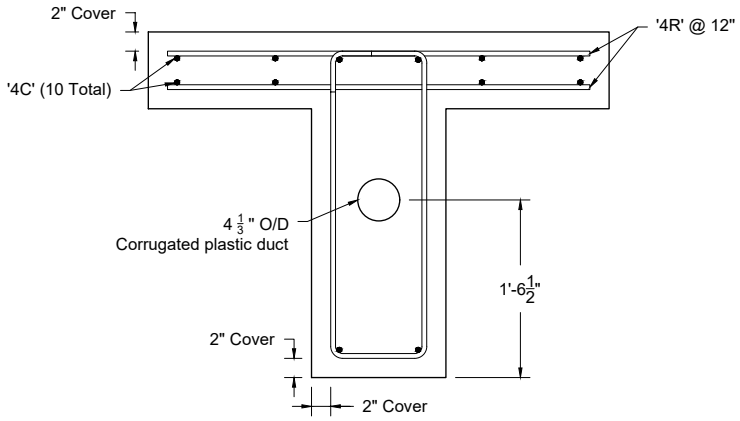

Cross Section A - A

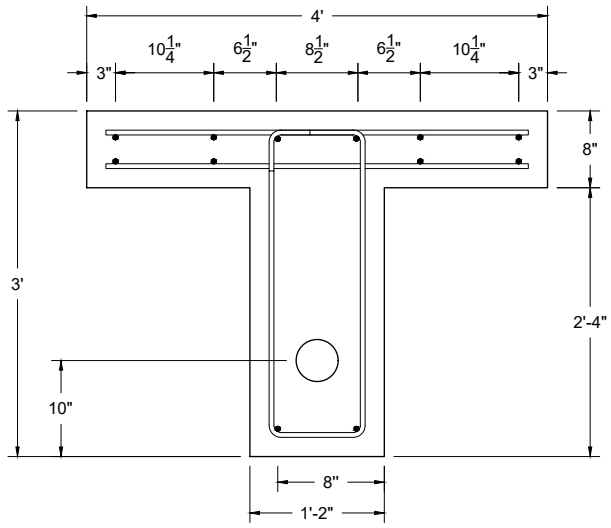

Cross Section B - B

FDOT Research
Bond performance of post-tensioning tendons with corrosion Inhibitor
BED31-977-07

University of Florida
Dept. of Civil and Coastal Engineering

Task 2: Design Drawings
Specimen D19P
Sheet 13 of 15

13

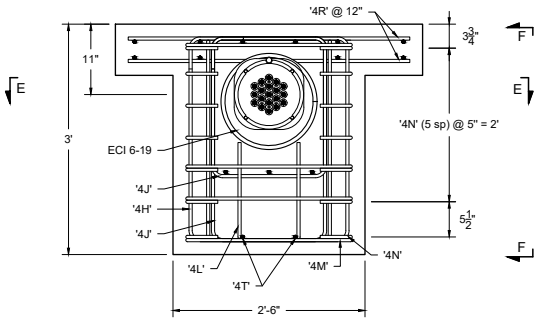

Section D - D
Refer to sheet 4

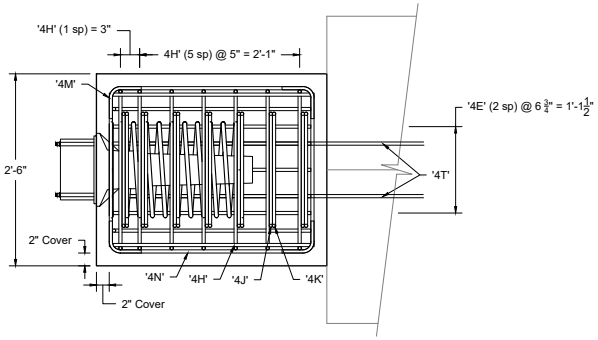

Section E - E

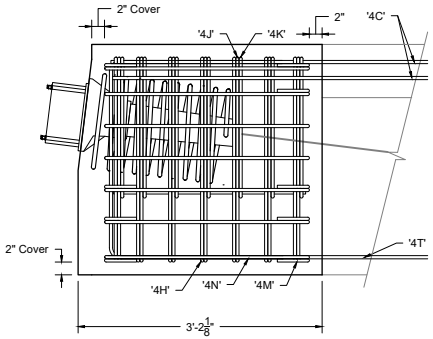

Section F - F

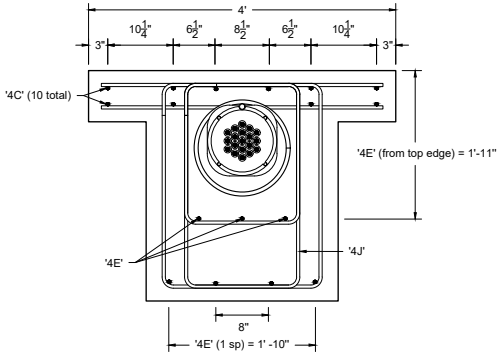

Section G - G
Refer to sheet 10

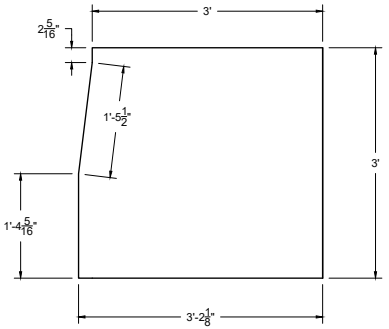

End Block Dimensions

FDOT Research
Bond performance of post-tensioning tendons with corrosion Inhibitor
BED31-977-07

University of Florida
Dept. of Civil and Coastal Engineering

Task 2: Design Drawings
Specimen D19P: End Block Details
Sheet 14 of 15

14

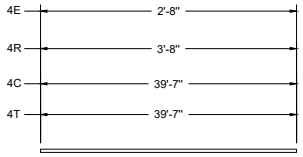

4E, 4R, 4C, 4T

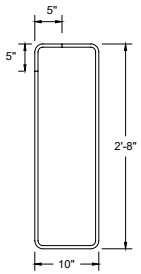

4G

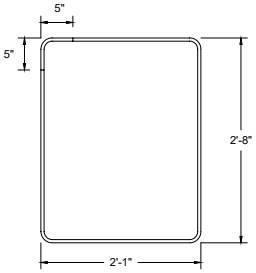

4H

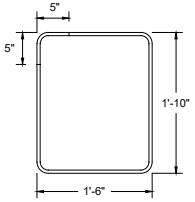

4K

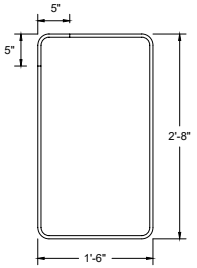

4J

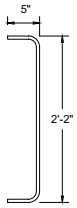

4M

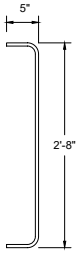

4N

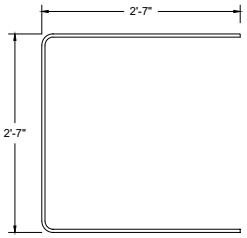

4S

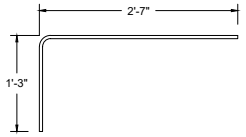

4L

Bill of material: H19 beam				
Piece	Size	Qty.	Length	Notes
4C	#4	10	39' -7''	
4T	#4	2	39' -7''	
4R	#4	40	3'-8''	
4E	#4	10	2' -8''	
4G	#4	37	7'-2''	
4H	#4	14	9'-8''	
4J	#4	14	8'-6''	
4K	#4	14	6'-10''	
4M	#4	18	2'-9''	
4N	#4	28	3'-3''	
4S	#4	4	7'-6''	
4L	#4	4	3'-9''	

FDOT Research
Bond performance of post-tensioning tendons with corrosion Inhibitor
BED31-977-07

University of Florida
Dept. of Civil and Coastal Engineering

Task 2: Design Drawings
Specimen D19P: Rebar Schedule
Sheet 15 of 15

15

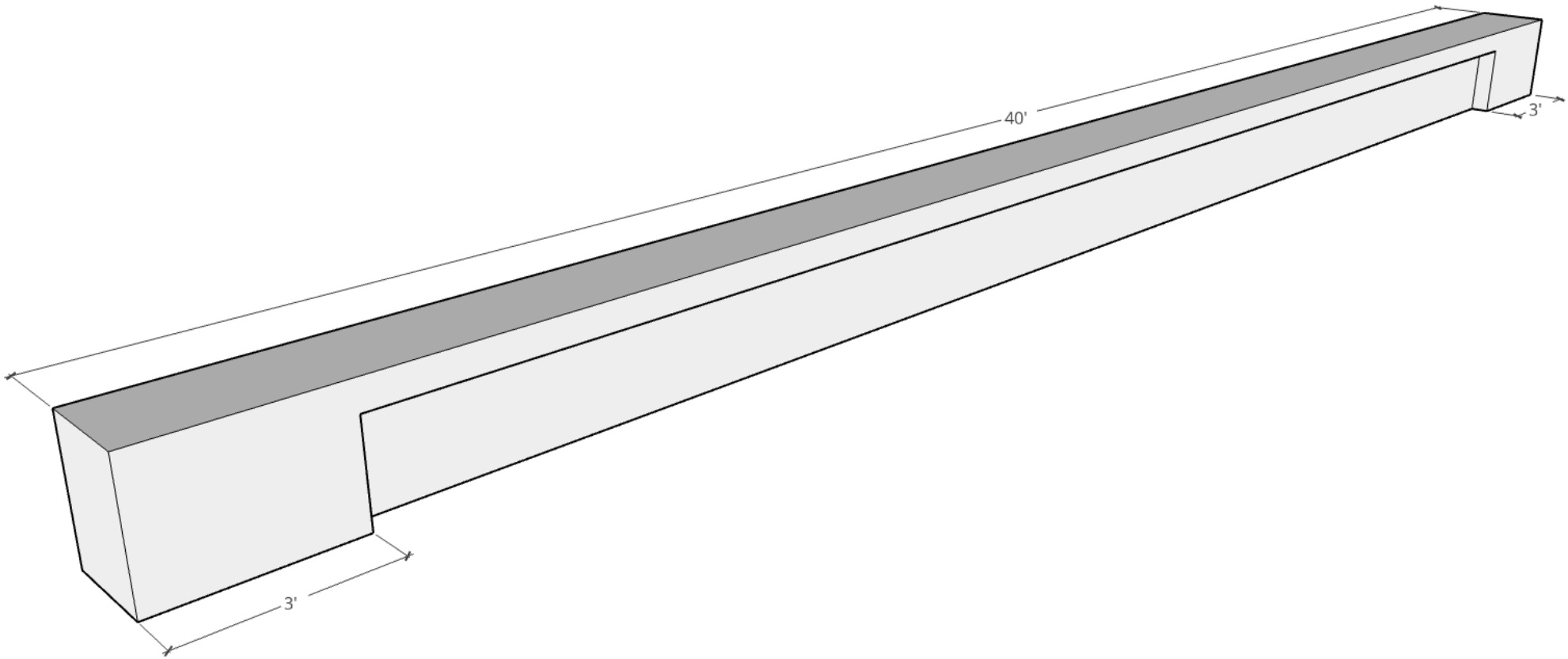

S06 beam: 3D view

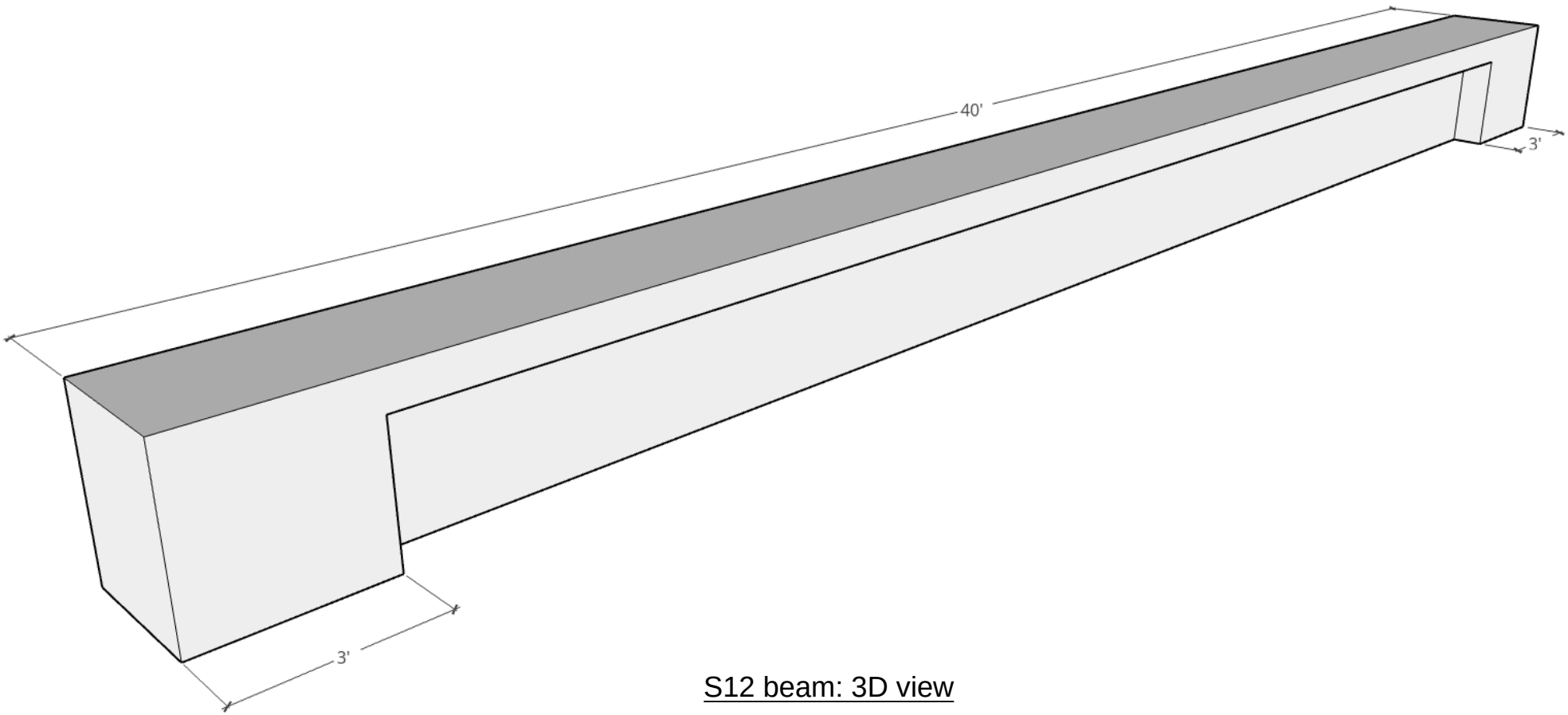

S12 beam: 3D view

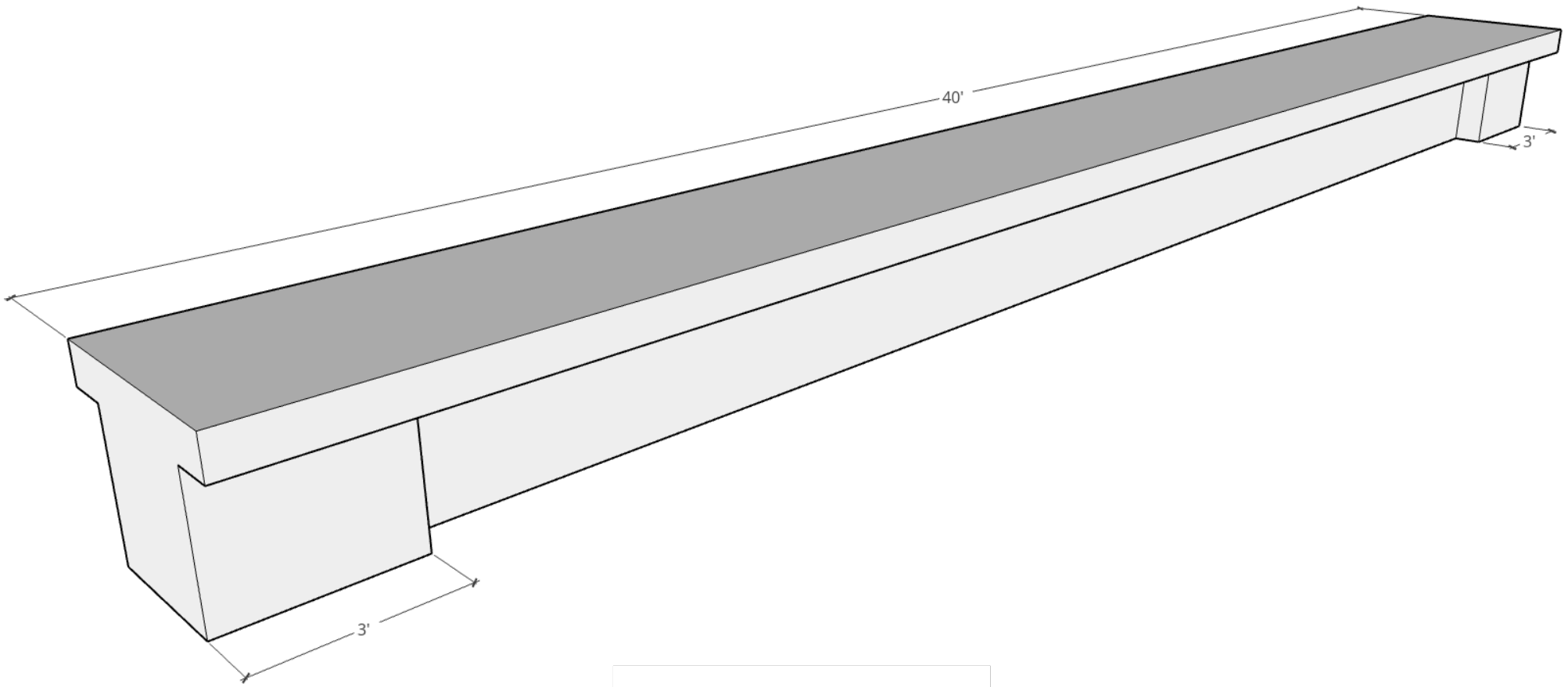

S19/D19M/D19P beam: 3D view

APPENDIX B
BEAM SPECIMEN INSTRUMENTATION DRAWINGS

Instrumentation drawings for the experimental test plan of the beam specimens are provided on the following pages.

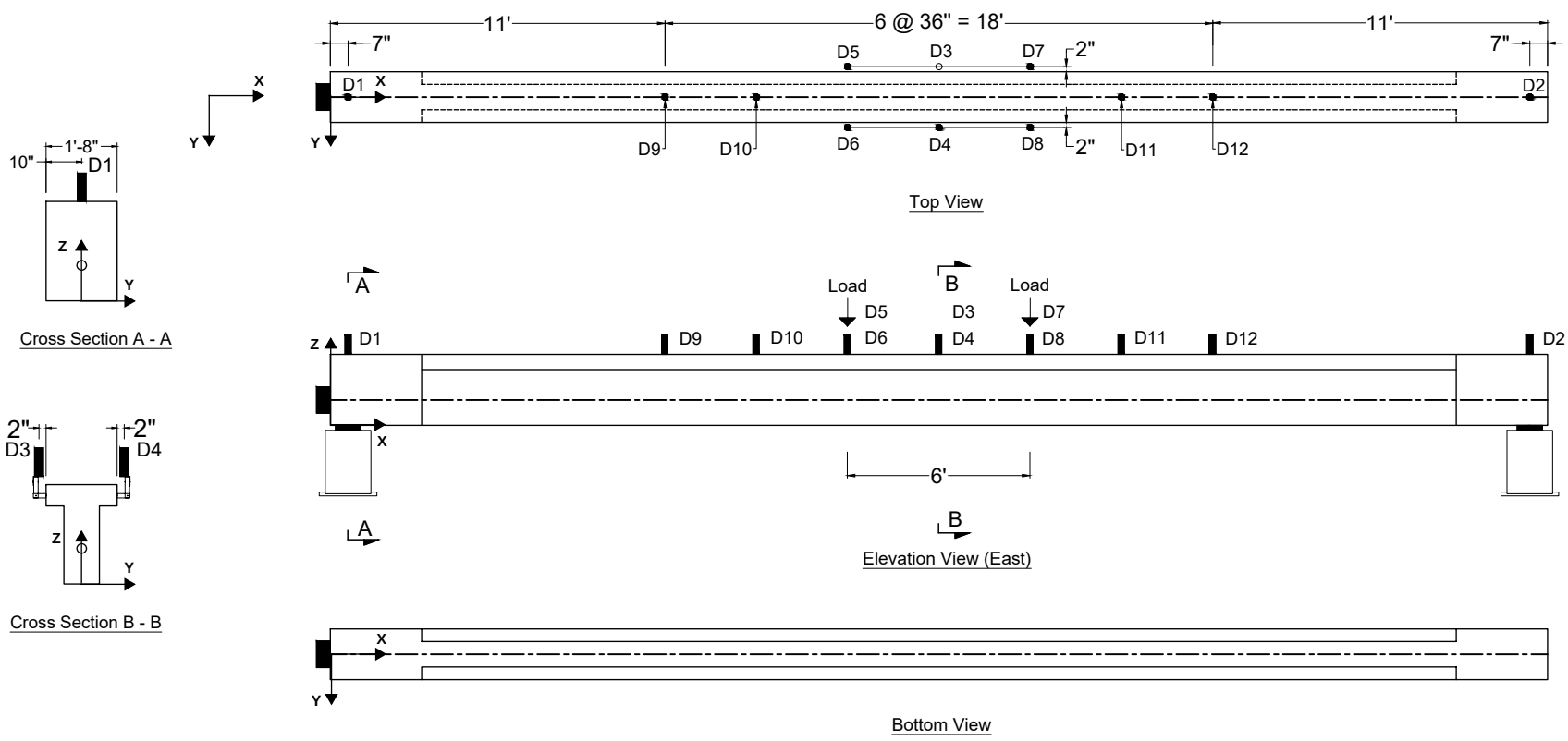

Key:

- Laser displacement transducer (D)
- 60-mm concrete strain gage (S)
- Fiber optics sensors (FOS)
- Digital image correlation (DIC)
- Vibrating wire strain gage (V)

Instrument	X(in.)	Y(in.)	Z(in.)	Orientation
D1	7	0	28	Z
D2	473	0	28	Z
D3	240	-12	28	Z
D4	240	12	28	Z
D5	204	-12	28	Z
D6	204	12	28	Z
D7	276	-12	28	Z
D8	276	12	28	Z
D9	132	0	28	Z

Instrument	X(in.)	Y(in.)	Z(in.)	Orientation
D10	168	0	28	Z
D11	312	0	28	Z
D12	348	0	28	Z

Note: Reference Z = 0 as the bottom surface of the beam

FDOT Research
Bond performance of post-tensioning tendons with corrosion Inhibitor
BED31-977-07

University of Florida
Dept. of Civil and Coastal Engineering

Task 3: Experimental Test Plan
Specimen S06: Displacement gages
Sheet 1 of 25

1

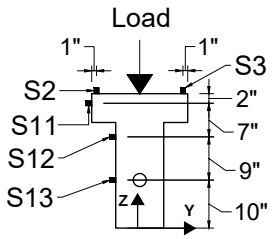

Cross Section A - A

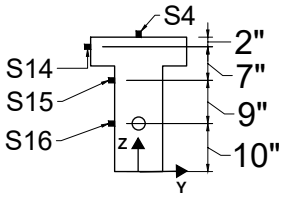

Cross Section B - B

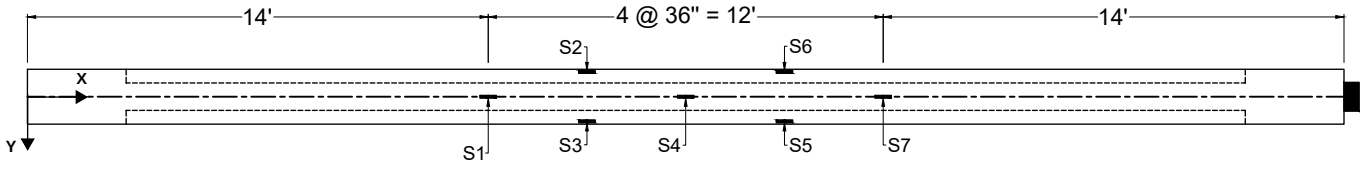

Top View

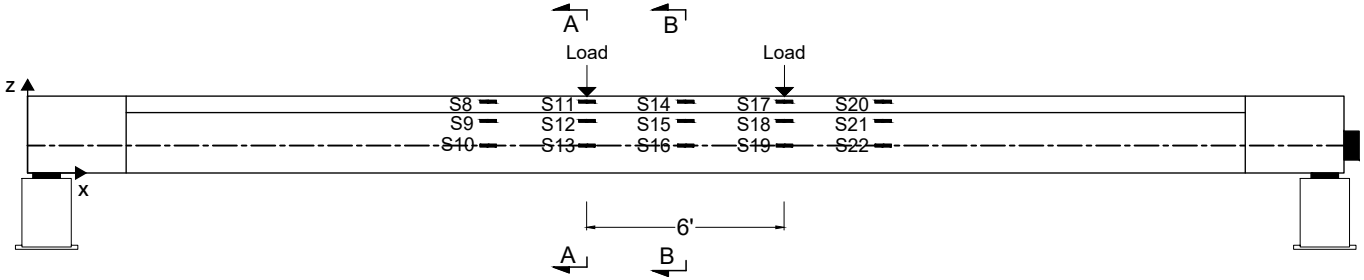

Elevation View (East)

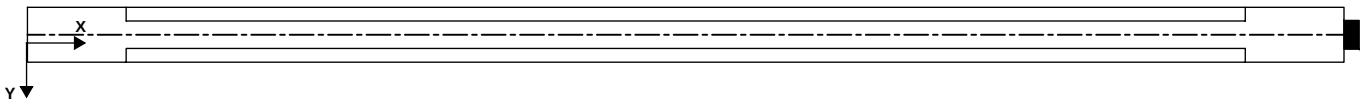

Bottom View

Key:

- Laser displacement transducer (D)
- 60-mm concrete strain gage (S)
- Fiber optics sensors (FOS)
- Digital image correlation (DIC)
- Vibrating wire strain gage (V)

Instrument	X(in.)	Y(in.)	Z(in.)	Orientation
S1	312.0	0.0	28.0	X
S2	276.0	-9.0	28.0	X
S3	276.0	9.0	28.0	X
S4	240.0	0.0	28.0	X
S5	204.0	9.0	28.0	X
S6	204.0	-9.0	28.0	X
S7	168.0	0.0	28.0	X
S8	312.0	-10.0	26.0	X
S9	312.0	-5.0	19.0	X
S10	312.0	-5.0	10.0	X
S11	276.0	-10.0	26.0	X

Instrument	X(in.)	Y(in.)	Z(in.)	Orientation
S12	276.0	-5.0	19.0	X
S13	276.0	-5.0	10.0	X
S14	240.0	-10.0	26.0	X
S15	240.0	-5.0	19.0	X
S16	240.0	-5.0	10.0	X
S17	204.0	-10.0	26.0	X
S18	204.0	-5.0	19.0	X
S19	204.0	-5.0	10.0	X
S20	168.0	-10.0	26.0	X
S21	168.0	-5.0	19.0	X
S22	168.0	-5.0	10.0	X

Note: Reference Z = 0 as the bottom surface of the beam

FDOT Research
Bond performance of post-tensioning tendons with corrosion Inhibitor
BED31-977-07

University of Florida
Dept. of Civil and Coastal Engineering

Task 3: Experimental Test Plan
Specimen S06: 60-mm concrete strain gage
Sheet 2 of 25

2

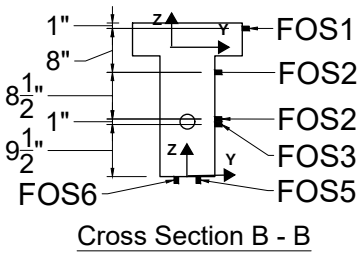

Cross Section B - B

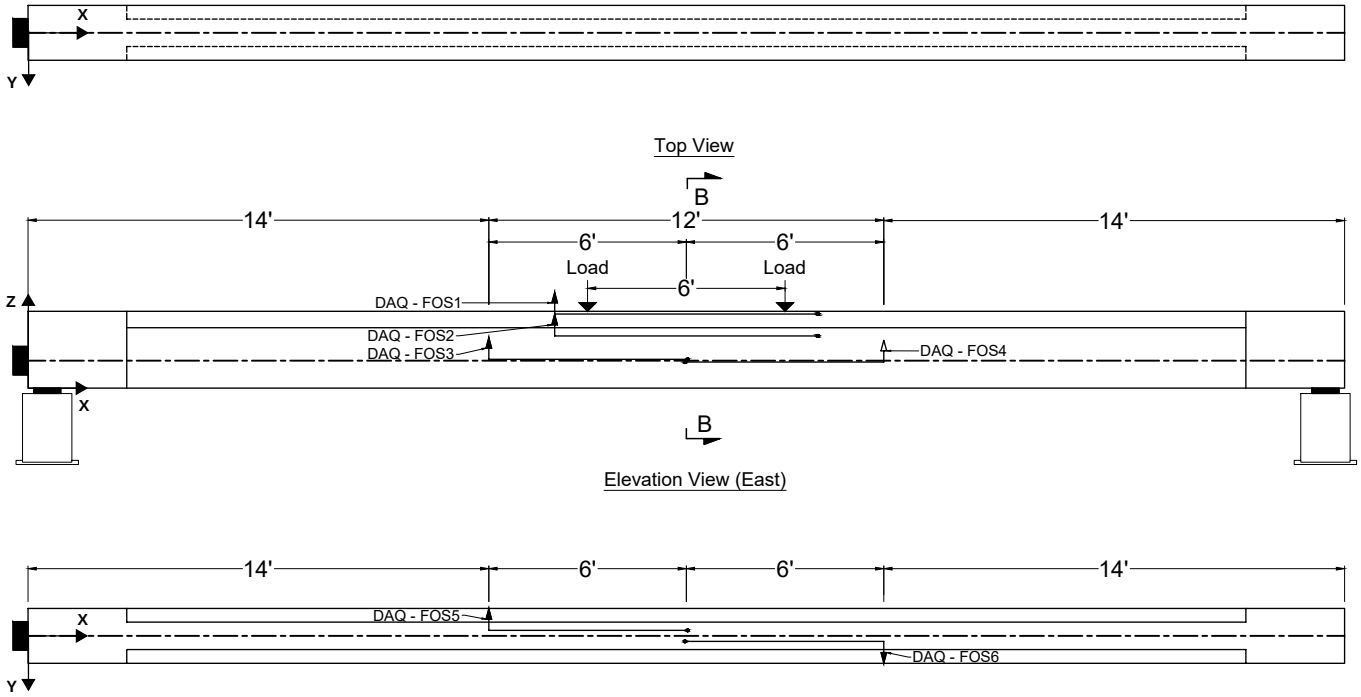

Key:

- Laser displacement transducer (D)
- 60-mm concrete strain gage (S)
- Fiber optics sensors (FOS)
- Digital image correlation (DIC)
- Vibrating wire strain gage (V)

Instrument	Start			End			Orientation
	X(in.)	Y(in.)	Z(in.)	X(in.)	Y(in.)	Z(in.)	
FOS1	192.0	10.0	27.0	288.0	10.0	27.0	X
FOS2	192.0	5.0	19.0	288.0	5.0	19.0	X
FOS3	168.0	5.0	10.5	240.5	5.0	10.5	X
FOS4	312.0	5.0	9.5	239.5	5.0	9.5	X
FOS5	168.0	-2.0	0.0	240.5	-2.0	0.0	X
FOS6	312.0	2.0	0.0	239.5	2.0	0.0	X

Note: Reference Z = 0 as the bottom surface of the beam

FDOT Research
Bond performance of post-tensioning tendons with corrosion Inhibitor
BED31-977-07

University of Florida
Dept. of Civil and Coastal Engineering

Task 3: Experimental Test Plan
Specimen S06: Fiber optics sensors
Sheet 3 of 25

3

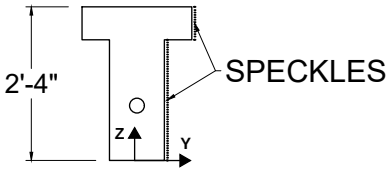

Cross Section B - B

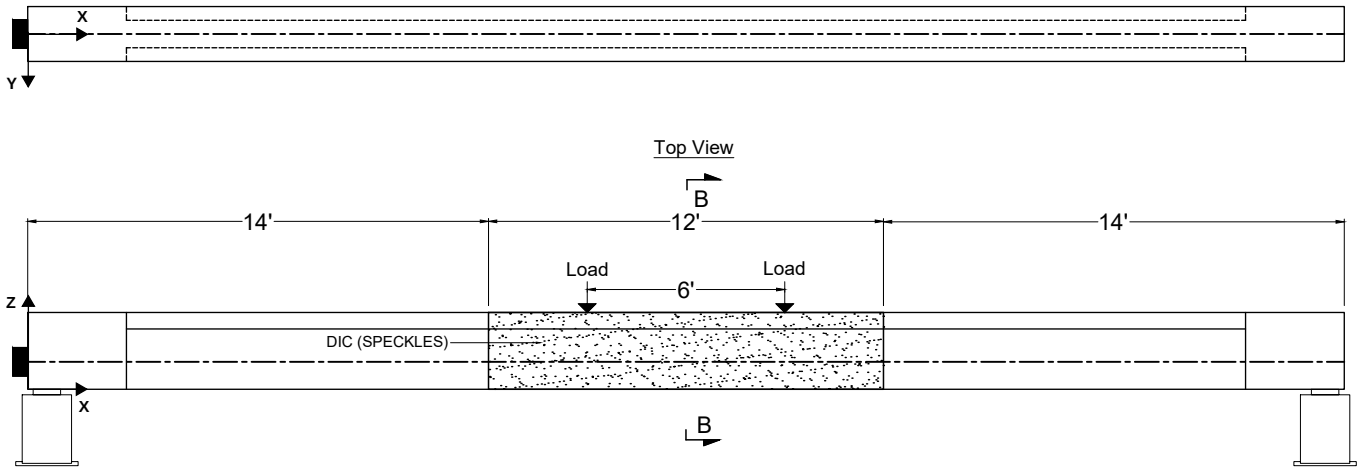

Elevation View (East)

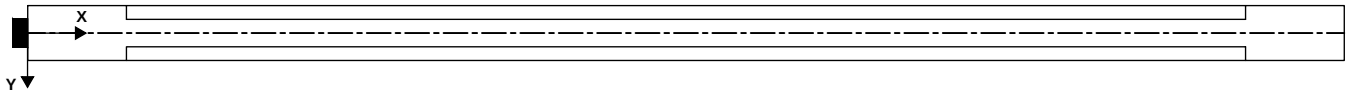

Bottom View

Key:

- Laser displacement transducer (D)
- 60-mm concrete strain gage (S)
- Fiber optics sensors (FOS)
- Digital image correlation (DIC)
- Vibrating wire strain gage (V)

Instrument	Area		Orientation
	length (ft)	height (ft)	
DIC	12.0	2.4	XZ

Note: Reference Z = 0 as the bottom surface of the beam

FDOT Research
Bond performance of post-tensioning tendons with corrosion Inhibitor
BED31-977-07

University of Florida
Dept. of Civil and Coastal Engineering

Task 3: Experimental Test Plan
Specimen S06: Digital image correlation
Sheet 4 of 25

4

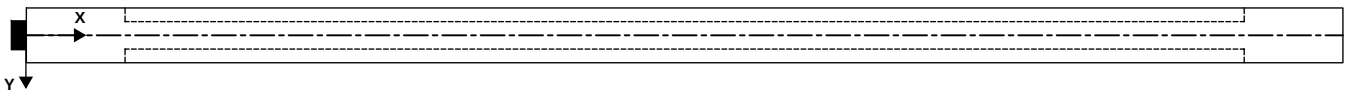

Top View

B

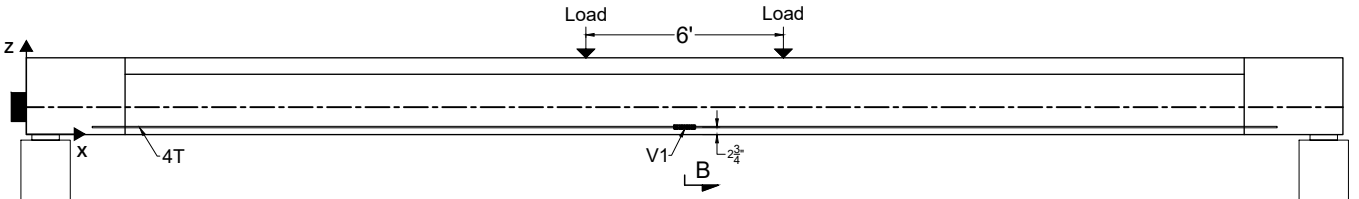

Elevation View (East)

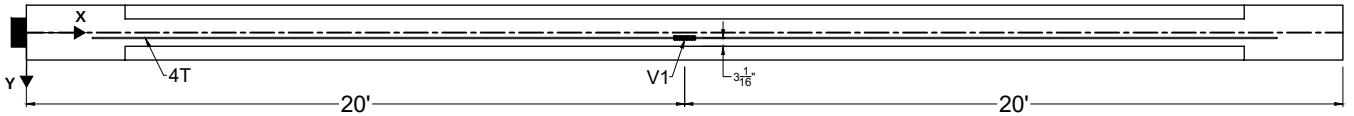

Bottom View

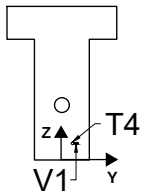

Cross Section B - B

Key:

- Laser displacement transducer (D)
- 60-mm concrete strain gage (S)
- Fiber optics sensors (FOS)
- Digital image correlation (DIC)
- Vibrating wire strain gage (V)

Instrument	X(in.)	Y(in.)	Z(in.)	Orientation
V1	240.0	2.0	2.8	X

Note: Reference Z = 0 as the bottom surface of the beam

FDOT Research
Bond performance of post-tensioning tendons with corrosion Inhibitor
BED31-977-07

University of Florida
Dept. of Civil and Coastal Engineering

Task 3: Experimental Test Plan
Specimen S06: Vibrating wire strain gage
Sheet 5 of 25

5

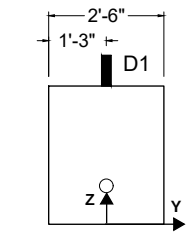

Cross Section A - A

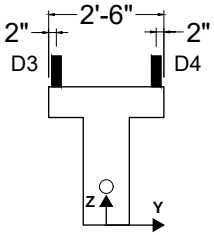

Cross Section B - B

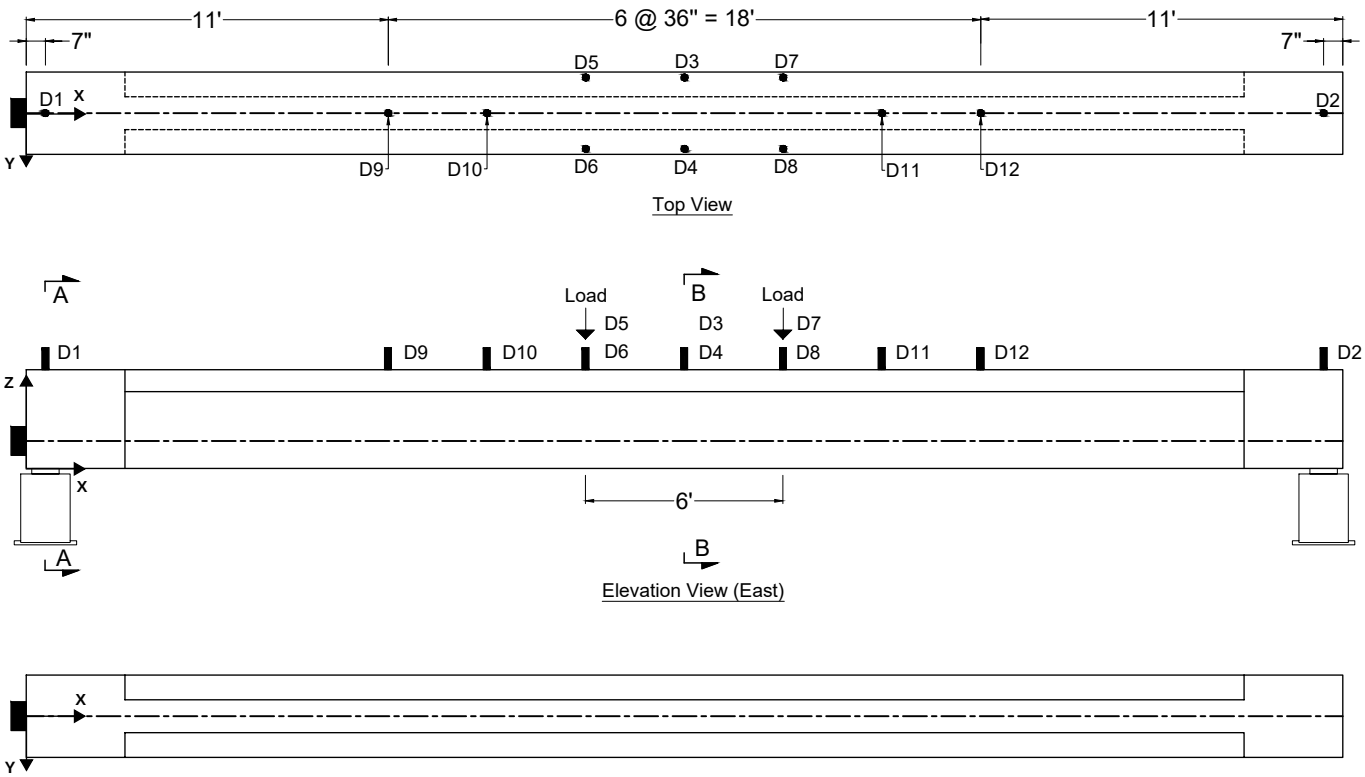

Key:

- Laser displacement transducer (D)
- 60-mm concrete strain gage (S)
- Fiber optics sensors (FOS)
- Digital image correlation (DIC)
- Vibrating wire strain gage (V)

Instrument	X(in.)	Y(in.)	Z(in.)	Orientation
D1	7.0	0.0	36.0	Z
D2	473.0	0.0	36.0	Z
D3	240.0	-12.0	36.0	Z
D4	240.0	12.0	36.0	Z
D5	204.0	-12.0	36.0	Z
D6	204.0	12.0	36.0	Z
D7	276.0	-12.0	36.0	Z
D8	276.0	12.0	36.0	Z
D9	132.0	0.0	36.0	Z

Instrument	X(in.)	Y(in.)	Z(in.)	Orientation
D10	168.0	0.0	36.0	Z
D11	312.0	0.0	36.0	Z
D12	348.0	0.0	36.0	Z

Note: Reference Z = 0 as the bottom surface of the beam

FDOT Research
Bond performance of post-tensioning tendons with corrosion Inhibitor
BED31-977-07

University of Florida
Dept. of Civil and Coastal Engineering

Task 3: Experimental Test Plan
Specimen S12: Laser displacement transducer
Sheet 6 of 25

6

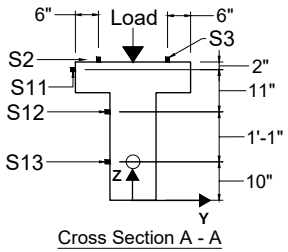

Cross Section A - A

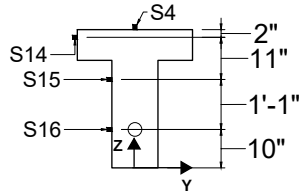

Cross Section B - B

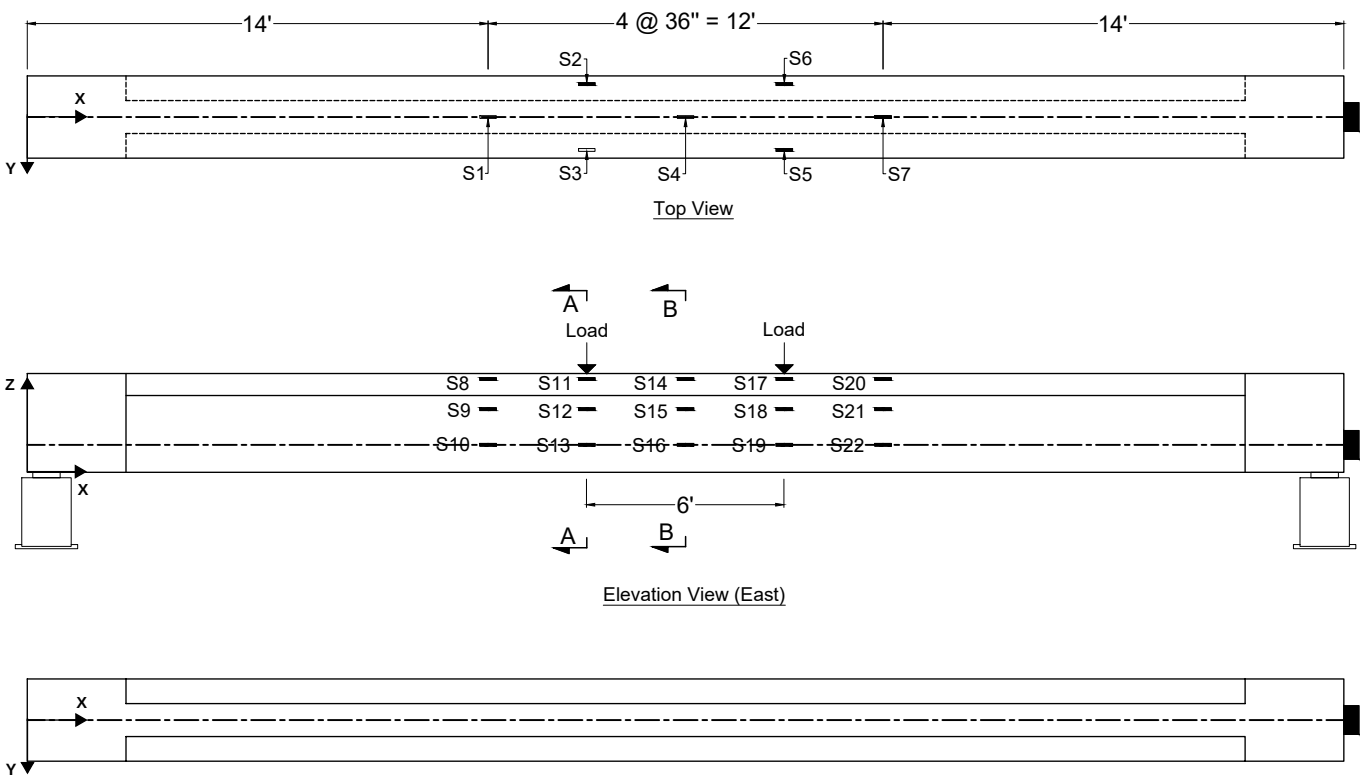

Instrument	X(in.)	Y(in.)	Z(in.)	Orientation
S1	312.0	0.0	36.0	X
S2	276.0	-12.0	36.0	X
S3	276.0	12.0	36.0	X
S4	240.0	0.0	36.0	X
S5	204.0	12.0	36.0	X
S6	204.0	-12.0	36.0	X
S7	168.0	0.0	36.0	X
S8	312.0	-15.0	34.0	X
S9	312.0	-6.0	23.0	X
S10	312.0	-6.0	10.0	X
S11	276.0	-15.0	34.0	X

Instrument	X(in.)	Y(in.)	Z(in.)	Orientation
S12	276.0	-6.0	23.0	X
S13	276.0	-6.0	10.0	X
S14	240.0	-15.0	34.0	X
S15	240.0	-6.0	23.0	X
S16	240.0	-6.0	10.0	X
S17	204.0	-15.0	34.0	X
S18	204.0	-6.0	23.0	X
S19	204.0	-6.0	10.0	X
S20	168.0	-15.0	34.0	X
S21	168.0	-6.0	23.0	X
S22	168.0	-6.0	10.0	X

Note: Reference Z = 0 as the bottom surface of the beam

Key:

- Laser displacement transducer (D)
- 60-mm concrete strain gage (S)
- Fiber optics sensors (FOS)
- Digital image correlation (DIC)
- Vibrating wire strain gage (V)

FDOT Research
Bond performance of post-tensioning tendons with corrosion inhibitor
BED31-977-07

University of Florida
Dept. of Civil and Coastal Engineering

Task 3: Experimental Test Plan
Specimen S12: 60-mm concrete strain gage
Sheet 7 of 25

7

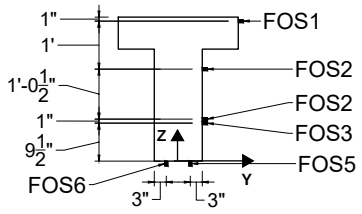

Cross Section B - B

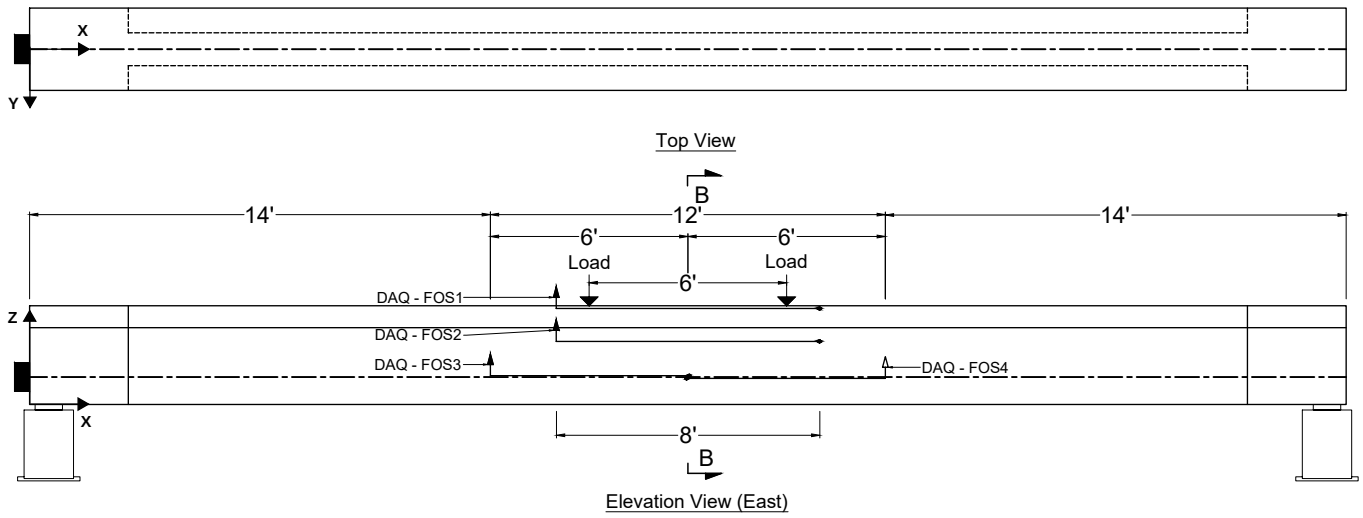

Key:

- Laser displacement transducer (D)
- 60-mm concrete strain gage (S)
- Fiber optics sensors (FOS)
- Digital image correlation (DIC)
- Vibrating wire strain gage (V)

Instrument	Start			End			Orientation
	X(in.)	Y(in.)	Z(in.)	X(in.)	Y(in.)	Z(in.)	
FOS1	192.0	15.0	35.0	288.0	15.0	35.0	X
FOS2	192.0	6.0	23.0	288.0	6.0	23.0	X
FOS3	168.0	6.0	10.5	240.5	6.0	10.5	X
FOS4	312.0	6.0	9.5	239.5	6.0	9.5	X
FOS5	168.0	-3.0	0.0	240.5	-3.0	0.0	X
FOS6	312.0	3.0	0.0	239.5	3.0	0.0	X

Note: Reference Z = 0 as the bottom surface of the beam

FDOT Research
Bond performance of post-tensioning tendons with corrosion Inhibitor
BED31-977-07

University of Florida
Dept. of Civil and Coastal Engineering

Task 3: Experimental Test Plan
Specimen S12: Fiber optics sensors
Sheet 8 of 25

8

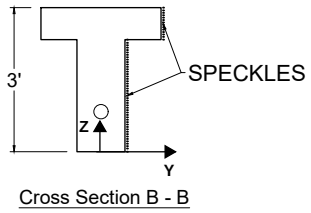

Cross Section B - B

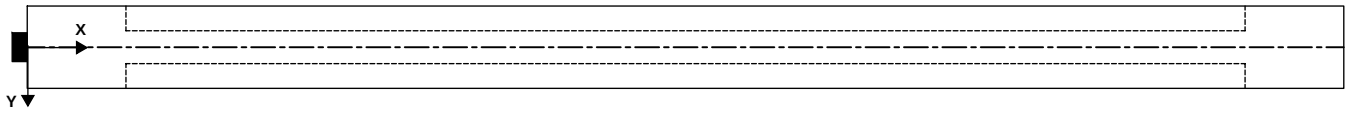

Top View

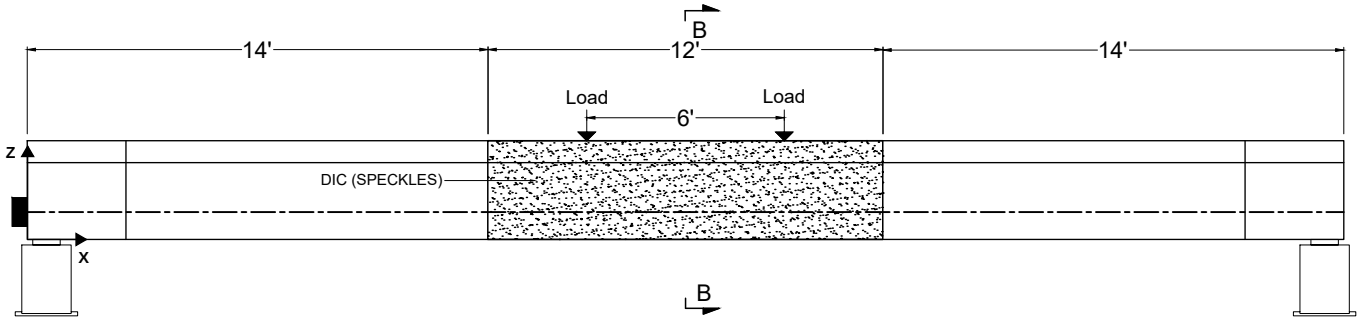

Elevation View (East)

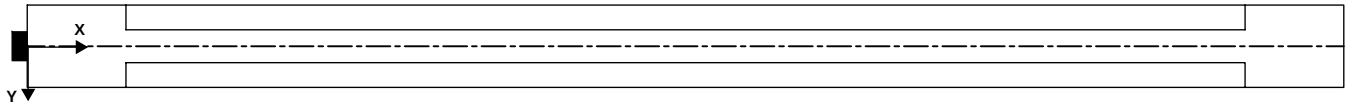

Bottom View

Key:

- Laser displacement transducer (D)
- 60-mm concrete strain gage (S)
- Fiber optics sensors (FOS)
- Digital image correlation (DIC)
- Vibrating wire strain gage (V)

Instrument	Area		Orientation
	length (ft)	height (ft)	
DIC	12.0	3.0	XZ

Note: Reference Z = 0 as the bottom surface of the beam

FDOT Research
Bond performance of post-tensioning tendons with corrosion Inhibitor
BED31-977-07

University of Florida
Dept. of Civil and Coastal Engineering

Task 3: Experimental Test Plan
Specimen S12: Digital image correlation
Sheet 9 of 25

9

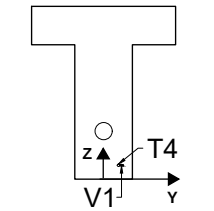

Cross Section B - B

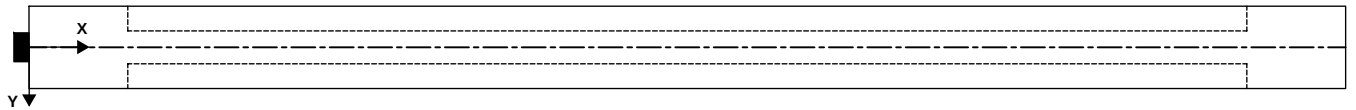

Top View

B

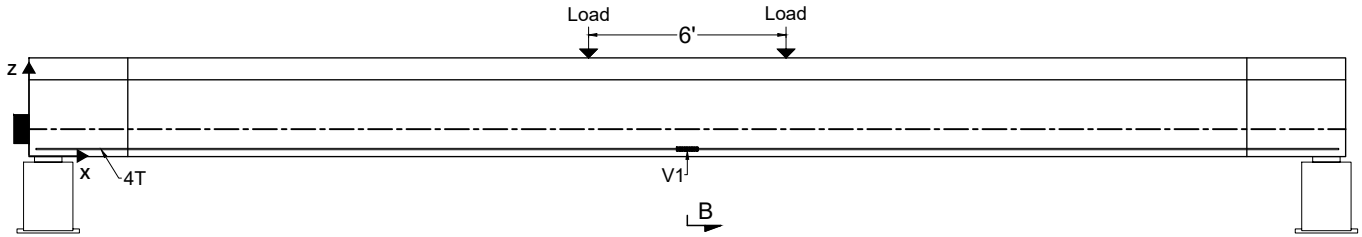

Elevation View (East)

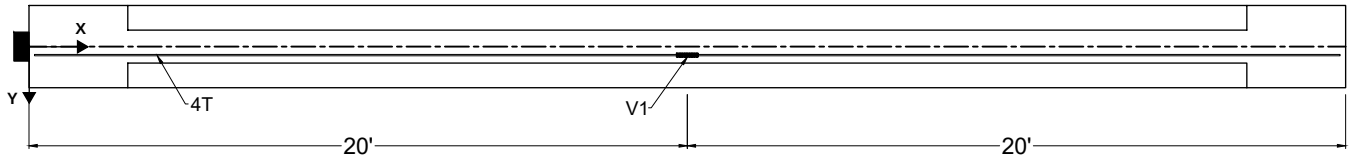

Bottom View

Key:

- Laser displacement transducer (D)
- 60-mm concrete strain gage (S)
- Fiber optics sensors (FOS)
- Digital image correlation (DIC)
- Vibrating wire strain gage (V)

Instrument	X(in.)	Y(in.)	Z(in.)	Orientation
V1	240.0	3.1	2.8	X

Note: Reference Z = 0 as the bottom surface of the beam

FDOT Research
Bond performance of post-tensioning tendons with corrosion Inhibitor
BED31-977-07

University of Florida
Dept. of Civil and Coastal Engineering

Task 3: Experimental Test Plan
Specimen S12: Vibrating wire strain gage
Sheet 10 of 25

10

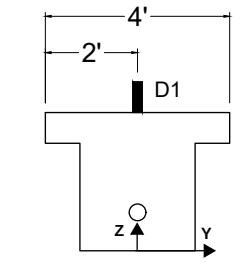

Cross Section A - A

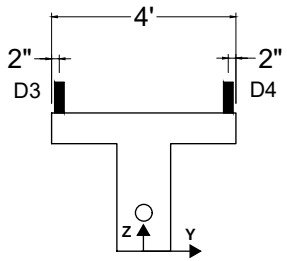

Cross Section B - B

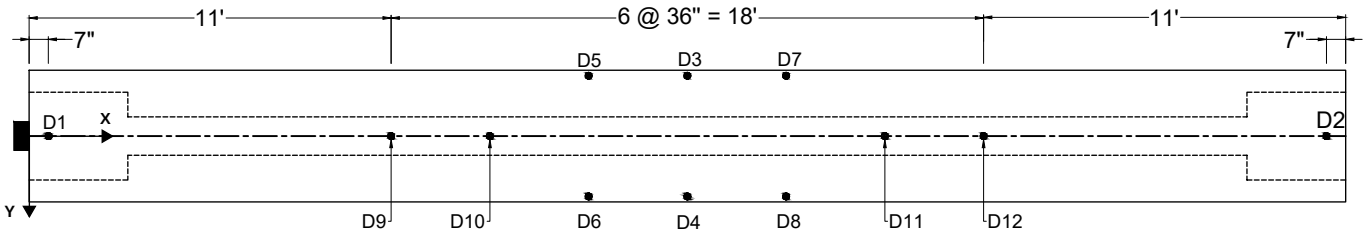

Top View

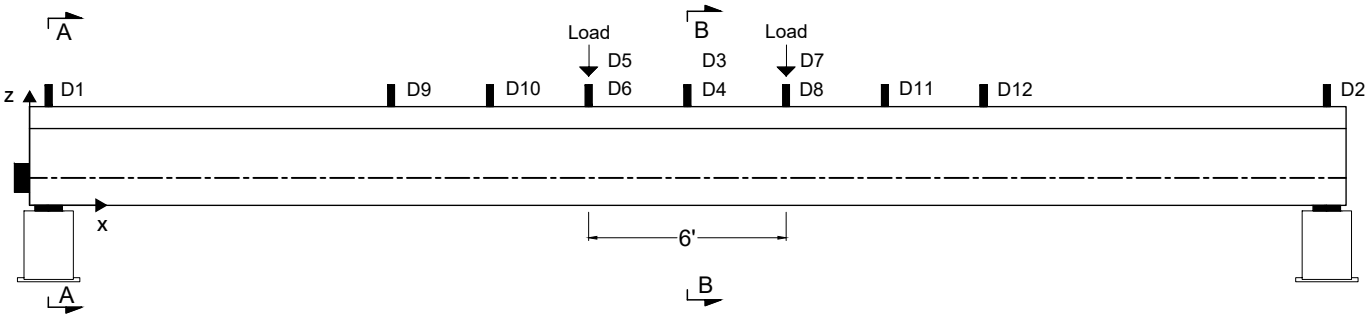

Elevation View (East)

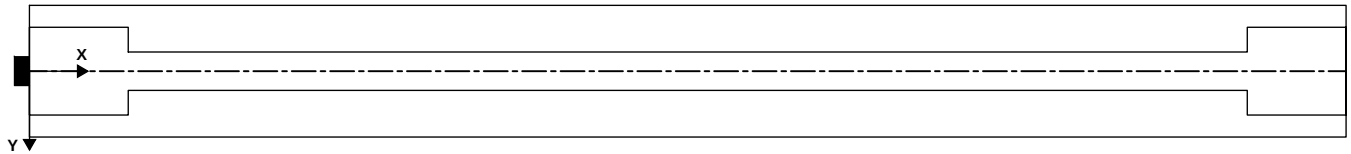

Bottom View

Key:

- Laser displacement transducer (D)
- 60-mm concrete strain gage (S)
- Fiber optics sensors (FOS)
- Digital image correlation (DIC)
- Vibrating wire strain gage (V)

Instrument	X(in.)	Y(in.)	Z(in.)	Orientation
D1	7.0	0.0	36.0	Z
D2	473.0	0.0	36.0	Z
D3	240.0	-22.0	36.0	Z
D4	240.0	22.0	36.0	Z
D5	204.0	-22.0	36.0	Z
D6	204.0	22.0	36.0	Z
D7	276.0	-22.0	36.0	Z
D8	276.0	22.0	36.0	Z
D9	132.0	0.0	36.0	Z

Instrument	X(in.)	Y(in.)	Z(in.)	Orientation
D10	168.0	0.0	36.0	Z
D11	312.0	0.0	36.0	Z
D12	348.0	0.0	36.0	Z

Note: Reference Z = 0 as the bottom surface of the beam

FDOT Research
Bond performance of post-tensioning tendons with corrosion inhibitor
BED31-977-07

University of Florida
Dept. of Civil and Coastal Engineering

Task 3: Experimental Test Plan
Specimen S19: Laser displacement transducer
Sheet 11 of 25

11

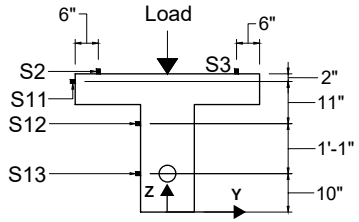

Cross Section A - A

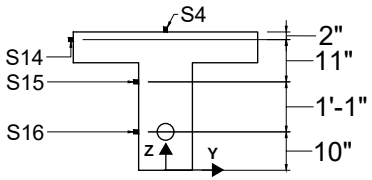

Cross Section B - B

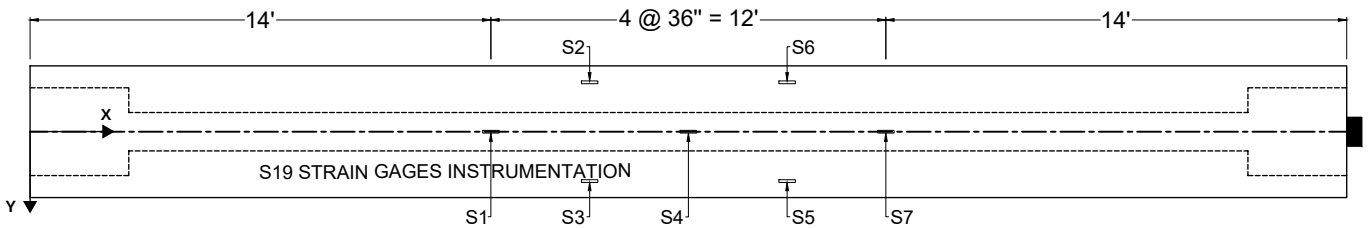

Top View

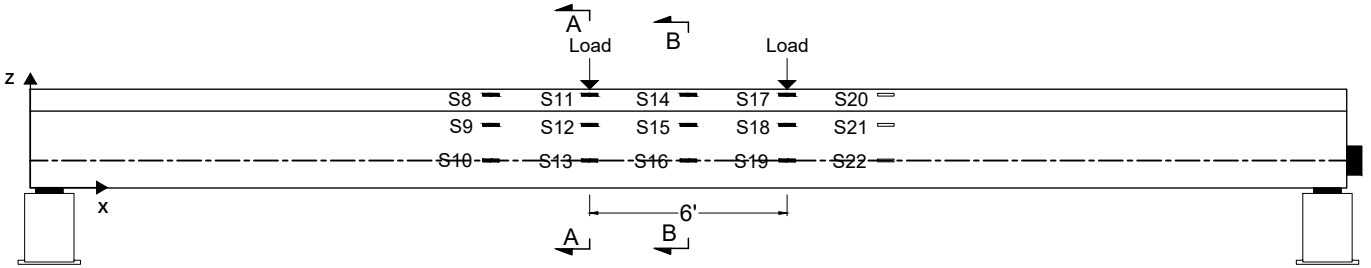

Elevation View (West)

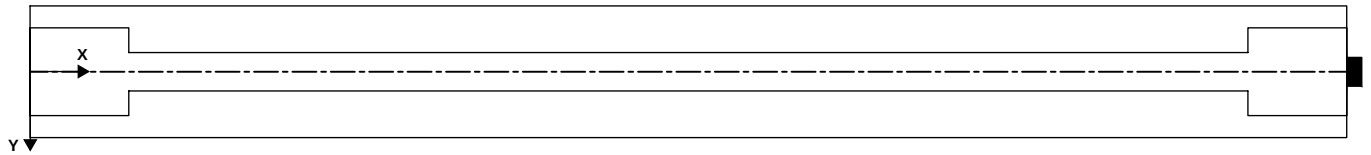

Bottom View

Key:

- Laser displacement transducer (D)
- 60-mm concrete strain gage (S)
- Fiber optics sensors (FOS)
- Digital image correlation (DIC)
- Vibrating wire strain gage (V)

Instrument	X(in.)	Y(in.)	Z(in.)	Orientation
S1	312.0	0.0	36.0	X
S2	276.0	-18.0	36.0	X
S3	276.0	18.0	36.0	X
S4	240.0	0.0	36.0	X
S5	204.0	18.0	36.0	X
S6	204.0	-18.0	36.0	X
S7	168.0	0.0	36.0	X
S8	312.0	-24.0	34.0	X
S9	312.0	-7.0	23.0	X
S10	312.0	-7.0	10.0	X
S11	276.0	-24.0	34.0	X

Instrument	X(in.)	Y(in.)	Z(in.)	Orientation
S12	276.0	-7.0	23.0	X
S13	276.0	-7.0	10.0	X
S14	240.0	-24.0	34.0	X
S15	240.0	-7.0	23.0	X
S16	240.0	-7.0	10.0	X
S17	204.0	-24.0	34.0	X
S18	204.0	-7.0	23.0	X
S19	204.0	-7.0	10.0	X
S20	168.0	-24.0	34.0	X
S21	168.0	-7.0	23.0	X
S22	168.0	-7.0	10.0	X

Note: Reference Z = 0 as the bottom surface of the beam

FDOT Research
Bond performance of post-tensioning tendons with corrosion inhibitor
BED31-977-07

University of Florida
Dept. of Civil and Coastal Engineering

Task 3: Experimental Test Plan
Specimen S19: 60-mm concrete strain gage
Sheet 12 of 25

12

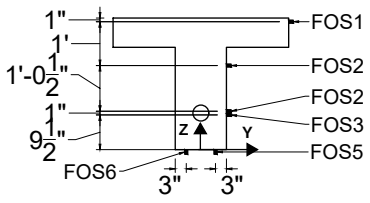

Cross Section B - B

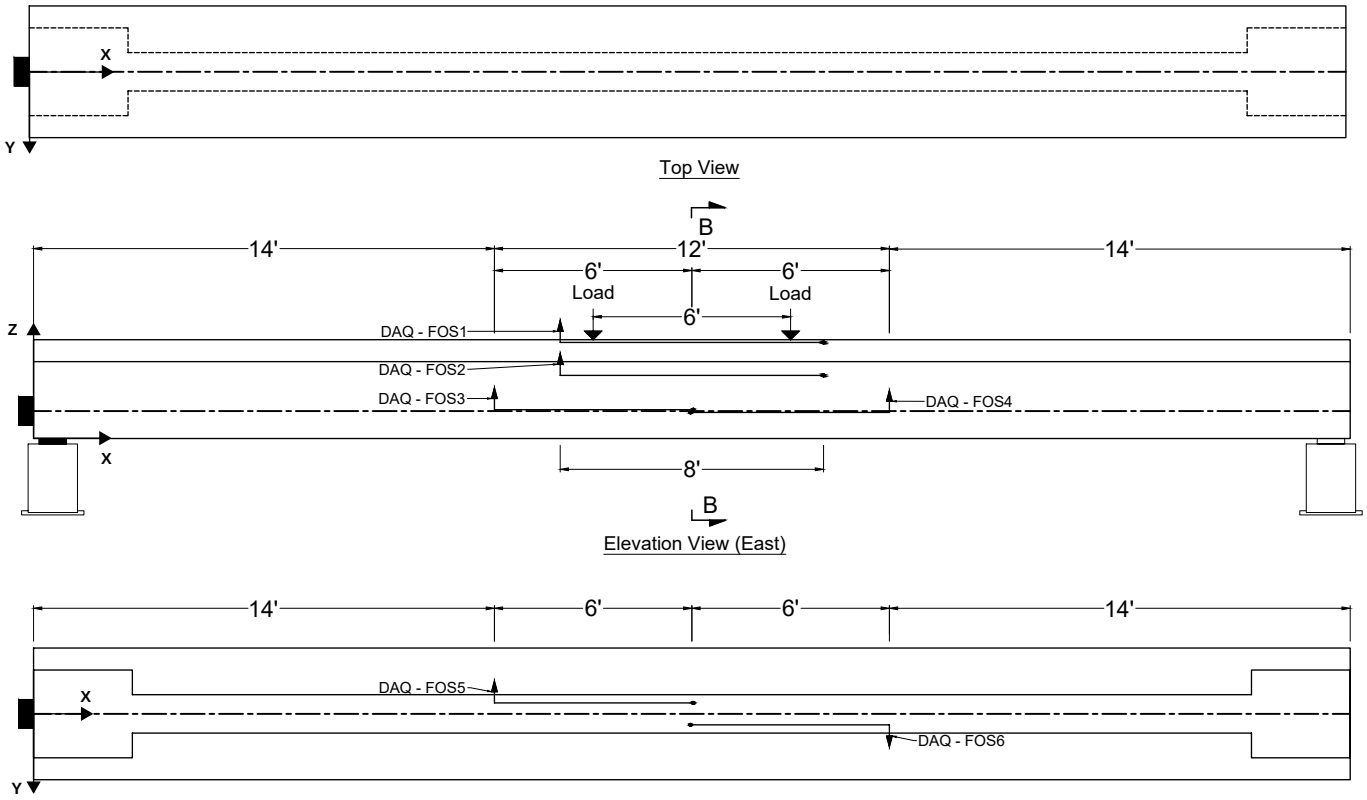

Key:

- Laser displacement transducer (D)
- 60-mm concrete strain gage (S)
- Fiber optics sensors (FOS)
- Digital image correlation (DIC)
- Vibrating wire strain gage (V)

Instrument	Start			End			Orientation
	X(in.)	Y(in.)	Z(in.)	X(in.)	Y(in.)	Z(in.)	
FOS1	192.0	24.0	35.0	288.0	24.0	35.0	X
FOS2	192.0	7.0	23.0	288.0	7.0	23.0	X
FOS3	168.0	7.0	10.5	240.5	7.0	10.5	X
FOS4	312.0	7.0	9.5	239.5	7.0	9.5	X
FOS5	168.0	-4.0	0.0	240.5	-4.0	0.0	X
FOS6	312.0	4.0	0.0	239.5	4.0	0.0	X

Note: Reference Z = 0 as the bottom surface of the beam

FDOT Research
Bond performance of post-tensioning tendons with corrosion Inhibitor
BED31-977-07

University of Florida
Dept. of Civil and Coastal Engineering

Task 3: Experimental Test Plan
Specimen S19: Fiber optics sensors
Sheet 13 of 25

13

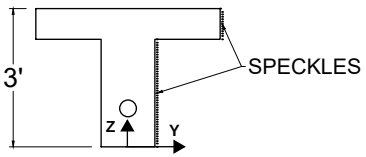

Cross Section B - B

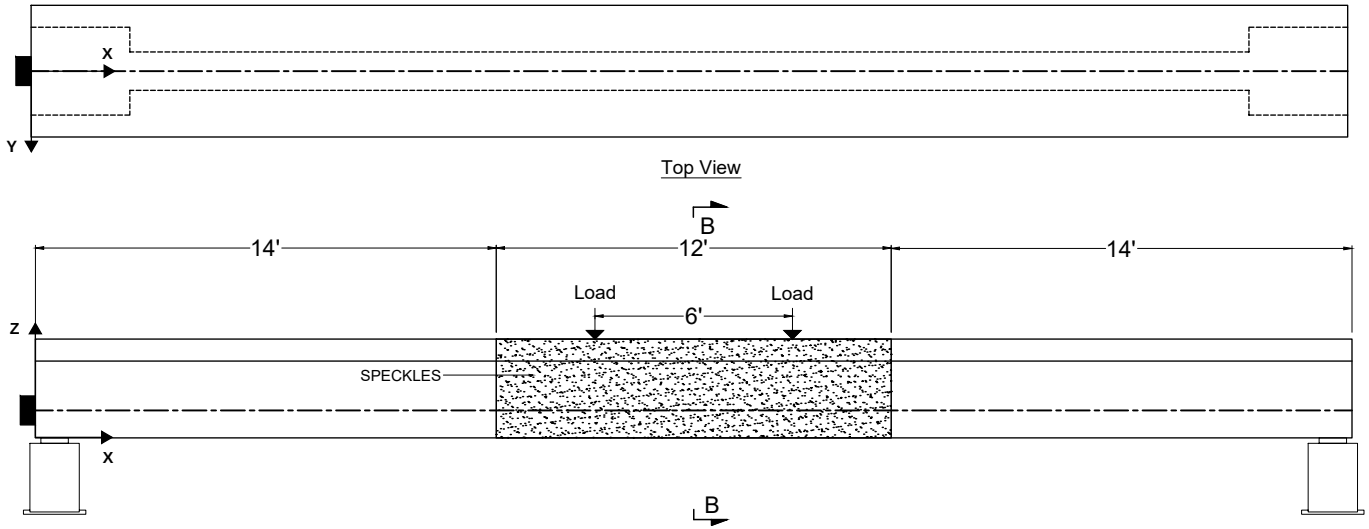

Top View

Elevation View (East)

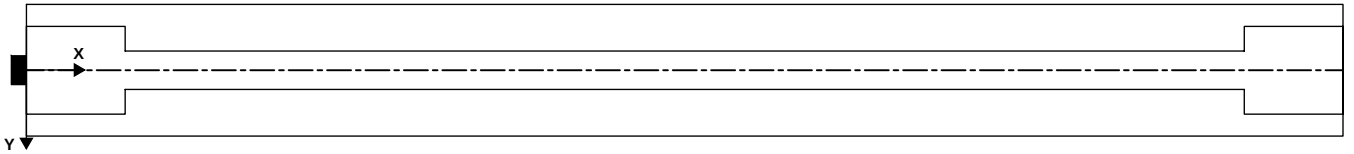

Bottom View

Key:

- Laser displacement transducer (D)
- 60-mm concrete strain gage (S)
- Fiber optics sensors (FOS)
- Digital image correlation (DIC)
- Vibrating wire strain gage (V)

Instrument	Area		Orientation
	length (ft)	height (ft)	
DIC	12.0	3.0	XZ

Note: Reference Z = 0 as the bottom surface of the beam

FDOT Research
Bond performance of post-tensioning tendons with corrosion Inhibitor
BED31-977-07

University of Florida
Dept. of Civil and Coastal Engineering

Task 3: Experimental Test Plan
Specimen S19: Digital image correlation
Sheet 14 of 25

14

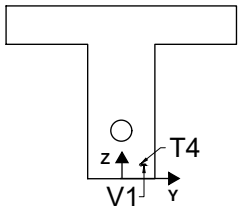

Cross Section B - B

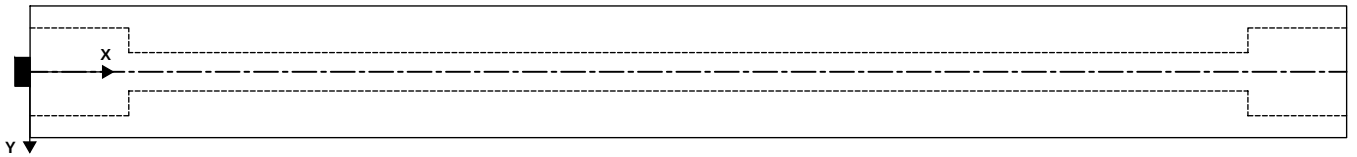

Top View

B

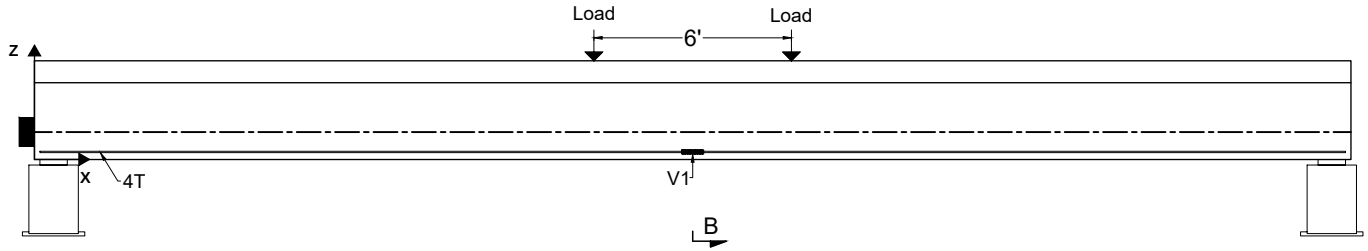

Elevation View (East)

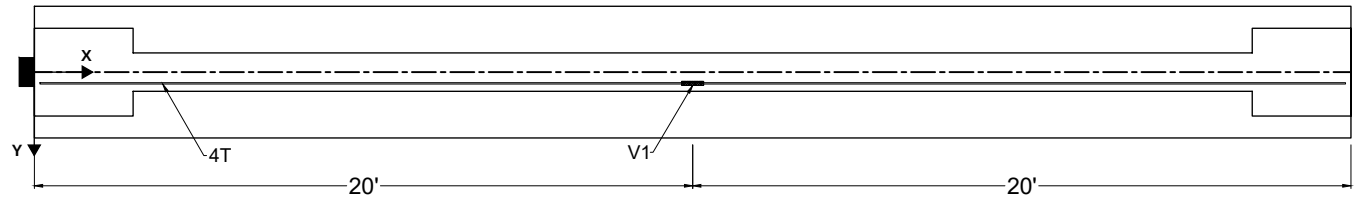

Bottom View

Key:

- Laser displacement transducer (D)
- 60-mm concrete strain gage (S)
- Fiber optics sensors (FOS)
- Digital image correlation (DIC)
- Vibrating wire strain gage (V)

Instrument	X(in.)	Y(in.)	Z(in.)	Orientation
V1	240.0	4.1	2.8	X

Note: Reference Z = 0 as the bottom surface of the beam

FDOT Research
Bond performance of post-tensioning tendons with corrosion Inhibitor
BED31-977-07

University of Florida
Dept. of Civil and Coastal Engineering

Task 3: Experimental Test Plan
Specimen S19: Vibrating wire strain gage
Sheet 15 of 25

15

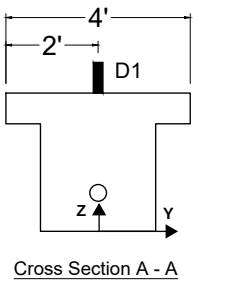

Cross Section A - A

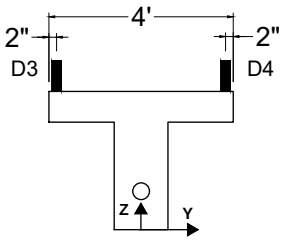

Cross Section B - B

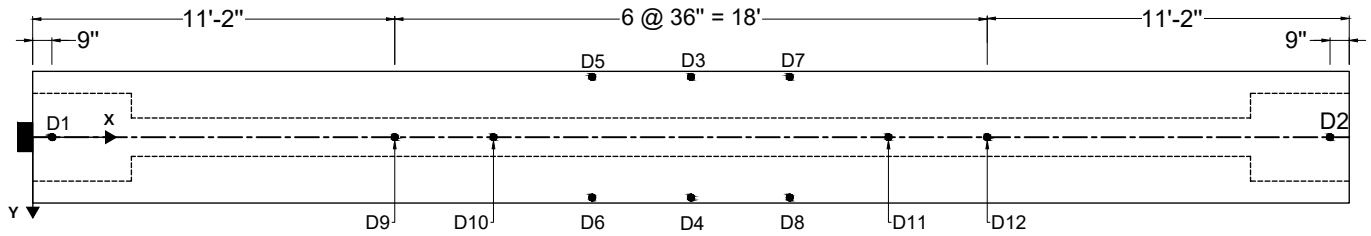

Top View

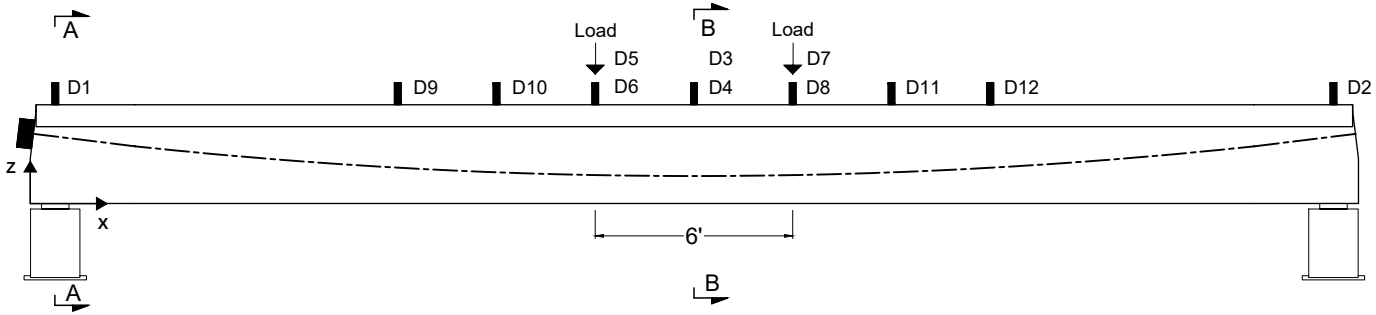

Elevation View (East)

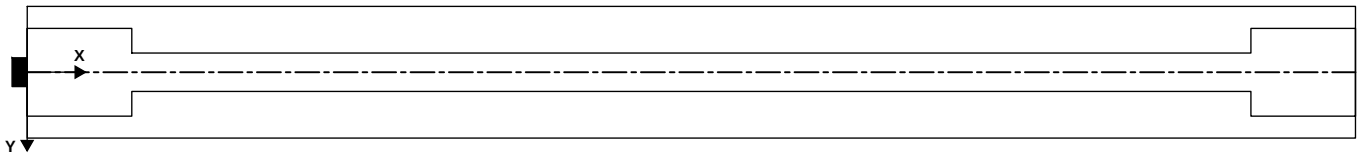

Bottom View

Key:

- Laser displacement transducer (D)
- 60-mm concrete strain gage (S)
- Fiber optics sensors (FOS)
- Digital image correlation (DIC)
- Vibrating wire strain gage (V)

Instrument	X(in.)	Y(in.)	Z(in.)	Orientation
D1	9.0	0.0	36.0	Z
D2	475.0	0.0	36.0	Z
D3	242.0	-22.0	36.0	Z
D4	242.0	22.0	36.0	Z
D5	206.0	-22.0	36.0	Z
D6	206.0	22.0	36.0	Z
D7	278.0	-22.0	36.0	Z
D8	278.0	22.0	36.0	Z
D9	134.0	0.0	36.0	Z

Instrument	X(in.)	Y(in.)	Z(in.)	Orientation
D10	170.0	0.0	36.0	Z
D11	314.0	0.0	36.0	Z
D12	350.0	0.0	36.0	Z

Note: Reference Z = 0 as the bottom surface of the beam

FDOT Research
Bond performance of post-tensioning tendons with corrosion inhibitor
BED31-977-07

University of Florida
Dept. of Civil and Coastal Engineering

Task 3: Experimental Test Plan
Specimen D19M : Laser displacement transducer
Sheet 16 of 25

16

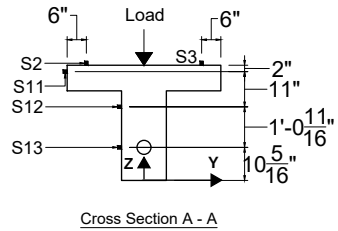

Cross Section A - A

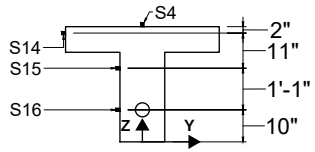

Cross Section B - B

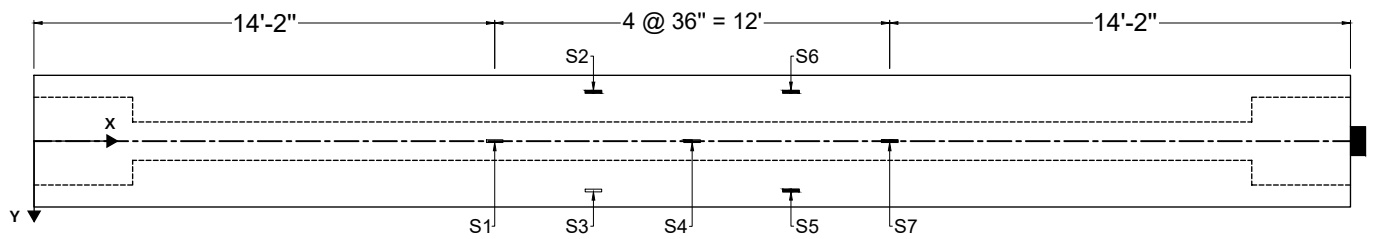

Top View

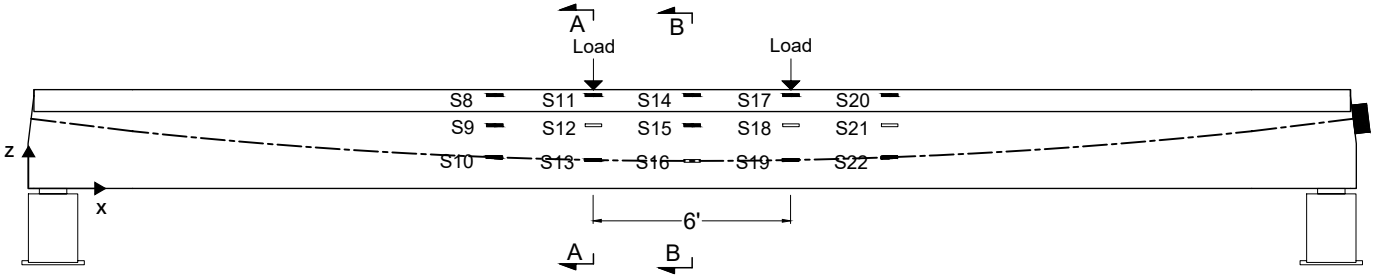

Elevation View (East)

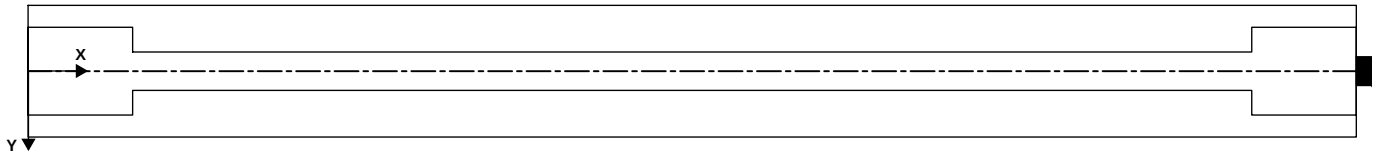

Bottom View

Key:

- Laser displacement transducer (D)
- 60-mm concrete strain gage (S)
- Fiber optics sensors (FOS)
- Digital image correlation (DIC)
- Vibrating wire strain gage (V)

Instrument	X(in.)	Y(in.)	Z(in.)	Orientation
S1	314.0	0.0	36.0	X
S2	278.0	-18.0	36.0	X
S3	278.0	18.0	36.0	X
S4	242.0	0.0	36.0	X
S5	206.0	18.0	36.0	X
S6	206.0	-18.0	36.0	X
S7	170.0	0.0	36.0	X
S8	314.0	-24.0	34.0	X
S9	314.0	-7.0	23.0	X
S10	314.0	-7.0	11.0	X
S11	278.0	-24.0	34.0	X

Instrument	X(in.)	Y(in.)	Z(in.)	Orientation
S12	278.0	-7.0	23.0	X
S13	278.0	-7.0	10.3	X
S14	242.0	-24.0	34.0	X
S15	242.0	-7.0	23.0	X
S16	242.0	-7.0	10.0	X
S17	206.0	-24.0	34.0	X
S18	206.0	-7.0	23.0	X
S19	204.0	-7.0	10.3	X
S20	170.0	-24.0	34.0	X
S21	170.0	-7.0	23.0	X
S22	170.0	-7.0	11.0	X

Note: Reference Z = 0 as the bottom surface of the beam

FDOT Research
Bond performance of post-tensioning tendons with corrosion Inhibitor
BED31-977-07

University of Florida
Dept. of Civil and Coastal Engineering

Task 3: Experimental Test Plan
Specimen D19M : 60-mm concrete strain gage
Sheet 17 of 25

17

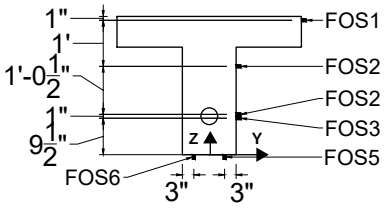

Cross Section B - B

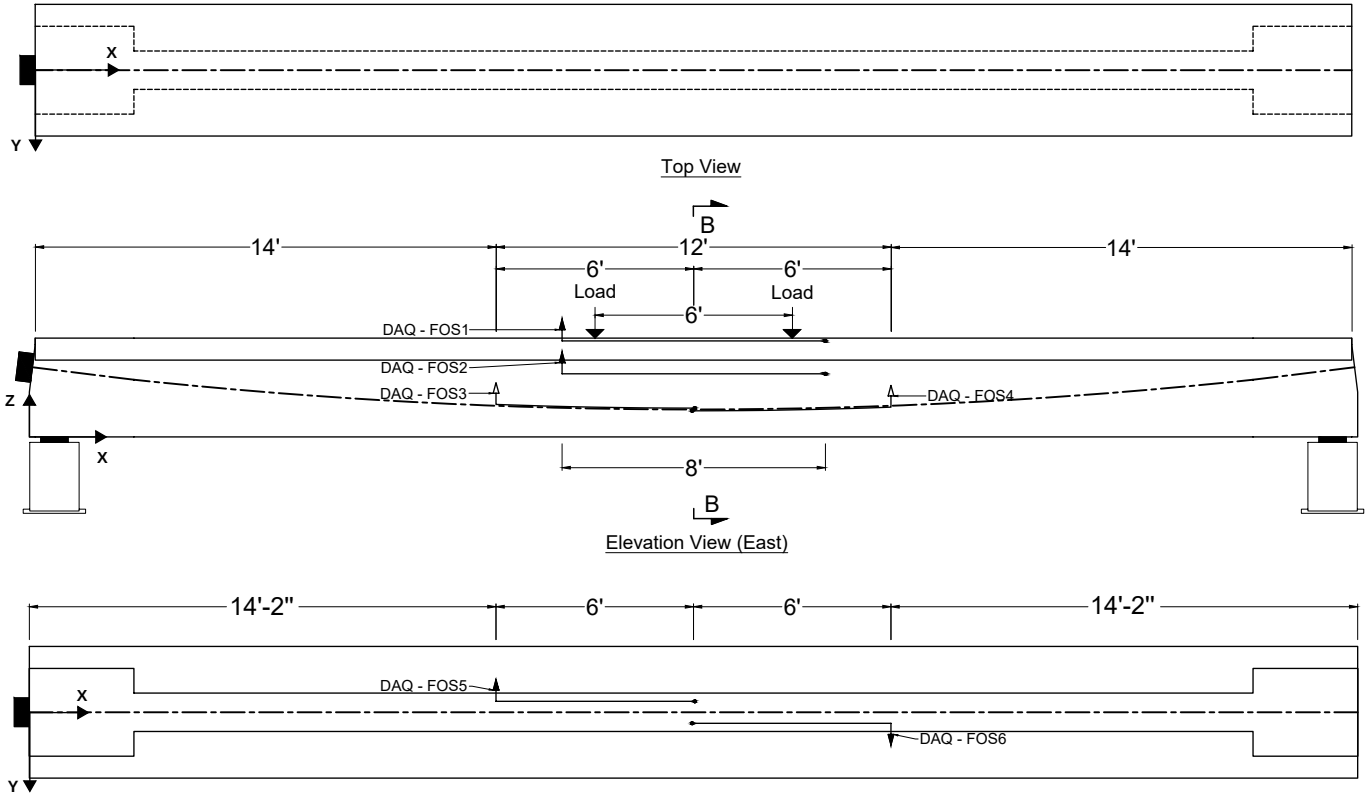

Key:

- Laser displacement transducer (D)
- 60-mm concrete strain gage (S)
- Fiber optics sensors (FOS)
- Digital image correlation (DIC)
- Vibrating wire strain gage (V)

Instrument	Start			Midpoint			End			Orientation	Note
	X(in.)	Y(in.)	Z(in.)	X(in.)	Y(in.)	Z(in.)	X(in.)	Y(in.)	Z(in.)	X	
FOS1	194.0	24.0	35.0				290.0	24.0	35.0	X	
FOS2	194.0	7.0	23.0				290.0	7.0	23.0	X	
FOS3	170.0	7.0	11.5	206.0	7.0	10.8	242.5	7.0	10.5	X	Install sensor along tendon profile
FOS4	314.0	7.0	10.5	278.0	7.0	9.8	241.5	7.0	9.5	X	Install sensor along tendon profile
FOS5	170.0	-4.0	0.0				242.5	-4.0	0.0	X	
FOS6	314.0	4.0	0.0				241.5	4.0	0.0	X	

Note: Reference Z = 0 as the bottom surface of the beam

FDOT Research
Bond performance of post-tensioning tendons with corrosion Inhibitor
BED31-977-07

University of Florida
Dept. of Civil and Coastal Engineering

Task 3: Experimental Test Plan
Specimen D19M : Fiber optics sensors
Sheet 18 of 25

18

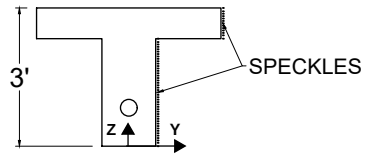

Cross Section B - B

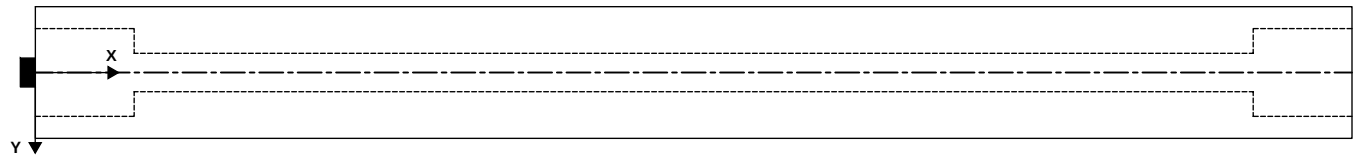

Top View

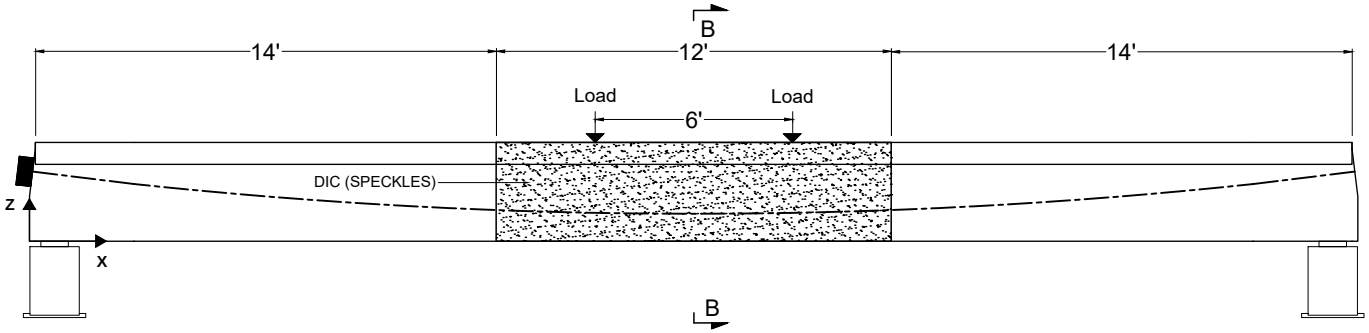

Elevation View (East)

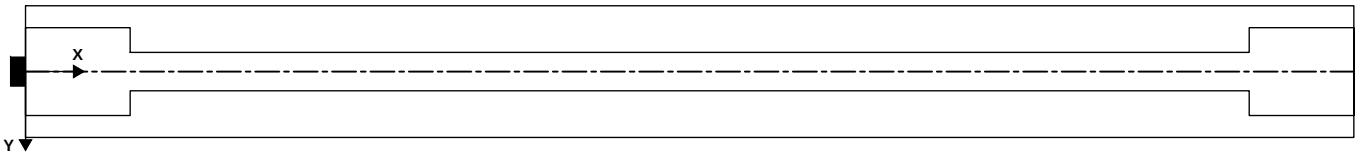

Bottom View

Key:

- Laser displacement transducer (D)
- 60-mm concrete strain gage (S)
- Fiber optics sensors (FOS)
- Digital image correlation (DIC)
- Vibrating wire strain gage (V)

Instrument	Area		Orientation
	length (ft)	height (ft)	
DIC	12.0	3.0	XZ

Note: Reference Z = 0 as the bottom surface of the beam

FDOT Research
Bond performance of post-tensioning tendons with corrosion Inhibitor
BED31-977-07

University of Florida
Dept. of Civil and Coastal Engineering

Task 3: Experimental Test Plan
Specimen D19M : Digital image correlation
Sheet 19 of 25

19

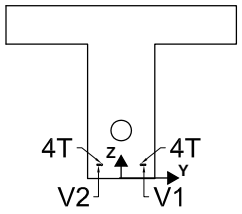

Cross Section B - B

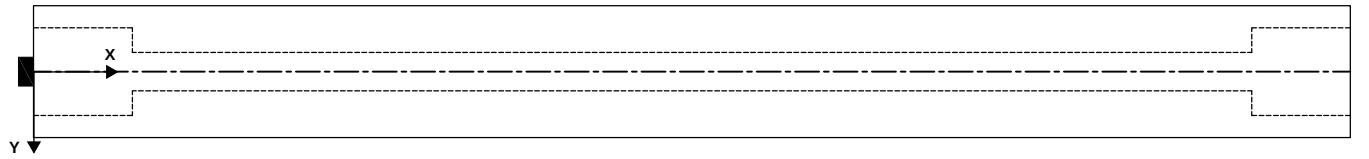

Top View

B

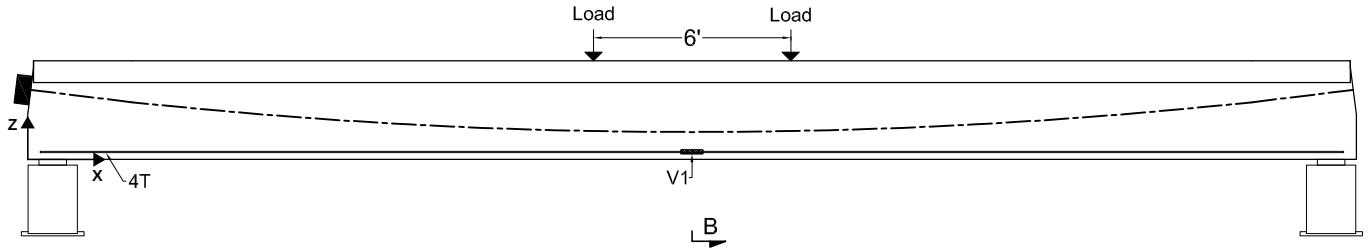

B

Elevation View (East)

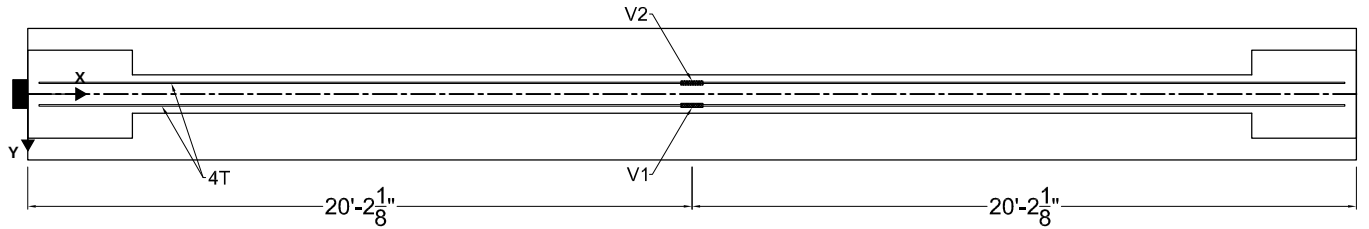

Bottom View

Key:

- Laser displacement transducer (D)
- 60-mm concrete strain gage (S)
- Fiber optics sensors (FOS)
- Digital image correlation (DIC)
- Vibrating wire strain gage (V)

Instrument	X(in.)	Y(in.)	Z(in.)	Orientation
V1	242.0	4.1	2.8	X
V2	242.0	-4.1	2.8	X

Note: Reference Z = 0 as the bottom surface of the beam

FDOT Research
Bond performance of post-tensioning tendons with corrosion Inhibitor
BED31-977-07

University of Florida
Dept. of Civil and Coastal Engineering

Task 3: Experimental Test Plan
Specimen D19M : Vibrating wire strain gage
Sheet 20 of 25

20

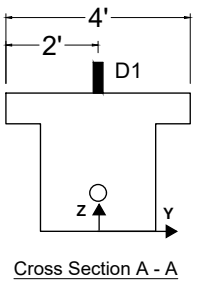

Cross Section A - A

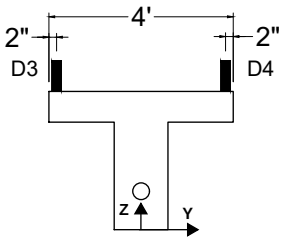

Cross Section B - B

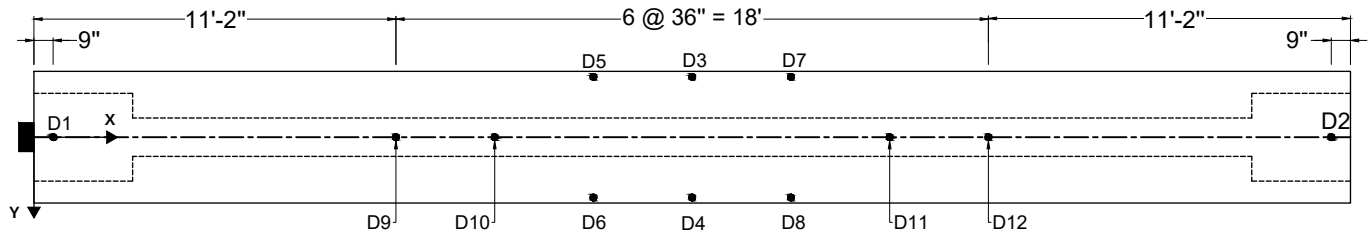

Top View

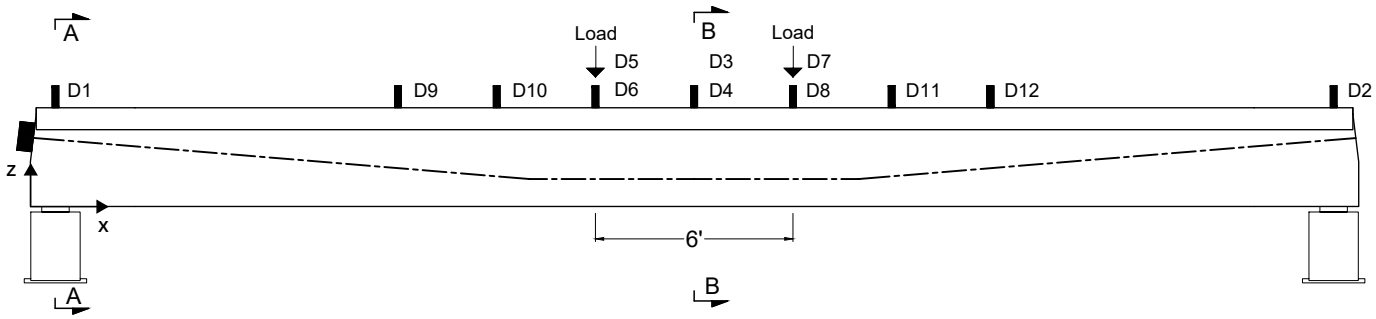

Elevation View (East)

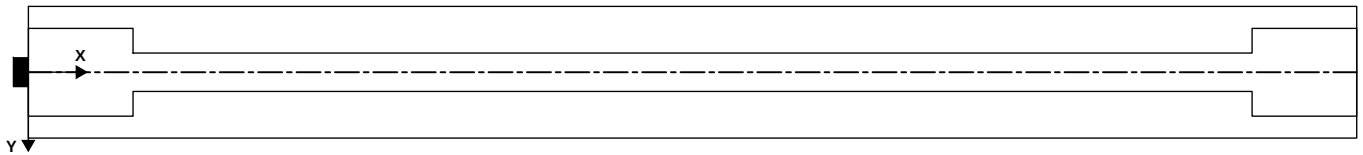

Bottom View

Key:

- Laser displacement transducer (D)
- 60-mm concrete strain gage (S)
- Fiber optics sensors (FOS)
- Digital image correlation (DIC)
- Vibrating wire strain gage (V)

Instrument	X(in.)	Y(in.)	Z(in.)	Orientation
D1	9.0	0.0	36.0	Z
D2	475.0	0.0	36.0	Z
D3	242.0	-22.0	36.0	Z
D4	242.0	22.0	36.0	Z
D5	206.0	-22.0	36.0	Z
D6	206.0	22.0	36.0	Z
D7	278.0	-22.0	36.0	Z
D8	278.0	22.0	36.0	Z
D9	134.0	0.0	36.0	Z

Instrument	X(in.)	Y(in.)	Z(in.)	Orientation
D10	170.0	0.0	36.0	Z
D11	314.0	0.0	36.0	Z
D12	350.0	0.0	36.0	Z

Note: Reference Z = 0 as the bottom surface of the beam

FDOT Research
Bond performance of post-tensioning tendons with corrosion inhibitor
BED31-977-07

University of Florida
Dept. of Civil and Coastal Engineering

Task 3: Experimental Test Plan
Specimen D19P : Laser displacement transducer
Sheet 21 of 25

21

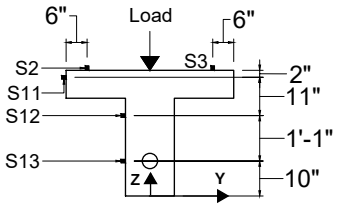

Cross Section A - A

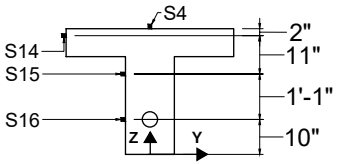

Cross Section B - B

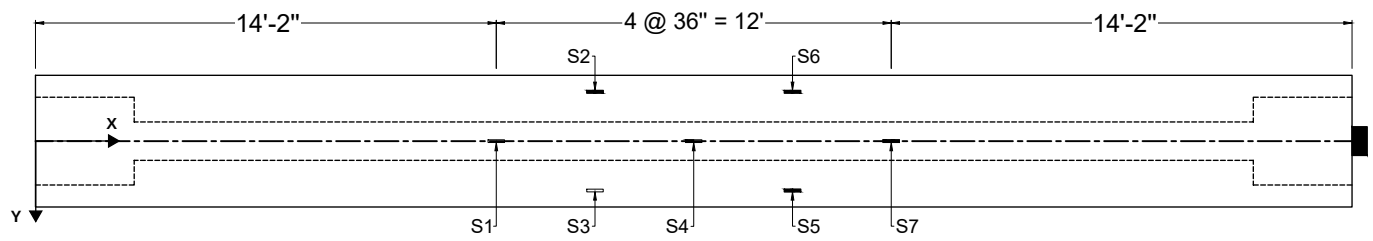

Top View

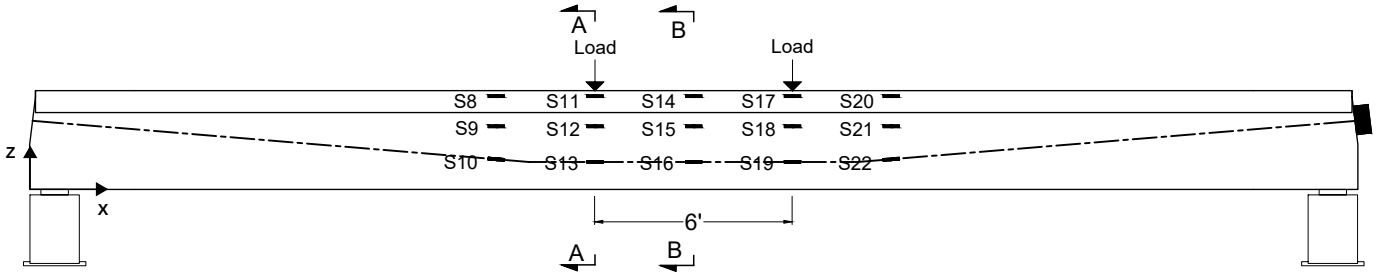

Elevation View (East)

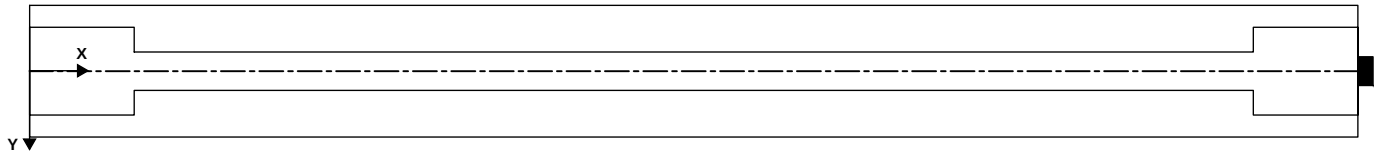

Bottom View

Key:

- Laser displacement transducer (D)
- 60-mm concrete strain gage (S)
- Fiber optics sensors (FOS)
- Digital image correlation (DIC)
- Vibrating wire strain gage (V)

Instrument	X(in.)	Y(in.)	Z(in.)	Orientation
S1	314.0	0.0	36.0	X
S2	278.0	-18.0	36.0	X
S3	278.0	18.0	36.0	X
S4	242.0	0.0	36.0	X
S5	206.0	18.0	36.0	X
S6	206.0	-18.0	36.0	X
S7	170.0	0.0	36.0	X
S8	314.0	-24.0	34.0	X
S9	314.0	-7.0	23.0	X
S10	314.0	-7.0	11.0	X
S11	278.0	-24.0	34.0	X

Instrument	X(in.)	Y(in.)	Z(in.)	Orientation
S12	278.0	-7.0	23.0	X
S13	278.0	-7.0	10.3	X
S14	242.0	-24.0	34.0	X
S15	242.0	-7.0	23.0	X
S16	242.0	-7.0	10.0	X
S17	206.0	-24.0	34.0	X
S18	206.0	-7.0	23.0	X
S19	204.0	-7.0	10.3	X
S20	170.0	-24.0	34.0	X
S21	170.0	-7.0	23.0	X
S22	170.0	-7.0	11.0	X

Note: Reference Z = 0 as the bottom surface of the beam

FDOT Research
Bond performance of post-tensioning tendons with corrosion Inhibitor
BED31-977-07

University of Florida
Dept. of Civil and Coastal Engineering

Task 3: Experimental Test Plan
Specimen D19P : 60-mm concrete strain gage
Sheet 22 of 25

22

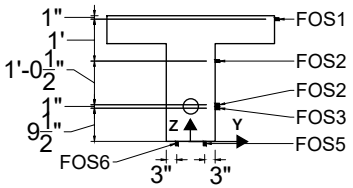

Cross Section B - B

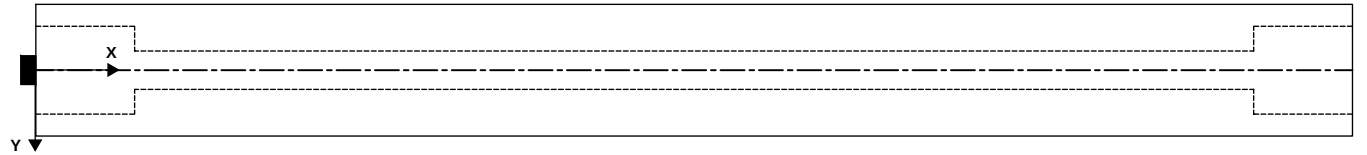

Top View

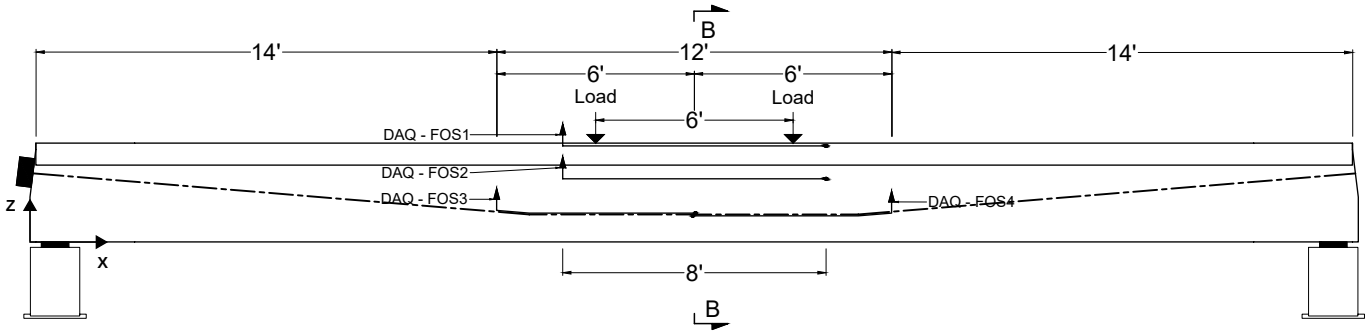

Elevation View (East)

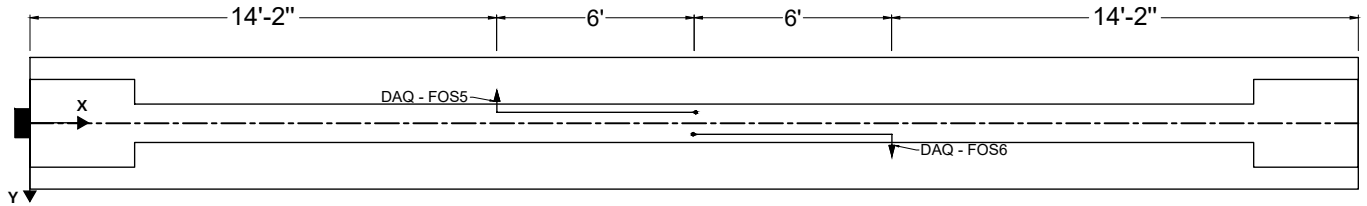

Bottom View

Key:

- Laser displacement transducer (D)
- 60-mm concrete strain gage (S)
- Fiber optics sensors (FOS)
- Digital image correlation (DIC)
- Vibrating wire strain gage (V)

Instrument	Start			Harped point (kink)			End			Orientation	Note
	X(in.)	Y(in.)	Z(in.)	X(in.)	Y(in.)	Z(in.)	X(in.)	Y(in.)	Z(in.)		
FOS1	194.0	24.0	35.0				290.0	24.0	35.0	X	
FOS2	194.0	7.0	23.0				290.0	7.0	23.0	X	
FOS3	170.0	7.0	11.5	182.0	7.0	10.5	242.5	7.0	10.5	X	Install sensor along tendon profile
FOS4	314.0	7.0	10.5	314.0	7.0	9.5	241.5	7.0	9.5	X	Install sensor along tendon profile
FOS5	170.0	-4.0	0.0				242.5	-4.0	0.0	X	
FOS6	314.0	4.0	0.0				241.5	4.0	0.0	X	

Note: Reference Z = 0 as the bottom surface of the beam

FDOT Research
Bond performance of post-tensioning tendons with corrosion Inhibitor
BED31-977-07

University of Florida
Dept. of Civil and Coastal Engineering

Task 3: Experimental Test Plan
Specimen D19P : Fiber optics sensors
Sheet 23 of 25

23

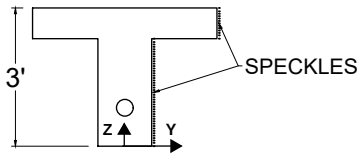

Cross Section B - B

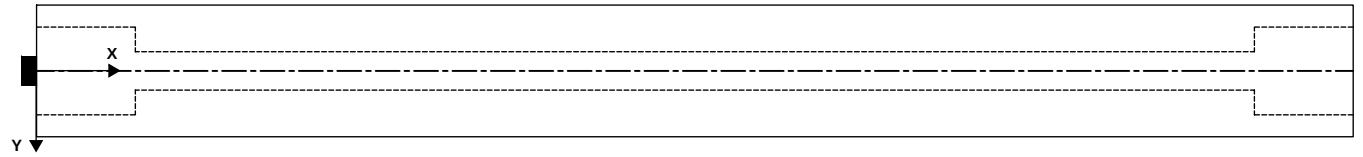

Top View

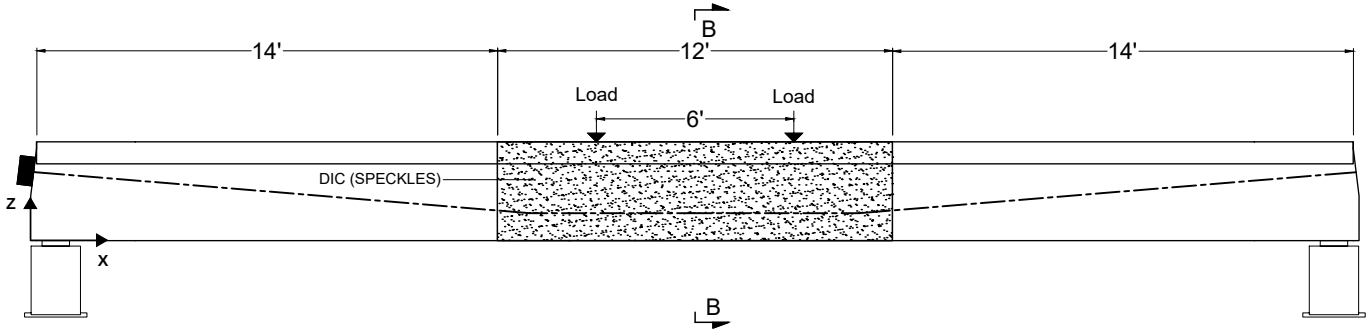

Elevation View (East)

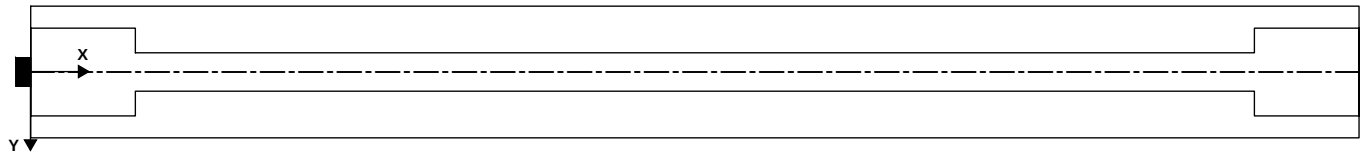

Bottom View

Key:

- Laser displacement transducer (D)
- 60-mm concrete strain gage (S)
- Fiber optics sensors (FOS)
- Digital image correlation (DIC)
- Vibrating wire strain gage (V)

Instrument	Area		Orientation
	length (ft)	height (ft)	
DIC	12.0	3.0	XZ

Note: Reference Z = 0 as the bottom surface of the beam

FDOT Research
Bond performance of post-tensioning tendons with corrosion Inhibitor
BED31-977-07

University of Florida
Dept. of Civil and Coastal Engineering

Task 3: Experimental Test Plan
Specimen D19P : Digital image correlation
Sheet 24 of 25

24

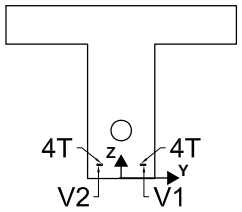

Cross Section B - B

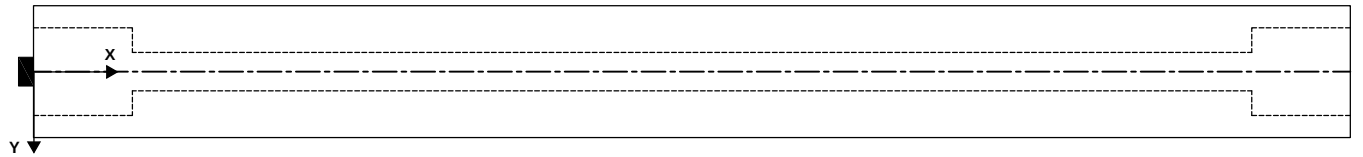

Top View

B

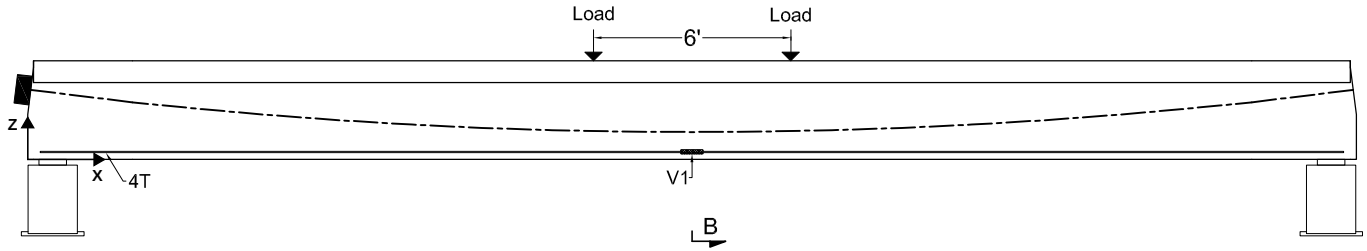

B

Elevation View (East)

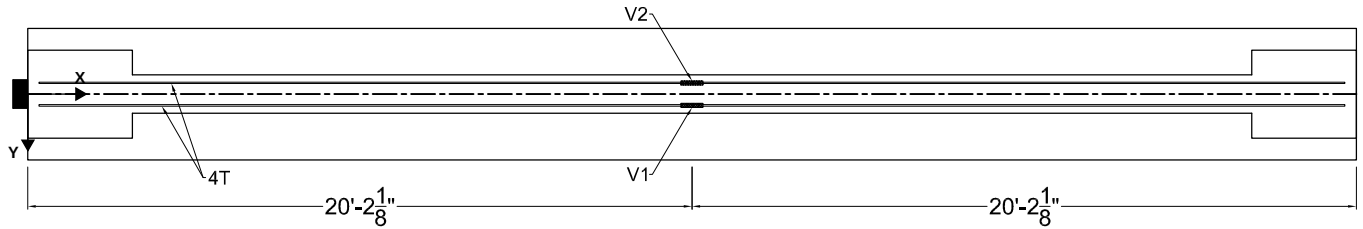

Bottom View

Key:

- Laser displacement transducer (D)
- 60-mm concrete strain gage (S)
- Fiber optics sensors (FOS)
- Digital image correlation (DIC)
- Vibrating wire strain gage (V)

Instrument	X(in.)	Y(in.)	Z(in.)	Orientation
V1	242.0	4.1	2.8	X
V2	242.0	-4.1	2.8	X

Note: Reference Z = 0 as the bottom surface of the beam

FDOT Research
Bond performance of post-tensioning tendons with corrosion Inhibitor
BED31-977-07

University of Florida
Dept. of Civil and Coastal Engineering

Task 3: Experimental Test Plan
Specimen D19P : Vibrating wire strain gage
Sheet 25 of 25

25

APPENDIX C
POST-TENSIONING PROCEDURE

The procedures for post-tensioning of beam specimens are provided on the following pages.

Procedure for Post-tensioning of S06 Beams

Specimens S06 will be post-tensioned after the concrete reaches the specified compressive strength (8500 psi). Anchorage hardware needed for the post-tensioning stage is listed in Table C.1. Figure C.1 shows the strand layout in the anchor heads. Target PT force corresponds to 70% of f_{pu} (specified tensile strength of prestressing strands, 270 ksi). Table C.2 presents the jacking forces and corresponding pressures on the multistrand jack for the PT tendon.

Table C.1. Required hardware for post-tensioning of beam specimen S06.

Beam specimen	0.6-in. PT strands			Dead end	Live end
	No. of tendons	No. of strands/ tendon	Length of strands (ft)		
S06	1	06	46	(1) wedge plate/anchor head (6) wedges	(1) multistrand jack (1) jack stressing plate (1) wedge plate/anchor head (6) wedges

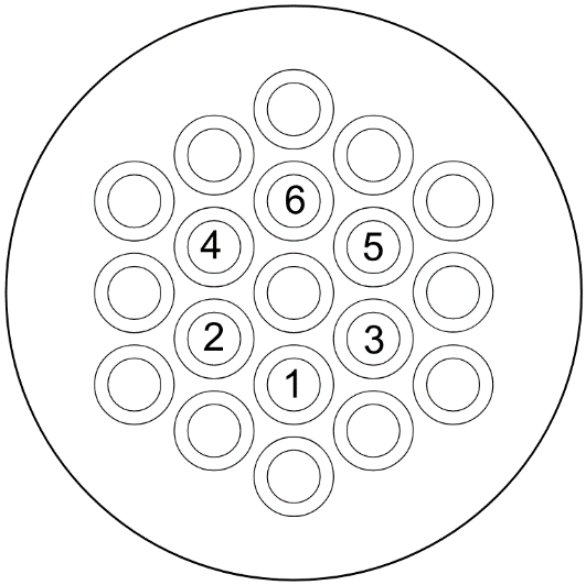

Figure C.1. Layout of prestressing strands in post-tensioning anchor heads for specimen S06.

Table C.2. Specimen jack force (per tendon) and pressure on multistrand jack (S06)

% of P_{jack}		5%	20%	40%	60%	80%	100%
Force (kip)		12	49	98	148	197	246
Pressure (psi)	Pressure gage (Master)	210	500	890	1280	1680	2070

Post-tensioning procedure:

- Push prestressing strands by hand into PT duct following the layouts provided in Figure C.1 and prevent twisting of the strands anywhere along the tendon length.
- Install wedge plate on dead end (0° rotation pattern).
- Install wedge plate on live end (0° rotation pattern).
- Install wedges on strands at both ends of the specimen.
- Check that the strand pattern on wedge plate is same for the live end and dead end
- Hoist the multistrand jack into position for stressing the live end while ensuring proper alignment of the strands between the wedge plate and jack.
- Use multistrand jack at the live end to cinch washers into place.
- Stress multistrand jack to 20% of P_{jack} (final jacking force) and reset the jack to remove any slack in the tendon.
- Measure the elongation of the tendon at each load step: 5%, 20%, 40%, 60% and 80% of P_{jack}.
- Complete the jacking process by stressing the multistrand jack to 100% of P_{jack}, then mark and measure the final elongation.

Procedure for Post-tensioning of S12 Beams

Specimens S12 will be post-tensioned after the concrete reaches the specified compressive strength (8500 psi). Anchorage hardware needed for the post-tensioning stage is listed in Table C.3. Figure C.2 shows the strand layout in the anchor heads. Target PT force corresponds to 70% of f_{pu} (specified tensile strength of prestressing strands, 270 ksi). Table C.4 presents the jacking forces and corresponding pressures on the multistrand jack for the PT tendon.

Table C.3. Required hardware for post-tensioning of beam specimen S12.

Beam specimen	0.6-in. PT strands			Dead end	Live end
	No. of tendons	No. of strands/ tendon	Length of strands (ft)		
S12	1	12	46	(1) wedge plate/anchor head (12) wedges	(1) multistrand jack (1) jack stressing plate (1) wedge plate/anchor head (12) wedges

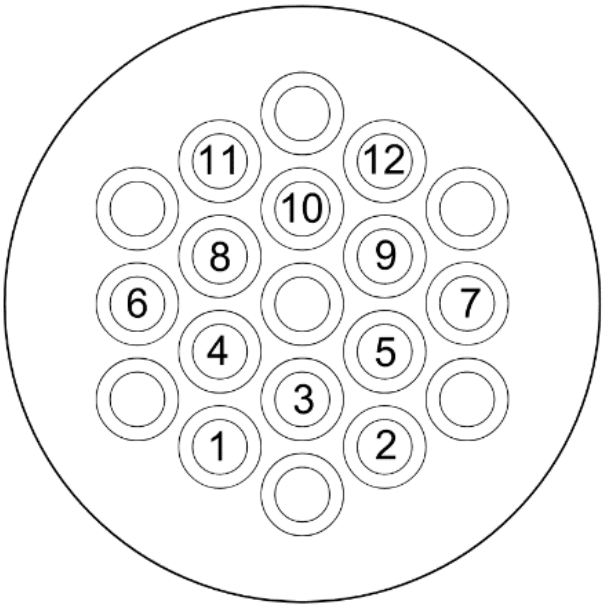

Figure C.2. Layout of prestressing strands in post-tensioning anchor heads for specimen S12.

Table C.4. Specimen jack force (per tendon) and pressure on multistrand jack (S12)

% of P_{jack}		5%	20%	40%	60%	80%	100%
Force (kip)		25	98	197	295	394	492
Pressure (psi)	Pressure gage (Master)	310	890	1680	2460	3240	4020

Post-tensioning procedure:

- Push prestressing strands by hand into PT duct following the layouts provided in Figure C.2 and prevent twisting of the strands anywhere along the tendon length.
- Install wedge plate on dead end (0° rotation pattern).
- Install wedge plate on live end (0° rotation pattern).
- Install wedges on strands at both ends of the specimen.
- Check that the strand pattern on wedge plate is same for the live end and dead end
- Hoist the multistrand jack into position for stressing the live end while ensuring proper alignment of the strands between the wedge plate and jack.
- Use multistrand jack at the live end to cinch washers into place.
- Stress multistrand jack to 20% of P_{jack} (final jacking force) and reset the jack to remove any slack in the tendon.
- Measure the elongation of the tendon at each load step: 5%, 20%, 40%, 60% and 80% of P_{jack}.
- Complete the jacking process by stressing the multistrand jack to 100% of P_{jack}, then mark and measure the final elongation.

Procedure for Post-tensioning of S19 Beams

Specimens S19 will be post-tensioned after the concrete reaches the specified compressive strength (8500 psi). Anchorage hardware needed for the post-tensioning stage is listed in Table C.5. Figure C.3 shows the strand layout in the anchor heads. Target PT force corresponds to 70% of f_{pu} (specified tensile strength of prestressing strands, 270 ksi). Table C.6 presents the jacking forces and corresponding pressures on the multistrand jack for the PT tendon.

Table C.5. Required hardware for post-tensioning of beam specimen S19.

Beam specimen	0.6-in. PT strands			Dead end	Live end
	No. of tendons	No. of strands/ tendon	Length of strands (ft)		
S19	1	19	46	(1) wedge plate/anchor head (19) wedges	(1) multistrand jack (1) jack stressing plate (1) wedge plate/anchor head (19) wedges

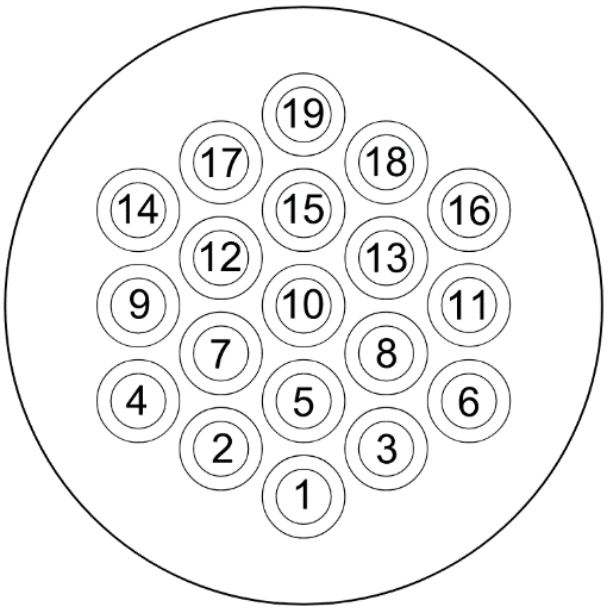

Figure C.3. Layout of prestressing strands in post-tensioning anchor heads for specimen S19.

Table C.6. Specimen jack force (per tendon) and pressure on multistrand jack (S19)

% of P_{jack}		5%	20%	40%	60%	80%	100%
Force (kip)		39	156	312	467	623	779
Pressure (psi)	Pressure gage (Master)	420	1350	2590	3830	5060	6300

Post-tensioning procedure:

- Push prestressing strands by hand into PT duct following the layouts provided in Figure C.3 and prevent twisting of the strands anywhere along the tendon length.
- Install wedge plate on dead end (0° rotation pattern).
- Install wedge plate on live end (0° rotation pattern).
- Install wedges on strands at both ends of the specimen.
- Check that the strand pattern on wedge plate is same for the live end and dead end
- Hoist the multistrand jack into position for stressing the live end while ensuring proper alignment of the strands between the wedge plate and jack.
- Use multistrand jack at the live end to cinch washers into place.
- Stress multistrand jack to 20% of P_{jack} (final jacking force) and reset the jack to remove any slack in the tendon.
- Measure the elongation of the tendon at each load step: 5%, 20%, 40%, 60% and 80% of P_{jack}.
- Complete the jacking process by stressing the multistrand jack to 100% of P_{jack}, then mark and measure the final elongation.

Procedure for Post-tensioning of D19-M Beams

Specimens D19-M will be post-tensioned after the concrete reaches the specified compressive strength (8500 psi). Anchorage hardware needed for the post-tensioning stage is listed in Table C.7. Figure C.4 shows the strand layout in the anchor heads. Target PT force corresponds to 70% of f_{pu} (specified tensile strength of prestressing strands, 270 ksi). Table C.8 presents the jacking forces and corresponding pressures on the multistrand jack for the PT tendon.

Table C.7. Required hardware for post-tensioning of beam specimen D19-M.

Beam specimen	0.6-in. PT strands			Dead end	Live end
	No. of Tendons	No. of strands/ tendon	Length of strands (ft)		
D19-M	1	19	46.5	(1) wedge plate/anchor head (19) wedges	(1) multistrand jack (1) jack stressing plate (1) wedge plate/anchor head (19) wedges

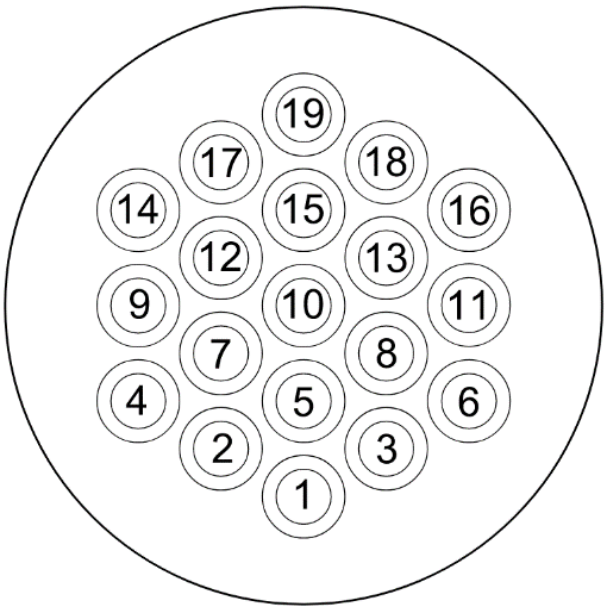

Figure C.4. Layout of prestressing strands in post-tensioning anchor heads for specimen D19-M.

Table C.8. Specimen jack force (per tendon) and pressure on multistrand jack (D19-M)

% of P_{jack}		5%	20%	40%	60%	80%	100%
Force (kip)		39	156	312	467	623	779
Pressure (psi)	Pressure gage (Master)	420	1350	2590	3830	5060	6300

Post-tensioning procedure:

- Push prestressing strands by hand into PT duct following the layouts provided in Figure C.4 and prevent twisting of the strands anywhere along the tendon length.
- Install wedge plate on dead end (0° rotation pattern).
- Install wedge plate on live end (0° rotation pattern).
- Install wedges on strands at both ends of the specimen.
- Check that the strand pattern on wedge plate is same for the live end and dead end
- Hoist the multistrand jack into position for stressing the live end while ensuring proper alignment of the strands between the wedge plate and jack.
- Use multistrand jack at the live end to cinch washers into place.
- Stress multistrand jack to 20% of P_{jack} (final jacking force) and reset the jack to remove any slack in the tendon.
- Measure the elongation of the tendon at each load step: 5%, 20%, 40%, 60% and 80% of P_{jack}.
- Complete the jacking process by stressing the multistrand jack to 100% of P_{jack}, then mark and measure the final elongation.

Procedure for Post-tensioning of D19-P Beams

Specimens D19-P will be post-tensioned after the concrete reaches the specified compressive strength (8500 psi). Anchorage hardware needed for the post-tensioning stage is listed in Table C.9. Figure C.5 shows the strand layout in the anchor heads. Target PT force corresponds to 70% of f_{pu} (specified tensile strength of prestressing strands, 270 ksi). Table C.10 presents the jacking forces and corresponding pressures on the multistrand jack for the PT tendon.

Table C.9. Required hardware for post-tensioning of beam specimen D19-P.

Beam specimen	0.6-in. PT strands			Dead end	Live end
	No. of Tendons	No. of strands/ tendon	Length of strands (ft)		
D19-P	1	19	46.5	(1) wedge plate/anchor head (19) wedges	(1) multistrand jack (1) jack stressing plate (1) wedge plate/anchor head (19) wedges

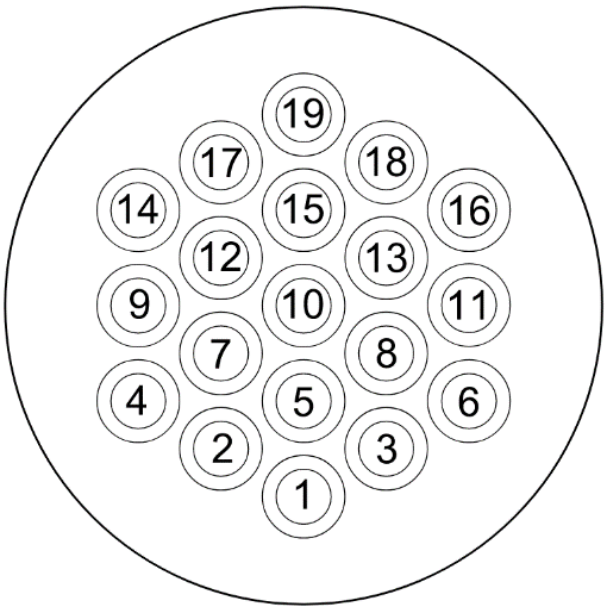

Figure C.5. Layout of prestressing strands in post-tensioning anchor heads for specimen D19-P.

Table C.10. Specimen jack force (per tendon) and pressure on multistrand jack (D19-P)

% of P_{jack}		5%	20%	40%	60%	80%	100%
Force (kip)		39	156	312	467	623	779
Pressure (psi)	Pressure gage (Master)	420	1350	2590	3830	5060	6300

Post-tensioning procedure:

- Push prestressing strands by hand into PT duct following the layouts provided in Figure C.5 and prevent twisting of the strands anywhere along the tendon length.
- Install wedge plate on dead end (0° rotation pattern).
- Install wedge plate on live end (0° rotation pattern).
- Install wedges on strands at both ends of the specimen.
- Check that the strand pattern on wedge plate is same for the live end and dead end
- Hoist the multistrand jack into position for stressing the live end while ensuring proper alignment of the strands between the wedge plate and jack.
- Use multistrand jack at the live end to cinch washers into place.
- Stress multistrand jack to 20% of P_{jack} (final jacking force) and reset the jack to remove any slack in the tendon.
- Measure the elongation of the tendon at each load step: 5%, 20%, 40%, 60% and 80% of P_{jack}.
- Complete the jacking process by stressing the multistrand jack to 100% of P_{jack}, then mark and measure the final elongation.

APPENDIX D
GROUT INJECTION PROCEDURE

The procedures for grot injection of beam specimens are provided on the following pages.

Procedure for Grouting of S06 Beams

Each S06 specimen will be grouted after post-tensioning of the tendon. To achieve a fully bonded post-tensioned system, the corrugated metal duct carrying the 6-strand tendon will be grouted with pre-packaged grout. The pre-packaged grout to be used for the project is a non-shrink grout from the FDOT Approved Product List specified to be used as duct filler for bonded post-tensioned structures as shown in Table D.1.

Table D.1. Grout preparation for S06 beam specimens.

Beam specimens	Wet volume per specimen (cu. ft)	Grout specifications		
		Grout type	Mixing ratio by weight (Water: Grout)	Compressive strength 28 days
S06	1	Pre-packaged (Euco Cable Grout PTX)	0.25	> 7,000 psi

For the S06 beam specimens that will be treated with corrosion inhibitor (S06-M-T and S06-M-CT), the wedge plate, exposed wedge faces, strand surfaces, and grout cap shall be prepared so as to enable efficient removal of grout prior to corrosion inhibitor injection. A combination of duct tape and grease shall be applied to prevent bonding of grout to key steel surfaces that must remain unimpeded in order for corrosion inhibitor to be injected.

Grout cubes shall be prepared from the same batch of grout that was used to pump the specimens. Given that all three S06 specimens are pumped from the same batch of grout, the grout cubes obtained directly from the pump should be able to accurately represent the grout characteristics of any of the beams. A total of 24 grout cubes will be cast, comprising two sets (6 cubes) to measure the 7-day and 28-day compressive strengths. Each set will consist of three grout cubes to determine the average compressive strength in accordance with ASTM C109, “Standard Test Method for Compressive Strength of Hydraulic Cement Mortars (Using 50 mm [2 in.] Cube Specimens).” Another three sets of grout cubes (a total of 9 cubes) will be cast to determine the untreated strengths, which will be compared with those of cubes (three sets of cubes) soaked in the corrosion inhibitor fluid at three different treatment ages. Table D.2 shows the matrix of grout cubes to be cast for S06 beams.

Table D.2. Number of grout cubes to cast for S06 beams.

Beam specimen	Number of untreated grout cubes	Number of treated (soaked) grout cubes	Total number of grout cubes to cast
S06	15	9	24

Procedure for Grouting of S12 Beams

Each S12 specimen will be grouted after post-tensioning of the tendon. To achieve a fully bonded post-tensioned system, the corrugated metal duct carrying the 12-strand tendon will be grouted with pre-packaged grout. The pre-packaged grout to be used for the project is a non-shrink grout from the FDOT Approved Product List specified to be used as duct filler for bonded post-tensioned structures as shown in Table D.3.

Table D.3. Grout preparation for S12 beam specimens.

Beam specimens	Wet volume per specimen (cu. ft)	Grout specifications		
		Grout type	Mixing ratio by weight (Water: Grout)	Compressive strength 28 days
S12	2.1	Pre-packaged (Euco Cable Grout PTX)	0.25	> 7,000 psi

For the S12 beam specimen that will be treated with corrosion inhibitor (S12-P-T), the wedge plate, exposed wedge faces, strand surfaces, and grout cap shall be prepared so as to enable efficient removal of grout prior to corrosion inhibitor injection. A combination of duct tape and grease shall be applied to prevent bonding of grout to key steel surfaces that must remain unimpeded in order for corrosion inhibitor to be injected.

Grout cubes shall be prepared from the same batch of grout that was used to pump the specimens. Given that the two S12 specimens are pumped from the same batch of grout, the grout cubes obtained directly from the pump should be able to accurately represent the grout characteristics of any of the beams. A total of 24 grout cubes will be cast, comprising two sets (6 cubes) to measure the 7-day and 28-day compressive strengths. Each set will consist of three grout cubes to determine the average compressive strength in accordance with ASTM C109, “Standard Test Method for Compressive Strength of Hydraulic Cement Mortars (Using 50 mm [2 in.] Cube Specimens).” Another three sets of grout cubes (a total of 9 cubes) will be cast to determine the untreated strengths, which will be compared with those of cubes (three sets of cubes) soaked in the corrosion inhibitor fluid at three different treatment ages. Table D.4 shows the matrix of grout cubes to be cast for S12 beams.

Table D.4. Number of grout cubes to cast for S12 beams.

Beam specimen	Number of untreated grout cubes	Number of treated (soaked) grout cubes	Total number of grout cubes to cast
S12	15	9	24

Procedure for Grouting of S19 Beams

Each S19 specimen will be grouted after post-tensioning of the tendon. To achieve a fully bonded post-tensioned system, the corrugated metal duct carrying 19 strands tendon will be grouted with Portland cement grout. The plain cement grout to be used for the project (shown in Table D.5) is representative of the duct filler used in existing bridges in Florida constructed before the 'new' directions for post-tensioning was implemented (indicating the use of pre-packaged grout) in the year 2000.

Table D.5. Grout preparation for S19 beam specimens.

Beam specimens	Wet volume per specimen (cu. ft)	Grout specifications	
		Grout type	Mixing ratio by weight (Water: Grout)
S19	3.0	Type I/II Portland cement	0.44

For the S19 beam specimen that will be treated with corrosion inhibitor (S19-M-T), the wedge plate, exposed wedge faces, strand surfaces, and grout cap shall be prepared so as to enable efficient removal of grout prior to corrosion inhibitor injection. A combination of duct tape and grease shall be applied to prevent bonding of grout to key steel surfaces that must remain unimpeded in order for corrosion inhibitor to be injected.

Grout cubes shall be prepared from the same batch of grout that was used to pump the specimens. Given that the two S19 specimens are pumped from the same batch of grout, the grout cubes obtained directly from the pump should be able to accurately represent the grout characteristics of any of the beams. A total of 24 grout cubes will be cast, comprising two sets (6 cubes) to measure the 7-day and 28-day compressive strengths. Each set will consist of three grout cubes to determine the average compressive strength in accordance with ASTM C109, "Standard Test Method for Compressive Strength of Hydraulic Cement Mortars (Using 50 mm [2 in.] Cube Specimens)." Another three sets of grout cubes (a total of 9 cubes) will be cast to determine the untreated strengths, which will be compared with those of cubes (three sets of cubes) soaked in the corrosion inhibitor fluid at three different treatment ages. Table D.6 shows the matrix of grout cubes to be cast for S19 beams.

Table D.6. Number of grout cubes to cast for S19 beams.

Beam specimen	Number of untreated grout cubes	Number of treated (soaked) grout cubes	Total number of grout cubes to cast
S19	15	9	24

Procedure for Grouting of D19-M Beams

Each D19-M specimen will be grouted after post-tensioning of the tendon. To achieve a fully bonded post-tensioned system, the corrugated metal duct carrying 19 strands with draped tendon profile will be grouted with Legacy grout (Portland cement with admixtures). The legacy grout to be used for the project (shown in Table D.7) is representative of the duct filler used in existing bridges in Florida constructed before the 'new' directions for post-tensioning was implemented (indicating the use of pre-packaged grout) in the year 2000.

Table D.7. Grout preparation for D19-M beam specimens.

Beam specimens	Wet volume per specimen (cu. ft)	Grout specifications	
		Grout type	Mixing ratio by weight (Water: Cement)
D19-M	3.25	Type I/II Portland cement with admixtures	0.45

For the D19-M beam specimen that will be treated with corrosion inhibitor (D19-M-T), the wedge plate, exposed wedge faces, strand surfaces, and grout cap shall be prepared so as to enable efficient removal of grout prior to corrosion inhibitor injection. A combination of duct tape and grease shall be applied to prevent bonding of grout to key steel surfaces that must remain unimpeded in order for corrosion inhibitor to be injected.

Grout cubes shall be prepared from the same batch of grout that was used to pump the specimens. Given that the two D19-M specimens are pumped from the same batch of grout, the grout cubes obtained directly from the pump should be able to accurately represent the grout characteristics of any of the beams. A total of 18 grout cubes will be cast, comprising two sets (6 cubes) to measure the 7-day and 28-day compressive strengths. Each set will consist of three grout cubes to determine the average compressive strength in accordance with ASTM C109, "Standard Test Method for Compressive Strength of Hydraulic Cement Mortars (Using 50 mm [2 in.] Cube Specimens)." Another three sets of grout cubes (a total of 12 cubes) will be cast to determine the untreated strengths, which will be compared with those of cubes (two sets of cubes) soaked in the corrosion inhibitor fluid at two different treatment ages. Table D.8 shows the matrix of grout cubes to be cast for D19-M beams.

Table D.8. Number of grout cubes to cast for D19-M beams.

Beam specimen	Number of untreated grout cubes	Number of treated (soaked) grout cubes	Total number of grout cubes to cast
D19-M	12	6	18

Procedure for Grouting of D19-P Beams

Each D19-P specimen will be grouted after post-tensioning of the tendon. To achieve a fully bonded post-tensioned system, the corrugated metal duct carrying 19 strands with draped tendon profile will be grouted with Legacy grout (Portland cement with admixtures). The legacy grout to be used for the project (shown in Table D.9) is representative of the duct filler used in existing bridges in Florida constructed before the 'new' directions for post-tensioning was implemented (indicating the use of pre-packaged grout) in the year 2000. The D19-P specimens are grouted using the same batch of grout mix injected into the D19-M specimens.

Table D.9. Grout preparation for D19-M beam specimens.

Beam specimens	Wet volume per specimen (cu. ft)	Grout specifications	
		Grout type	Mixing ratio by weight (Water: Cement)
D19-P	3.25	Type I/II Portland cement with admixtures	0.45

For the D19-P beam specimen that will be treated with corrosion inhibitor (D19-P-T), the wedge plate, exposed wedge faces, strand surfaces, and grout cap shall be prepared so as to enable efficient removal of grout prior to corrosion inhibitor injection. A combination of duct tape and grease shall be applied to prevent bonding of grout to key steel surfaces that must remain unimpeded in order for corrosion inhibitor to be injected.

Grout cubes were prepared from the same batch of grout used to pump the beam specimens. Since both the D19-M and D19-P couplets were grouted using the same batch of grout, the grout cubes obtained directly from the pump accurately represent the grout characteristics for all beams in both couplets. Accordingly, the same set of 18 grout cubes (Table D.8), cast from grout collected directly from the grout pump used for the D19-M and D19-P beam specimens, is used to represent the grout strength for the D19-P beam specimens as well.

APPENDIX E
BEAM CRACKING PROCEDURE

The procedure for pre-impregnation cracking of beam specimen is provided on the following page.

Pre-cracking of S06-M-CT Beam Specimen

Specimen S06-M-CT, one of the three S06 beam specimens, will be pre-cracked before it is injected with the corrosion inhibitor. After the grout in the S06-M-CT beam specimen has reached the required compressive strength, it will be fully instrumented and subjected to four-point bending as shown in Figure E.1. Load will be applied using an Enerpac RR40018 actuator.

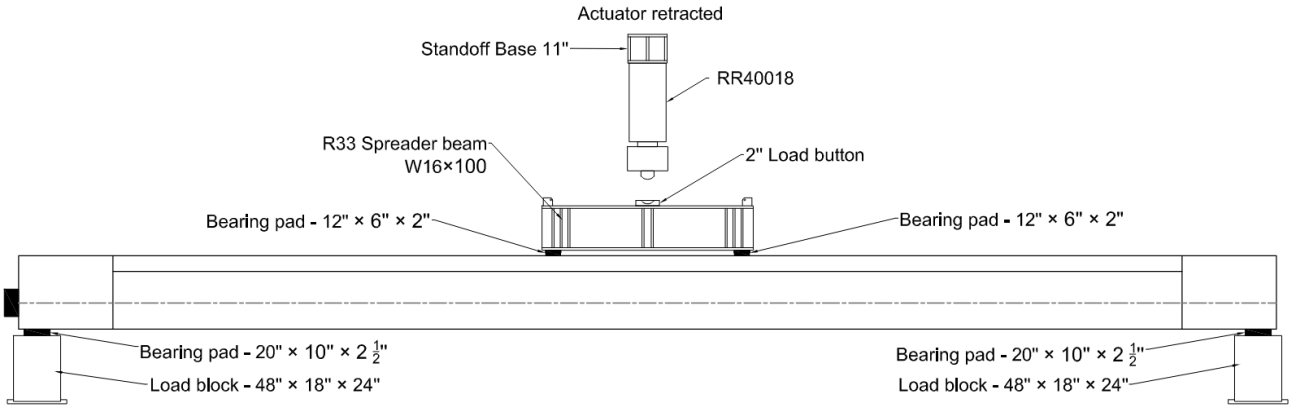

Figure E.1. Test setup for pre-impregnation cracking beam specimen S06.

Load will be applied at a rate of 0.25 kip/sec (15 kip/min). At multiple incremental load levels leading up to the estimated (i.e. pre-computed) cracking load, pauses will be used to visually inspect the beam for possible initiation of bottom flange (tension face) cracking. Loading will be terminated when prominent cracking extending approximately up to the tendon elevation is visually confirmed. Load will then be removed from the beam specimen. The specimen will be subsequently treated with corrosion inhibitor at the same time that specimen S06-M-T is treated with corrosion inhibitor.

APPENDIX F
CORROSION INHIBITOR IMPREGNATION

The procedures for corrosion inhibitor impregnation of beam specimens are provided on the following page.

Procedure for Corrosion Inhibitor Impregnation of Beam Specimens

Six beam specimens (S06-M-T, S12-P-T, S19-M-T, S06-M-CT, D19-M-T and D19-P-T) will be impregnated with corrosion inhibitor, as follows:

- After grouting, the anchorage ends will be prepared for impregnation of inhibitor by removing the PT end caps, removing grout within the cap (and grout surrounding the exposed strands), and removing grout surrounding the wedges. (Note: Power washing of the wedge plates shall not be performed as this process could potentially introduce water into the tendon.) After grout removal, the PT end caps will be re-installed until the date of corrosion inhibitor injection.
- Specimen S06-M-T, S12-P-T, S19-M-T, D19-M-T and D19-P-T will be injected with corrosion inhibitor without pre-cracking whereas specimen S06-M-TC will be pre-cracked before impregnation of corrosion inhibitor.
- Vector personnel will set up the Post-Tech PTI Impregnation System and will impregnate corrosion inhibitor into the live end anchorage, through the entire length of the beam, and exiting the dead-end anchorage.
- Flexural testing of treated beam specimens will take place at a point in time not less than 7 days after injection of corrosion inhibitor.

APPENDIX G
FLEXURAL TESTING PROCEDURE

The procedures for flexural testing of beam specimens are provided on the following pages.

Testing Protocol for S06 Beam Specimens

Beam specimens S06 (untreated and treated) will be tested in a four-point bending setup as shown in Figure G.1. The beam will be subjected to two-point loads offset 3ft from either side of midspan (i.e., 6 ft apart). Each beam will be simply supported at both ends on bearing pads. Load will be applied using an Enerpac RR40018 actuator.

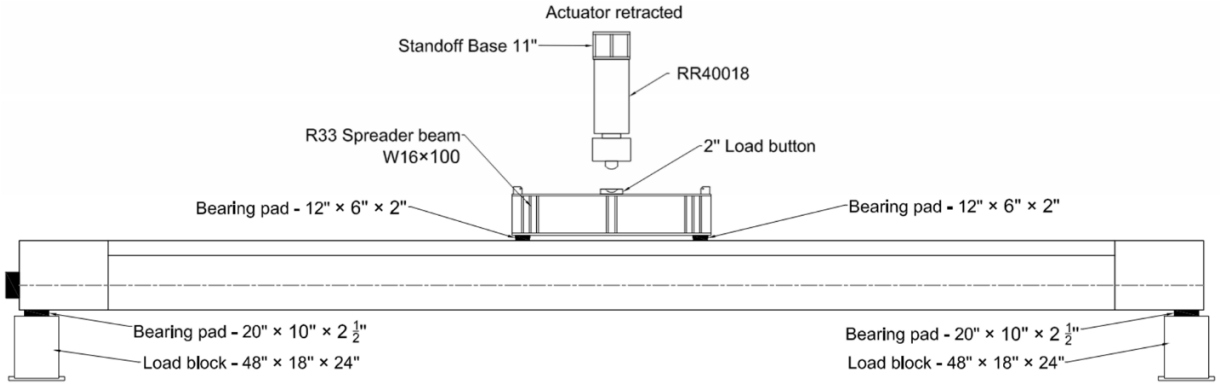

Figure G.1. Test setup for beam specimen S06.

Loading will be applied at a rate of 0.25 kip/sec (15 kip/min). Loading will be paused at key stages (Mcr, 20% Mn, 40% Mn, 60% Mn, and 70% Mn) as shown in Table G.1 to visually inspect the beam and to mark cracks.

Table G.1. Loading procedure for beam specimen S06

Intent	Applied Load (kip)	Expected deflection. at load point (in.) [D3/D4]
20% M_n	3.9	0.05
40% M_n	16.0	0.25
M_{cr}	24.7	0.39
60% M_n	28.1	0.47
70% M_n	34.2	1.59
M_n (ε_c= 0.003)	52.4	13.38

Ideally, the test will terminate when either compressive concrete crushing occurs, or when a plateau of load (vs. displacement) is reached. However, selected channels of instrumentation data will additionally be monitored (Figure G.2) so that testing can be terminated if applied loads or resulting displacement are found to significantly exceed the maximum expected values shown below.

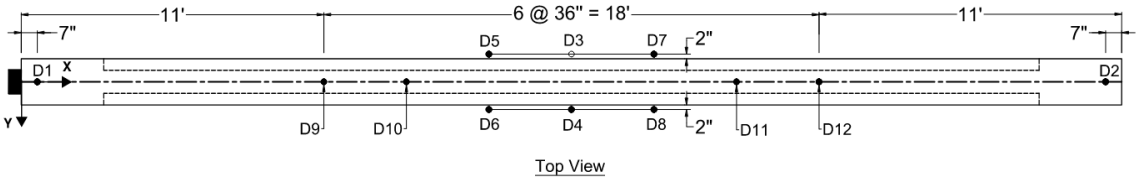

(a)

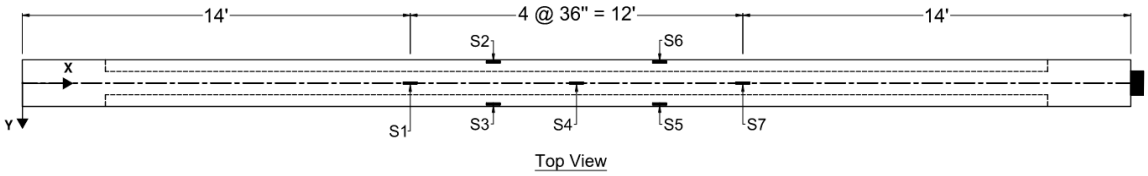

(b)

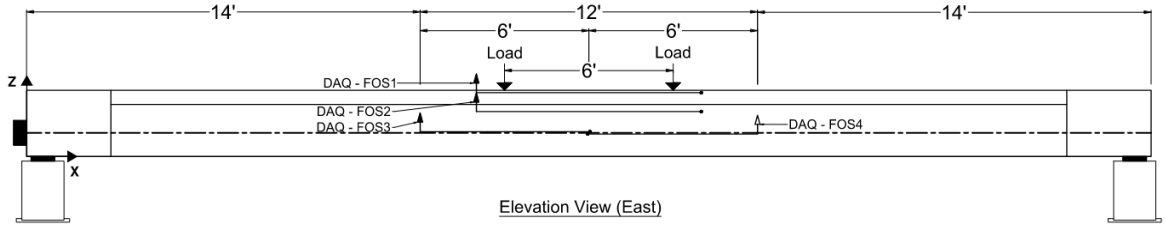

(d)

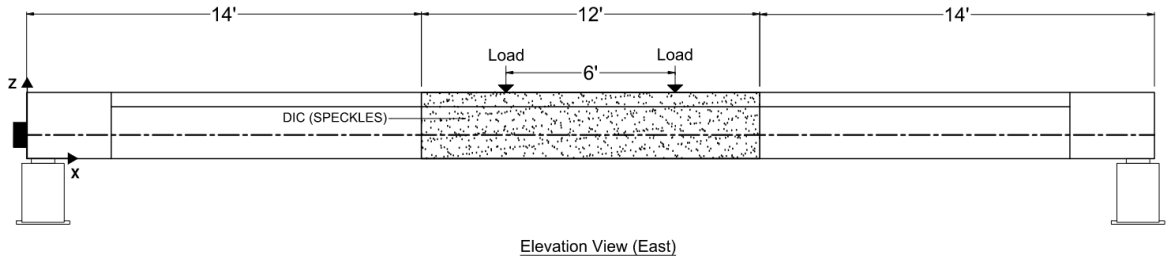

(e)

Figure G.2. Positions of instrumentation to monitor in real-time on S06 beam specimens: (a) Laser displacement transducer; (b) foil strain gage; (c) fiber optic sensor; and (d) digital image correlation.

Testing Protocol for S12 Beam Specimens

Beam specimens S12 (untreated and treated) will be tested in a four-point bending setup as shown in Figure G.3. The beam will be subjected to two-point loads offset 3ft from either side of midspan (i.e., 6 ft apart). Each beam will be simply supported at both ends on bearing pads. Load will be applied using an Enerpac RR40018 actuator.

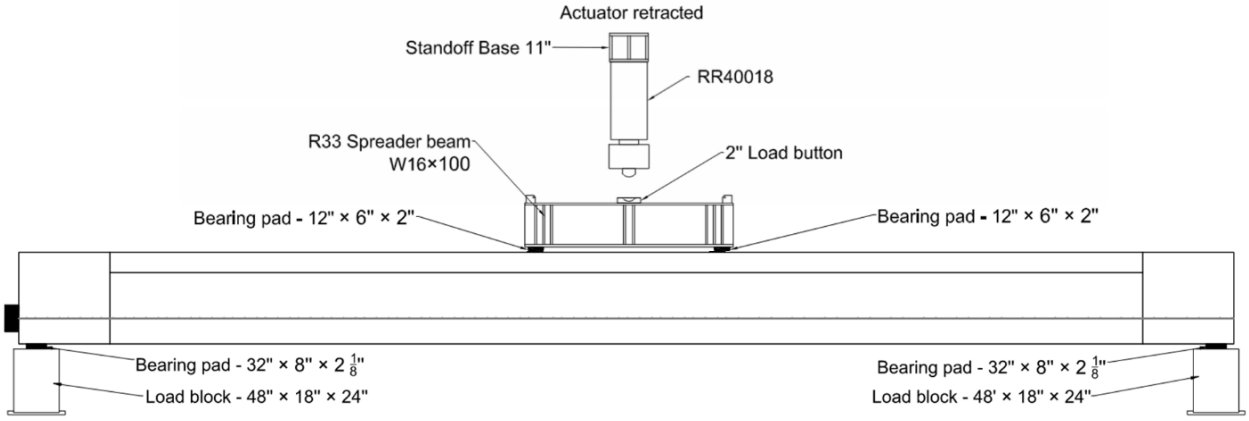

Figure G.3. Test setup for beam specimen S12.

Loading will be applied at a rate of 0.25 kip/sec (15 kip/min). Loading will be paused at key stages (Mcr, 20% Mn, 40% Mn, 60% Mn, and 70% Mn) as shown in Table G.2 to visually inspect the beam and to mark cracks.

Table G.2. Loading procedure for beam specimen S12

Intent	Applied Load (kip)	Expected deflection at load point (in.) [D3/D4]
20% M_n	20.9	0.12
40% M_n	55.6	0.32
M_{cr}	79.1	0.46
60% M_n	90.3	0.67
70% M_n	107.6	1.17
ε_c= 0.003 (M_n)	159.6	9.12

Ideally, the test will terminate when either compressive concrete crushing occurs, or when a plateau of load (vs. displacement) is reached. However, selected channels of instrumentation data will additionally be monitored (Figure G.4) so that testing can be terminated if applied loads or

resulting displacement are found to significantly exceed the maximum expected values shown below.

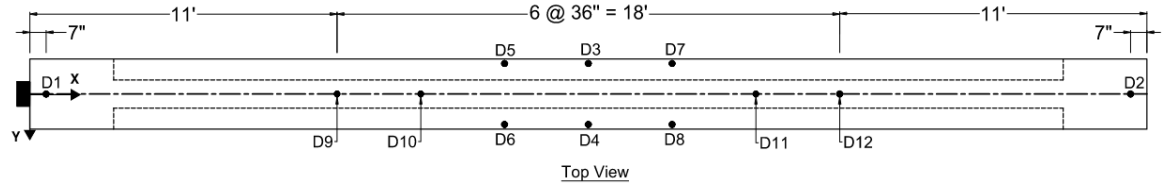

(a)

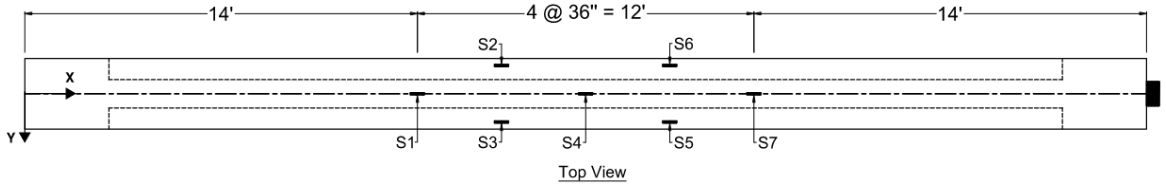

(b)

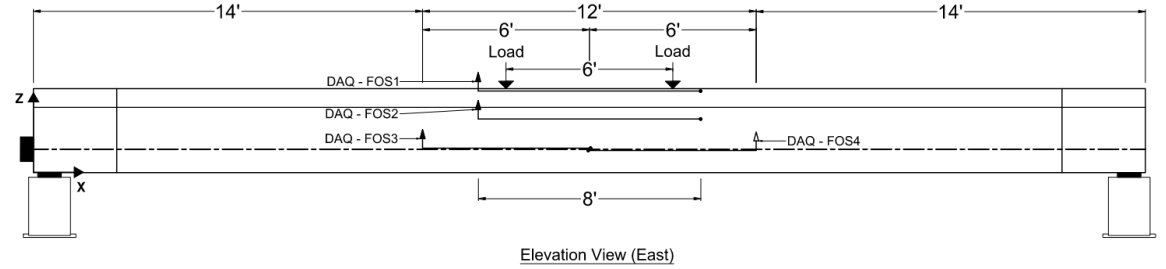

(c)

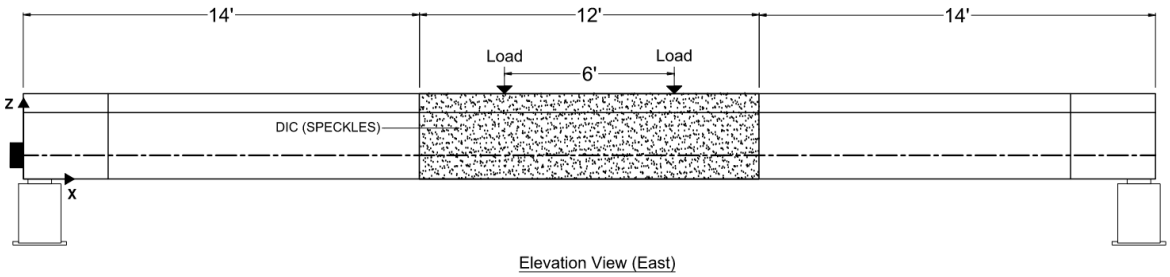

(d)

Figure G.4. Positions of instrumentation to monitor in real-time on S06 beam specimens: (a) Laser displacement transducer; (b) foil strain gage; (c) fiber optic sensor; and (d) digital image correlation.

Testing Protocol for S19 Beam Specimens

Beam specimens S19 (untreated and treated) will be tested in a four-point bending setup as shown in Figure G.5. The beam will be subjected to two-point loads offset 3ft from either side of midspan (i.e., 6 ft apart). Each beam will be simply supported at both ends on bearing pads. Load will be applied using an Enerpac RR40018 actuator.

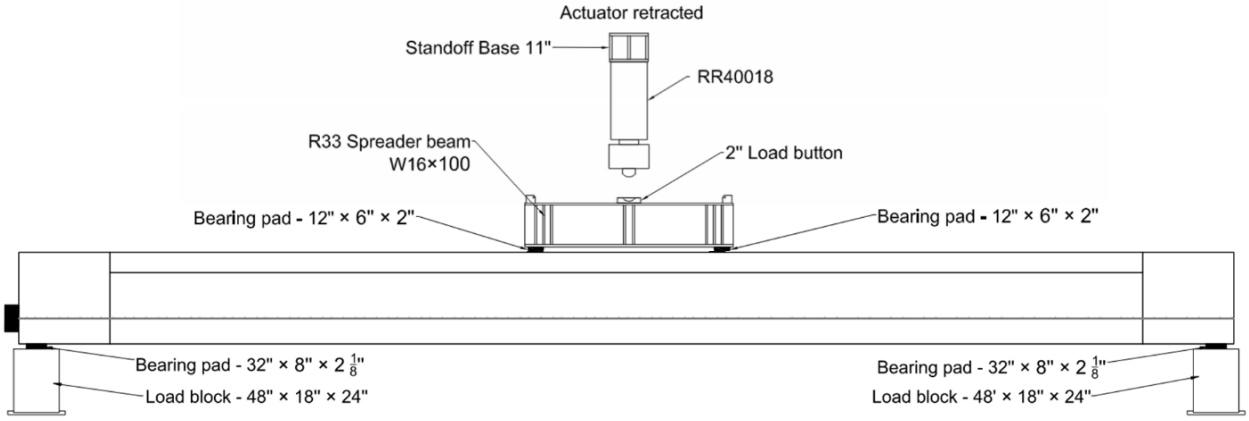

Figure G.5. Test setup for beam specimen S19.

Loading will be applied at a rate of 0.25 kip/sec (15 kip/min). Loading will be paused at key stages (Mcr, 20% Mn, 40% Mn, 60% Mn, and 70% Mn) as shown in Table G.3 to visually inspect the beam and to mark cracks.

Table G.3. Loading procedure for beam specimen S19

Intent	Applied Load (kip)	Expected deflection at load point (in.) [D3/D4]
20% M_n	36.7	0.14
40% M_n	92.0	0.38
M_{cr}	135.6	0.56
60% M_n	147.3	0.73
70% M_n	175.0	1.22
ε_c= 0.003 (M_n)	258.0	9.57

Ideally, the test will terminate when either compressive concrete crushing occurs, or when a plateau of load (vs. displacement) is reached. However, selected channels of instrumentation data will additionally be monitored (Figure G.6) so that testing can be terminated if applied loads or resulting displacement are found to significantly exceed the maximum expected values shown below.

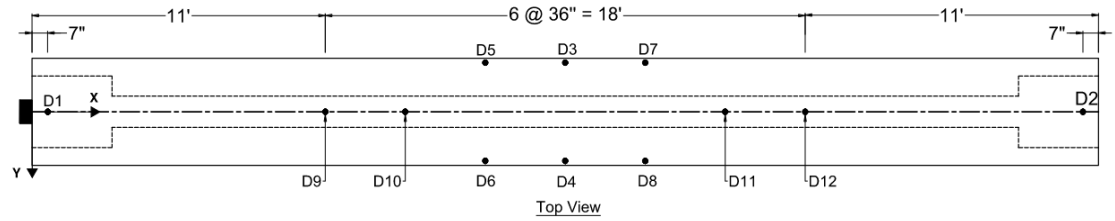

(a)

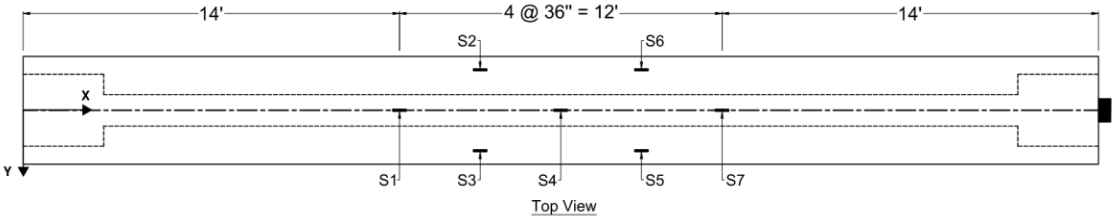

(b)

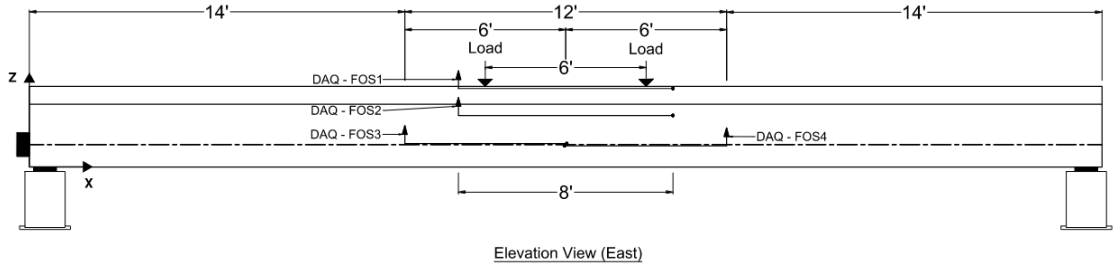

(c)

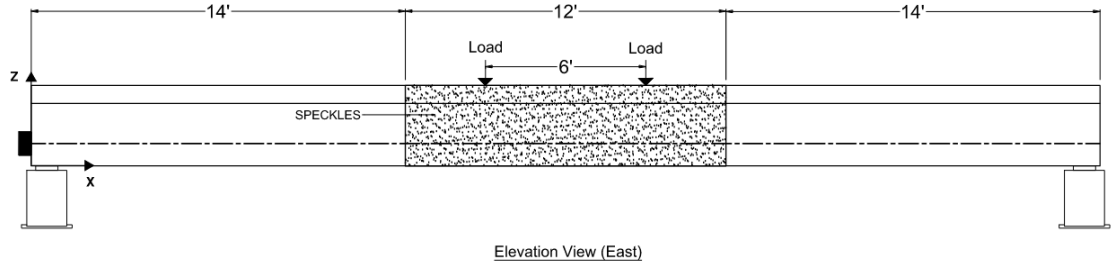

(d)

Figure G.6. Positions of instrumentation to monitor in real-time on S19 beam specimens: (a) Laser displacement transducer; (b) foil strain gage; (c) fiber optic sensor; and (d) digital image correlation.

Testing Protocol for D19-M Beam Specimens

Beam specimens D19-M (untreated and treated) will be tested in a four-point bending setup as shown in Figure G.7. The beam will be subjected to two-point loads offset 3ft from either side of midspan (i.e., 6 ft apart). Each beam will be simply supported at both ends on bearing pads. Load will be applied using an Enerpac RR40018 actuator.

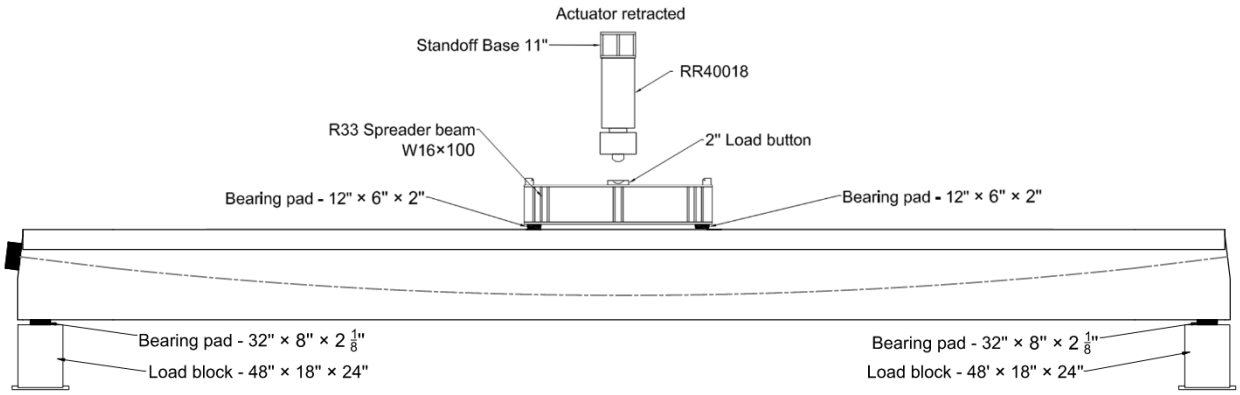

Figure G.7. Test setup for beam specimen D19-M.

Loading will be applied at a rate of 0.25 kip/sec (15 kip/min). Loading will be paused at key stages (Mcr, 20% Mn, 40% Mn, 60% Mn, and 70% Mn) as shown in Table G.4 to visually inspect the beam and to mark cracks.

Table G.4. Loading procedure for beam specimen D19-M

Intent	Applied Load (kip)	Expected deflection at load point (in.) [D3/D4]
20% M_n	38.0	0.16
40% M_n	94.0	0.39
M_{cr}	139.4	0.60
60% M_n	150.0	0.79
70% M_n	178.2	1.46
ε_c= 0.003 (M_n)	264.8	11.91

Ideally, the test will terminate when either compressive concrete crushing occurs, or when a plateau of load (vs. displacement) is reached. However, selected channels of instrumentation data will additionally be monitored (Figure G.8) so that testing can be terminated if applied loads or resulting displacement are found to significantly exceed the maximum expected values shown below.

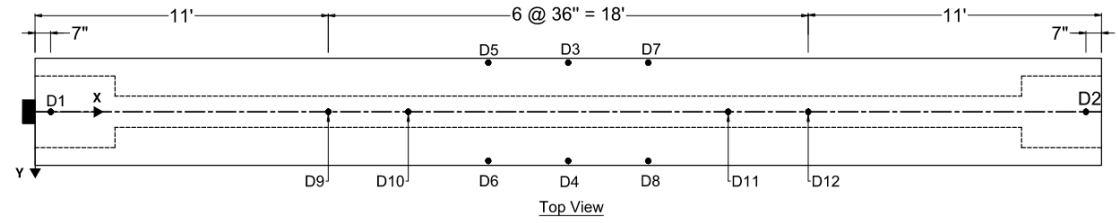

(a)

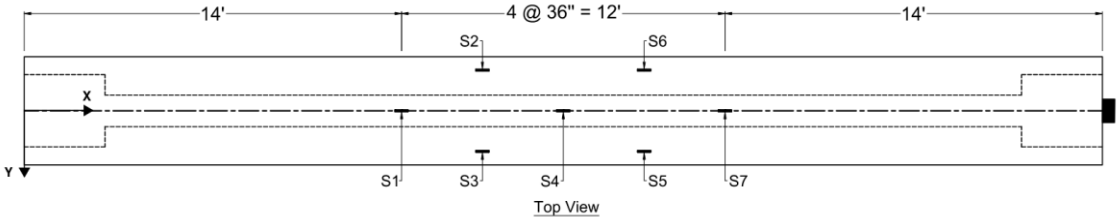

(b)

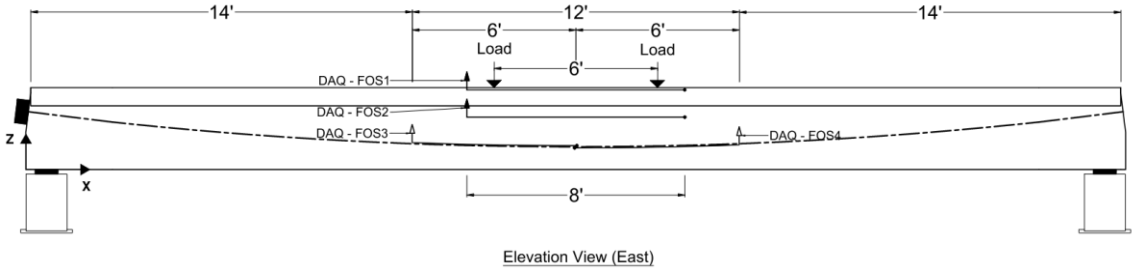

(c)

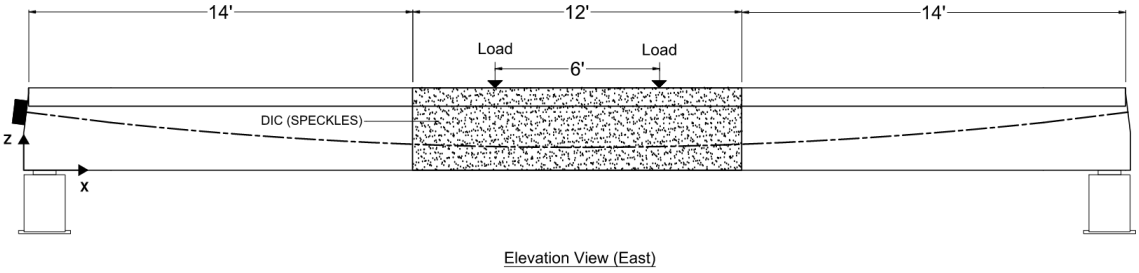

(d)

Figure G.8. Positions of instrumentation to monitor in real-time on D19-M beam specimens: (a) Laser displacement transducer; (b) foil strain gage; (c) fiber optic sensor; and (d) digital image correlation.

Testing Protocol for D19-P Beam Specimens

Beam specimens D19-P (untreated and treated) will be tested in a four-point bending setup as shown in Figure G.9. The beam will be subjected to two-point loads offset 3ft from either side of midspan (i.e., 6 ft apart). Each beam will be simply supported at both ends on bearing pads. Load will be applied using an Enerpac RR40018 actuator.

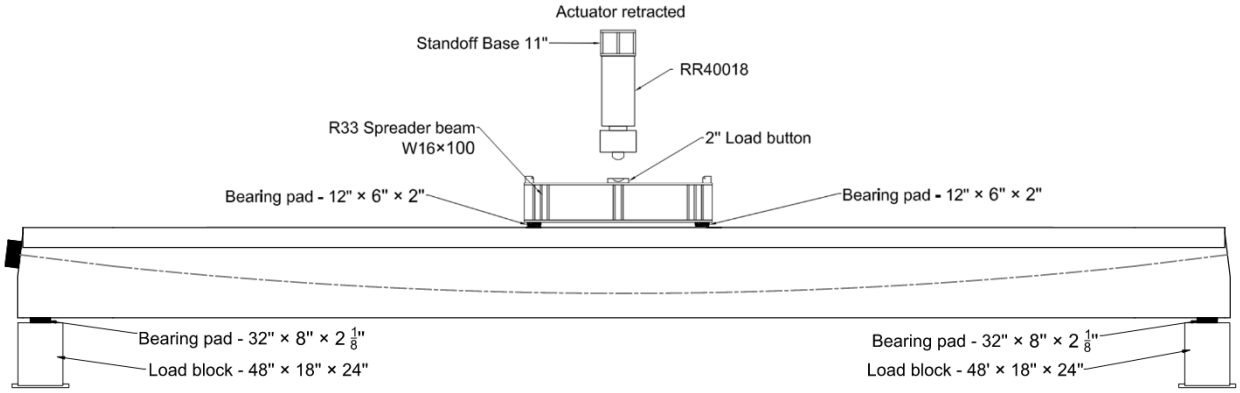

Figure G.9. Test setup for beam specimen D19-P.

Loading will be applied at a rate of 0.25 kip/sec (15 kip/min). Loading will be paused at key stages (Mcr, 20% Mn, 40% Mn, 60% Mn, and 70% Mn) as shown in Table G.5 to visually inspect the beam and to mark cracks.

Table G.5. Loading procedure for beam specimen D19-P

Intent	Applied Load (kip)	Expected deflection at load point (in.) [D3/D4]
20% M_n	38.0	0.16
40% M_n	94.0	0.39
M_{cr}	139.4	0.60
60% M_n	150.0	0.79
70% M_n	178.2	1.46
ε_c= 0.003 (M_n)	264.8	11.91

Ideally, the test will terminate when either compressive concrete crushing occurs, or when a plateau of load (vs. displacement) is reached. However, selected channels of instrumentation data will additionally be monitored (Figure G.10) so that testing can be terminated if applied loads or resulting displacement are found to significantly exceed the maximum expected values shown below.

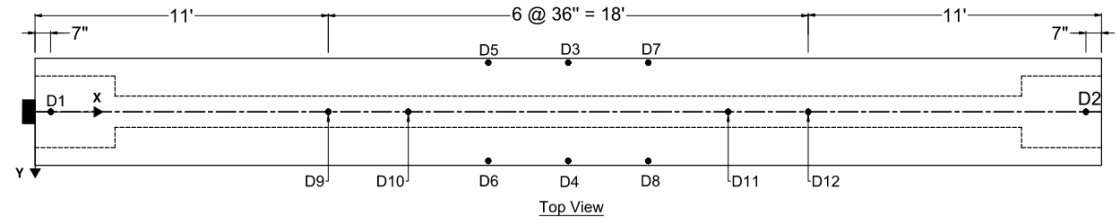

(a)

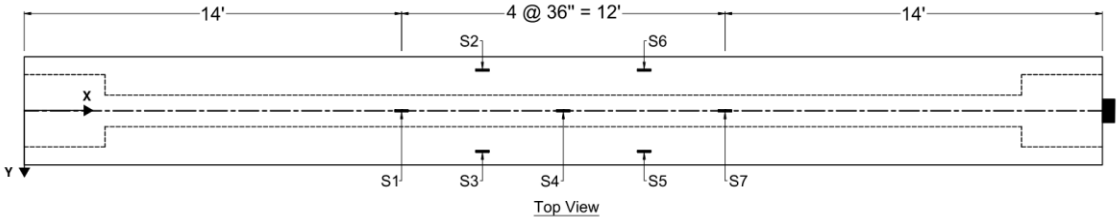

(b)

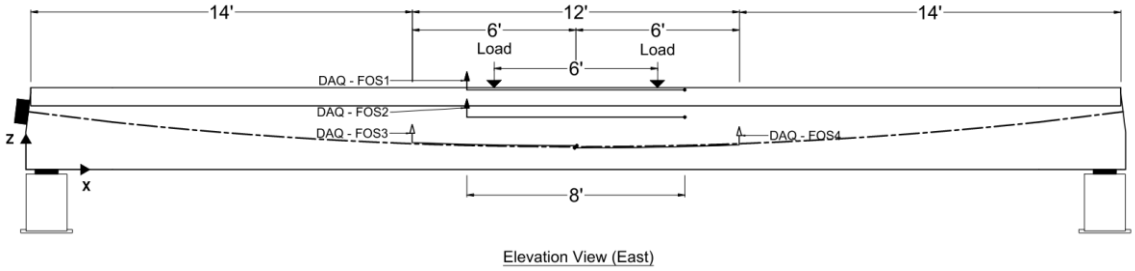

(c)

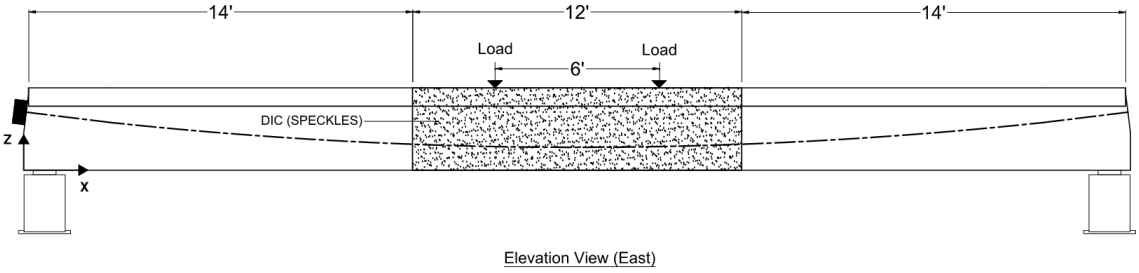

(d)

Figure G.10. Positions of instrumentation to monitor in real-time on D19-P beam specimens: (a) Laser displacement transducer; (b) foil strain gage; (c) fiber optic sensor; and (d) digital image correlation.